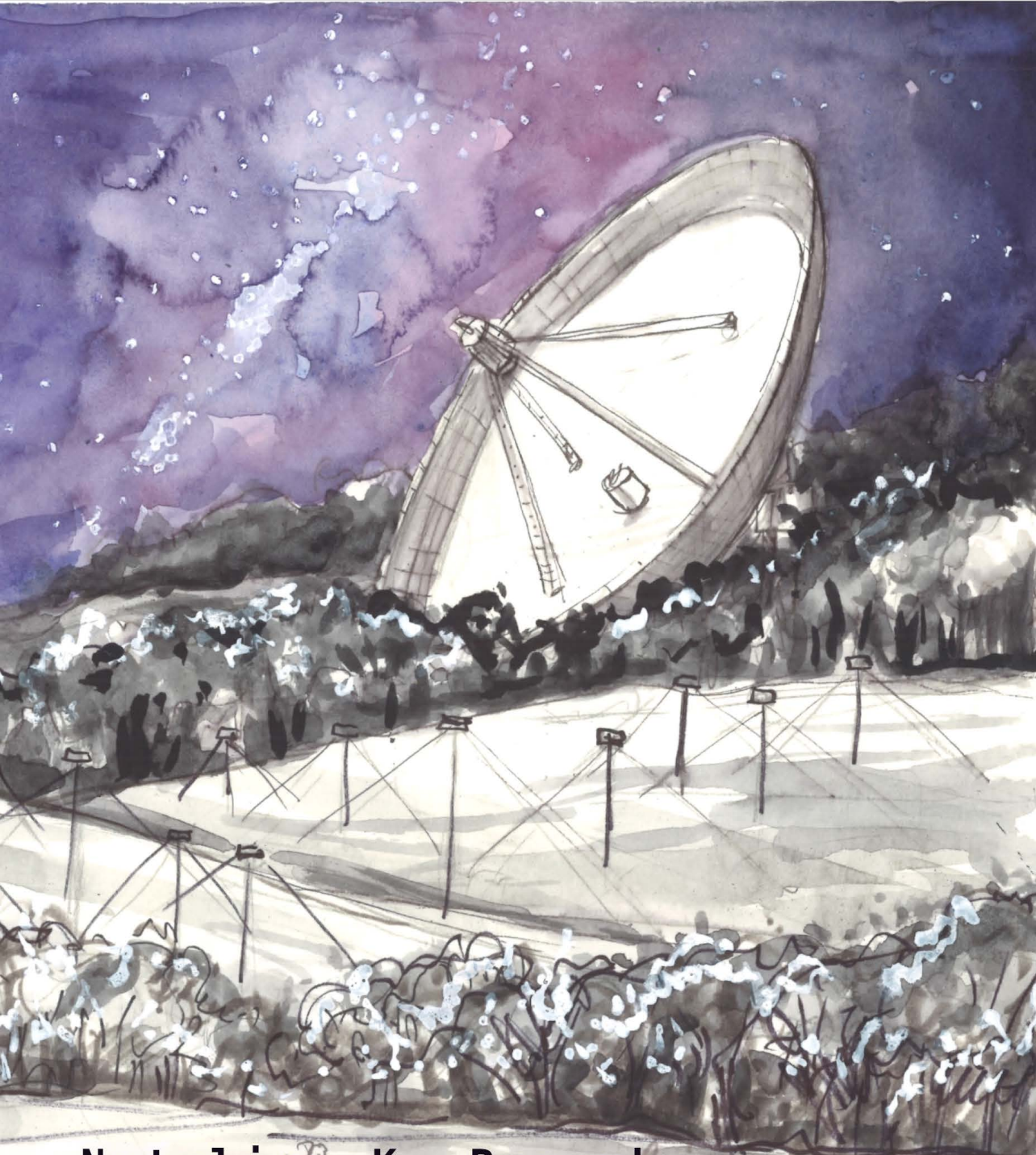

Nataliya K. Porayko

PROBING THE INTERSTELLAR MEDIUM AND DARK MATTER WITH PULSARS

Probing the Interstellar Medium and Dark Matter with Pulsars

Dissertation

zur

Erlangung des Doktorgrades (*Dr. rer. nat.*)

der

Mathematisch-Naturwissenschaftlichen Fakultät

der

Rheinischen Friedrich–Wilhelms–Universität, Bonn

vorgelegt von

Nataliya Konstantinovna Porayko

aus

Moskau, Russland

Bonn 2020

Angefertigt mit Genehmigung der Mathematisch-Naturwissenschaftlichen Fakultät
der Rheinischen Friedrich–Wilhelms–Universität Bonn

1. Referent: Prof. Dr. Michael Kramer
2. Referent: Prof. Dr. Frank Bertoldi
Tag der Promotion: 28.10.2019
Erscheinungsjahr: 2020

Diese Dissertation ist auf dem Hochschulschriftenserver der ULB Bonn unter
http://nbn-resolving.de/urn:nbn:de:hbz:5n-56982 elektronisch publiziert

Abstract

by Nataliya K. Porayko

for the degree of

Doctor rerum naturalium

Pulsars are rapidly rotating, highly magnetised neutron stars which emit electromagnetic radiation from their magnetic poles in the form of highly collimated beams. Their extreme properties, such as strong gravitational fields and supranuclear densities in their interiors, along with their high rotational stabilities, make them not only fascinating objects, but also unique laboratories for a wide variety of physical experiments. Pulsars are also known as a powerful tool to probe the interstellar medium (ISM) and its constituents in the Miky Way. Before reaching Earth, pulsar radiation propagates through the matter which fills the space between the source and observer. This matter leaves a distinct imprint in the registered signals from pulsars. In this thesis we focus on investigating these propagation effects in order to probe the non-baryonic entities in the Milky Way, namely interstellar magnetic fields and dark matter.

The first part of the thesis is dedicated to the investigation of Galactic magnetic fields, which are a major agent in the dynamics and energy balance of the ISM, and general evolution of the Galaxy. Small-scale turbulent magnetic fields in the Milky Way can be probed by monitoring variations in the Faraday rotation of linearly polarised radiation of pulsars. Following this idea, we use high-cadence, low-frequency observations from a set of selected pulsars carried out with German LOw-Frequency ARray (LOFAR) stations. The method that is used to determine the Faraday rotation measures (RMs) of pulsar signals is the Bayesian generalised Lomb-Scargle periodogram technique, developed in this thesis. We find that measured RMs are strongly affected by the highly time-variable terrestrial ionosphere. The observed ionospheric RM variations are five to six orders of magnitude larger than the astrophysical signal from a magnetised plasma. We have mitigated the ionospheric contribution assuming a thin-layer model of the ionosphere. Within this approximation, the electron densities are reconstructed from GPS-derived ionospheric maps, and magnetic fields are obtained from semi-empirical geomagnetic models. We show the comparison of different ionospheric maps and investigate the systematics and correlated noise generated by the residual ionospheric Faraday rotation using several-month-long pulsar observations. We conclude that for the best ionospheric maps the ionospheric RM corrections are accurate to $\sim 0.06 - 0.07\,\mathrm{rad\,m^{-2}}$, which defines our sensitivity towards long-term astrophysical RM variations. Following these results, we investigate the sensitivity to the turbulence in the magnetised ISM between the pulsar and observer. For this purpose, we have used three-year-long LOFAR pulsar observations. No astrophysically credible signal has been detected. We

discuss implications of the non-detection and analyse the possibilities for future investigations.

The second part of this thesis deals with dark matter – a matter which accounts for about a quarter of the energy density of the Universe, and the nature of which is still under debate. The ultralight scalar field dark matter (also known as "fuzzy" dark matter), consisting of bosons with extremely low masses of $m \sim 10^{-22}\,\mathrm{eV}$ and is one of the compelling dark matter candidates, which solves some of the problems of the conventional cold dark matter hypothesis. It was shown by Khmelnitsky and Rubakov that "fuzzy" dark matter in the Milky Way induces oscillating gravitational potentials, leaving characteristic imprints in the times of arrival of radio pulses from pulsars. We search for traces of ultralight scalar-field dark matter in the Galaxy using the latest Parkes Pulsar Timing Array dataset that contains the times of arrival of 26 pulsars regularly monitored for more than a decade. No statistically significant signal has been detected. Therefore, we set an upper limit on the local dark matter density assuming the "fuzzy" dark matter hypothesis. Our stringent upper limits are obtained in the low-boson-mass regime: for boson masses $m < 10^{-23}\,\mathrm{eV}$, our upper limits are below $6\,\mathrm{GeV\,cm^{-3}}$, which is one order of magnitude above the local dark-matter density inferred from kinematics of stars in the Milky Way. We conclude by discussing the prospects of detecting the "fuzzy" dark matter with future radio astronomical facilities.

To my ancestors and offspring

Acknowledgements

This PhD thesis is not only my personal achievement, but it was rather supported and motivated by many people.

In the beginning, I would like to thank my scientific advisers, who had direct influence on the work presented here. Many thanks to Dr. Aristeidis Noutsos, who has supervised me on a regular basis, for his wise compromise between ruling me with an iron fist and giving me full scientific freedom. I would like to thank my scientific adviser Dr. P.W. Verbiest for showing me practical scientific hacks and highlighting pitfalls of the scientific world, which are to be avoided. Special thanks to my adviser Dr. Caterina Tiburzi, who was ready to help 24 hours/7 days a week. Caterina, I appreciate your careful supervision and motivation, especially during periods of frustration and hopelessness. I am very thankful that I had a chance to be supervised by one of the icons of pulsar astronomy Prof. Dr. Michael Kramer. Due to his status, it was challenging to get a hold of him at the office, however, he was always available in virtual space and was able to solve critical issues in a microsecond (no exaggeration here!).

Big thanks to post-docs and staff members at the MPIfR and Bielefeld University. It was a great pleasure to work shoulder to shoulder with these outstanding experts. I would like to highlight Julian Dönner, Olaf Wucknitz and Jörn Künsemöller for their help with LOFAR data and software. Many thanks to David Champion, Gregory Desvignes, Ann Mao and Dominic Schnitzeler for their scientific assistance.

I would like to acknowledge the excellent work of our secretaries and administration: Frau Kira Kühn, Frau Barbara Menten and Frau Tuyet-Le Tran, who were always helpful in clarifying the subtlety of German laws and trying to protect us from direct interaction with the German bureaucracy. Special thanks goes to Frau Schneider for spreading positive vibes to everyone who passes by the reception desk of the MPIfR.

I would like to acknowledge my friends from the MPIfR for an absolutely unique atmosphere which gave birth to many interesting discussions and ideas (and potential start-ups). In particular, Mary Cruses, Alessandro Ridolfi, Vika Yankelevich, Hans Nguyen, Marina Beresina, Joey Martinez, James McKee, Nicolas Caballero and Patrick Lazarus. Many thanks to Eleni Graikou, my long-term officemate. Although, we had our ups and downs, I still think tandem Eleni-Natasha was quite successful. I would like to thank Tilemachos Athanasiadis and Ralph Eatough, who have brought out the musician in me. And of course, I would like to thank my boyfriend Henning Hilmarsson, for his $\infty + 1$ patience and kindness.

I would like to acknowledge my external collaborators. Thanks to Yuri Levin, Xingjiang Zhu and George Hobbs, who offered me an interesting project with the Australian PPTA group (which eventually became one of the chapters of this thesis) and were of great assistance throughout the project. I would like to thank my colleagues and friends from SAI and ITEP. In particular my former scientific advisers Prof. Dr. Valentin Rudenko and Dr. Dmitry Litvinov, my colleagues Prof. Dr. Konstantin Postnov and Prof. Dr. Sergei Blinnikov with whom I have continued exciting scientific

collaboration and who have always impressed me by the breadth of their knowledge and their scientific intuition.

I would also like to thank Aristeidis Noutsos, Joris Verbiest, Michael Kramer, Caterina Tiburzi, Henning Hilmarsson, Dominic Schnitzeler, Sergei Blinnikov, Ann Mao, James McKee for reading all or parts of my thesis. Your comments helped me to improve both the stylistics and content of the text.

Thanks to many people outside of work. A special mention is for my friend Nastia Naumenko for sharing with me her highly peculiar view of life. I would also like to thank her for drawing the cover picture of this thesis. My university friends (my ugly cousins), especially Elena Kyzingasheva and Anna Sinitovish, who encouraged me to stay in academia. I would like to acknowledge Tim Keshelava, Bulat Nizamov, Valera Vasiliev, Misha Ivanov and Sasha Zhamkov for their up-to-date scientific news and enlightening discussions. I would also like to thank my flatmate Katharina Rotté, who showed me many sides of German culture.

Finally, I would like to thank my family, who was far away physically, but always close mentally. To my cousin Julia for cheering us up. Many thanks to my grandparents, my mom and dad, who were triggering my interest in science since childhood, and who have taught me to "handle so, dass du die Menschheit sowohl in deiner Person, als in der Person eines jeden anderen jederzeit zugleich als Zweck, niemals bloß als Mittel brauchst."

Contents

1 Introduction **3**
- 1.1 Historical overview . . . 4
- 1.2 Birth of a neutron star . . . 4
- 1.3 Fundamental properties of NSs and pulsars . . . 5
  - 1.3.1 Emission properties of pulsars . . . 6
  - 1.3.2 Spin-down, braking index and pulsar ages . . . 9
  - 1.3.3 Pulsar evolution . . . 12
- 1.4 Propagation of pulsar signals through the media . . . 13
  - 1.4.1 Dispersion . . . 13
  - 1.4.2 Scattering and Scintillation . . . 15
  - 1.4.3 Faraday rotation . . . 16
- 1.5 Scientific applications of pulsars . . . 18
- 1.6 Pulsars as probes of the interstellar medium and dark matter . . . 20
  - 1.6.1 The interstellar medium . . . 20
  - 1.6.2 Dark matter . . . 22
- 1.7 Thesis outline . . . 24

2 Practical aspects of pulsar observations **27**
- 2.1 Radio observations of pulsars . . . 27
- 2.2 Low-frequency pulsar observations with phased arrays . . . 29
  - 2.2.1 German LOFAR stations. German long-wavelength consortium. . . 31
- 2.3 Pulsar timing . . . 34
- 2.4 On probing pulsar polarisation . . . 40
  - 2.4.1 Stokes parameters . . . 40
  - 2.4.2 Modelling the Faraday effect: RM measurement techniques . . . 42

3 Bayesian Generalised Lomb-Scargle Periodogram **49**
- 3.1 Basic definitions . . . 49
- 3.2 Derivation of the marginalised posterior probability . . . 51
- 3.3 Limitations of the method and ways for further improvement . . . 53

4 Testing the ionospheric Faraday rotation with LOFAR **57**
- 4.1 Introduction . . . 58
- 4.2 Observations and Data Reduction . . . 60
  - 4.2.1 On modelling the ionospheric RM variations: thin layer ionospheric model . . . 62
- 4.3 Systematics in the RM residuals . . . 67
  - 4.3.1 Analysis of RM residuals on timescales up to one year . . . 69
  - 4.3.2 Analyis of RM residuals on timescales beyond one year . . . 72
- 4.4 Discussions and Conclusions . . . 74

5 Investigation of interstellar turbulence with pulsars **81**
5.1 Introduction . . . 82
5.2 Observations . . . 83
5.3 RM variations from the turbulent ISM: mathematical description . . . 84
5.3.1 Theoretical structure function of RM variations . . . 86
5.3.2 Theoretical covariance function of RM variations . . . 87
5.4 Comparison with observations: parameter estimation and upper limits . 88
5.4.1 Structure function analysis . . . 88
5.4.2 Covariance function analysis . . . 89
5.5 Conclusions . . . 96

6 PPTA constraints on ultralight scalar-field dark matter **99**
6.1 Introduction . . . 100
6.2 The pulsar timing residuals from fuzzy dark matter . . . 104
6.3 PPTA data and noise properties . . . 105
6.3.1 Observations and timing analysis . . . 105
6.3.2 The likelihood function . . . 106
6.3.3 Noise modeling . . . 108
6.4 Search techniques and Results . . . 113
6.4.1 Bayesian analysis . . . 113
6.4.2 Frequentist analysis . . . 117
6.4.3 Upper limits . . . 118
6.5 Future prospects . . . 120
6.6 Conclusions . . . 123

7 Concluding remarks and future plans **125**
7.1 Studying the magnetised ISM with pulsars . . . 125
7.1.1 Future plans . . . 126
7.2 Studying dark matter with pulsars . . . 127
7.2.1 Future plans . . . 128

A Earth-term limits and effects of SSE **131**

B Noise properties for six PPTA pulsars **133**

Bibliography **135**

Nomenclature

Astronomical and Physical Constants

Speed of light	$c = 2.9979 \times 10^{10}\,\mathrm{cm\,s^{-1}}$
Gravitational constant	$G = 6.670 \times 10^{-8}\,\mathrm{dynes\,cm^2\,gr{-}1}$
Planck's constant	$h = 6.626 \times 10^{-27}\,\mathrm{erg\,s}$
Electron mass	$m_\mathrm{e} = 9.110 \times 10^{-28}\,\mathrm{gr}$
Proton mass	$m_\mathrm{p} = 1.673 \times 10^{-24}\,\mathrm{gr}$
Astronomical unit	$1\,\mathrm{AU} = 1.496 \times 10^{13}\,\mathrm{cm}$
Parcec	$1\,\mathrm{pc} = 3.086 \times 10^{18}\,\mathrm{cm}$
Solar mass	$1\,\mathrm{M_\odot} = 1.989 \times 10^{27}\,\mathrm{gr}$
Solar radius	$1\,\mathrm{R_\odot} = 6.960 \times 10^{10}\,\mathrm{cm}$
Solar luminosity	$1\,\mathrm{L_\odot} = 3.9 \times 10^{33}\,\mathrm{erg\,s^{-1}}$

Frequently Used Acronyms

ADC	Analogue-to-digital converter
BGLSP	Bayesian generalised Lomb-Scargle periodogram
CDM	Cold dark matter
CME	Coronal mass ejection
CPU	Central processing unit
DFT	Discrete fourier transform
DM	Dispersion measure
EoS	Equation of state
ESE	Extreme scattering event
FDM	"Fuzzy" dark matter
FFT	Fast Fourier transform
FT	Fourier transform
GLOW	German Long-Wavelength consortium
GPS	Global Positioning System
GPU	Graphical processing unit
GW	Gravitational wave
HBA	High-band antenna
IRI	International Reference Ionosphere
ISM	Interstellar medium
LBA	Low-band antenna
LOFAR	LOw-Frequency ARray
LoS	Line of sight
MRP	Mildly recycled pulsar
MSP	Millisecond pulsar
NFW	Navarro-Frenk-White
NS	Neutron star
PSR	Pulsar
PFB	Polyphase filterbank
PPTA	Parkes pulsar timing array
PPA	Polarisation position angle
PTA	Pulsar timing array
QCD	Quantum chromodynamics
RFI	Radio frequency interference
RM	Rotation measure
rms	Root-mean square
SF	Structure function
S/N	Signal-to-noise ratio
SMBHB	Super-massive black hole binary
SKA	Square Kilometer Array
SSB	Solar System barycenter
SSE	Solar System ephemerides
TEC	Total electron content
TOA	Time of arrival
TT	Terrestrial Time
WN	White noise

Chapter 1

Introduction

Contents

1.1 Historical overview . . . 4
1.2 Birth of a neutron star . . . 4
1.3 Fundamental properties of NSs and pulsars . . . 5
1.3.1 Emission properties of pulsars . . . 6
1.3.2 Spin-down, braking index and pulsar ages . . . 9
1.3.3 Pulsar evolution . . . 12
1.4 Propagation of pulsar signals through the media . . . 13
1.4.1 Dispersion . . . 13
1.4.2 Scattering and Scintillation . . . 15
1.4.3 Faraday rotation . . . 16
1.5 Scientific applications of pulsars . . . 18
1.6 Pulsars as probes of the interstellar medium and dark matter 20
1.6.1 The interstellar medium . . . 20
1.6.2 Dark matter . . . 22
1.7 Thesis outline . . . 24

First discovered in 1967 by J. Bell and A. Hewish (Hewish et al., 1968), pulsars are rapidly rotating, highly-magnetised neutrons stars (NSs) which emit electromagnetic radiation in the form of highly collimated beams. As they rotate, the emission beams sweep across the surrounding space in a similar fashion to a lighthouse. For this reason a distant observer registers the signal in the form of regular pulses of electromagnetic emission.

Pulsars are believed to be formed during the final gravitational collapse of massive stars and, therefore, they are characterised by extreme properties, e.g. super-nuclear densities and strong magnetic fields. Pulsars have stimulated research in many different branches of physics from magneto-hydrodynamics to general relativity, including the strong-field regime of relativistic gravity, and established themselves as powerful physical tools of probing a wide variety of astrophysical problems.

This chapter provides a brief introduction to the subject of pulsars, aspects of their formation, characteristics and observed phenomenology. The scientific application of pulsars with a particular emphasis on probing the interstellar medium (ISM) and dark matter is presented as well.

1.1 Historical overview

The concept of a NS started to develop in the early 1930s. While working on the evolution of stars, S. Chandrasekhar discovered the stellar mass limit[1], known today as the *Chandrasekhar limit*, above which an electron-degenerate stellar core cannot hold itself up against its own gravitational self-attraction, and is subject to further gravitational collapse (Chandrasekhar, 1931). Basing on the works of S. Chandrasekhar, L. Landau further speculated on the existence of stars with masses exceeding the Chandrasekhar limit, which eventually leads to extremly high densities of the stellar matter, such that "nuclei come into contact resulting in one gigantic nucleus" (Landau, 1932). The actual theoretical discovery of a star composed entirely of neutrons was made by W. Baade and F. Zwicky (Baade & Zwicky, 1934), shortly after the discovery of the neutron (Chadwick, 1932). In their work they have as well pondered the possible formation scenario of NSs via supernova explosions. A few years later R.Oppenheimer and G.Volkoff led the pioneering work on the structure of NSs and calculated the NS mass upper limit (Oppenheimer & Volkoff, 1939). Despite some interest in the topic in the following decades (e.g. Gamow & Schoenberg, 1941; Migdal, 1959; Ambartsumyan & Saakyan, 1960), NSs remained purely theoretical until the year 1967, when J. Bell, a graduate student at Cambridge University in England, detected a *pulsar*, an extraterrestrial source producing strictly periodic intensity fluctuations at radio frequencies (Hewish et al., 1968). During the first year after the discovery, the nature of pulsars was under debate: it was proposed that the pulsations could be produced by hot spots on surfaces of rotating white dwarfs (Ostriker, 1968), or could be due to the orbital motion of close binaries (Saslaw, 1968). However, the observed short pulse periods of the newly found Vela and Crab pulsars (Large et al., 1968; Staelin & Reifenstein, 1968) and the gradual spin-down in the pulsation rate of pulsars (Davies et al., 1969) did not support those models. Eventually, the link between pulsars and rotating NSs was suggested by T.Gold (Gold, 1968, 1969), basing on theoretical ideas by Pacini (1967), who had predicted just a few months before the discovery of pulsars the magnetic dipole emission of highly spinning magnetised NSs. High-precision mass measurements of pulsars (e.g. Taylor & Weisberg, 1989) and their association with supernovae remnants (e.g. Large et al., 1968; Staelin & Reifenstein, 1968; Frail & Kulkarni, 1991), along with other observational properties, left no room for doubt that pulsars are indeed rotating NSs.

1.2 Birth of a neutron star

NSs are thought to be the final stage of the evolution of massive ($\gtrsim 8M_\odot$) main-sequence stars[2]. During its life, a star supports itself against self-gravity by nuclear

[1] Due to unrealistic assumptions on the electron/nucleon ratio originally the limit calculated in Chandrasekhar (1931) was $0.91M_\odot$. This number was reconsidered later in e.g. Landau (1932).

[2] The link between the main-sequence mass of the star and the compact remnant is still under debate. According to current thinking, main-sequence stars with masses in the approximate range $8 - 20M_\odot$ leave NSs (Woosley et al., 2002, and reference therein). It is believed that a black hole is

fusion. For stars with low masses, the temperature and pressure in their cores is not high enough to ignite elements heavier than carbon. As a consequence, those stars end up as CO or He white dwarfs, supported by electron degenerate pressure. In contrast, the central temperature in the cores of more massive stars exceeds 3×10^9 K, which is sufficient to start silicon burning and to develop an *iron core*. The fusion of ^{56}Fe is an endothermic process, meaning that energy needs to be contributed in order to convert iron to heavier elements. Therefore, the iron core rapidly becomes unstable. Being unable to provide enough energy pressure to sustain its self-gravity, it starts to collapse, giving rise to a *core-collapse supernova*. This process is accompanied by the *neutronisation* of the core matter via inverse β-decay and photo-disentagration of ^{56}Fe into α-particles and neutrons. Consequently, the contracted core predominantly consists of cold degenerate neutrons with a small admixture of electrons and protons. At nuclear densities ($\sim10^{14}$g cm^{-3}), when interaction between nucleons is far from being negligible, the neutron gas becomes incompressible. The sudden 'stiffness' of the Equation of State (EoS) terminates the collapse of the core. At the same time the outer layers of the star are *bounced* outwards, forming a *supernova explosion*. The latter process signifies the birth of a NS[3]. For details on the evolution of massive stars see Arnett (1996); Woosley et al. (2002); Nadyozhin & Imshennik (2005) and reference therein. The resultant NS is not homogenous (e.g. Shapiro & Teukolsky, 1983; Chamel & Haensel, 2008). The atmosphere is formed by very hot (10^6 K) non-degenerate matter, which encapsulates the iron crust. Probing deeper into the star the density gradually increases, and the iron lattice dissolves into superfluid neutron gas with a small portion of superconductive protons. The composition of the inner core is poorly known and strongly depends on the EoS of the matter at super-nuclear densities (see Becker, 2009, for a review).

1.3 Fundamental properties of NSs and pulsars

Due to the conservation of the magnetic field flux and angular momentum, the resultant compact ball, which is $\sim 10-20$ km in diameter, possesses a strong magnetic field (up to 5×10^{12} G) and a high spin period ranging from a few milliseconds to seconds (Lorimer & Kramer, 2004). The formed magnetic field of a NS is dipolar to first order. The fast rotation of the magnetic dipole reinforces the generation of an electric field (Deutsch, 1955), whose magnitude then exceeds the gravitational force of the NS. Under this condition, charged particles are pulled off from the surface and they fill the space around the NS, forming a 'cocoon' called *magnetosphere*. The magnetosphere can co-rotate with a pulsar only up to a distance, called the *light cylinder radius*, $R_{\rm L}$, at which the speed of a co-rotating reference frame equals the speed of light (see Figure 1.1). Up to the radius of the light cylinder, the magnetic field lines of the NS are

formed, if a star has a larger mass. However, stars with masses around $50M_\odot$, due to their strong stellar winds and consequent stellar mass loss, can also in some cases end their lives as NSs (e.g. Spera et al., 2015; Ertl et al., 2016).

[3]Although the vast majority of NSs are formed via core-collapse supernovae, some alternative formation channels have been considered. See Heger et al. (2003) and Dessart et al. (2006) for details.

closed. In this region, the electrostatic field of charged particles in the magnetosphere shields the electric field generated by the rotating dipole. Beyond the light cylinder radius, the magnetic field lines of the NS are open. In this region, the plasma which is leaving the magnetosphere in the form of a relativistic wind must be continuously replenished by the pair production and charged particles lifted from the stellar surface (Spitkovsky, 2004), so the charge density of the open magnetosphere tends to restore the Goldreich-Julian density (Kramer et al., 2006a). It is the open magnetosphere that is subject to charged particle acceleration and consequent radiation generation in the form of highly collimated radio beams. Therefore, the size of the emission beam is mainly determined by the size of the open-field-line region. If the magnetic dipole is inclined by some angle $\alpha_{\rm m}$ from the rotation axis, the radiation beam co-rotating with the pulsar can sweep past an observer. As a consequence, the NS is observed as a pulsar. The period of repetition of the radio pulses coincides with the rotational period of the pulsar. Described above is a simplified model of the radio emission formation, which was developed in the works of Goldreich & Julian (1969); Radhakrishnan & Cooke (1969) and Komesaroff (1970). Within this thesis we will refer to it as the *standard model* of pulsar emission.

1.3.1 Emission properties of pulsars

Flux density spectra Pulsar emission is broadband. However, it is mainly visible at radio wavelengths. Within the standard model, the pulsar radio emission is formed in the following manner. As it was discussed before, in the active part of the magnetosphere the charged particles (electrons and positrons) are accelerated to very high energies by the strong electric field, induced by the time-variable magnetic flux. The relativistic particles moving along the open magnetic field lines will produce photons through the *curvature radiation* mechanism. These photons can eventually produce electron-positron pairs, which will undergo to further acceleration and hence they will emit even more energetic electromagnetic radiation. This secondary plasma generates the radiation in different spectral bands, depending on the part of the magnetosphere in which the radiation was actually formed. It is generally accepted that the observed radio emission is formed by the secondary plasma in a so-called *polar cap* in the vicinity to the magnetic poles of the pulsar at approximately $\leq$10 % of the light cylinder radius from the pulsar surface (see Figure 1.1). The spectrum of the resultant curvature emission, produced by the ensemble of charged particles with a range of energies, follows the power-law:

$$P(\nu) \sim \nu^{\kappa}, \tag{1.1}$$

where κ is the *spectral index* of the pulsar. This power-law spectrum has been confirmed by a number of observations. The measured mean spectral index is around -1.6 (e.g. Lorimer et al., 1995; Kramer et al., 1998; Bates et al., 2013). However, some of the pulsars show a more complex behaviour, namely flattening or turning over at lower frequencies (Izvekova et al., 1981; Maron et al., 2000).

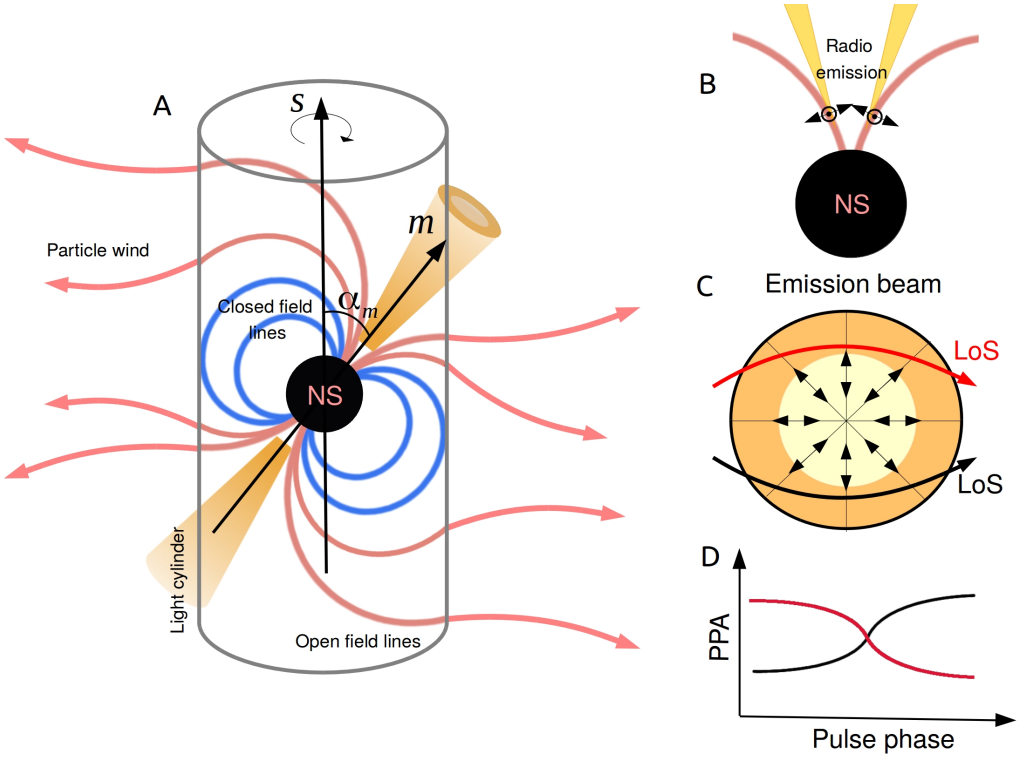

Figure 1.1: A) A schematic model of a pulsar. The NS is spinning around the spin axes $\boldsymbol{s}$. The corresponding light cylinder (the imaginary surface at which the corotation speed equals to speed of light) is shown with a grey thick line. The closed magnetic field lines encapsulated within the light cylinder, are shown in blue. The open magnetosphere and pulsar wind are shown in pink. The pulsar radiation beam shown in yellow, is aligned with the magnetic moment, $\boldsymbol{m}$. The angle between the spin axis $\boldsymbol{s}$ and magnetic moment $\boldsymbol{m}$ is α_m. B) The zoomed-in region where the pulsar radiation originates. The plane of linear polarisation of the ordinary mode is shown with black arrows. The plane of polarisation of the extraordinary mode is perpendicular to the plane of the figure. C) The pole-on view of the emission beam of the pulsar. The projections of the magnetic field lines are shown with thin black lines. The plane of linear polarisation of the received signal is shown with black arrows (only the ordinary mode is considered). As the LoS (thick red and black arrows) cuts the beam, the observer sees the typical S-shape swing in the PPA vs pulse phase diagram (sub-plot D). Note that the shape of the S-swing can change depending on the geometry of the beam.

The deviations from the simple power-law spectrum can be due to plasma instabilities, which are thought to take place in pulsar magnetosphere (Malofeev & Malov, 1980). The observed turnovers at GHz frequencies (Kijak et al., 2017), which exhibit some of the pulsars, could be caused by free-free absorption in the surrounding material (Rajwade et al., 2016).

Polarisation Soon after their discovery, pulsars established themselves as strongly linearly polarised radio sources. The degree of linear polarization is on average 40−60% but has been measured as 100% in some cases (Lyne & Smith, 1968). The origin of a large fraction of linear polarisation can be successfully explained within the standard model of pulsar emission as the consequence of curvature radiation of relativistic charged particles in the magnetosphere. The generated emission is elliptically polarised. The electric field of the radiation oscillates perpendicular to the magnetic field lines mainly in the plane of the orbit (ordinary mode). Besides the ordinary waves, there is a second component oscillating perpendicular to the orbit (extraordinary mode). Due to the different refractive indices, ordinary and extraordinary waves have different trajectories in the pulsar magnetosphere (Ginzburg, 1970). Therefore, two modes are expected to be beamed in different directions, after exciting the magnetosphere. Assuming that only one of the modes is visible, the polarisation position angle (PPA), which characterises the orientation of the plane of polarisation with respect to the line of sight (LoS) (see Section 2.4.1), changes gradually across the beam. As the pulsar rotates, the LoS crosses the beam, creating the typical S-swing in the PPA vs pulse-phase diagram (Radhakrishnan & Cooke, 1969, see Figure 1.1). These S-shape swings have been observed for some pulsars, which reaffirms the validity of the standard model (e.g. Johnston et al., 2008b). However, the majority of pulsars exhibit drastic changes of the PPA by 90°, which is commonly referred to as orthogonal jumps (Xilouris et al., 1998; Everett & Weisberg, 2001; Johnston et al., 2008b; Noutsos et al., 2015). It is speculated that these jumps may mark the transition between the ordinary and extraordinary modes (see e.g. Cordes et al., 1978; Petrova, 2001; Beskin & Philippov, 2012).

Pulsars also exhibit a small fraction of circular polarisation (typically less than 10%, Gould & Lyne, 1998). This can be due to the *Faraday conversion* of the linearly polarised component to circularly polarised light, taking place in the relativistic plasma of pulsar magnetospheres (Sazonov, 1969; Pacholczyk & Swihart, 1970; Kennett & Melrose, 1998; Ilie et al., 2019).

Individual and integrated pulse profiles Pulsar emission is not a stationary process which produces the radiation uniformly across the beam. In fact, short-term instabilities in the outflowing plasma can be the origin of the observed complex behaviour of *individual* pulses from a pulsar (see Figure 1.2). These individual pulses can exhibit a large variety of morphological characteristics, including giant pulses (Heiles & Campbell, 1970), nulling (Backer, 1970), drifting subpulses (Drake & Craft, 1968), and jitter (Helfand et al., 1975; Jenet et al., 1998). At the

same time, the *integrated* pulse profiles, which are formed by summing together hundreds or thousands of individual pulses, are remarkably stable in a given frequency band (Helfand et al., 1975; Rathnasree & Rankin, 1995). According to the simplified standard model of pulsar emission, the intensity of emitted radio waves decreases with increasing curvature radius of the magnetic field lines. In this case the radiation beam is shaped as a hollow cone (Komesaroff, 1970). As the LoS crosses the radiation cone, a one- or two-component profile should be observed. For the majority of sources, integrated pulse profiles have a more complex structure exhibiting multiple components, which can suggest the existence of unevenly distributed long-lived emitting patches in the open magnetosphere (Lyne & Manchester, 1988; Karastergiou & Johnston, 2007). Alternatively, the variety of pulse morphology can also be explained within the double-core-cone (Rankin, 1993) or the fan shaped beam models (Wang et al., 2014).

Despite many attempts to create a consistent model of pulsar emission which accounts for all observational data accumulated since the discovery of the first pulsar, there are still numerous theoretical aspects of the emission mechanism that are under debate. The scientific community is still in active search of a consistent solution (see e.g. Beskin et al., 1988; Asseo et al., 1990; Timokhin & Arons, 2013; Philippov et al., 2019)

1.3.2 Spin-down, braking index and pulsar ages

Long-term pulsar observations have shown that the pulsar spin frequency ν tends to decrease with time (Davies et al., 1969). Magnetic dipole radiation, gamma-ray emission and high-energy particle outflow are commonly considered to be the processes responsible for the gradual reduction of the rotational energy of pulsars. The general expression used to describe the spin-down rate of pulsars is a power-law (Lorimer & Kramer, 2004):

$$\dot{\nu} = -K\nu^n, \tag{1.2}$$

where K is a constant and n is the *braking index*, which can be further expressed as a function of the first and second spin frequency time derivatives:

$$n = \frac{\nu\ddot{\nu}}{\dot{\nu}^2}. \tag{1.3}$$

The braking index is an important quantity, which can shed light on the possible mechanisms responsible for the pulsar energy losses. Under the assumption that all pulsar rotational energy $E_{\rm rot}$ is lost through magnetic dipolar emission $\dot{E}_{\rm dp}$, the pulsar spin-down rate is:

$$\overbrace{J\nu\dot{\nu}}^{\dot{E}_{\rm rot}} = \overbrace{\frac{2}{3}\frac{|\boldsymbol{m}|^2\nu^4\sin^2\alpha_m}{c^3}}^{\dot{E}_{\rm dp}} \Rightarrow \dot{\nu} = -\frac{2|\boldsymbol{m}|^2\sin^2\alpha_m}{3Jc^3}\nu^3, \tag{1.4}$$

where $\boldsymbol{m}$ is the magnetic moment of the dipole and J is the NS moment of inertia. Comparing Equations (1.2) and (1.4) yields $n = 3$ for magnetic dipole radiation.

The braking indices can only be derived for pulsars for which ν, $\dot{\nu}$, and $\ddot{\nu}$ are known. The $\ddot{\nu}$ decreases rapidly with pulsar age, therefore the braking index has only been measured for young pulsars. Recent works (Archibald et al., 2016; Espinoza et al., 2017) estimate the braking indices to be in the range $0.9 < n < 3.15$, suggesting that dipole radiation is not the only process responsible for the observed pulsar spin-down. Moreover, in Johnston & Karastergiou (2017) it was shown that the observed braking index can change with time due to the decay of the inclination angle between the magnetic and rotation axes or due to a decay of the magnetic field itself.

Another useful characteristic that can be assessed by measuring ν and $\dot{\nu}$ is the *characteristic age* of a pulsar. From Equation (1.2) one gets:

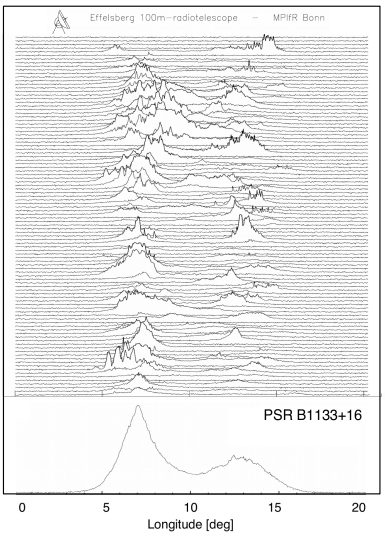

Figure 1.2: Individual pulses (top panel) and the integrated profile (bottom panel) of PSR B1133+16. The individual pulses vary in intensity and shape, while the averaged profile is impressively stable. The plot also exhibits pulse nulling. These data were taken with the Effelsberg telescope at 1.41 GHz. The plot is adapted from Kramer (1995).

$$\tau_n = \frac{\nu}{(n-1)\dot{\nu}} \left[1 - \left(\frac{\nu}{\nu_0} \right)^{n-1} \right], \tag{1.5}$$

where ν_0 is the initial spin frequency of the pulsar. Assuming again pure magnetic dipole braking ($n = 3$) and $\nu \ll \nu_0$ this expression simplifies to:

$$\tau_c = \frac{\dot{\nu}}{2\nu}. \tag{1.6}$$

For the vast majority of pulsars their age cannot be measured directly, unless through associations with supernova remnants, or, in even rarer cases, through association with an observed supernova explosion. τ_c gives an order-of-magnitude estimate of the age of slow pulsars. However, this value should be taken with caution, as Equation (1.6) is based on the simplified assumption of pure magnetic dipole braking, which doesn't seem to hold in reality (see discussions above). This is especially true for pulsars in binary systems, undergoing different evolutionary scenarios, which includes accretion and consequent spin-up of the pulsar[4].

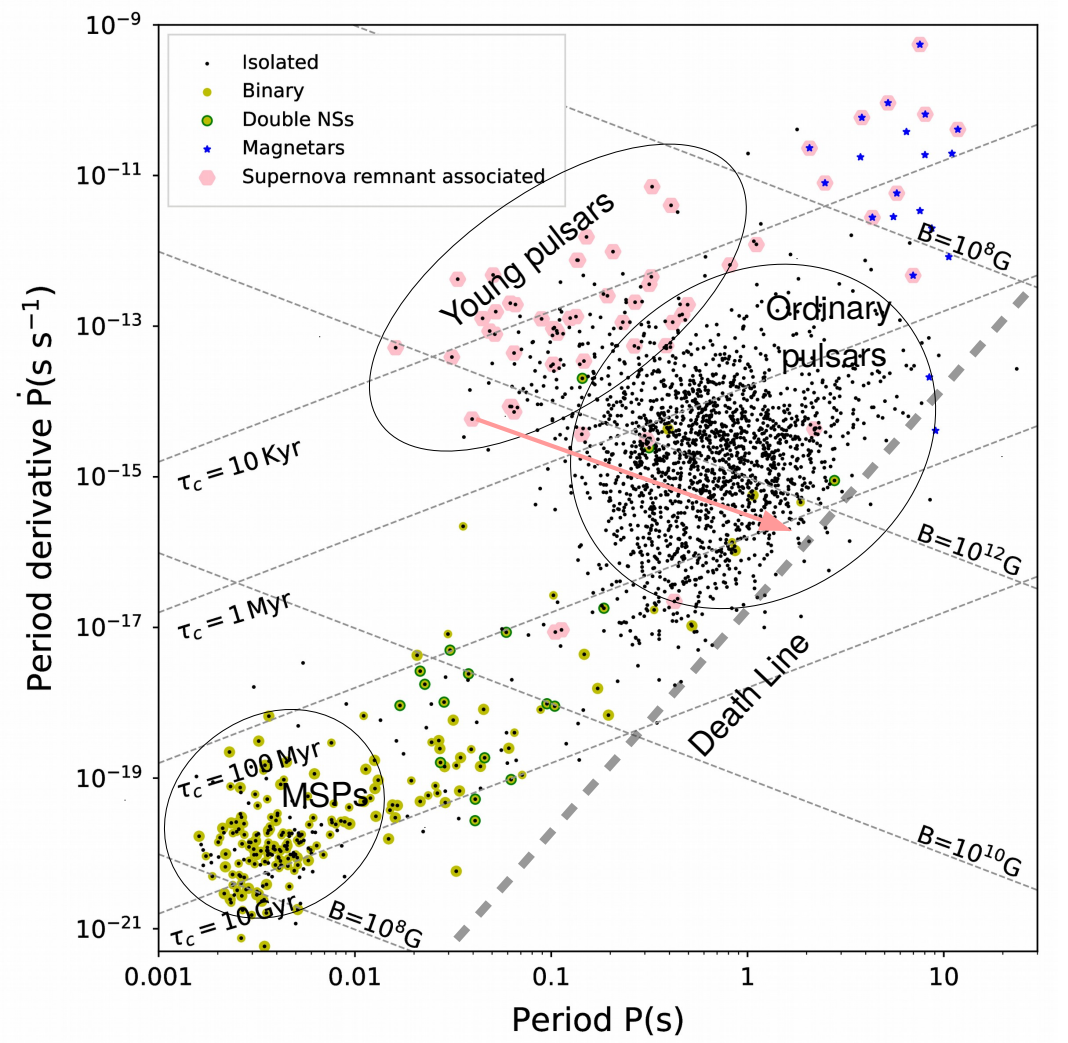

Figure 1.3: Period-Period derivative (P-$\dot{P}$) diagram of the currently known 2703 pulsars according to the ATNF catalogue (version 1.60, Manchester et al., 2005). The thin grey dashed lines show constant characteristic ages (Equation (1.6)) and constant magnetic field strengths (see Lorimer & Kramer, 2004). The ellipses show the most important subclasses of pulsars: young, ordinary and MSPs. The grey thick line represents the conventional death line model (Chen & Ruderman, 1993). The position of the death line depends on the mechanisms which drive the pulsar radio emission. The fact that there are few pulsars below the death line suggests that the physics of pulsar emission is not yet fully understood. The pink arrow shows the approximate path of an isolated pulsar during its rotation-powered phase assuming no magnetic decay (n=3). Mildly recycled pulsars are located in the 'transition' zone between the ordinary pulsars and MSPs.

1.3.3 Pulsar evolution

Isolated pulsars Many of the younger pulsars (i.e., observed close to their birth) are associated with their corresponding supernova remnants[5]. This evolutionary stage is characterised by short rotational periods ($0.01 - 1$ s) and large period derivatives ($> 10^{-15}$ s s^{-1}), implying small characteristic ages (< 100 kyr). Isolated pulsars are destined to reduce their spin frequency, due to the energy loss processes discussed in the previous section. Young pulsars will eventually turn into *regular* pulsars with periods of $\sim 0.5-1$ s. In turn, ordinary pulsars continue to spin down until they reach a point where their accelerating electric field potential is not high enough to eject charged particles in the magnetosphere. As a result, the pulsar radio emission ceases. At this stage, a NS becomes undetectable at almost all wavelengths[6].

A convenient way of tracing pulsar evolution is by using the so-called period-period derivative (P-$\dot{P}$) diagram (see Figure 1.3). During its lifetime, an isolated pulsar moves towards the bottom-right of the plot; the 'death line' marks the beginning of the 'radio-quiet' evolutionary stage.

Pulsars in binary systems For a pulsar in a binary system, its evolution is more complex than of an isolated pulsar due to the possible mass transfer from its stellar companion (e.g. Bhattacharya & van den Heuvel, 1991; Tauris & van den Heuvel, 2006). The accretion process starts when the companion star turns into a giant or supergiant and fills its Roche lobe. During this stage the Alfvén radius, $R_{\rm A} = \left(\frac{|\boldsymbol{m}|^4}{2GM\dot{M}^2}\right)^{1/7}$, becomes smaller than the light cylinder radius $R_{\rm L}$ and the corotation radius, $R_{\rm c} = \left(\frac{GM}{4\pi^2\nu^2}\right)^{1/3}$, where M is the mass of the NS (Lipunov, 1992). The mass exchange circularises the orbit and *recycles* the pulsar to millisecond periods (Radhakrishnan & Srinivasan, 1982). The accretion also increases the mass of the pulsar and suppresses its magnetic fields, which leads to orders of magnitude lower energy loss rates than in regular pulsars (e.g. Cumming et al., 2001). During the mass transfer the system is observed as an X-ray binary. After the mass transfer is terminated, the recycled pulsar returns to the rotationally-powered state. It is generally accepted that *millisecond pulsars* (MSPs), which are located at the bottom-left of the P-$\dot{P}$ diagram, are formed exactly through this scenario. *Mildly recycled* pulsars (MRPs) are believed to be formed from binary systems with more massive companion stars (Tauris & van den Heuvel, 2006), resulting in the faster evolution of the stellar companion and a shortened accretion stage. Being only partially spun up, MRPs have periods in the range $10 - 200$ ms and are located in the 'transition' zone between

[4] Moreover, the resultant spin frequencies of spin-up pulsars are so high that the assumption $\nu \ll \nu_0$ breaks down.

[5] The Crab and Vela pulsars are the most famous examples (Staelin & Reifenstein, 1968; Large et al., 1968)

[6] These pulsars emit only thermal optical or UV emission (Pavlov et al., 2017), which is extremely hard to detect due to their tiny radii.

regular pulsars and MSPs. In contrast to young and regular pulsars, recycled pulsars show remarkable rotational stability, which makes them a valuable tool for astrophysics and fundamental science, as discussed in the Section 1.5.

1.4 Propagation of pulsar signals through the media

Before being registered on Earth, pulsar emission is propagating through three distinct magnetoionic media: the ISM in our Galaxy, the interplanetary medium (Solar wind) and the terrestrial ionosphere. Although the ISM is a very dilute ionised gas, it affects the pulsar radiation the most in comparison to the other two, as the electromagnetic waves from pulsars must travel substantial distances of the order of hundreds of pc through the ISM. With constantly increasing precision of astronomical observations, for some sorts of astronomical problems, e.g. pulsar observations near the Solar conjunction (Tiburzi et al., 2019), the propagation effects of the other two media become noticeable and should be taken into account along with the ISM effects.

On its way through magnetoionic media, beamed pulsar radiation at radio frequencies is affected in several ways, primarily by *dispersion* and *Faraday rotation*. On top of that, if the intervening plasma contains inhomogeneities, e.g. in the form of turbulence or filaments, two other propagation effects, *scintillation* and *scattering* take place. All these four effects have strong dependencies with the inverse of the radiation frequency, and can significantly corrupt the broad-band signal, particularly at low observing frequencies.

1.4.1 Dispersion

It can be shown from Maxwell's equations that the group velocity v_g of electromagnetic waves propagating through plasmas depends on the wave's frequency: $v_\mathrm{g}(f) = cn(f)$, where c is the speed of light and n is the refractive index. This phenomenon is known in optics as dispersion. For a non-relativistic cold magnetised ionised medium, the dispersive delay (when compared to propagation time in vacuum) of a pulse is given by (Suresh & Cordes, 2019):

$$\Delta t = \int \frac{\mathrm{d}r}{cn(f)} - \frac{L}{c} \simeq \frac{e^2}{2\pi m_e c} \overbrace{\int n_e \mathrm{d}r}^{\mathrm{DM}} \frac{1}{f^2} \pm \frac{c^2}{2\pi} \overbrace{\frac{e^3}{2\pi (m_e c^2)^2} \int n_e \boldsymbol{B} \mathrm{d}\boldsymbol{r}}^{\mathrm{RM}} \frac{1}{f^3} + \frac{3e^4}{8\pi^2 m_e^2 c} \overbrace{\int n_e^2 \mathrm{d}r}^{\mathrm{EM}} \frac{1}{f^4}, \tag{1.7}$$

where n_e is the electron density, m_e is the mass of the electron, $\boldsymbol{B}$ is the magnetic field vector, L is the distance to the pulsar, and $\mathrm{d}\boldsymbol{r}$ is an infinitesimal distance interval along the LoS from the source to the observer. The $\pm$ sign in the second term corresponds to left- and right-hand polarised waves respectively. The integration runs along the optical path from the source to the observer. The above expression for the propagation time can be rewritten in terms of LoS-integrated observables, known as *dispersion measure*

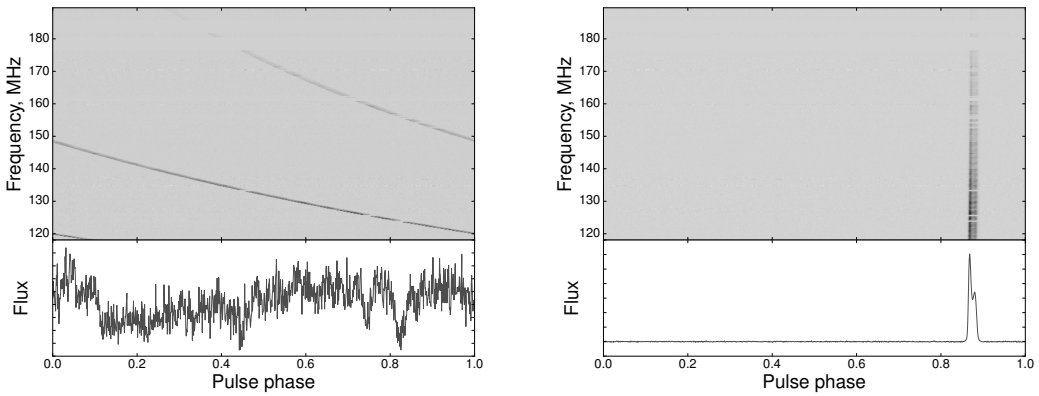

Figure 1.4: The effect of dispersion on timing data of PSR J0837+0610 (DM=12.89 rad m^2). This observation was taken with the German LOFAR HBA. *Left*: the pulsar signal shows a characteristic quadratic sweep due to the dispersion effect across the frequency band. The integrated flux profile shown in the bottom panel is fully smeared. *Right*: the same pulsar observation, but de-dispersed. The bottom panel shows the restored flux profile.

(DM), *rotation measure* (RM)[7] and *emission measure* (EM):

$$\Delta t = 4.15\,\mathrm{ms}\frac{\mathrm{DM}}{f^2} \pm 2.86\times10^{-9}\,\mathrm{ms}\frac{\mathrm{RM}}{f^3} + 0.25\times10^{-9}\,\mathrm{ms}\frac{\mathrm{EM}}{f^4}\,, \tag{1.8}$$

where we have used the standard units for DM (pc cm^{-3}), RM (rad m^{-2}), EM (pc cm^{-6}), and f (GHz). With current instrumentation we are only sensitive to the DM term, which is nine to ten orders of magnitude greater than the other two. To a high accuracy the difference in the arrival time of a pulsar signal received at two observing frequencies f_1 and f_2 is therefore:

$$\delta t \simeq 4.15\times\mathrm{ms}\frac{\mathrm{DM}}{\mathrm{pc\ cm^{-3}}}\left[\left(\frac{f_1}{\mathrm{GHz}}\right)^{-2} - \left(\frac{f_2}{\mathrm{GHz}}\right)^{-2}\right]. \tag{1.9}$$

Even for relatively nearby pulsars with DM=30 pc cm^{-3} observed at central frequency of 150 MHz, the dispersive delay across a bandwidth of 100 MHz is ∼10 s, which exceeds the periods of the vast majority of pulsars (see Figure 1.3), rendering them undetectable. The process of compensation for this effect is called *de-dispersion* (Lorimer & Kramer, 2004) and is described in Section 2.1.

For the majority of pulsars DM changes with time. The main contribution to these changes comes from the turbulent ISM as the pulsar moves relative to the Earth, and the LoS intersects different parts of the ionised media. The induced variations are typically of order 10^{-3} pc cm^{-3} on a several year timescale (Keith et al., 2013; Jones et al., 2017). As we will see in Chapter 6 the DM variations from the ISM, if not

[7] See Section 1.4.3.

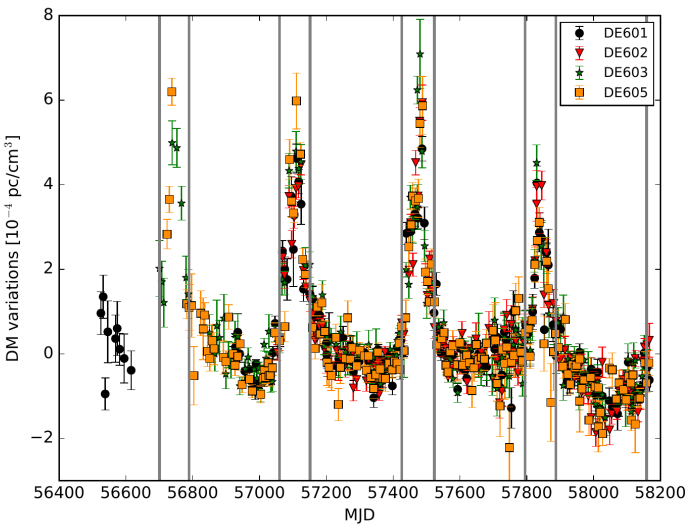

Figure 1.5: The DM time series of PSR J0034−0534, which exhibits obvious variations due to the Solar wind. Multiple colours indicate different German LOFAR stations. The grey lines show a Solar angle of 50°. The plot is taken from Tiburzi et al. (2019).

properly taken into account, induce stochastic irregularities in the times-of-arrival of radio pulses from pulsars, and strongly degrade the sensitivity of the pulsar timing (see Section 2.3) to gravitational wave (GW) detection (see also Lentati et al., 2016).

The next largest contribution comes from the Solar wind. For the pulsars observed near the Solar conjunction the induced DM fluctuations are up to 5×10^{-4} pc cm^{-3} (Tiburzi et al., 2019, see Figure 1.5). The proper modelling of DM variations induced by the Solar heliosphere will be of great importance for the next generation of high-precision pulsar timing experiments. The non-stationary terrestrial ionosphere creates DM fluctuations of order 10^{-5} pc cm^{-3}, which have not yet been resolved by current instruments.

1.4.2 Scattering and Scintillation

In addition to temporal variations in DM, electron density homogeneities in the medium between the pulsar and the observer are the cause of two other observed effects, namely scattering and scintillation.

The wavefront of an electromagnetic wave, propagating through an inhomogeneous plasma, becomes crinkled: the phase varies randomly along the wavefront. In other words, different rays are bent by various degrees and, thus, take multiple paths from the source to the observer. Due to longer propagation paths, a geometrical time delay occurs, which depends on the relative configuration of the source, observer and scattering medium (Williamson, 1972). The pulse profile will therefore be broadened. The broadening is commonly modelled by the convolution of the intrin-

sic pulse shape with a one-sided exponential function with a characteristic scattering timescale τ_s. In the case where the scattering medium is represented by a thin slab, placed approximately between the source and the observer, the time constant will be $\tau_s = L(L-\Delta)\theta^2/2\Delta c \simeq L\theta^2/2c$, where Δ is the distance from the observer to the scattering scree and θ is the scattering angle (Williamson, 1972)[8]. The time constant τ_s scales with observing frequency as $\theta^2 \sim (\Delta\Phi/k)^2 \sim f^{-4}$ when electron density irregularities are all assumed to have the same size, where $\Delta\Phi$ is the cumulative phase shift and k is the wavenumber. If electron density irregularities follow the Kolmogorov law, τ_s scales with frequency as $\sim f^{-4.4}$.

As the effect of pulse broadening cannot be adequately removed, pulsar surveys are strongly limited by scattering, making it difficult to detect pulsars with τ_s larger than the pulse period. Scattering is one of the main challenges when searching for short period pulsars in regions with high plasma density, e.g. in the vicinity of the Galactic center (e.g. Spitler et al., 2014).

Another phenomenon, closely related to scattering, is called scintillation. Let us assume that the turbulent medium between the source and the observer is replaced by an effective thin slab. As before, immediately beyond the thin screen there are phase modulations, but no amplitude modulations. At some distance Δ from the screen, the phase modulations are converted to amplitude variations through the interference between the rays coming from different parts of the crinkled wavefront. As a result, an interference pattern is formed in the plane of the observer. In other words, the plasma screen acts as an irregular diffraction grating. Depending on the relative velocity of the source, observer and plasma screen, the intensity registered at Earth changes. When the distance Δ is substantial, i.e. the observer is in the far field, Frauhnofer diffraction is observed, referred to in pulsar astronomy as *strong* scintillation, in contrast to *weak* scintillation, described by the Fresnel diffraction equations (see reviews in Rickett, 1990; Narayan, 1992). Scintillation can only happen if the phases of the interacting waves are below $\sim$1 radian, i.e. $2\pi\delta\nu\tau_s \ll 1$, where $\delta\nu$ is known as the decorellation bandwidth. That is to say, the waves with frequencies outside of the decorrelation bandwidth will not contribute to the interference pattern.

The ISM screens induce strong scintillation for most of the pulsars at distances more than about 100 pc and at frequencies higher than 1.4 GHz (e.g. Lyne & Rickett, 1968; Roberts & Ables, 1982). Scintillation caused by the ionosphere, which is located much closer to the observer than the ISM screens, falls in the regime of weak scattering when observed at 1.4 GHz. Strong scintillation due to the ionosphere can be observed at much larger wavelengths (e.g. Fallows et al., 2014). Ionospheric scintillation has not yet been observed directly in pulsar data as it is challenging to separate them from scintillation induced by the ISM and the Solar wind.

1.4.3 Faraday rotation

When pulsar radiation propagates through the ionised magnetised medium with a non-zero magnetic-field component along the LoS, Faraday rotation of the signal takes

[8] When the scattering medium is extended over the whole LoS $\tau_s = 3L\theta^2/2\pi^2 c$.

place, which is a rotation of the plane of linearly polarised pulsar emission. Linearly polarised waves can be represented as the superposition of left- and right-hand circularly polarised waves of equal amplitude. The origin of the Faraday rotation phenomenon lies in the difference of the phase velocities of these waves, which occurs in the magnetised medium and is equivalent to a rotation of the plane of linear polarization.

Analogous to Equation (1.8), the phase shift of an electromagnetic wave propagating in the cold ionised magnetised medium (when compared to the phase of an electromagnetic wave propagating in vacuum) is (Lorimer & Kramer, 2004):

$$\Delta\Phi = \frac{2\pi f L}{c} - \int \frac{2\pi f}{v_{\rm ph}} \mathrm{d}r \simeq 2\pi \left[\frac{e^2}{2\pi m_e c} \frac{\mathrm{DM}}{f} \pm \frac{c^2}{2\pi} \frac{\mathrm{RM}}{f^2} + \frac{3e^4}{8\pi^2 m_e^2 c} \frac{\mathrm{EM}}{f^3} \right], \tag{1.10}$$

where $v_{\rm ph}$ is the phase velocity. The expression for differential phase rotation between the right- and left-hand polarised waves immediately follows from the equation above, and is given by:

$$\delta\Psi_{\rm F}(f) = \Phi_{\rm R} - \Phi_{\rm L} = 2\frac{c^2}{f^2}\mathrm{RM}, \tag{1.11}$$

with

$$\mathrm{RM} = \frac{e^3}{2\pi(m_e c^2)^2} \int n_e \boldsymbol{B} \mathrm{d}\boldsymbol{r}, \tag{1.12}$$

$n_{\rm e}$ is in cm^{-3}, $|\boldsymbol{B}|$ is in μG, $|\mathrm{d}\boldsymbol{r}|$ is in pc. Conventionally, RM is positive if the magnetic field is directed towards the observer, and negative in the opposite direction. As one can see from the above expressions, the effect is stronger at lower observing frequencies. The RM is an informative quantity on the magnetic fields and electron densities in the ISM. Moreover, by measuring RM and DM of a pulsar simultaneously, one can infer the average magnetic field strength along the LoS $\langle B_{||} \rangle$ (e.g. Mitra et al., 2003):

$$\langle B_{||} \rangle = \frac{\int n_{\rm e} \boldsymbol{B} \mathrm{d}\boldsymbol{r}}{\int n_{\rm e} \mathrm{d}r} = 1.23\mu\mathrm{G} \left(\frac{\mathrm{RM}}{\mathrm{rad\,m^{-2}}} \right) \left(\frac{\mathrm{DM}}{\mathrm{cm^{-3}pc}} \right). \tag{1.13}$$

The above expression should be taken with caution, as DM and RM can be dominated by very different scales. For more robust constraints on the magnetic field, the extra information about the gas distribution along the LoS must be used (see e.g. Eatough et al., 2013).

Due to the intrinsic time variability of intervening media and the relative motion between the pulsar and the observer, the RM of pulsars is not immutable. In contrast to DM variations the major contribution to changes in RM comes from the terrestrial ionosphere [9]. Being driven by Solar activity, the ionospheric RM varies on diurnal, seasonal and Solar-cycle timescales. Fluid instabilities and gravity waves induce variability on smaller timescales with coherence lengths of $\sim 10 - 100$ km (see e.g. Hoogeveen & Jacobson, 1997; Helmboldt et al., 2012; Buhari et al., 2014; Loi et al., 2015). RM variations arise both due to intrinsic ionospheric variability and geometrical effects, which

[9] This is true for the majority of pulsars. Although there are a few examples where RM variatons are caused predominantly by extreme environments such as the magnetised environment around a Be-star (Johnston et al., 2005) and the Galactic center magnetar (Desvignes et al., 2018).

involve differing LoS paths through the ionosphere and varying angles between the geomagnetic field and the LoS. The resultant ionospheric RM varies from 1 to 4 $\mathrm{rad\,m^{-2}}$ (positive in northern hemisphere and negative in southern hemisphere).

The contribution from the turbulent ISM is expected to be five to six orders of magnitude smaller than the ionospheric variations on a year timescale. As the pulsar moves in the tangent plane, the turbulent ISM induces time-correlated noise with an excess in power at low frequencies in the RM time series of a pulsar

Observations of pulsars close to the Solar conjuction can potentially be used to probe the heliospheric magnetic field and electron density. The heliospheric RM is expected to be comparable to the ionospheric contribution, being $\sim 6\,\mathrm{rad\,m^{-2}}$ at an elongation of 2.5°, dropping below $0.5\,\mathrm{rad\,m^{-2}}$ at 5° from the Sun (Oberoi & Lonsdale, 2012, and references therein). *Coronal mass ejections* (CMEs), which are violent expulsions of magnetised plasma in the corona and the Solar wind, induce additional signatures in RM datasets of background sources. CMEs with favourable geometries can result in strong RM variability, up to $0.05\,\mathrm{rad\,m^{-2}}$ (Jensen et al., 2010). The Faraday rotation due to CMEs and the Solar corona have been observed with linearly polarised beacons near the Sun (Bird et al., 1985; Levy et al., 1969). These signatures have not yet been probed with pulsars as it is extremely challenging to disentangle these effects from ionospheric RMs.

1.5 Scientific applications of pulsars

According to the ATNF catalogue (Manchester et al., 2005), there are over 2700 known pulsars, and new pulsar searching campaigns are undertaken with great enthusiasm from the community. The constantly growing interest in pulsar astronomy is reinforced by the wealth of scientific highlights in the past, as well as by potential for future discoveries. Due to their unique properties, pulsars serve as laboratories for probing extreme physics, which is not possible to do on Earth. Moreover, their high rotational stability, which is the basis of the high-precision pulsar timing technique (see Section 2.3), essentially makes them very precise 'celestial clocks', reinforcing the usefulness of pulsars.

One of the greatest successes in pulsar astronomy is testing the relativistic theories of gravity in the strong-field regime, by means of high-precision timing of pulsars in binary systems. PSR B1913+16 was the first binary pulsar discovered (by R. Hulse and J. Taylor at the Arecibo radio telescope, Puerto Rico: Hulse & Taylor, 1975). Only a few years after the discovery of PSR B1913+16, timing data enabled the detection of three relativistic effects. This includes the orbital decay due to GW emission, which provided the first indirect confirmation of the existence of GWs (Taylor et al., 1979). For this discovery R. Hulse and J. Taylor were awarded the Nobel prize in physics in 1993.

Six relativistic parameters have been resolved by timing the *Double Pulsar* system PSR J0737−3039A/B, an even more spectacular binary system than B1913+16, in which both members were detectable pulsars (Burgay et al., 2003; Lyne et al., 2004).

Kramer et al. (2006b) showed that General Relativity (GR) correctly describes the system at the 99.95 % level, which makes it the most stringent test of GR in strong-field conditions. The precise measurements of relativistic effects allowed to measure the masses of the two NSs with an accuracy of 10^{-4} $M_\odot$. The recent discovery of the *triple system* J0337+1715 (Ransom et al., 2014) provides the opportunity for even more stringent tests of GR validity in the strong-field regime (Archibald et al., 2018). Other MSP-white dwarf binary systems are also extensively used to put constraints on different classes of alternative theories of gravity (see e.g. Freire et al., 2012).

High-precision mass measurements of pulsars in binary systems can reveal the nature of the very dense NS interiors. The maximum possible mass of a NS strongly depends on the EoS of matter at supra-nuclear densities. Those densities cannot be reproduced in terrestrial laboratories, which makes high-mass pulsars an important and unique tool for probing the EoS of high-density matter. The highest pulsar masses measured to date are $2.01(4)M_\odot$ for PSR J0348+0432 (Antoniadis et al., 2013) and $2.1(1)M_\odot$ for PSR J0740+6620 (Cromartie et al., 2019). These measurements already rule out some of the 'softest' EoSs[10]. By simultaneously measuring the masses and radii of NSs one can make the current constraints on EoSs even more powerful. However, due to pulsars' small sizes, there is no straightforward way to directly determine the pulsar radii (Özel & Freire, 2016). A future measurement of the spin-orbit coupling in a highly relativistic binary, such as the Double Pulsar system, will allow the moment of inertia of a NS to be determined for the first time (Lyne et al., 2004), which will enable the radius of a NS to be determined.

Another ambitious project, which became possible due to the high rotational stability of pulsars, is the detection of GWs in the nHz regime between 10^{-9} and 10^{-7} Hz. Sazhin (1978) and Detweiler (1979a) were the first to realise that the passage of a continuous low-frequency GW will perturb the regular propagation of pulses from pulsars. The primary sources of such low-frequency GWs can be inspiraling super-massive black hole binaries (SMBHB) believed to be located in the centers of galaxies (e.g. Koushiappas & Zentner, 2006; Malbon et al., 2007). The GW background, created by the association of SMBHBs, will induce stochastic correlated signatures in the timing signals of different pulsars (Phinney, 2001). For an isotropic stochastic GW background, the correlations depend only on the angular separation of pulsars, following the Hellings and Downs correlation pattern (Hellings & Downs, 1983). Both continuous GWs and a GW background are nowadays probed with a network of MSPs with extremely high rotational stabilities, known as Pulsar Timing Arrays (PTAs, Foster & Backer, 1990). There are three separate PTA projects underway: the European Pulsar Timing Array (EPTA, Desvignes et al., 2016), the North American Nanohertz Observatory for Gravitational Waves (NANOGrav, Arzoumanian et al., 2018a) and the Parkes Pulsar Timing Array (PPTA, Manchester et al., 2013), which are cooperating under the International Pulsar Timing Array (IPTA), boosting the sensitivity of the resultant dataset (Verbiest et al., 2016). The recent upper limits on the amplitudes of GW sources set with above-mentioned PTAs can be found in e.g. Shannon et al. (2015); Lentati et al.

[10] See https://www3.mpifr-bonn.mpg.de/staff/pfreire/NS_masses.html

(2015); Babak et al. (2016); Aggarwal et al. (2018) and Arzoumanian et al. (2018b).

On top of that, other correlated signals can be present in the timing data of PTAs. For instance, one of the essential requirements of high-precision pulsar timing is firm knowledge of the planetary masses and orbits in the Solar System. The errors in the Solar System ephemerides (SSE) will create a recognisable pattern in the timing data. The current PTA sensitivity allows us to verify and refine the planetary ephemerides, estimated with alternative methods (Champion et al., 2010; Arzoumanian et al., 2018b; Caballero et al., 2018).

Another very interesting practical application of pulsars is deep-space navigation (Chester & Butman, 1981; Sheikh et al., 2006; Becker et al., 2013). A set of known pulsars can form a kind of 'Galactic Global Positioning System' (GPS). The position of a space vessel is triangulated by comparing the received pulsar signals with a known database of pulsar parameters. For spacecraft navigation it is more convenient to use X-ray rather than radio pulsars, due to the vastly less demanding collecting area requirements of X-ray telescopes. The accuracy in spacecraft position that can be achieved with current data is better than 20 km (Deng et al., 2013).

1.6 Pulsars as probes of the interstellar medium and dark matter

This section presents a brief overview of the ISM with an emphasis on the ISM turbulence and dark matter. Here we also introduce scalar field dark matter, which is one of the viable alternatives to cold dark matter. Finally, we briefly review the methods of probing the ISM and dark matter with pulsars.

1.6.1 The interstellar medium

Despite what it may look like at first glance, the space between stars is not empty, but filled with material, known as the ISM. This includes interstellar gas and dust grains, bathed in cosmic rays, magnetic fields and electromagnetic radiation, generated by many sources including the cosmic microwave background. Although the ISM is very dilute, it plays an important role in astrophysics, being a reservoir of material for stars and planets. During their lives, stars return the material back in the form of stellar winds or, more dramatically, via supernova explosions, thereby enriching the ISM with the products of nuclear burning in their interiors. Thus, the ISM actively participates in the chemical evolution and contains information on the chemical history of galaxies.

The major part of the baryonic ISM (around 99% by mass, Hildebrand, 1983) is in a gas phase. The interstellar gas is mostly hydrogen, which makes up 70% of the mass. Another 28% is in the form of helium, and 2% are heavier elements. The interstellar gas exists in different *phases* with different physical properties (temperature, density and ionisation state). Those are molecular H_2, atomic HI (warm and cold), and ionised HII (warm and hot) hydrogen. Molecular hydrogen is found in the form of dense molecular clouds, observed as dark opaque blobs in the Milky Way. These cold molecular clouds

are of great importance, as they are strongly associated with star forming regions (Stahler & Palla, 2005). Although, a substantial part of the ISM mass is tied to these compact clouds, the ISM volume is mostly filled with hot HII (∼50%) and some mixture of warm HII and HI (∼50%) (Draine, 2011).

The dynamics of the ISM is governed by turbulence. To sustain the turbulent cascade, kinetic energy should be regularly pumped into the system. In the case of the ISM, there are multiple physical processes responsible for the energy injection, including supernova explosions, expanding ionising shells (e.g. McKee, 1989; Krumholz et al., 2006; Lee et al., 2012), galactic compression in the spiral arms (e.g. Dobbs et al., 2008), and magneto-rotational instabilities (e.g. Piontek & Ostriker, 2007). On smaller scales the turbulence is driven by stellar winds and protostellar jets (Norman & Silk, 1980; Banerjee et al., 2007; Tamburro et al., 2009). The injected energy cascades down through a sequence of downsizing eddies. When the size of the eddies becomes comparable to the mean free path, the kinetic energy dissipates into random thermal motion.

The density fluctuation spectrum of classical incompressible subsonic turbulence (Kolmogorov, 1941), i.e. the speed of turbulent flows is smaller than the speed of sound in the medium, is a power-law with $P(k) \sim k^{-11/3}$. Multiple studies have shown that density fluctuations in the warm ionised medium follow the Kolmogorov spectrum (Gaensler et al., 2011; Burkhart et al., 2012), which implies subsonic regime of the turbulence. In other colder and denser phases of the ISM, such as HI and H_2, the turbulence is supersonic. In this case the Kolmogorov description is not suitable. Due to its complexity and 3D-structure, the properties of the supersonic turbulence are mainly investigated via computer simulations. Recent theoretical works (Kritsuk et al., 2007; Federrath et al., 2010) along with observations (Lazarian, 2009; Hennebelle & Falgarone, 2012) suggest that in the supersonic turbulence regime, the measured density spectra are much shallower than in the case of Kolmogorov turbulence.

The overall picture of turbulence is further complicated by the presence of interstellar magnetic fields. Due to the high electric conductivity of the ISM, the magnetic fields are closely coupled to the matter. Therefore, the interstellar magnetic fields actively participate in the turbulent flow and, in turn, affect the dynamics of the turbulence. For instance, the magnetic fields lead to anisotropy of the turbulence, i.e. energy cascades differently in the directions parallel and perpendicular to the field lines (see e.g. Lazarian et al., 2015). Moreover, it is thought that *small-scale dynamos* taking place in the ISM, initiate an *inverse cascade*, which brings the magnetic energy up to the injection scales (Cho & Lazarian, 2009; Beresnyak, 2012; Zrake, 2014). It is generally accepted that such small-scale dynamos are responsible for the amplification of the primordial 'seed' magnetic fields towards the present μG values (Kazantsev, 1968; Brandenburg & Subramanian, 2005), thus, playing an important role in the formation of large-scale *turbulent isotropic* magnetic fields. Despite all the complications, the power-law description of the turbulence in magnetised interstellar plasmas still seems to be valid (see e.g. Maron & Goldreich, 2001).

Pulsar observations can significantly increase our knowledge of the ionised ISM and physical processes taking place between its constituents. The large number of

known pulsars in the Galaxy provides sufficient sampling of the ISM by a multitude of LoSs. The interstellar dispersion of pulsar signals allows us to probe the integrated electron densities between the pulsar and observer (see Section 1.4.1). By measuring the DM of an ensemble of pulsars, the electron density distribution in the Galaxy can be reconstructed as has been attempted by Cordes et al. (1991); Cordes & Lazio (2003); Yao et al. (2017) amongst others. In the same manner the Faraday rotation of highly linearly polarised pulsar signals (see Section 1.4.3) enables the large-scale structure of the Galactic magnetic fields to be probed (e.g. Han et al., 2006; Noutsos et al., 2008). Pulsars can also significantly enlarge our knowledge of the ISM turbulence. Electron-density fluctuations can be probed on multiple scales from 10^{-5} AU up to 100 pc through scintillation and scattering (see Section 1.4.2), as well as through monitoring of time-variable DM of pulsars (e.g. Armstrong et al., 1995). The variations of the RM of a pulsar, as it propagates in the plane orthogonal to the LoS, and the LoS crosses different parts of the turbulent ISM, can shed light on the physics of the turbulent magnetic fields. The attempt to measure the latter variations has been undertaken in this thesis.

1.6.2 Dark matter

The most recent estimate of the total mass of the Galaxy encapsulated within a radius of 20 kpc, gives $1.91(17)\times10^{11}\mathrm{M}_{\odot}$ (Posti & Helmi, 2019). However, only a small fraction of this mass is contained in stars and the ISM, while a substantial part (to be specific $1.37(17)\times10^{11}\mathrm{M}_{\odot}$) is in the form of non-luminous matter of yet unknown nature, known as *dark matter*. The striking proof of the existence of dark matter at galactic scales is *rotation curves* of galaxies, which show the relation between the circular velocities of stars and gas and their distance around the Galactic center. The typical rotation curve exhibits flattening even far beyond the visible disk, which in strong tension with the observed galactic surface brightness. The discrepency can be explained by the presence of extended non-visible dark matter halos. Measuring the rotation curve of our own Galaxy is less straightforward. Nevertheless, the presence of dark matter in the Galaxy can be inferred via accurate reconstruction of the gravitational potential using observed velocity dispersion of globular clusters (Posti & Helmi, 2019) or a large sample of stars (Bienaymé et al., 2014). The observational evidence of dark matter on larger scales is also compelling. The difference between the luminous and dynamically inferred mass observed in galaxy clusters, confirms the presence of dark matter in the intergalactic medium (Zwicky, 1933; Diaferio et al., 2008). On cosmological scales the observational features in the power spectrum of the cosmic microwave background (Planck Collaboration et al., 2016) suggest the presence of a fluid interacting with itself and with other baryonic matter almost only gravitationally. Despite much more observational evidence of dark matter at different astronomical scales, it has not yet been found in direct-detection experiments on Earth (Tanabashi et al., 2018).

Currently, the most commonly accepted dark matter candidate is cold dark matter, which is impressively successful in matching theoretical predictions to observational data at large cosmological scales (see Bertone et al., 2005; Primack, 2012, for a review).

On the contrary, at kpc to Mpc scales, the cold dark matter hypothesis has been poorly tested and in most cases is inconsistent with observations (see e.g. Del Popolo & Le Delliou, 2017, reference therein).

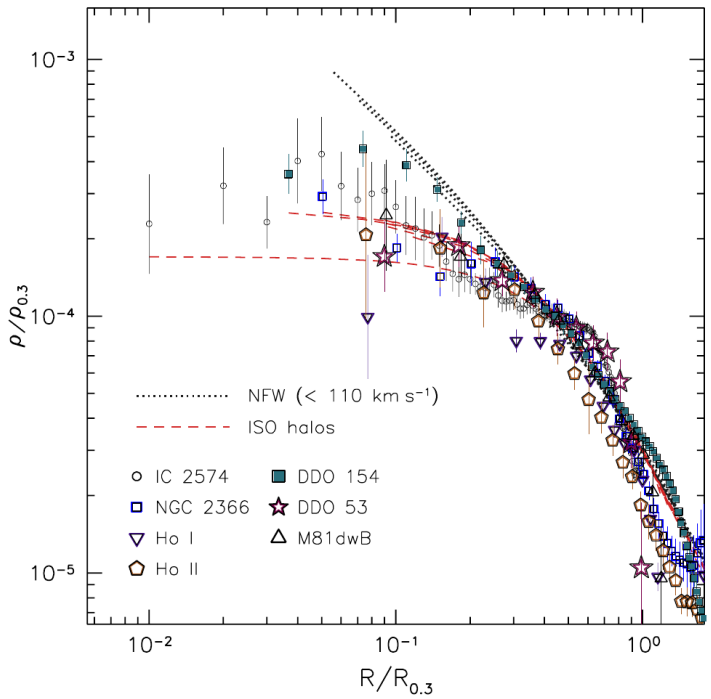

Figure 1.6: Dark matter density profiles obtained from rotation curves of seven low surface brightness galaxies. The black dotted lines show the family of cold dark matter predictions (Navarro et al., 1996a). The red lines show the family of best-fit pseudo-isothermal halo models (e.g. Begeman et al., 1991). The plot was adapted from (Oh et al., 2011)

One of the difficulties, for example, is associated with the small number of satellite galaxies observed around larger galaxies, in contrast to the abundance of sub-galactic halos predicted by cold dark matter simulations (Klypin et al., 1999) Another issue is the 'cuspy' cores seen in simulations (Navarro et al., 1996a), while the majority of observed galaxy rotation curves suggest shallower density profiles Oh et al. (e.g. 2011); McGaugh et al. (e.g. 2016, see Figure 1.6). Some of these problems can be possibly solved within the cold dark matter paradigm by including baryonic physics in N-body simulations to account for photoionisation of intergalactic gas, supernova explosions, star formation, and other related processes (Navarro et al., 1996a; Somerville, 2002; Macciò et al., 2010; Governato et al., 2012). However, the nuances of baryonic feedback inclusion are still under debate (e.g. Klypin et al. (2015); Schneider et al. (2017)). On the other hand, in order to find solutions to the cusp-core and missing-satellite problems, part of the scientific community questions the cold dark matter hypothesis

itself. Among the promising alternatives, usually involving a small-scale suppression in the matter power spectrum, are warm dark matter (Colín et al., 2000; Bode et al., 2001), self-interacting dark matter (Spergel & Steinhardt, 2000), self-annihilating dark matter (Kaplinghat et al., 2000) and *fuzzy dark matter* (FDM) (Turner, 1983; Hu et al., 2000; Goodman, 2000; Hui et al., 2017).

Pulsars are instrumental in understanding the nature of dark matter. Timing of the Double Pulsar and eccentric binaries have provided stringent constraints on the family of tensor-vector-scalar theories, one of the dark matter alternatives constituting the modification of Newtonian gravity in the weak-field regime (Freire et al., 2012). Dark matter in the form of ultracompact minihalos (Clark et al., 2016; Kashiyama & Oguri, 2018), or primordial black holes (Seto & Cooray, 2007; Blinnikov et al., 2016; Clesse & García-Bellido, 2017) can also be probed with pulsars. In this thesis we focus specifically on testing the FDM hypothesis in which dark matter is composed of spin-0 extremely light bosons. For sufficiently light ($10^{-23} - 10^{-20}$ eV) bosons, the $\sim$ pc-kpc de Broglie wavelength smooths the inhomogeneities at sub-galactic scales, whereas on cosmological scales it is indistinguishable from cold dark matter (Sarkar et al., 2016; Hložek et al., 2018). As these bosons are extremely light and interact very weakly with baryonic matter, their detection in a laboratory is extremely challenging (Arvanitaki et al., 2010). In the boson mass range $3 \times 10^{-21} - 3 \times 10^{-20}$ eV the FDM can be probed via resonant binary pulsars (Blas et al., 2017, Heusgen et al, in prep.). In Chapter 6 we explore the possibility of detection of FDM with PTAs in an even more low-mass regime, from $\sim 10^{-23}$ to 10^{-22} eV.

1.7 Thesis outline

This thesis deals with the investigation of the turbulent ISM, namely magnetic fields, and dark matter in our Galaxy. The thesis is organised as follows:

- In Chapter 2 we provide an overview of general aspects of pulsar observations. The specifications of data acquisition in radio band are discussed. Nuances of pulsar polarimetry including propagation of polarised pulsar emission through the ionised magnetised plasma are revised. Multiple commonly used methods, which allow to estimate the RM of Faraday-rotated pulsar signals are described in detail.

- In Chapter 3 we present a new application of the Bayesian Lomb-Scargle Periodogram for rotation-measure estimation.

- In Chapter 4 we discuss the Faraday rotation caused by the terrestrial ionosphere. We describe ways to eliminate the ionospheric contribution and carefully investigate the systematics, caused by improper ionospheric modelling. We conclude that currently the imperfections of the ionospheric modelling are the main limiting factor of interstellar magnetic-field investigation with pulsars.

- In Chapter 5, after subtracting the ionospheric contribution, we attempt to measure the interstellar turbulent magnetic fields, and set an upper limit on the amplitude of any magnetic-field fluctuations.
- In Chapter 6 we discuss one of the viable dark matter candidates, FDM. We investigate the prospects of FDM detection with PTAs, and set an upper limit on the density of dark matter with PPTA Data Release 2.
- Finally, in Chapter 7 we summarise our results and discuss future prospects for ISM and dark-matter investigation with pulsars.

Chapter 2

Practical aspects of pulsar observations: from observables to fundamental results

Contents

2.1 Radio observations of pulsars 27
2.2 Low-frequency pulsar observations with phased arrays 29
2.2.1 German LOFAR stations. German long-wavelength consortium. 31
2.3 Pulsar timing 34
2.4 On probing pulsar polarisation 40
2.4.1 Stokes parameters 40
2.4.2 Modelling the Faraday effect: RM measurement techniques . . . 42

Since their discovery in the radio band, pulsars have been observed over a wide range of the electromagnetic spectrum, starting at low radio frequencies (10 MHz) up to very high-energy γ-rays (100 TeV). Although the means of data acquisition are different in different parts of the spectrum, there are several things in common: e.g. weak pulsar signals require huge collecting areas and long integration times; tiny periods of pulsations can be resolved with high time resolution instruments. The most fruitful type of observations, which have significantly expanded our understanding of pulsars, have been carried out at radio frequencies.

2.1 Radio observations of pulsars

The traditional way of studying pulsars is by observing them with radio telescopes. The principal scheme of a modern telescope involves two main components: a *frontend* and a *backend*. The frontend is the initial receiving system of the telescope, which collects and amplifies the signal. For typical single-dish radio telescopes the collecting area is formed by a reflecting surface, which usually has the shape of a paraboloid. The largest steerable parabolic reflectors extensively used for pulsar observations are the 100-m Effelsberg radio telescope in Germany, the 76-m Lovell Telescope in the UK, the 105-m Robert C. Byrd Green Bank Telescope in the USA, the 64-m Parkes radio telescope in Australia, and the 64-m Sardinia radio telescope. The largest *non-steerable* reflectors, such as the 300-m Arecibo radio telescope in Puerto Rico and the

brand-new 500-m FAST radio telescope in China, are designed as spherical caps. In some modern observing systems based on phased arrays, the collecting reflectors are completely removed from the scheme (see Section 2.2).

The reflectors coherently sum the signal in the focus of the antenna, where it is gathered by the receiver *feed horn*, which converts the incoming radiation into a series of electric voltages. Afterwards, the analogue voltages are driven through a chain of amplifiers and bandpass filters. The latter attenuate all the frequencies outside of the band of interest. Commonly, the signal received at radio frequency f is *down-converted* to lower frequencies by modulating the original signal with a monochromatic signal of fixed frequency f_{LO} by a Local Oscillator. As a result, two new signals with two new intermediate frequencies are produced, $f_{\mathrm{IM}} = f \pm f_{\mathrm{LO}}$, from which the lower one is chosen with a bandpass filter. The main reasons for down-conversion are to facilitate the process of transmission through the hardware and to avoid negative feedback, caused by the amplified signals that can possibly escape from the hardware system.

While the frontend is a general-purpose system developed for a broad variety of radio astronomical applications, the backend is a more special purpose equipment, which is responsible for further digitisation and processing of the data. The digitisation is handled by Analogue-to-digital converters (ADCs), which must sample the analogue signal with a sampling frequency two times higher than the resultant bandwidth, following the Nyquist theorem (Nyquist, 1928; Kotelnikov, 1933; Shannon, 1949). Afterwards, the data are channelised with polyphase filter bank (PFB) technique. A PFB produces a power spectrum of the signal, significantly suppressing the effects of spectral leakage and scalloping loss, which are inherent to classic discrete fourier transforms (DFT).

In order to compensate for the frequency-dependent dispersion of pulsar signals, which was discussed in Section 1.4.1, the data are de-dispersed. The backend applies a proper dispersive delay given by Equation (1.9), corresponding to the best available DM, to each frequency channel, making the signal aligned across the whole band. This method is known as *incoherent de-dispersion*, and is easy to apply, as well as being computationally inexpensive. Although it is limited by the dispersive smearing within each individual frequency channel.

One can overcome this issue by using another method, called *coherent de-dispersion* (Hankins & Rickett, 1975). Within this approach the dispersive delay is expressed in terms of the phase shift $\Delta\Psi$ (see Equation (1.9)). In the frequency domain this effect can be described by the transfer function H, which is to first order[1]:

$$H = \mathrm{e}^{-i\Delta\Phi} \simeq \mathrm{e}^{-\frac{e^2}{mec}\frac{\mathrm{DM}}{f}i}. \tag{2.1}$$

In order to correct for the dispersion, the raw voltages are Fourier transformed with the fast Fourier transform (FFT). The phase of each Fourier component is derotated by an amount that is proportional to the best-known DM of the pulsar, by applying the inverse of the transfer function, H^{-1}. The coherent de-dispersion is very computationally

[1] The expression can be further expanded as a Taylor series around the central frequency f_0: $\frac{1}{f} \simeq \frac{1}{f_0} - \frac{f-f_0}{f_0^2} + \frac{(f-f_0)^2}{f_0^3}$.

expensive, as the method implies several FFTs and matrix-matrix multiplication of the full-time-resolution data. Nowadays, modern observing systems make efficient use of both central processing units (CPUs) and graphical processing units (GPUs), and are able to perform real-time coherent de-dispersion of pulsar observations (e.g. De & Gupta, 2016).

Finally, the signal is converted to a suitable format, corresponding to the observing mode that has been chosen. There are three main data formats, which are extensively used in radio pulsar astronomy:

***baseband* data** are essentialy the raw voltages sampled at Nyquist frequency. Although this data format provides the maximum flexibility in terms of further processing, the baseband data are demanding in terms of storage space. Therefore, this data format is used for special radioastronomical studies such as observation of the Galactic center magnetar (e.g. Desvignes et al., 2018), construction of the Large European Array for Pulsars (LEAP) (Bassa et al., 2016) or investigations of giant radio pulses (e.g. Karuppusamy et al., 2010).

***filterbank* data** are baseband data channelised with PFB. Commonly the frequency and time resolution of filterbank format are reduced to more manageable values, in order to simplify further processing and storage of the data. Filterbank data are extensively used for pulsar searches (see e.g Ransom, 2001), as well as fast radio burst searches (see e.g. Farah et al., 2018).

***folded* data** are used to observe pulsars with known characteristics. The size of the data is significantly reduced via a procedure known as *folding*. From a few hundreds to a few thousands of single pulses are summed up coherently modulo the pulse period with the pulsar *ephemerides* taken into account (see Section 2.3). The final folded archive is the collection of the integrated profiles and has the format of a time-frequency-pulse-phase and polarisation data cube.

2.2 Low-frequency pulsar observations with phased arrays

Although the first steps of pulsar astronomy have been taken at long wavelengths ($<$ 300 MHz, Cole, 1969; Staelin & Reifenstein, 1968; Rankin et al., 1970), the field fairly quickly shifted towards higher frequencies (300-2000 MHz). Partially, this shift was motivated by the growing quantity of radio astronomical facilities sensitive to higher frequencies, due to the discovery of 21-cm line of hydrogen at 1420 MHz (Ewen & Purcell, 1951), and the strong demand for higher angular resolution observations. Specifically for pulsar observations, the main reason was associated with propagation effects in the ISM and the terrestrial ionospheric plasma, and the lack of adequate technologies to deal with them. For almost 40 years there was a dearth of pulsar observations below 200 MHz. The majority of those have been conducted sporadically by the first era of low-frequency interferometers: the Large Phased Array (LPA) in Russia (Malofeev et al., 2000), the Clark Lane TPT synthesis telescope (Mahoney & Erickson, 1985) in the USA, the Ukraine T-shaped Radio telescope (Novikov et al., 1984) and

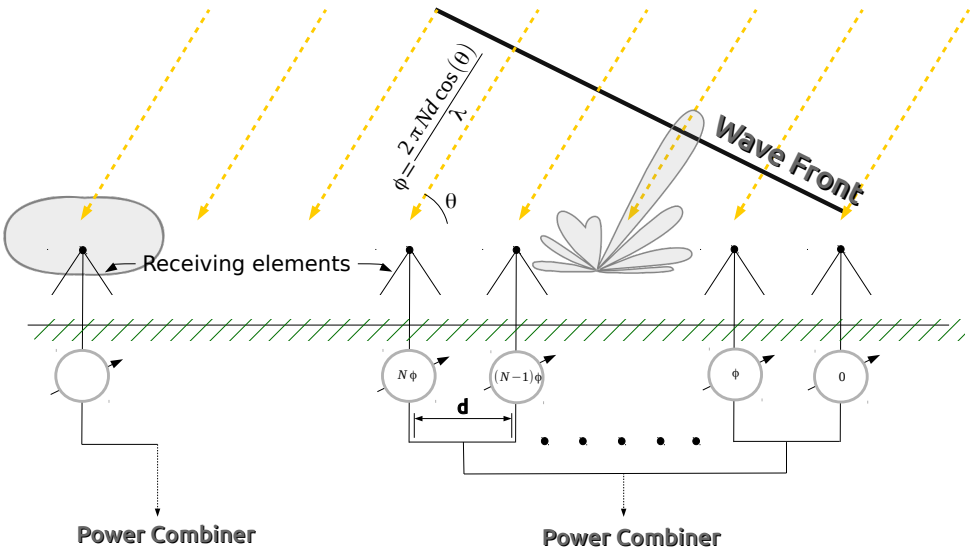

Figure 2.1: The scheme of phased arrays formed by the inverted-V antennas, fixed above the reflecting grid. *Left*: the phased array composed of one receiving element. The antenna beam pattern, shown in light grey, is omnidirectional. *Right*: the phased array composed of N elements, equally spaced by a distance d. The times of arrival of the signal from the source at different antenna elements are different, thus, time delays need to be incorporated at each signal path before summing in the output. The resultant antenna beam pattern is shown in light grey.

the Gauribidanur Radio Telescope in India (Asgekar & Deshpande, 1999). In the last two decades, the astronomical community has taken steps towards more sensitive and advanced instruments, which are capable of patching up the low-frequency gap. Insatiable interest in the HI line at cosmological distances, the origin of cosmic magnetism, the detection of steep-spectrum pulsars (Conway et al., 1963), and high-redshift radio galaxies were the main motivations for the ambitious international Square Kilometer Array (SKA) (Lazio & Gaensler, 2007). Naturally, there has been a growing demand for the construction of low-frequency *digital* telescopes, which are smaller and more affordable SKA pathfinders and at the same time can be used as sensitive observatories on their own. At low frequencies a dish-based design would be impractical[2], while a set of multiple stationary antennas, so-called phased arrays, would provide the required sensitivity.

The concept of phased arrays was first introduced by the German physicist Karl Ferdinand Braun in 1905, who was awarded the Nobel prize in 1909 "in recognition of

[2]The full-width half-maximum of the main lobe is proportional to the observational wavelength λ and inversely proportional to the diameter of a telescope D: FWHM$=1.02\lambda/D$. Thus, in order to achieve the given angular resolution in low-frequencies, the diameter of a telescope should be increased respectively.

their [Guglielmo Marconi and Karl Braun] contributions to the development of wireless telegraphy". For more than six decades phased arrays have been extensively utilised for a variety of purposes, such as wireless communication, meteorology and radio astronomy. The basic principles of a typical phased array, formed by a set of equally-spaced elements, is demonstrated in Figure 2.1. The huge collecting area of a usual radio reflector is replaced with a set of receivers. If the front of electromagnetic waves emitted by an astronomical source does not arrive directly from the zenith, the signal arrives at the elements out of phase. The separate time delays between different receivers are fixed, so the signals from multiple receivers are combined coherently at the output. As a result the antenna is steered electronically, eliminating the need for any mechanical rotation of the array. In the older schemes the difference in optical paths of the signals received by different antenna elements was compensated by the use of variable circuits[3] before the digitization stage. Nowadays, the signals from multiple antenna elements are first digitised and then handled by the adding electronics, which sums up the signals 'in-phase'. The advantages of digital phased arrays are:

- Agile beam redirection as the beam is redirected electronically;
- Multifunctional capability such as multibeaming: ability to track multiple targets simultaneously.

Among the most striking disadvantages are:

- Relatively high power consumption;
- High demand for powerful data processing facilities and storage infrastructure.

Due to revolutionary advances in digital electronics, high performance computing and storage capacity in recent decades, the concept of digital phased arrays has nowadays been successfully implemented in a number of next-generation instruments, namely the Long Wavelength Array (LWA) in the USA (Ellingson et al., 2009), the Murchison Widefield Array (MWA) and the Australian SKA Pathfinder (ASKAP) in Australia (Tingay et al., 2013; Johnston et al., 2008a), the Precision Array to Probe the Epoch of Reionization (PAPER) and MeerKat in South Africa (Parsons et al., 2010; Booth & Jonas, 2012) and the Low Frequency Array (LOFAR) in Europe (van Haarlem et al., 2013).

2.2.1 German LOFAR stations. German long-wavelength consortium.

LOFAR is a set of phased-array telescopes operating at very low frequencies from the ionospheric cut-off (which is around 10 MHz) up to 270 MHz. Each LOFAR station exploits two types of antennas: low-band antennas (LBA) and high-band antennas

[3] The concept of beam forming has originally been reported by Friis & Feldman (1937), where they have introduced the first multiple steerable antenna (MUSA). Interestingly, before the era of electronic control, in order to form multiple independent beams the early types of scanned arrays were using mechanically rotated phase shifters.

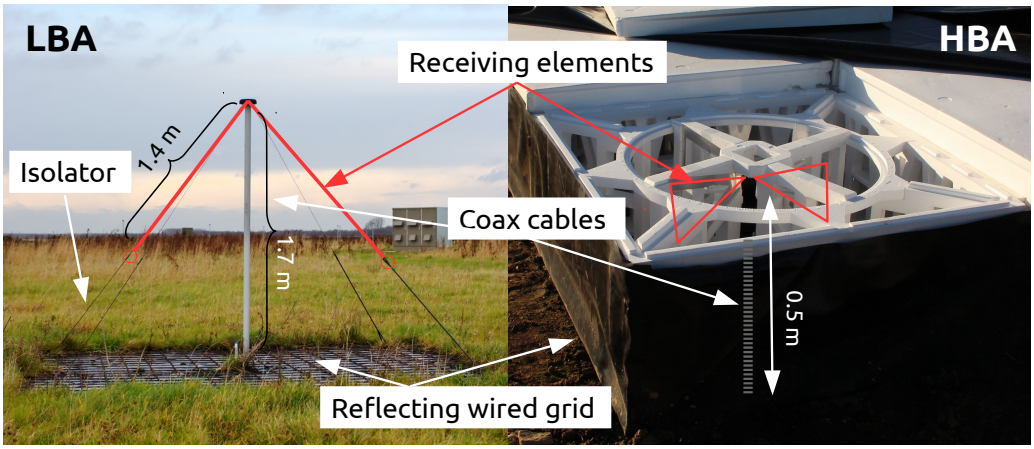

Figure 2.2: The principal scheme of inverted-V LBA (left panel) and bow-tie HBA (right panel). Credit: A.R. Offringa, M. Soida

(HBA), which are sensitive to the frequency ranges 8-80 MHz and 110-270 MHz, respectively. Both LBA and HBA elements consist of two crossed omnidirectional dipoles (see Figure 2.2), which makes each element sensitive to two orthogonal linear polarizations. Due to the design specifications, the HBA antennas are laid in a uniform grid, which causes strong sidelobes. At the same time the quasi-random distribution of the LBAs provides optimal *uv* coverage and reduces the sidelobes of the beam.

The telescope is composed of 24 core and 14 remote stations in the Netherlands, and 13 international stations, distributed all around Europe (see Table 2.1). Six of the stations are located in Germany: DE601 in Effelsberg, DE602 in Unterweilenbach, DE603 in Tautenburg, DE604 in Bornim, DE605 in Jülich and DE609 in Norderstedt. Most of the observing time the German stations operate in conjunction with the core stations as a part of the long-baseline interferometer. Additionally, the German stations are used individually as stand-alone telescopes within the GLOW (the German Long-Wavelength) consortium, to perform an observations of pulsars at low frequencies (from ∼110 to 200 MHz) using the HBAs. The GLOW consortium is an association of German universities and research institutes, which promotes the use of the meter-wavelength spectral window for astrophysical purposes. GLOW members operate the German LOFAR stations and the GLOW consortium is further involved in the planned SKA project. More details can be found at `https://www.glowconsortium.de`.

Pulsar observations are recorded in the so-called *beam-formed* mode, which, in contrast to imaging mode, can provide sub-millisecond time resolution. The simplified scheme of data flow in a single German HBA station in beam-formed mode is displayed in Figure 2.3. In order to increase the efficiency of the system, the HBAs of each station are grouped into tiles of 4×4 elements that involves the initial analog beamforming and signal amplification for each polarization. At this stage the beam size of one tile is 20°.

Table 2.1: The LOFAR stations in Europe. See details in van Haarlem et al. (2013).

# of stations	Type			Site
24	Core stations	2× 24 HBA tiles	96 LBAs	The Netherlands
14	Remote stations	48 HBA tiles	96 LBAs	The Netherlands
6	International stations	96 HBA tiles	96 LBAs	Germany
3	International stations	96 HBA tiles	96 LBAs	Poland
1×4	International stations	96 HBA tiles	96 LBAs	France, Ireland, Sweden, the UK
1×2	International stations (under construction/planned)	96 HBA tiles	96 LBAs	Latvia, Italy

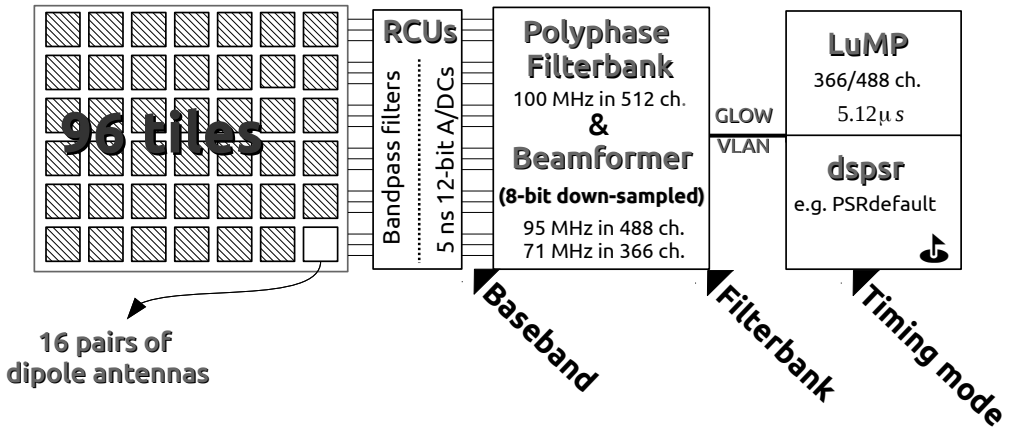

Figure 2.3: The scheme of the data flow in German LOFAR stations: from raw voltages, recorded at the station, to PSRFITS archives in timing format (PSRdefault observing mode).

After initial filtering and amplification the signal from each tile arrives via coax cables at the RCU (ReCeiver Unit), where it is digitised with a 12-bit ADC. The time resolution of the digitised data is 5 ns, provided by a 200-MHz Rubidium clock, which yields 100 MHz of bandwidth. The need for a mixing stage is precluded as the LOFAR ADCs use the wide-band direct-conversion architecture (van Haarlem et al., 2013). The required frequency band is selected with a bandpass filter, which is placed just before the ADC. Specifically for GLOW pulsar observations the second Nyquist zone from 100 to 200 MHz (RCU-mode 5) is used. The whole list of possible observing frequencies, clock rates and RCU outputs is given in McKay-Bukowski et al. (2015). Afterwards, the digitised signal arrives at the remote signal processing boards (RSPs), where it is split in 1024×5 ns chunks and channelised in 512 frequency bins of 195 kHz with the PFB technique. The subsequent beamforming stage is done via a phase-gradient technique in the frequency domain. Due to the limited capacity of the electronics, the beamforming supports only 488 out of 512 frequency channels, thus, the bandwidth is reduced to 95 MHz. All 488 channels are used only for DE601 observations, while for the other five

GLOW stations the bandwidth is further reduced to 71 MHz (366 channels), by picking the frequency range with the highest sensitivity of the LOFAR HBA band. Finally, the beamformed and channelised data are recorded on machines at the Max-Planck-Institut für Radioastronomie in Bonn and at the Jülich Supercomputing Centre using the LuMP (LOFAR und MPIfR Pulsare) Software[4]. The datasets are then coherently de-dispersed and converted to more manageable PSRFITS archives (Hotan et al., 2004) with the DSPSR software[5] (van Straten & Bailes, 2011). There are three main processing modes, which are run on the recording machines:

- **PSRdefault** The standard processing mode, which is used for the majority of GLOW observations. The data are folded modulo the pulse period (timing mode) and stored as PSRFITS archives. The time resolution is 10 sec; the pulse profile is split in 1024 phase bins; the bandwidth is split in 366 or 488 channels depending on the station; the required disk space for a 1-hour observation is $\sim$ 1 GB.

- **PSRsinglepulse** Processing mode created for single-pulses studies. The data are stored in the form of a set of PSRFITS archives; the timespan of a single archive corresponds to the duration of one pulse; the pulse profile is split in 1024 phase bins; the size of a single archive is $\sim$ 1 MB.

- **PSRextrahighfreqres** The frequency resolution of the data can be increased. The data are folded modulo the pulse period as in the PSRdefault mode; stored as a set of PSRFITS archives; the time resolution is 10 sec; the pulse profile is split in 1024 phase bins; the bandpass is split in 14724 or 19032 frequency channels (depending on the station) of 0.005 MHz; the occupied disk space is $\sim$ 20 GB for 1 hour of data.

2.3 Pulsar timing

Pulsar timing is one of the main techniques which astronomers use for further investigation of pulsars, following their initial detection. Pulsar timing strongly relies on the rotational stability of pulsars, which is in some cases comparable to the stability of atomic clocks (Taylor, 1991; Hobbs et al., 2012). Therefore, the observed periodic signals from some pulsars can be treated as very stable celestial frequency standards. In brief, the basic idea of pulsar timing consists of high-precision measurements of times-of-arrival (TOAs) of pulses, which are later fitted to a physical model capable of correctly describing the pulsar rotation and motion, as well as any propagation effects. This model, which is often referred to as *ephemerides*, includes a necessary minimum set of parameters that can adequately describe the propagation time of the signal between the pulsar and the observer. The parameters that are commonly included in the model are astrometric (e.g. the position and proper motion of the pulsar), propagation (the dispersion measure, see Section 1.4.1), and intrinsic parameters describing

[4] https://github.com/AHorneffer/lump-lofar-und-mpifr-pulsare
[5] http://dspsr.sourceforge.net/

the spin evolution of the pulsar. For pulsars in binary systems this list should be further extended to include parameters which describe the motion of the pulsar in the binary orbit along with any relativistic effects of the orbital motion. Pulsar timing is an iterative procedure, in which any new TOAs are compared to the model, and the latter is repeatedly improved. Long-term campaigns aimed at precise TOA registration enables determination of timing ephemerides with high precision, which can be of use for a variety of astrophysical applications. In this section we will further expand on the theoretical and practical principles of pulsar timing: from TOA computation to the determination of timing parameters.

Generating the TOAs Although individual pulses differ significantly in both intensity and shape (see Chapter 1), the pulse profile averaged over a few hundred rotations is generally quite stable (Helfand et al., 1975; Rathnasree & Rankin, 1995). Therefore, the TOAs are computed from integrated profiles $P(t)$, which are obtained by folding the pulsar observations modulo the pulse period[6]. The TOA of the folded archive is computed with respect to an epoch t_i, related to some reference point, which is usually associated with the single pulse closest to the middle of the sub-integration. The integrated archives $P(t)$ are cross-correlated[7] with the pulse *template* $T(t)$, which is a high signal-to-noise (S/N) profile computed by adding multiple observations together, or by fitting the real profile with the sum of analytic components (e.g. Kramer, 1994). It is implied that $P(t)$ is (e.g. Taylor, 1992):

$$P(t) = a + bT(t - \tau) + n(t), \tag{2.2}$$

where a is a flux density offset, b is a scaling factor, $n(t)$ is the instrumental and sky noise, and τ is a phase shift. Therefore, the measured TOA$=\tau + t_i$. The approximate precision of obtained TOAs can be expressed as the ratio of the pulse width W to its S/N (e.g Lorimer & Kramer, 2004):

$$\sigma_{\mathrm{TOA}} \simeq \frac{W}{\mathrm{S/N}} = \frac{W^{\frac{3}{2}}}{S_{\mathrm{mean}}\sqrt{P - W}} \frac{T_{\mathrm{sys}}}{\sqrt{n_{\mathrm{p}} \Delta t \Delta \nu}}, \tag{2.3}$$

where S_{mean} is the mean flux density, P is the pulse period, n_{p} is the number of polarisations. From Equation (2.3) one can see that observational setups with lower system temperatures T_{sys} and longer integration times Δt and larger bandwidths $\Delta \nu$ provide more precise TOAs.

The timing model In order to model the observed TOAs registered at the telescope, they should be first recalculated to the times of pulse emission at the pulsar's comoving reference frame. This transformation includes a set of geometric, relativistic and propagation time delays which are briefly introduced below (see Figure 2.4, Edwards et al., 2006):

[6] The initial set of parameters that is commonly known for a newly discovered pulsar is the approximate position, the spin period and the dispersion measure.

[7] The cross-correlation procedure is commonly carried out in the Fourier domain (Taylor, 1992), which yields higher precision than traditional fitting in the time domain.

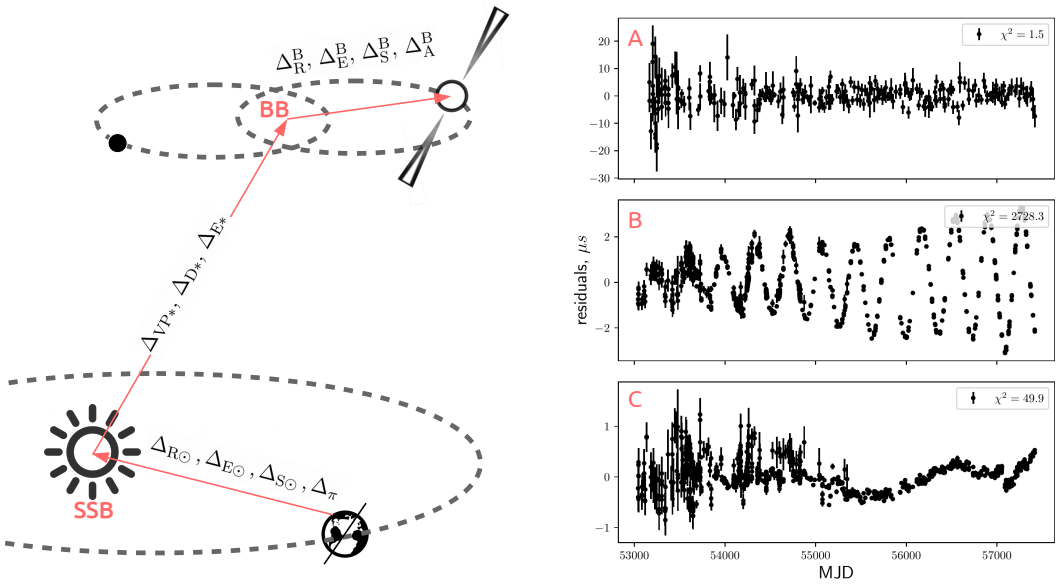

Figure 2.4: *Left*: The geometry of pulsar timing with highlighted time corrections related to corresponding reference frame transformations. *Right*: Real timing residuals of PPTA pulsars, which will be described in Chapter 6. *From top to bottom*: A) White timing residuals of PSR J0613−0200 with $\chi^2_{\rm red} = 1.5$; B) the timing data of PSR J0437−4715 with characteristic systematics caused by an incorrect proper motion; C) the timing residuals of PSR J0437−4715 perturbed by a strong unmodelled intrinsic noise.

$$t_{\rm psr} = t_{\rm obs} + \underbrace{\Delta_{\rm clk} - (\Delta_{\rm R\odot} + \Delta_{\rm E\odot} + \Delta_{\rm S\odot} + \Delta_{\pi})}_{\text{Barycentric corrections}} + \\ + \underbrace{(\Delta_{\rm VP*} + \Delta_{\rm D*} + \Delta_{\rm E*})}_{\text{Interstellar corrections}} + \underbrace{(\Delta^{\rm B}_{\rm R} + \Delta^{\rm B}_{\rm E} + \Delta^{\rm B}_{\rm S} + \Delta^{\rm B}_{\rm A})}_{\text{Binary corrections}}. \tag{2.4}$$

- $\Delta_{\rm clk}$ The TOAs are measured with observatory atomic clocks (e.g. Hydrogen time standard), which are very precise only on the time-scales of several weeks. This is not sufficient for the purposes of long-term timing. The correction term $\Delta_{\rm clk}$ adjusts the TOAs measured with local clocks to a much more stable time standard, Terrestrial Time (TT), referred to Earth's geoid (Hobbs et al., 2012). The most precise TT available is the one produced by the *Bureau International des Poids et Mesures*, which is the average over hundreds of atomic clocks located at multiple time laboratories across the globe. This organisation annually publishes a version of the terrestrial timescale, referred to as TT(BIPMXX), where XX is the year of the release (Petit, 2004).
- $\Delta_{\rm R\odot}, \Delta_{\rm E\odot}, \Delta_{\rm S\odot}$ The reference frame of the telescope, used for TOA registration, is non-inertial: the telescope is located on a spinning Earth which revolves around the Sun. $\Delta_{\rm R\odot}$, $\Delta_{\rm E\odot}$ and $\Delta_{\rm S\odot}$ are used to recalculate the *topocentric* TOAs to the barycentric TOAs, measured at the Solar System barycenter (SSB), which is an inertial reference frame to a good approximation. The *Solar System Rømer* delay $\Delta_{\rm R\odot}$ is essentially the classical geometrical delay equal to the light travel time in vacuum between the telescope site and the SSB. $\Delta_{\rm S\odot}$ is a relativistic *Shapiro* delay (Shapiro, 1964), which incorporates the excess path that the light has to travel in the curved space-time in the vicinity to Solar System bodies. In practice, only the influence of the most massive objects, namely the Sun, Jupiter, Saturn, Uranus and Neptune, is taken into account. $\Delta_{\rm E\odot}$ is the *Einstein* delay, which is associated with special and general relativistic time dilation between the reference frame of the telescope and the SSB: the clock, which is moving relative to the observer and/or is under the influence of a stronger gravitational field than the observer goes slower than the observer's clock. This effect is time-varying due to the changing gravitational field of in the vicinity of Earth, as it moves around the Sun on an elliptical orbit (e.g. Irwin & Fukushima, 1999).
- Δ_{π} is an optional *timing parallax* delay, which arises due to the actual curvature of the wavefront emitted from the pulsar. In contrast to a plane wavefront approximation, the spherical wavefront induces a delay in the TOAs with a half-year periodic modulation, as the Earth orbits the Sun (Backer & Hellings, 1986). The magnitude of this effect decreases inversely proportional to the pulsar distance, thus the timing parallax is measurable for a very limited number of nearby pulsars.

In order to compute the barycentric terms $\Delta_{\rm R\odot}, \Delta_{\rm E\odot}, \Delta_{\rm S\odot}, \Delta_{\pi}$ one needs to

have precise knowledge of the SSE, i.e. the positions and the masses of the Solar System objects, especially the Sun and the massive planets. The most accurate SSE are regularly published by the *Jet Propulsion Laboratory* (JPL) and Numérique Planétaire de l'Observatoire de Paris (INPOP) . The most up-to-date versions are DE436 and INPOP17A. Recent papers have shown that current pulsar-timing experiments are sensitive to the choice of SSE (Tiburzi et al., 2016; Arzoumanian et al., 2018b) and can be used to refine the masses of Solar System bodies (Champion et al., 2010; Caballero et al., 2018).

- $\Delta_{\mathrm{VP}*}$ is the *vacuum propagation* delay, which is the light travel time in vacuum between the SSB and the pulsar's barycenter. In pulsar timing experiments it is assumed that the distance between the SSB and the pulsar's barycenter does not change considerably. Therefore, the vacuum propagation delay is a assumed to be constant offset.
- $\Delta_{\mathrm{D}*}$ is the *dispersion* delay, which arises due to the frequency-dependence of the group velocity of electromagnetic waves. For the ISM the *dispersion* delay is inversely proportional to the square of the radiation frequency at the SSB, f_{SSB}:

$$\Delta_{\mathrm{D}*} \sim \frac{\mathrm{DM}}{f_{\mathrm{SSB}}^2}\,. \tag{2.5}$$

  This effect was discussed in detail in Section 1.4.1.
- $\Delta_{\mathrm{E}*}$ is the Einstein delay, which in this case describes the time dilation between the SSB and the pulsar's co-moving reference frame. As the pulsar mass is assumed to be unchanging, $\Delta_{\mathrm{E}*}$ is simply a constant offset[8].

In the case of an isolated pulsar the above set of corrections is enough to recalculate the topocentric TOAs to the pulse emission times. If the pulsar is part of a binary system, an additional set of parameters should be introduced. For wide non-relativistic systems those are seven Keplerian parameters[9]. If the pulsar is moving in a strong gravitational field of a companion, e.g. another NS, relativistic orbital effects need to be taken into account. These effects are explained by additional seven parameters[10], known as *post-Keplerian parameters* (Damour & Deruelle, 1986; Damour & Taylor, 1992). In order to account for the motion of the pulsar in its orbit, the TOAs measured at the binary system barycenter are recalculated to the pulsar's comoving reference frame.

- $\Delta_{\mathrm{R}}^{\mathrm{B}}$, $\Delta_{\mathrm{E}}^{\mathrm{B}}$, $\Delta_{\mathrm{S}}^{\mathrm{B}}$ are the *orbital Rømer*, *orbital Shapiro* and *orbital Einstein* delays, associated with the coordinate transformation from the binary system

[8] Some other time delays were precluded from the list due to their negligibility.

[9] These are the orbital inclination i, longitude of the ascending node $\Omega_{\mathrm{p}}^{\mathrm{asc}}$, longitude of periastron ω_{p}, semi-major axis a_{p}, eccentricity e, orbital period P_{b} and the epoch of passage at periastron T_0.

[10] These are the rate of advance of periastron $\dot{\omega}$, time dilation and gravitational redshift γ, orbital decay $\dot{P}_{\mathrm{b}}$, range r and shape s of the Shapiro delay, and orbital deformation parameters δ_θ and δ_r. The last two are particularly challenging to detect due to their strong covariance with other orbital and spin parameters.

barycenter to the pulsar's comoving frame. These terms are analogous to those used to correct topocentric TOAs to the SSB reference frame.

- $\Delta_{\rm A}^{\rm B}$ is the additional abberation term, caused by the pulsar's rotation and transverse motion with respect to the observer.

Once the topocentric TOAs, $t_{\rm obs}$, are recalculated to the pulse emission times $t_{\rm psr}$ via Equation (2.4), one needs to describe the pulsar's rotational evolution in the reference frame co-moving with the pulsar's center of mass. As was discussed in Chapter 1, pulsars mainly spin down due to electromagnetic wave emission. The current rotational phase at epoch t is given by (Lorimer & Kramer, 2004)[11]:

$$\frac{\phi(t)}{2\pi} = \frac{\phi_0}{2\pi} + \nu(t - t_0) + \frac{1}{2}\dot{\nu}(t - t_0)^2 + ..., \tag{2.6}$$

where ϕ_0 is the rotational phase measured at epoch t_0. Within the lighthouse model approximation, each single rotation of the pulsar counts as 2π towards the rotational phase ϕ. The pulsar's spin frequency ν[Hz] and spin-down rate $\dot{\nu}$[Hz s^{-1}] are the final parameters in our timing model.

The process of fitting for timing parameters is commonly conducted via linearised χ^2-minimization evaluated with the TEMPO/TEMPO2 software (Taylor & Weisberg, 1989; Hobbs et al., 2006)[12]. The reduced χ^2 is defined as:

$$\chi^2_{\rm red} = \frac{1}{n_{\rm DoF}} \sum_{i=1}^{n_{\rm TOA}} \left(\frac{\phi(t_i) - \phi_0}{\sigma_i} \right)^2, \tag{2.7}$$

where the number of degrees of freedom is the difference between the number of TOAs and the number of timing parameters, $n_{\rm DoF} = n_{\rm TOA} - n_{\rm par}$. The timing uncertainties σ_i of the i-th TOA are estimated within a template-matching technique described above. The value $\phi(t_i) - \phi_0$ is usually referred to as a *timing residual*. The minimum $\chi^2_{\rm red}$ of the converged solution provides information on the predictive power of a timing model. If a timing model fully describes the data, the $\chi^2_{\rm red}$ is close to unity. Recognisable patterns in the timing residuals and large values of $\chi^2_{\rm red}$ indicate the presence of unmodelled processes, or that some effects were not adequately taken into account (see Figure 2.4) or that uncertainties determined through template matching were underestimated. For instance, the majority of pulsars, especially the young ones, experience so-called *intrinsic timing noise*, which shows itself as correlated structures in the timing residuals with an excess of power at lower frequencies. This intrinsic noise is of an unknown nature and cannot be adequately mitigated, thus can significantly degrade the sensitivity of a timing dataset.

Although the least-square linear fit carried out in TEMPO/TEMPO2 is broadly used in pulsar timing it relies on a number of assumptions, which do not hold

[11] The first two terms (ν and $\dot{\nu}$) are usually enough to describe the rotational evolution of stable pulsars.

[12] http://tempo.sourceforge.net/, https://bitbucket.org/psrsoft/tempo2

in reality. Covariances between timing parameters, as well as the presence of correlated noise such as intrinsic timing noise, can bias the timing solution. In order to account for these issues, more advanced methods have been developed that exploit Bayesian parameter sampling (Lentati et al., 2014) and χ^2-mapping (Lazarus et al., 2014).

Pulsar timing provides a number of unique applications in physics and astrophysics, ranging from strong tests of gravity and condensed matter physics to establishing a pulsar timescale. Some of the examples of how pulsar timing has contributed to science have already been given in Chapter 1. Specifically for this thesis we will apply high-precision timing observations of stable MSPs visible from the southern hemisphere (PPTA data) to put constraints on *fuzzy dark matter*. The details and the results of this study are presented in Chapter 6.

2.4 On probing pulsar polarisation

In this section we introduce a mathematical framework within which polarisation properties of pulsars are studied. We discuss how the polarisation properties are affected by the ISM. Lastly, we review the techniques which are used to estimate the RM with pulsar data.

2.4.1 Stokes parameters

As was discussed in Chapter 1, pulsar radiation is commonly substantially polarised, both linearly and circularly. In order to recover the full polarisation information of the pulsar signal $\boldsymbol{E}(t)$, the receiver of the radio telescope has two receptors, which sample two orthogonal polarisation states of the incoming light, $E_x(t)$ and $E_y(t)$:

$$\boldsymbol{E}(t) = E_x(t) \cdot \hat{\boldsymbol{i}} + E_y(t) \cdot \hat{\boldsymbol{j}}, \tag{2.8}$$

where $\hat{\boldsymbol{i}}$ and $\hat{\boldsymbol{j}}$ are the unit vectors in the directions of the x- and y-axis respectively, and the components of the electric field are:

$$\begin{aligned} E_x(t) &= \mathcal{E}_x \cos(2\pi f t + \phi_x), \\ E_y(t) &= \mathcal{E}_y \cos(2\pi f t + \phi_y). \end{aligned} \tag{2.9}$$

Equations (2.9) can be reformulated into an elliptical equation in rotated Cartesian coordinates:

$$\left(\frac{E_x}{\mathcal{E}_x}\right)^2 + \left(\frac{E_y}{\mathcal{E}_y}\right)^2 - 2\left(\frac{E_x}{\mathcal{E}_x}\right)\left(\frac{E_y}{\mathcal{E}_y}\right)\cos(\Delta\phi) = \sin^2(\Delta\phi), \tag{2.10}$$

where $\Delta\phi = \phi_x - \phi_y$. In the special case of $\Delta\phi = 0$ or π, the ellipse reduces to a line: $E_y = \pm\frac{\mathcal{E}_x}{\mathcal{E}_y}E_x$. When $\Delta\phi = \pm\frac{\pi}{2}$ and $\mathcal{E}_x = \mathcal{E}_y$, the ellipse degenerates into circle.

The above expressions are only valid for monochromatic waves with time-constant values for $\mathcal{E}_x, \mathcal{E}_y$ and $\Delta\phi$. In reality, the emission of celestial radio sources can be

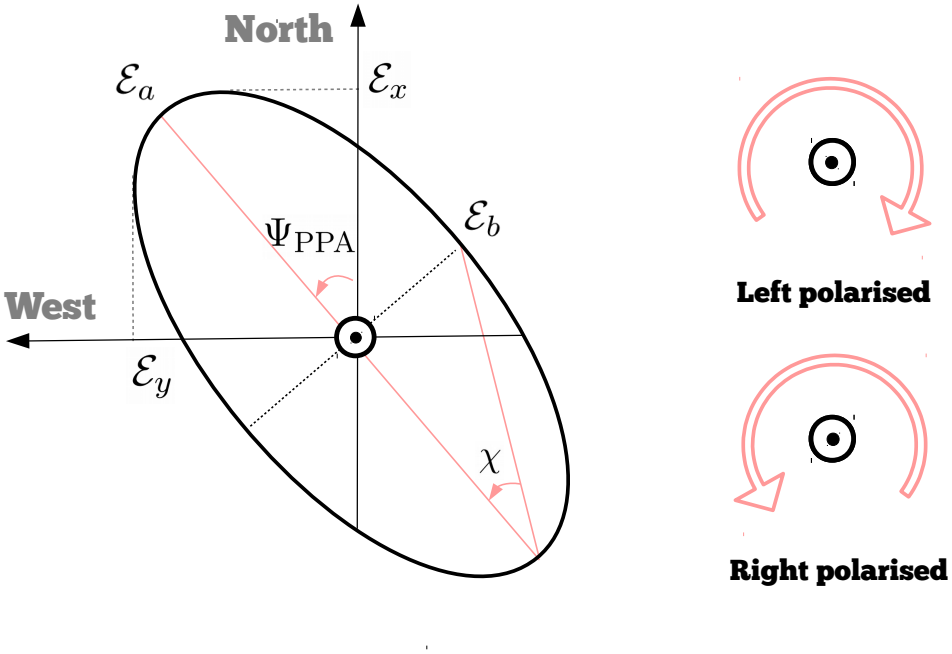

Figure 2.5: Polarisation ellipse. The angle χ defines the polarisation state, while the angle $\Psi_{\rm PPA}$ defines the position of the polarisation ellipse in Cartesian coordinates. The directions of the x- and y-axes, as well as the left- and right-handed circular polarisations have been chosen according to IAU/IEEE convention.

represented as the superposition of statistically independent waves with a variety of polarisations. In order to study such signals radio astronomers use so-called Stokes parameters (Stokes, 1851), which are related to the time-averaged components of the electric field:

$$\begin{aligned} I &= \langle \mathcal{E}_x^2 + \mathcal{E}_y^2 \rangle, \\ Q &= \langle \mathcal{E}_x^2 - \mathcal{E}_y^2 \rangle = Ip\cos(2\chi)\cos(2\Psi_{\rm PPA}), \\ U &= \langle 2\mathcal{E}_x\mathcal{E}_y\cos(\Delta\phi) \rangle = Ip\cos(2\chi)\sin(2\Psi_{\rm PPA}), \\ V &= \langle 2\mathcal{E}_x\mathcal{E}_y\sin(\Delta\phi) \rangle = Ip\sin(2\chi), \end{aligned} \tag{2.11}$$

where χ and the *polarisation position angle* (PPA) $\Psi_{\rm PPA}$ define the orientation of the polarisation ellipse in the Cartesian coordinate system (see Figure 2.5). The Stokes parameter I is the measure of the total intensity, Q and U represent the linearly polarised components, while V is related to the circularly polarised counterpart of the radiation. The linearly polarised intensity is given by $L = \sqrt{Q^2 + U^2}$. Generally, an astrophysical signal can be regarded as the sum of two components: completely polarised and randomly polarised. The ratio between the completely polarised component and the total flux is characterised by the polarisation fraction p, which is defined as $p = \frac{\sqrt{Q^2+U^2+V^2}}{I}$. In case of fully polarised radiation $p = 1$.

Alternatively, the Stokes parameters can be expressed as the function of cross-correlation intensities, XX, YY, $\mathrm{Re}(XY)$ and $\mathrm{Im}(YX)$, which is the common output of multiplying polarimeters:

$$\begin{aligned} I &= XX + YY, \\ Q &= XX - YY, \\ U &= 2\mathrm{Re}(XY), \\ V &= 2\mathrm{Im}(YX). \end{aligned} \tag{2.12}$$

The set of four Stokes parameters I, Q, U, V are the main observables, which are extensively used to investigate the polarisation properties of pulsars.

2.4.2 Modelling the Faraday effect: RM measurement techniques

While propagating through the ISM, the intrinsic polarisation properties of a pulsar are altered. Namely the polarisation ellipse shown in Figure 2.5 starts to rotate due to the Faraday effect described in Section 1.4.3. For a point source[13], the observed PPA rotation is proportional to the square of observational wavelength λ, where RM is a

[13]The trivial λ^2 dependency for the point source turns into a more sophisticated form in the case of extended objects with angular sizes greater than the typical size of turbulent cells in the ISM (e.g. Burn, 1966; Tribble, 1991; Sokoloff et al., 1998; O'Sullivan et al., 2012). This is not the case for pulsars, the angular size of which is negligibly small in comparison to the typical turbulent cell scales in the Milky Way (Haverkorn et al., 2006).

coefficient of proportionality:

$$\begin{aligned} \Psi_{\rm PPA} &= \Psi_0 + \Psi_{\rm F}/2 = \Psi_0 + \lambda^2 {\rm RM}, \\ {\rm RM} &= 0.81\,{\rm rad\,m^{-2}} \int n_e \boldsymbol{B} {\rm d}\boldsymbol{r}, \end{aligned} \tag{2.13}$$

where $n_{\rm e}$ is in cm^{-3}, $|\boldsymbol{B}|$ is in μG, $|{\rm d}\boldsymbol{r}|$ is in pc, and Ψ_0 is the initial PPA at the pulsar. Proper modelling and estimation of Faraday rotation is necessary if one wants to recover the intrinsic properties of pulsar radiation, or if one is interested in the magnetic characteristics of the intervening medium itself: magnetic fields, and magnetic properties of turbulence. The broadband capabilities of modern radio facilities operating at longer wavelengths with narrow frequency channels across the band, enables us to measure RM with higher precision. The set of tools that astronomers are using to derive RMs of polarised sources from the full-Stokes data are outlined below.

PPA fitting The traditional way of computing the RM of a polarised source is to perform a linear fit to the PPA determined at multiple observing frequencies against λ^2 (Cooper & Price, 1962). The PPA can be expressed as a function of direct observables: Stokes Q and U. By dividing U by Q, from Equations (2.11) one gets:

$$\Psi_{\rm PPA}(f) = \Psi_0 + \lambda^2 {\rm RM} = \frac{1}{2}\tan^{-1}\left(\frac{U(f)}{Q(f)}\right), \tag{2.14}$$

Hereafter, Q and U imply the Stokes parameters summed across the phase bins of the on-pulse region:

$$U = \sum_{\rm ON} \mathcal{U}_i, Q = \sum_{\rm ON} \mathcal{Q}_i.$$

The upper panel of Figure 2.6 demonstrates the linear trend in PPA as a function of λ^2 and the best-fit solution. The uncertainties on the resultant RM can be determined via the Fisher information matrix.

The major disadvantage of the method is the so-called $n\pi$-ambiguity problem (e.g. Brentjens & de Bruyn, 2005). Effect arises because the measured $\Psi_{\rm PPA}$ has periodicity of π. For high RM values the $n\pi$-ambiguity causes multiple jumps on PPA plots, which significantly complicates the fitting procedure (e.g. Noutsos et al., 2008). In the case the frequency band is significantly undersampled, an infinite number of equally valid RM solutions arise, corresponding to the PPA modulo $n\pi$. The effect is demonstrated in the lower panel of Figure 2.6. The red line shows the true signal, while the grey line indicates an alternative solution.

Strictly speaking, PA fitting is only valid for *Faraday simple* sources, i.e. point sources, such as pulsars, which have negligible intrinsic Faraday rotation (e.g. Wang et al., 2011) and do not suffer from depolarisation effects (Sokoloff et al., 1998). For unresolved extended foreground sources, the radiation of which takes multiple paths from the source to the observer and, thus, is Faraday rotated by varying degrees, the simple linear PPA dependency is no longer applicable. Furthemore, depolarization occurs when both synchrotron-emitting and Faraday rotating sources are present in the beam volume (differential Faraday rotation).

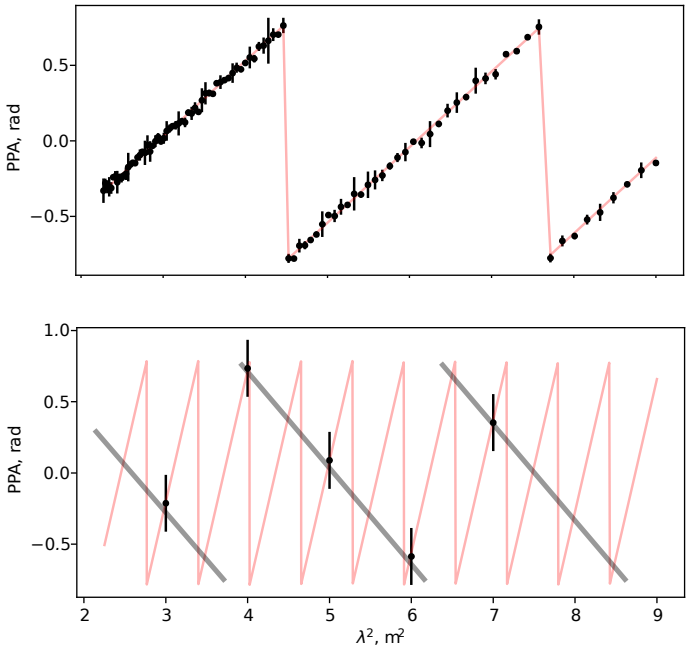

Figure 2.6: Simulated change in PPA as a function of λ^2 due to Faraday rotation. A bandwidth of 100 MHz with 150 MHz central frequency is assumed. The black data points show one possible PPA realisation, while the red lines show the true-simulated signal. The wraps in both panels reflect the $n\pi$-ambiguity effect, which PPA is subject to (see Equation 2.14). *Top panel*: the injected RM is 0.5 rad m^{-2}. The sampling frequency of 1 MHz allows to successfully recover the injected signal. *Bottom panel*: The injected RM is 2.5 rad m^{-2}. The plot shows how the $n\pi$-ambiguity can bias the process of RM determination. The λ^2 domain is significantly undersampled. The overplotted grey line show an alternative solution, corresponding to RM$=-0.7$ rad m^{-2}.

These problems can be eradicated when other, more general, methods for RM determination, such as QU-fitting and RM synthesis, are applied.

RM synthesis RM synthesis, a technique that was initially proposed by Burn (1966), and then further developed by Brentjens & de Bruyn (2005), is nowadays broadly used in the field (e.g. Mao et al., 2010; Noutsos et al., 2015). It can be shown that a non-zero RM gives rise to harmonic signals in both of the Stokes Q and U, which are shifted by $\pi/2$ with respect to each other (see the Equations (2.11)). The theoretically predicted Stokes $Q_{\rm mod}$ and $U_{\rm mod}$ are given by:

$$\begin{aligned} Q_{\rm mod}(\lambda^2) &= Ip\cos(2\chi)\cos(2\Psi_{\rm PPA}) = Ip\cos(2\chi)\cos(2{\rm RM}\lambda^2 + 2\Psi_0), \\ U_{\rm mod}(\lambda^2) &= Ip\cos(2\chi)\sin(2\Psi_{\rm PPA}) = Ip\cos(2\chi)\sin(2{\rm RM}\lambda^2 + 2\Psi_0). \end{aligned} \tag{2.15}$$

In order to not only estimate the absolute value of RM, but also determine its sign, one needs to perform an FFT on the measured complex linear polaristion $\boldsymbol{P} = Q + iU$, also known as the polarisation vector:

$$F({\rm RM}) = \int_{-\infty}^{+\infty} \boldsymbol{P}(\lambda^2) e^{-2i{\rm RM}\lambda^2} {\rm d}\lambda. \tag{2.16}$$

The peak in the power spectrum will correspond to the sought RM. *Faraday thick* structures, probed with extended sources, will be shown in the spectrum as extensive patterns with multiple peak. RM synthesis implements this simple idea, but with some nuances.

The main problem that arises in reality, is that $\boldsymbol{P}$ is defined for a finite number of frequency channels $N_{\rm ch}$. The situation is further exacerbated by irregular sampling in the λ^2 domain, as well as due to the excision of frequency channels because of RFI. The more incomplete the coverage of λ^2 is the stronger the side-lobes in the power spectrum, which can bias the RM determination process. For a realistic case the observed polarised flux can be expressed as:

$$\widetilde{\boldsymbol{P}}(\lambda^2) = W(\lambda^2)\boldsymbol{P}(\lambda^2). \tag{2.17}$$

$W(\lambda^2)$ is the windowing function, which is nonzero, where measurements were taken, and zero elsewhere. The windowing function $W(\lambda^2)$ can be generalised for the case of unequal performance of different frequency channels, by weighting $W(\lambda^2)$ with $({\rm S/N})^2$ for each frequency channel. Then, by making use of the convolution theorem, the Fourier transform (FT) of the unevenly sampled $\widetilde{\boldsymbol{P}}(\lambda^2)$ is:

$$\widetilde{F}({\rm RM}) = \int_{-\infty}^{+\infty} \widetilde{\boldsymbol{P}}(\lambda^2) {\rm e}^{-2i{\rm RM}\lambda^2} {\rm d}\lambda = F({\rm RM}) * \widetilde{W}({\rm RM}), \tag{2.18}$$

where $\widetilde{W}({\rm RM})$ is the FT of the window function. In practice, if ${\rm RM}(\delta\lambda^2) \ll 1$, where $\delta\lambda$ is the average bandwidth of the channels, the integrals can be rewritten

as sums:

$$\widetilde{F}(\mathrm{RM}) = \sum_{j=1}^{N_{\mathrm{ch}}} \widetilde{\boldsymbol{P}}(\lambda_j^2) \mathrm{e}^{-2i\mathrm{RM}(\lambda_j^2-\lambda_0^2)},$$
$$\widetilde{W}(\mathrm{RM}) = \sum_{j=1}^{N_{\mathrm{ch}}} W(\lambda_j^2) \mathrm{e}^{-2i\mathrm{RM}(\lambda_j^2-\lambda_0^2)}, \tag{2.19}$$

where λ_0 is the central wavelength, which is introduced in the equations to stabilise the rapidly oscillating behaviour of the real and imaginary parts of the FT of $\widetilde{\boldsymbol{P}}(\lambda^2)$ (Brentjens & de Bruyn, 2005; Heald, 2009). In order to recover the power spectrum of the original polarised flux, $F(\mathrm{RM})$, one needs to perform a deconvolution routine, for example one analogous to the CLEAN algorithm designed for the purposes of aperture synthesis (Högbom, 1974). More complete coverage in the λ^2-domain increases the quality of the reconstructed $F(\mathrm{RM})$.

The uncertainties on the measured RM are defined by the following semi-empirical expression[14]:

$$\sigma_{\mathrm{RM}} = \frac{\delta\phi}{2 \times (\mathrm{S/N})_L} = \frac{3.8}{2 \times \Delta\lambda^2 (\mathrm{S/N})_L}. \tag{2.20}$$

Larger bandwidths $\Delta\lambda^2$ decrease the width of the peak in the Faraday spectra $\delta\phi$ and, thus, increase the accuracy of the determined RM. The application of RM synthesis on example data of PSR J0953+0755 is demonstrated in the right-hand panel of Figure 2.7 C.

QU-fitting The Equations (2.15) can be utilised directly without any further manipulations, and a simultaneous fit of both $Q(\lambda^2)$ and $U(\lambda^2)$ can be performed. To find the best-fit $\widehat{\mathrm{RM}}$ one can minimise the sum of the squares of the residuals (or more generally a maximumise the likelihood):

$$\sum_{i=1}^{N_{\mathrm{ch}}} \frac{(Q_{\mathrm{obs},i} - Q_{\mathrm{mod}})}{\sigma_{Q,i}^2} + \frac{(U_{\mathrm{obs},i} - U_{\mathrm{mod}})}{\sigma_{U,i}^2}, \tag{2.21}$$

where σ_Q and σ_U are the uncertainties of the observed Stokes Q_{obs} and U_{obs}, respectively, measured as the root-mean-square of Q and U in the off-pulse region in each frequency channel. Q_{mod} and U_{mod} are the theoretically predicted Stokes parameters, which in case of a point source are described by Equations (2.15). Within frequentist inference the RM uncertainty can be calculated via the Fisher information matrix.

QU-fitting has been extensively investigated and developed in Schnitzeler & Lee (2017), where authors have taken into account speficitaions of broad-band pulsar observations, e.g. the observed power-law polarised flux density spectrum of pulsars. The QU-fitting has been also successfully enhanced and implemented for

[14] The factor 3.8 was empirically derived in Schnitzeler et al. (2009)

RM determination of extended sources (e.g. O'Sullivan et al., 2012; Schnitzeler et al., 2015; Ma et al., 2017). An example application of the method to pulsar data is demonstrated in the right-hand panel of Figure 2.7 A. This method was further developed within this thesis (see Chapter 3).

RMFIT is a brute-force method for the RM determination of pulsars, which is a subroutine of the PSRCHIVE package. The presumed RM range is split into steps. A given PSRFITS pulsar archive is derotated with user-defined trial RMs, in order to find the RM value that maximises the frequency-averaged linearly polarised intensity:

$$L(\mathrm{RM}) = \sum_{i=1}^{N_{\mathrm{ch}}} \sqrt{Q^2_{\mathrm{RM,i}} + U^2_{\mathrm{RM,i}}}.$$

The peak in the resultant RM spectrum is fitted with a Gaussian, the centroid of which determines the best-fit RM. The RM uncertainty is estimated as the width of the Gausssian divided by the $(\mathrm{S/N})_{\mathrm{L}}$. Figure 2.7 B shows RMFIT applied to the example data of PSR J0953+0755.

Bayesian Generalised Lomb-Scargle Periodogram is a method that is aimed at searching for periodicities in the data series. Within this thesis the method was adapted and applied for the first time to RM determination. The details of this technique are described in Chapter 3. The application of the method is demonstrated in Figure 2.7 D.

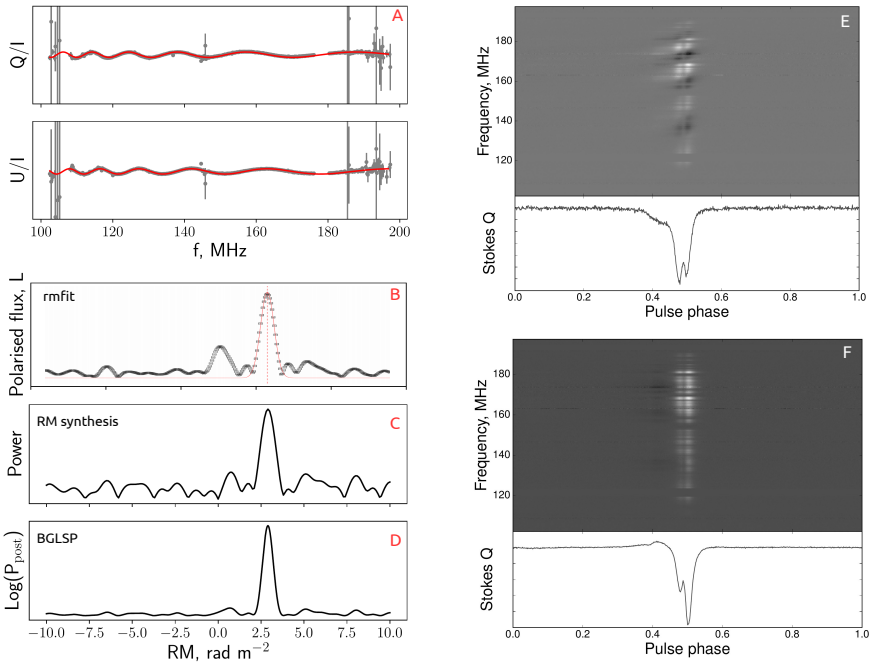

Figure 2.7: Faraday rotation of PSR J0953+0755 in the example data taken with LOFAR HBA. A) Normalised Q/I and U/I intensities as a function of observing frequency. The observed values for Q/I and U/I are shown with grey dots, while the red lines show the best-fit solution: RM=2.96±0.003 rad m^{-2}. B) Application of the RMFIT routine. The black line shows the linear intensity L, the best-fit Gaussian fitted to the peak of the RM spectrum is shown with the red line. The inferred value is RM=2.95±0.02 rad m^{-2}. C) Black line shows the RM spectrum constructed with the RM synthesis technique. The inferred value is RM=2.97±0.001 rad m^{-2}. D) The application of the BGLSP method. The black line shows the logarithm of the RM posterior probability. The inferred value is RM=2.96±0.003 rad m^{-2}. E) Stokes Q as a function of pulse phase and observing frequency. The top plot shows fluctuations in Stokes Q caused by the Faraday effect. The bottom plot shows the integrated Stokes Q profile, which is misrepresented due to a nonzero RM. F) The same as E), but after the signal was de-rotated with RM=2.96 rad m^{-2}. The shape of the integrated Q is correctly restored.

Chapter 3

Bayesian Generalised Lomb-Scargle Periodogram

The work presented in this section is based on Appendices A, B and C of the following article:

- N. K. Porayko, A. Noutsos, C. Tiburzi, J.P.W. Verbiest, A. Horneffer, J. Künsemöller, S. Osłowski, M. Kramer, D.H.F.M. Schnitzeler, J.M. Anderson, M. Brüggen, J.-M. Grießemeier, M. Hoeft, D.J. Schwarz, M. Serylak, O. Wucknitz; *"Testing the accuracy of the ionospheric Faraday rotation corrections through LOFAR observations of bright northern pulsars"*, 2019, MNRAS, 483, 4100

In this part of the publication, I have adapted the Bayesian Generalised Lomb-Scargle Periodogram technique and further develop it for the RM determination problem.

Contents

3.1 Basic definitions 49
3.2 Derivation of the marginalised posterior probability 51
3.3 Limitations of the method and ways for further improvement 53

As it was shown in Chapter 2, the effect of Faraday rotation induces harmonic signals in the observed Stokes Q and U with period equal to π/RM as a function of the square of the observational wavelength. Here we develop an algorithm, based on Bayesian generalised Lomb-Scargle periodogram, which incorporates Stokes I, Q and U in order to estimate the RM of a polarised radio point source. The algorithm also quantifies uncertainties of the fitted RM, assuming the noise of Stokes I, Q and U follow a Gaussian distribution. We also discuss limitations of the algorithm as well as prospects of future improvements.

3.1 Basic definitions

Building on the QU-fitting technique, described in Section 1.4.3, and taking into account the specifics of the observational setup, we further develop the method of RM determination for the case of point sources. As mentioned in Section 1.4.3, if the data are not influenced by the effects of multibeam propagation such as differential

Faraday rotation and wavelength-dependent polarization (Sokoloff et al., 1998), the induced variation in the polarization angle is simply proportional to the square of the observational wavelength λ.

Mathematically, the problem of RM determination can be described in the following way. The modelled Stokes $Q_{\rm mod}$ and $U_{\rm mod}$ can be expressed as (from Equation (2.15)):

$$\begin{aligned} Q_{\rm mod}(\lambda^2) &= I_{\rm mod} p \cos(2\chi)\cos(2{\rm RM}\lambda^2 + 2\psi_0), \\ U_{\rm mod}(\lambda^2) &= I_{\rm mod} p \cos(2\chi)\sin(2{\rm RM}\lambda^2 + 2\psi_0). \end{aligned} \tag{3.1}$$

In practice, we can only access measured Stokes parameters $I_{\rm obs}$, $Q_{\rm obs}$, $U_{\rm obs}$, corrupted by noise. For the sake of simplicity, as we do not know the intrinsic intensity of the source if we do not perform flux calibration, we use $Q_{\rm obs}/I_{\rm obs}$ and $U_{\rm obs}/I_{\rm obs}$, denoted as q and u, respectively. In this method, we assume that q and u are distributed normally around their mean values with variances:

$$\begin{aligned} \sigma_q &= \frac{Q}{I}\sqrt{\left(\frac{\sigma_Q}{Q}\right)^2 + \left(\frac{\sigma_I}{I}\right)^2}, \\ \sigma_u &= \frac{U}{I}\sqrt{\left(\frac{\sigma_U}{U}\right)^2 + \left(\frac{\sigma_I}{I}\right)^2}, \end{aligned} \tag{3.2}$$

where σ_I, σ_Q and σ_U are the standard deviations of the observed Stokes parameters in the off-pulse region.

To recover the RM, we have adapted the method of the Bayesian Generalised Lomb-Scargle Periodogram (BGLSP), described in Bretthorst (2001) and Mortier et al. (2015). Although we kept the spirit of the original BGLSP method, some modifications had to be introduced in order to make the method applicable to the problem of RM searching. To be more specific, we have synthesised the ideas from both Bretthorst (2001) and Mortier et al. (2015), and created an algorithm which recovers the period of a complex signal $Q + iU$ with the two constant offsets γ_q and γ_u, which are associated with the instrumental peak. This resultant algorithm can recover the harmonic signal in RM ranges from $\pi/[\lambda^2_{\rm max} - \lambda^2_{\rm min}]$ up to approximately the average Nyquist boundary $\pi/2\delta(\lambda^2)$, where $\delta(\lambda^2)$ is average bandwidth of the channels, determined by the size of the frequency channel, and $\lambda_{\rm min}$ and $\lambda_{\rm max}$ are the lowest and highest observational wavelengths, respectively. In case of LOFAR HBAs, the range of available RMs is $0.5 - 120\,{\rm rad\,m^{-2}}$.

By writing $c_i = \cos(2{\rm RM}\lambda_i^2 - \theta)$ and $s_i = \sin(2{\rm RM}\lambda_i^2 - \theta)$, the normalised Stokes $q_{\rm obs}$ and $u_{\rm obs}$ can be expressed as

$$\begin{aligned} q_{{\rm obs},i} &= Ac_i + Bs_i + \gamma_q + \varepsilon_{q,i}, \text{ and} \\ u_{{\rm obs},i} &= -As_i + Bc_i + \gamma_u + \varepsilon_{u,i}, \end{aligned} \tag{3.3}$$

where A and B are the amplitudes of the oscillation, and θ is an arbitrary phase reference point, which does not affect the RM and is defined in Section 3.2. The noise contributions $\varepsilon_{q,i}$ and $\varepsilon_{u,i}$ are assumed to be normally distributed, with standard deviations $\sigma_{q,i}$ and $\sigma_{u,i}$ and to vary independently across frequency channels.

As the integration time of our observations is not infinitely small, the rate of change of the ionospheric RM during the integration time will introduce an additional ambiguity to the measured RMs, which we have taken into account here by introducing the parameter η (see also Schnitzeler & Lee, 2017). It acts effectively as a multiplier for all the Q and U error bars (see Section 3.2) and is correlated with the reduced χ^2 value.

According to Bayes' theorem, the posterior probability $P_{\rm pst}$ can be written as

$$P_{\rm pst}({\rm parameters}|{\rm data}) = \frac{P_{\rm pr}({\rm parameters})P({\rm data}|{\rm parameters})}{P({\rm data})}, \tag{3.4}$$

where $P_{\rm pr}({\rm parameters})$ is the prior distribution of the unknown parameters, $P({\rm data}|{\rm parameters})$ is the likelihood function, $P({\rm data})$ is the so-called Bayesian evidence, which is a normalization factor in our case and plays an important role in the problem of model selection. Assuming uniform prior distributions of the parameters, the posterior probability is proportional to a likelihood :

$$\begin{aligned} &P_{\rm posterior}(A, B, \gamma_q, \gamma_u, {\rm RM}, \eta|q_{{\rm obs},i}, u_{{\rm obs},i}) \\ &\propto \Pi_{i=1}^{N_{\rm ch}} \frac{1}{\sqrt{2\pi}\sigma_{q,i}\eta} \exp\left(-\frac{(q_{{\rm obs},i} - Ac_i - Bs_i - \gamma_q)^2}{2(\sigma_{q,i}\eta)^2}\right) \\ &\times \Pi_{i=1}^{N_{\rm ch}} \frac{1}{\sqrt{2\pi}\sigma_{u,i}\eta} \exp\left(-\frac{(u_{{\rm obs},i} + As_i - Bc_i - \gamma_u)^2}{2(\sigma_{u,i}\eta)^2}\right). \end{aligned} \tag{3.5}$$

The resultant form for the posterior probability is analytically marginalised over the nuisance parameters [A, B, γ_q, γ_u] (see Equation (3.9)) and is provided in the next section. The parameter η was estimated separately, using Equation (3.11), and fixed to its maximum likelihood value.

3.2 Derivation of the marginalised posterior probability

Here we provide the derivation of the marginalised posterior probability $P_{\rm posterior}$ from Equation (3.5). Using similar notations to Mortier et al. (2015), we can determine the part of the expression for the posterior probability which depends on unknown parameters (called Sufficient Statistics) as[1]:

$$\begin{aligned} &\ln P_{\rm posterior}\,(A, B, \gamma_q, \gamma_u, {\rm RM}|q_{{\rm obs},i}, u_{{\rm obs},i}) \\ &\propto -\frac{1}{2}\sum_{i=1}^{N_{\rm ch}}\left[\frac{(q_{{\rm obs},i} - Ac_i - Bs_i - \gamma_q)^2}{\sigma_{q,i}^2} + \frac{(u_{{\rm obs},i} + As_i - Bc_i - \gamma_u)^2}{\sigma_{u,i}^2}\right] \\ &= \frac{1}{2}(-Y\hat{Y} + 2AY\hat{C} + 2BY\hat{S} + 2\gamma_q Y_q + 2\gamma_u Y_u - A^2\hat{C}C - B^2\hat{S}S - \gamma_q^2 W_q \\ &\quad - \gamma_u^2 W_u - 2A\gamma_q C_q - 2A\gamma_u C_u - 2B\gamma_q S_q - 2B\gamma_u S_u). \end{aligned} \tag{3.6}$$

The cross term $AB\sum_{i=1}^{N_{\rm ch}}(\omega_{q,i} - \omega_{u,i})\,c_i s_i$ can be suppressed by assuming that $\tan(2\theta) = \sum_{i=1}^{N_{\rm ch}}(\omega_{q,i} - \omega_{u,i})\sin\left(4{\rm RM}\lambda^2\right) / \sum_{i=1}^{N_{\rm ch}}(\omega_{q,i} - \omega_{u,i})\cos\left(4{\rm RM}\lambda^2\right)$. In the

[1] Parameter η will be introcuduced later in this chapter

above expression the following definitions were used:

$$\begin{aligned}
W_q &= \sum_{i=1}^{N} \omega_{q,i}, \text{ and } W_u = \sum_{i=1}^{N} \omega_{u,i}, \\
Y_q &= \sum_{i=1}^{N} \omega_{q,i} q_{\mathrm{obs},i}, \text{ and } Y_u = \sum_{i=1}^{N} \omega_{u,i} u_{\mathrm{obs},i}, \\
\hat{YY} &= \sum_{i=1}^{N} \omega_{q,i} q_{\mathrm{obs},i}^2 + \omega_{u,i} u_{obs,i}^2, \\
\hat{YC} &= \sum_{i=1}^{N} \omega_{q,i} q_{\mathrm{obs},i} c_i + \omega_{u,i} u_{obs,i} s_i, \\
\hat{YS} &= \sum_{i=1}^{N} \omega_{q,i} q_{\mathrm{obs},i} s_i - \omega_{u,i} u_{obs,i} c_i, \\
\hat{CC} &= \sum_{i=1}^{N} \omega_{q,i} c_i^2 + \omega_{u,i} s_i^2, \text{and } \hat{SS} = \sum_{i=1}^{N} \omega_{q,i} s_i^2 + \omega_{u,i} c_i^2, \\
C_q &= \sum_{i=1}^{N} \omega_{q,i} c_i, \text{ and } C_u = \sum_{i=1}^{N} \omega_{u,i} c_i, \\
S_q &= \sum_{i=1}^{N} \omega_{q,i} s_i \text{ and } S_u = \sum_{i=1}^{N} \omega_{q,i} s_i,
\end{aligned} \tag{3.7}$$

and the weights are defined in a traditional way as:

$$\omega_{q,i} = \frac{1}{\sigma_{q,i}^2} \text{ and } \omega_{u,i} = \frac{1}{\sigma_{u,i}^2}. \tag{3.8}$$

The resultant expression for the Sufficient Statistics after marginalization over nuisance parameters A, B, γ_q, γ_u is

$$\begin{aligned}
&P_{\mathrm{posterior}}\left(\mathrm{RM}|q_{\mathrm{obs}}, u_{\mathrm{obs}}\right) \\
&\propto \frac{1}{\sqrt{|4DF - E^2|\hat{CC}\hat{SS}}} \exp\left(M - \frac{\hat{YY}}{2} + \frac{DG^2 - EGJ + FJ^2}{E^2 - 4DF}\right),
\end{aligned} \tag{3.9}$$

where

$$
\begin{aligned}
D &= \frac{C_q^2\hat{S}\hat{S} + S_q^2\hat{C}\hat{C} - W_q\hat{C}\hat{C}\hat{S}\hat{S}}{2\hat{C}\hat{C}\hat{S}\hat{S}}, \\
F &= \frac{C_u^2\hat{S}\hat{S} + S_u^2\hat{C}\hat{C} - W_u\hat{C}\hat{C}\hat{S}\hat{S}}{2\hat{C}\hat{C}\hat{S}\hat{S}}, \\
E &= \frac{C_uC_q\hat{S}\hat{S} + S_uS_q\hat{C}\hat{C}}{\hat{C}\hat{C}\hat{S}\hat{S}}, \\
J &= \frac{C_q\hat{Y}\hat{C}\hat{S}\hat{S} + S_q\hat{Y}\hat{S}\hat{C}\hat{C} - Y_q\hat{C}\hat{C}\hat{S}\hat{S}}{\hat{C}\hat{C}\hat{S}\hat{S}}, \\
G &= \frac{C_u\hat{Y}\hat{C}\hat{S}\hat{S} + S_u\hat{Y}\hat{S}\hat{C}\hat{C} - Y_u\hat{C}\hat{C}\hat{S}\hat{S}}{\hat{C}\hat{C}\hat{S}\hat{S}} \text{ and} \\
M &= \frac{\hat{Y}\hat{C}^2\hat{S}\hat{S} + \hat{Y}\hat{S}^2\hat{C}\hat{C}}{2\hat{C}\hat{C}\hat{S}\hat{S}}.
\end{aligned}
\tag{3.10}
$$

The resultant expression can be easily generalised for the case of underestimated uncertainties in Stokes Q and U by including an extra free parameter η, such that $\omega_q \to \eta^{-2}\omega_q$ and $\omega_u \to \eta^{-2}\omega_u$. In this case the resultant marginalised posterior probability will be a function of two parameters: $P_{\text{posterior}}\,(\text{RM}, \eta | q_{\text{obs}}, u_{\text{obs}})$.

In order to determine the unknown parameters within the Bayesian framework, one needs to numerically reconstruct the 2D posterior probability, which can be effectively managed by Markov Chain Monte Carlo. In the frequentist approach, which is less computationally expensive and was used in this work, we are interested in the maximum likelihood estimation of the unknown parameters, which for η can be found analytically:

$$
\hat{\eta}^2 = -\frac{2}{2N_{\text{ch}} - 4}\left[M - \frac{\hat{Y}\hat{Y}}{2} + \frac{DG^2 - EGJ + FJ^2}{E^2 - 4DF}\right]. \tag{3.11}
$$

By performing a 1D grid search in the RM parameter space, we can successfully recover the RM posterior probability distribution (see Figure 2.6, 4.1). The uncertainty in the RM value is determined as the variance of the normal Gaussian distribution, fit to the resultant shape of the posterior probability.

3.3 Limitations of the method and ways for further improvement

By postulating that the observed Stokes I_{obs}, Q_{obs} and U_{obs} are normally distributed, one can derive that q and u will actually follow a Cauchy-like distribution. In Schnitzeler & Lee (2017) it was shown that the non-Gaussianity of q and u can bias the uncertainty of measured RMs in the low S/N regime. However, in the case of high S/N (i.e., $\sigma_I/I < 0.1$, see Hayya et al. (1975); Kuethe et al. (2000)), the resultant Cauchy distribution can be reasonably well approximated by the normal distribution. By selecting frequency channels above the threshold, and simulating the normally-distributed

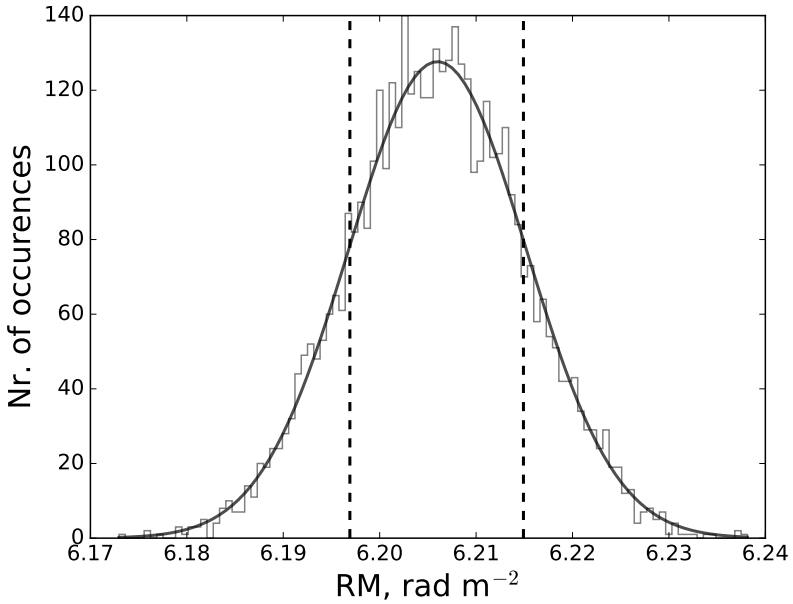

Figure 3.1: Distribution of the reconstructed RMs for simulated data of PSR J1136+1551 (grey line) and posterior probability of RM as predicted with the BGLSP method (black line). The vertical dashed lines show the quantiles of the reconstructed distribution $Q_{16\%}$ and $Q_{84\%}$. Half of the interquartile range of the RM distribution, reconstructed from the simulations, is $(Q_{84\%}-Q_{16\%})/2 = 0.009\,\mathrm{rad\,m^{-2}}$, while the 1σ uncertainty, determined with the BGLSP is $0.0092\,\mathrm{rad\,m^{-2}}$. The S/N of PSR J1136+1551 in linear intensity is $\simeq$50.

Stokes parameters in each of them, we have reconstructed the RM posterior distribution determined with the BGLSP method. For the two pulsars that we have included in the test (PSRs J0332+5434 and J1136+1551 observed with the LOFAR HBAs), we have found that the distribution of the resultant RMs can be well approximated by a normal one and its parameters (variance and mean) are in good agreement with those determined with the BGLSP. In Figure 3.1 we display the RM distribution for PSR J1136+1551. The properties of the reconstructed distribution are given in the caption.

Schnitzeler & Lee (2017) demonstrated that this problem can be avoided by introducing N_{ch} (number of frequency channels) nuisance parameters $I_{\mathrm{mod},i}$, and found the analytic expression for the likelihood, marginalised over these parameters, in the case of weakly polarised sources ($L_{\mathrm{mod}} \ll I_{\mathrm{mod}}$). The further analysis of non-Gaussianity of q and u and its influence on the distribution of the resultant RMs will be addressed in future work.

Another potential weakness of the method is so-called channel depolarisation, which arises due to the finite size of the frequency channels (Schnitzeler & Lee, 2015). When considering the channel depolarisation, the measured polarisation vector $\boldsymbol{P}$ at the chan-

nels central frequency f_c is:

$$\boldsymbol{P}(f_c, j) \sim \frac{\int_{f_j}^{f_{j+1}} \omega(f)\boldsymbol{P}(f)\mathrm{e}^{2\mathrm{iRM}(c/f)^2}\mathrm{d}f}{\int_{f_j}^{f_{j+1}} \omega(f)\mathrm{d}f}, \tag{3.12}$$

where $\omega(f)$ is the response function of the frequency channel. For the simplest case, when frequency channels have a top-hat response function in the λ^2 domain, the observed Stokes parameters are depolarised by a factor $\mathrm{sinc}(\mathrm{RM}\delta\lambda^2)$, which marginally depends on λ^2. For relatively small RMs and high frequency resolution, such that $RM\delta\lambda^2 \ll 1$, the sinc factor approaches 1. In the real datasets we expect to observe the top-hat response in the frequency rather than in the λ^2 domain, which causes the measured amplitude of the polarisation vector $\boldsymbol{P}$ (and, thus, Q and U) to have a complex dependency on frequency. The channel depolarisation can severely modulate the signal at the low-frequency part of the band, and possibly bias the resultant RM. However, in Schnitzeler & Lee (2015) it was shown that the effect becomes noticeable when the probed RM is larger than

$$\mathrm{RM}_{\mathrm{boundary}} \simeq 1.44 \times 10^4 \ \mathrm{rad\,m^{-2}} \left(\frac{f_{\mathrm{low}}}{\mathrm{GHz}}\right)^{\frac{5}{2}} \left(\frac{f_{\mathrm{high}}}{\mathrm{GHz}}\right)^{\frac{1}{2}} \left(\frac{\delta f}{\mathrm{GHz}}\right)^{-1}, \tag{3.13}$$

when a the large part of the observing band is affected by channel depolarisation. In the above expression, f_{low}, f_{high} are the low- and high-ends of the observing band, and δf is the size of the frequency channel. For the LOFAR HBAs $\mathrm{RM}_{\mathrm{boundary}} \simeq 100\,\mathrm{rad\,m^{-2}}$, significantly exeeding the RMs considered in this thesis ($< 70\,\mathrm{rad\,m^{-2}}$).

Chapter 4

Testing the accuracy of the ionospheric Faraday rotation corrections through LOFAR observations of bright northern pulsars

The work presented in this section is based on the main text of the following article:

- N. K. Porayko, A. Noutsos, C. Tiburzi, J.P.W. Verbiest, A. Horneffer, J. Künsemöller, S. Osłowski, M. Kramer, D.H.F.M. Schnitzeler, J.M. Anderson, M. Brüggen, J.-M. Grießemeier, M. Hoeft, D.J. Schwarz, M. Serylak, O. Wucknitz; *"Testing the accuracy of the ionospheric Faraday rotation corrections through LOFAR observations of bright northern pulsars"*, 2019, MNRAS, 483, 4100

For this part of the publication, I have partially performed the observations and reduction of the radio data. I have determined RMs of the pulsars with the BGLSP method. Further, I have devised and performed the analysis of the residual systematic and noises after mitigation of the ionospheric Faraday rotation.

Contents

4.1 Introduction **58**
4.2 Observations and Data Reduction **60**
4.2.1 On modelling the ionospheric RM variations: thin layer ionospheric model 62
4.3 Systematics in the RM residuals **67**
4.3.1 Analysis of RM residuals on timescales up to one year 69
4.3.2 Analyis of RM residuals on timescales beyond one year 72
4.4 Discussions and Conclusions **74**

Faraday rotation of polarized emission from pulsars measured at radio frequencies provides a powerful tool to investigate the interstellar and interplanetary magnetic fields. However, besides being sensitive to the astrophysical media, pulsar observations in radio are affected by the highly time-variable ionosphere. In this article, the amount of

ionospheric Faraday rotation has been computed by assuming a thin layer model. For this aim, ionospheric maps of the free electron density (based on Global Positioning System data) and semi-empirical geomagnetic models are needed. Through the data of five highly polarized pulsars observed with the individual German LOw-Frequency ARray stations, we investigate the performances of the ionospheric modelling. In addition, we estimate the parameters of the systematics and the correlated noise generated by the residual unmodelled ionospheric effects, and show the comparison of the different free-electron density maps. For the best ionospheric maps, we have found that the rotation measure corrections on one-year timescales after subtraction of diurnal periodicity are accurate to $\sim 0.06 - 0.07\,\mathrm{rad\,m^{-2}}$.

4.1 Introduction

Since their discovery (Hewish et al., 1968), pulsars have been a powerful tool to probe the magnetoionic plasma. Due to frequency-dependent dispersion delay and scattering of their signals, pulsars can be used to study, e.g., turbulence in the ionised interstellar medium (ISM) on many orders of magnitude (e.g. Rickett, 1977; Armstrong et al., 1995; You et al., 2007a), the distribution of free electrons in the Milky Way and the Local Bubble (e.g. Cordes & Lazio, 2002; Bhat et al., 1998), and the electron content of the Solar wind (e.g. You et al., 2007b; Howard et al., 2016). Magnetised plasma also induces Faraday rotation in linearly polarised radiation, that is, a rotation of the polarization angle Ψ depending on the radiation wavelength λ (see Section 2.4.2),

$$\Psi_{\mathrm{PPA}} = \Psi_0 + \mathrm{RM}\ \lambda^2, \tag{4.1}$$

From the above expression one can see that more accurate RM estimations can be achieved with broad-band instruments operating at longer wavelengths.

Due to the high percentage of linear polarisation, and low levels of magnetospheric Faraday rotation (e.g. Wang et al., 2011), pulsars are useful objects to measure RM induced by the ionised ISM, and hence the Galactic magnetic fields (e.g. Han et al., 2018).

Because the propagation effects strongly depend on λ, low frequencies are favoured for studies of these effects in pulsars[1]. Moreover, the steep spectra of pulsars (e.g. Bates et al., 2013) and the reduction of the linear polarisation fractions at high frequencies in pulsar emission (e.g. Johnston et al., 2008b), make the low-frequency band even more preferable for Faraday rotation studies.

Nevertheless, polarisation studies at low frequencies are challenging. Besides the effects of the magnetised ionised ISM, linearly polarised radiation can be noticeably rotated by the highly variable terrestial ionosphere. Moreover, it can significantly depolarise observations when averaging over several hours. For a review on the propagation of radio waves through the ionosphere, see e.g. Wilson et al. (2013) or Thompson et al. (2001).

[1] For strongly Faraday rotated sources, such as pulsars in the dense regions(e.g. magnetar in the Galactic center) and distant active galactic nuclei, RMs can be as well effectively probed with instruments, operating at $1 - 2$ GHz and higher frequencies.

In order to mitigate the ionospheric contribution to Faraday rotation, numerous techniques have been developed. One very promising approach is based on providing quasi-simultaneous observations of a known background source (e.g. the diffuse polarised background), located within the ionospheric correlation spatial scale with respect to the source of interest, to recover the ionospheric Faraday rotation (Lenc et al., 2016).

Alternatively, the ionospheric Faraday rotation can be estimated by combining models of the ionospheric electron density and of the geomagnetic field. In the majority of the studies that aimed to measure the interstellar Faraday rotation in astronomical sources (e.g. Weisberg et al., 2004; Han et al., 2006; Yan et al., 2011b), the ionospheric electron density was computed through the semi-empirical International Reference Ionosphere (IRI) model (Bilitza et al., 2014), which provides monthly-averaged ionospheric electron density profiles up to 2000 km, as a function of time and location. However, due to the sparsely distributed ground and space observatories that contribute to the IRI model, and the large averaging time, the modelled values of electron densities can significantly deviate from the real ones (Mosert et al., 2007). Higher accuracies can be reached by a technique described in Erickson et al. (2001), where the ionospheric electron densities are obtained through raw dual-frequency GPS data, recorded with a set of local GPS receivers. When applied to PSR J1932+1059, the variance of the differences between the observed RM as obtained at the VLA, and the predicted ionospheric RM as computed with the AIPS APGPS routine[2], was found to be 0.2 rad m^{-2}.

A handier and less computationally expensive alternative to this approach consists in using global ionospheric maps of electron column densities in the ionosphere, which are based on the available data from all the GPS stations spread around Earth. This technique was implemented and tested on a set of pulsars by Sotomayor-Beltran et al. (2013), showing a qualitatively good agreement between the expected and the observed values of Faraday rotation. However, Sotomayor-Beltran et al. (2013) have restricted their analysis to probing only two global ionospheric maps (ROBR and CODG), and the research was carried out on a set of observations with timespans of only several hours. The standard deviations of the residuals between the RMs, observed and modelled with CODG and ROBR, varied for different datasets in the ranges $0.12 - 0.20\,\mathrm{rad\,m^{-2}}$ and $0.07 - 0.20\,\mathrm{rad\,m^{-2}}$, respectively.

In this thesis, we aim to compare the performance, and estimate the accuracy of different publicly available global ionospheric maps, when applied to correct for ionospheric Faraday rotation in several months of pulsar data. For these goals, we used pulsar observations obtained with the international LOFAR stations in Germany. In Section 4.2 we describe the instrumental and observational setup and our data reduction, including a first application of a simple ionospheric modelling. In Section 4.3 we attempt to model the ionospheric Faraday rotation in our dataset and we analyse the systematics left in the RM residuals after ionospheric mitigation. In Sections 4.3.1, 4.3.2

[2]A similar approach is implemented in the ALBUS software https://github.com/twillis449/ALBUS_ionosphere

Table 4.1: Details of the observations used for the white noise plateau investigation (see Section 4.3.1) and for the long-term systematics (see Section 4.3.2)

	Jname	Site	$T_{\rm obs}$
Short-term	J0332+5434	DE609	2015-12-19 – 2016-06-13
	J0814+7429	DE605	2016-01-08 – 2017-04-30
	J1136+1551	DE601	2016-01-09 – 2016-10-09
	Jname	Site	$T_{\rm obs}$
Long-term	J0332+5434	DE605	2014-03-09 – 2017-02-11
	J0826+2637	DE603	2015-02-22 – 2017-02-03
	J1136+1551	DE601	2013-09-06 – 2016-12-31
	J1921+2153	DE605	2014-03-08 – 2017-02-11

we focus on how to correct for the systematics, and show the results obtained after the implementation of our additional corrections and the comparison of different global ionospheric maps. In Section 4.4 we then summarise our findings.

4.2 Observations and Data Reduction

All the obsevations were conducted with German LOFAR HBAs in stand-alone mode (see Section 2.2.1). Commonly the integration time per pulsar is ∼2-hours. The specifics for the dataset used in the presented analysis are summarised in Table 4.1. As it will be shown in the next sections, we focus our analysis on the characterization of potential short- and long-term trends in the residuals between the ionospheric models and the data. All the selected pulsars have high signal-to-noise ratio (S/N), which varies from ∼800 up to ∼2000, and a significant fraction of linear polarization (at least 10%), which allows us to measure the RM with high accuracy and precision. Besides this, for the purposes of the short-term analysis, we chose pulsars with a significant fraction of long, continuous observations (from a few hours to entire days). This allows us to properly identify also high-frequency systematics. For the purposes of the long-term analysis, this last requirement is not strictly necessary, and we thus selected pulsars with a long observing baselines.

After digitizing and beamforming, the data is recorded on machines at the Max-Planck-Institut für Radioastronomie in Bonn and at the Jülich Supercomputing Centre using the `LuMP` (LOFAR und MPIfR Pulsare) Software[3]. The datasets are then, coherently de-dispersed, folded modulo the pulse period and reduced to more manageable 10-second sub-integrations with the `DSPSR` software[4] (van Straten & Bailes, 2011), and stored as `PSRFITS` archives (Hotan et al., 2004). We then excise the radio-frequency interference with the `COASTGUARD`'s clean.py surgical algorithm (Lazarus et al., 2016).

In contrast to steerable radio telescopes, the LOFAR antennas are fixed on the ground, which causes a distortion of the polarisation signal, as well as decrease of the

[3] https://github.com/AHorneffer/lump-lofar-und-mpifr-pulsare
[4] http://dspsr.sourceforge.net/

intrinsic signal intensity, towards low elevations, due to the projection effects (Noutsos et al., 2015). For instance, such an instrumental response is responsible for the so-called instrumental peak at $0\,\mathrm{rad\,m^{-2}}$ in the RM spectrum while performing the RM synthesis analysis (Burn, 1966; Brentjens & de Bruyn, 2005). We mitigate these instrumental effects by applying a Jones calibration matrix based on the Hamaker measurement equations (see Hamaker et al., 1996; Smirnov, 2011). However, Noutsos et al. (2015) showed that across several hours of observations taken with the Superterp, the intrinsic signal intensity of the LOFAR antennas significantly degrades at low elevations ($\lesssim 30°$) even after the calibration procedure has been applied.

Due to the fact that radio observations in the LOFAR frequency band are quite sensitive to the highly variable ionospheric layer (van Weeren et al., 2016), we split pulsar archives into 15-minute subintegrations with the `PSRCHIVE` software package[5] (van Straten et al., 2012), which corresponds to the minimum time-sampling of ionospheric maps that we have tested (see Section 4.2.1). This reduces the unresolved contribution of ionospheric RM, while still providing a reasonable S/N.

After this, we estimate the RM for each of the 15-minute subintegrations, building an RM time series for each of the analysed datasets. For this, we use an optimised version of the classical RM synthesis technique, BGLSP, described in Chapter 3.

In Figure 4.1 we demonstrate the example of the BGLSP application to one of the 15-min observation of PSR J1136+1551. We clearly see systematic deviation from the modelled Q and U, which is reflected in the spectrum as a low-frequency excess of power around $0\,\mathrm{rad\,m^{-2}}$. The origin of these systematics is not known for certain, but it is highly likely that it is associated with instrumental properties, e.g. non-linearity in the instrumental setup. Because the spurious peak affects a small range of values around $0\,\mathrm{rad\,m^{-2}}$, we expect sources with significant larger RMs to be uneffected, suggesting little or no influence on our results. However, we point out that the results can be biased when dealing with astronomical sources with low RM values. In order to prove these considerations, we have performed two tests. Firstly, we tested the basic assumption that any discrepancies between the models and the data are induced by an effect that is strongly frequency dependent. Therefore, we have split data into two sub-bands and measured RM values separately for the bottom and upper half of the bandwidth. The results show that both RM values are in excellent agreement within the uncertainties. This suggests that the effect is not strongly depending on frequency. Still, we also tested whether a systematic effect could conspire to mimic a wrong RM value. As a worst case scenario, we have investigated the impact of systematics, in case they had a quadratic dependency on frequency, which would mimic the λ^2 dependency introduced by the physical effect of Faraday rotation. The simulated Stokes Q and U were evenly sampled in frequency with a realistic 20% of data loss due to radio-frequency interference. We run a Monte Carlo simulation with 10^3 realizations of this set-up, for increasing values of RMs from 0 to $20\,\mathrm{rad\,m^{-2}}$. A range of the systematic amplitudes were tested with reduced χ^2 of up to 10, as the reduced χ^2 detected in the data did not exceed this value. We found that, starting from an RM value of

[5] http://psrchive.sourceforge.net/

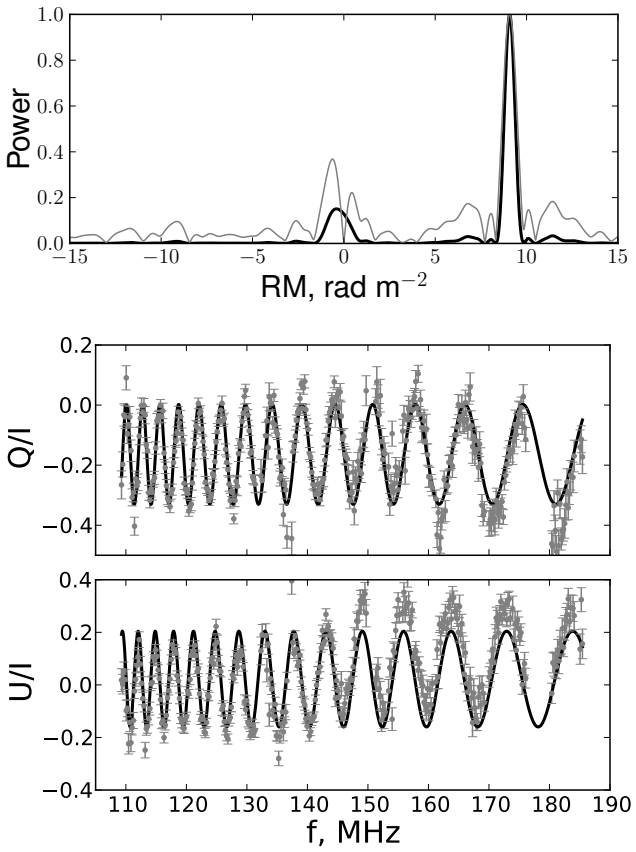

Figure 4.1: *Top panel*: A comparison between the RM spectrum obtained with the classical RM synthesis (grey line) and the logarithm of the RM posterior probability (black line) given by Equation (3.9) for a 15-minute observation of PSR J1136+1551. All the curves are normalised to the maximum values. The maximum peak corresponds to the observed pulsar RM=9.076 rad m^{-2}. *Bottom panel*: Harmonic variations of the Stokes parameters Q and U across the observed bandwidth (grey points). The black lines show the expected harmonic trend, given the pulsar's RM.

$\sim 6\,\mathrm{rad\,m^{-2}}$, the mean and variance of the distribution of the recovered RMs are in a good agreement with the results from BGLSP (see Figure 4.2). This behaviour is expected, since as soon as the source RM is larger than the width of the systematic feature, the two signals can be separated reliably.

With the reliability of our RM measurements established by these tests, we proceed to do a first attempt to mitigate the Faraday rotation ionospheric contribution.

4.2.1 On modelling the ionospheric RM variations: thin layer ionospheric model

If not taken into account, the ionosphere introduces noise in the measured RM values. This makes it impossible, for instance, to investigate RM variations caused by the

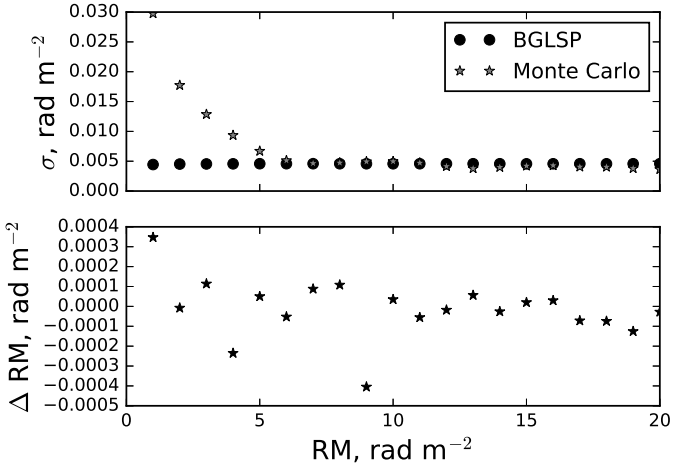

Figure 4.2: *Top panel*: The uncertainties on the RM values detected with BGLSP (black circles), overplotted with the variance of the distribution of the detected RMs obtained from Monte Carlo simulations (grey stars). The plot demonstrates that BGLSP uncertainties are underestimated for $|\mathrm{RM}|<6\,\mathrm{rad\,m^{-2}}$. *Lower panel*: The difference between the injected RMs and the mean values of the Monte Carlo distributions. No systematic deviations between BGLSP and Monte Carlo can be seen. For both panels the reduced χ^2 of the u and q fit was 10.

turbulent ionised ISM, which are expected to be $\sim 3-4$ orders of magnitude lower than the root-mean-square (rms) of the ionospheric RM fluctuations (see Equation (4.10)). We now briefly recap the ionospheric RM behavior and the ways to model it.

The ionospheric layer, partially consisting of free electrons and positively charged ionised molecules and atoms, extends from 50 km to beyond 2000 km above the Earth's surface (Rishbeth & Garriott, 1969). The ionospheric contribution to RM can be estimated to be of the order of $1-4\,\mathrm{rad\,m^{-2}}$, however, the essential complexity in treating the ionospheric RM comes from its strong variability, which typically changes during the day up to 80%. The ionization fraction of the ionospheric shell, mostly caused by photoionization processes involving the Sun's extreme ultra-violet and X-ray emission, varies significantly over timescales of minutes (due to Solar flares) up to years (11-year Solar cycle). Besides this, the ionosphere shows diurnal (caused by the relative motion of the Sun on the celestial sphere) and 27-day periodicities (due to the Solar rotation). As the Earth's atmosphere is not homogeneous and different molecules are dominating at different heights, the ionospheric shell, does not have a homogeneous electron density distribution, and achieves its maximum during the day time in the so-called F sublayer, which implies $\sim 50-60\%$ of all the electrons in the ionosphere (Bilitza et al., 2017). Because of this, the ionosphere can be reasonably well modelled by a thin shell located at the *effective ionospheric height*, which is usually estimated to be between 300 and 600 km above the Earth's surface.

As the projected thickness of the non-uniform ionospheric layer increases out from

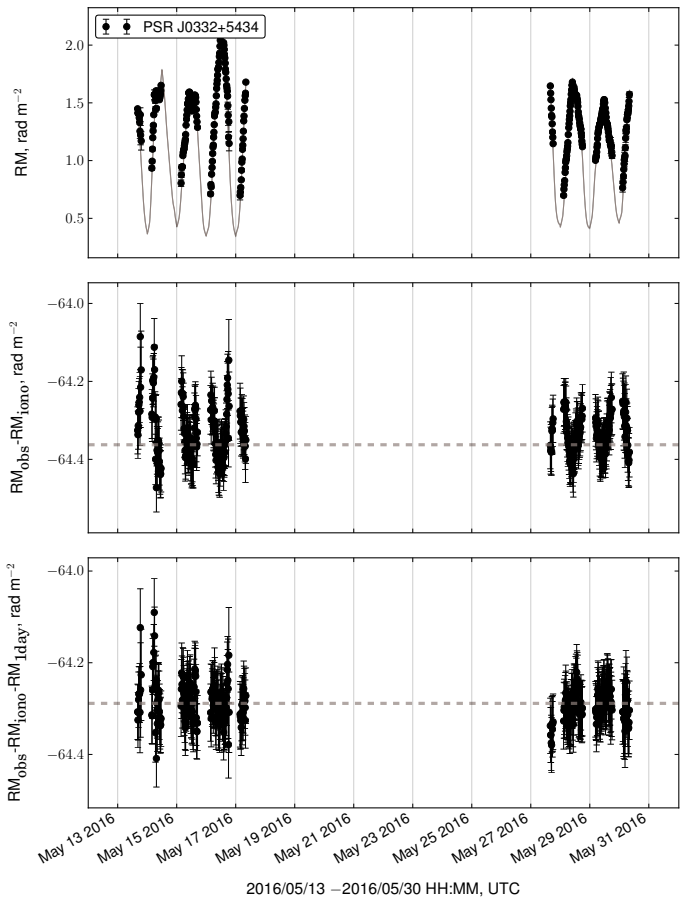

Figure 4.3: Example of application of JPLG ionospheric maps and POMME10 geomagnetic model to real data of PSR J0332+5434 observed by DE609. *Upper panel*: modelled ionospheric RM computed with `RMextract` using JPLG ionospheric maps (in grey), applied to measured RMs shifted by a constant value $\mathrm{RM_{ISM}}$ (black dots). The uncertainties on the modelled RM are smaller than the symbol used. *Middle panel*: residuals between observed and modelled RM (black dots) before subtraction of 1-day sinusoid. *Lower panel*: residuals between observed and modelled RM (black dots) after subtraction of 1-day sinusoid. The grey dashed line shows the constant value $\mathrm{RM_{ISM}}$. The uncertainties on the measured RMs are modified by the values determined through the analysis described in Section 4.3.1. Only the observations above $\sim 30°$ in elevation were used.

the zenith, it is common practice to discard data at low elevations. For this work we have used a 30° elevation cut-off[6]. In the case of the ionosphere, and with the mentioned assumptions, Equation (2.13) is reduced to (Sotomayor-Beltran et al., 2013):

$$\mathrm{RM_{iono}} = 2.6 \times 10^{-17} \mathrm{STEC} \times B_{\mathrm{iono}} \,\mathrm{rad\,m^{-2}}, \tag{4.2}$$

where STEC (Slant TEC, where TEC stands for 'Total Electron Content') is equal to the column density of electrons [$\mathrm{m^{-2}}$] at the cross-section between the LoS and the ionospheric shell and B_{iono} is the projection of the magnetic field [G] in the F-layer on the LoS. The thin layer approximation has already been implemented in several codes aimed at the estimation of the ionospheric RM (e.g. in Sotomayor-Beltran et al., 2013). In particular, for the work presented here we use the publicly available `RMextract` software[7], that estimates the ionospheric RM along a certain LoS and at a certain point in time making use of a geomagnetic field model and a global ionospheric map. An example of ionospheric RM calibration with RMextract, applied to the RM sequence of PSR J0332+5434, is demonstrated on Figure 4.3 (upper panel). From here on in this paper for demonstration purposes we have used JPLG maps, which have showed the second best result in our analysis and are commonly available for the majority of our observing epochs.

The geomagnetic field models are conventionally represented as spherical harmonical expansions of a scalar magnetic potential. Several geomagnetic models are publicly available, among which are the Enhanced Magnetic Model (EMM)[8], the International Geomagnetic Reference Field (IGRF) (Thébault et al., 2015), the World Magnetic Model[9], and POMME10[10]. The lower panel of Figure 4.4 shows a comparison of the ionospheric magnetic field given by EMM, POMME10 and IGRF12, for the years 2013 through 2018 for lines of sight from Germany in the direction of 30° in elevation (minimum elevation used in our work). The plot demonstrates clear systematic behaviour, although, on average between 2013 and 2018, there is less than 0.1% difference between different geomagnetic models. The discrepancy seems to be increasing with time. Thus, for the future datasets taken around 2020 geomagnetic models with non-evolving with time geomagnetic parameters will reach few per cent level difference between them and should be used with care. Figure 4.5 demonstrates that for low elevation observations this difference can hit 1% from the absolute value.

We have conducted a full analysis by making use of all three geomagnetic models. In order to be concise, we present only the results of POMME10 (Maus et al., 2006) here (see Table 4.2). In the case one of the other two geomagnetic models the results on parameter estimation and the presence of various systematics in the data remain unchanged.

[6] This number is partially motivated by the limitations of the polarization calibration method used in this work

[7] https://github.com/lofar-astron/RMextract

[8] https://www.ngdc.noaa.gov/geomag/EMM/

[9] https://www.ngdc.noaa.gov/geomag/WMM/DoDWMM.shtml

[10] http://geomag.org/models/pomme10.html

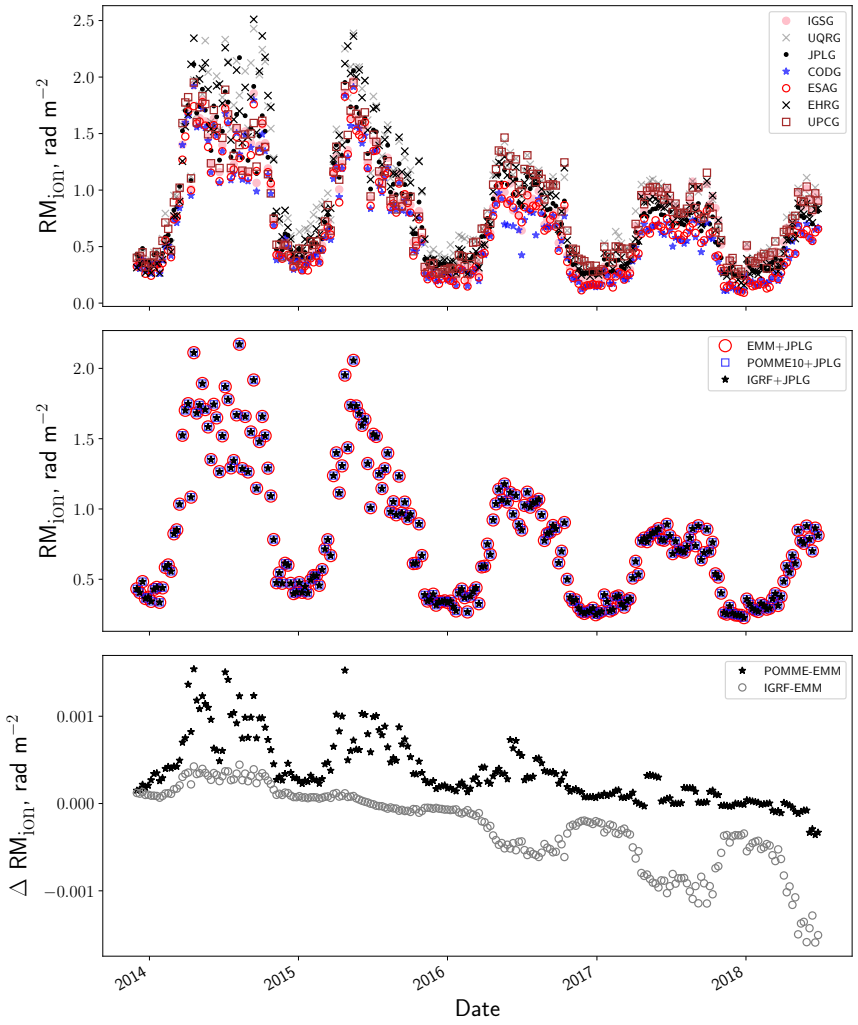

Figure 4.4: *Upper panel*: Comparison between ionospheric RMs in the direction of PSR J0332+5434 observed at constant 30° elevation, as modelled by different ionospheric maps (+POMME10 geomagnetic model). *Middle panel*: Comparison between ionospheric RMs in the direction of PSR J0332+5434 observed at constant 30° elevation, as modelled by POMME10, EMM and IGRF12 (+JPLG ionospheric map). *Bottom panel*: Difference between ionospheric RMs in the direction of PSR J0332+5434 observed at constant 30° elevation, as modelled by POMME10, EMM and IGRF12 (+JPLG ionospheric map). The empty circles show the difference between IGRF12 and EMM. The black stars show the difference between EMM and POMME10, which is on average less than 0.001 rad m^{-2} for observations above 30° in elevation.

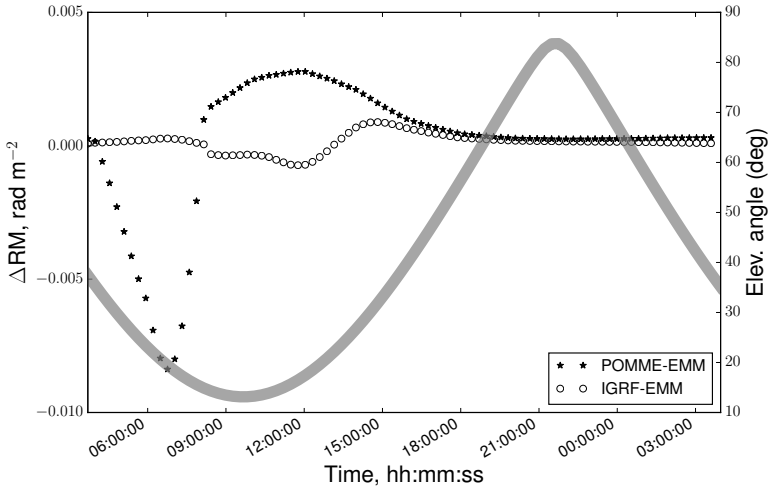

Figure 4.5: Difference between ionospheric RMs in the direction of PSR J0332+5434 observed at multiple elevations along the day, as modelled by POMME10, EMM and IGRF12. The empty circles show the difference between IGRF12 and EMM. The black stars show the difference between EMM and POMME10, which is on average less than $0.001\,\mathrm{rad\,m^{-2}}$ for observations above 30° in elevation. The thick gray line shows the change in PSR J0332+5434 elevation angle.

The global ionospheric maps (publicly available[11,12]) in IONEX[13] format, provide estimates of the vertical TEC. Several global ionospheric maps are available: CODG (from the University of Bern), ESAG and EHRG (European Space Agency), JPLG (Jet Propulsion Laboratory), UPCG and UQRG (Technical University of Catalonia, see Orús et al. (2005)), IGSG (International GNSS Service). Although the maps can be based on the same GPS data, the published TEC values can vary from group to group because of different interpolation schemes and different spatial and temporal resolution. In practice, the maps we have used, all have a spatial resolution of $2.5° \times 5°$(latitude $\times$ longitude). CODG and EHRG have a time resolution of 1 hour, UQRG of 0.25 hours and the remaining maps (ESAG, IGSG, JPLG and UPCG) have a time resolution of 2 hours.

4.3 Systematics in the RM residuals

The residual RM series, after subtraction of the ionospheric model from the observed RM values, show the presence of correlated structures and strong colored noise. For instance, Figure 4.6 shows the residual RMs for three different pulsars across about

[11] ftp://cddis.gsfc.nasa.gov/gnss/products/
[12] ftp://igs.ensg.ign.fr/
[13] https://igscb.jpl.nasa.gov/igscb/data/format/ionex1.pdf

a 2-month long timespan. As mentioned in the previous section, the ionospheric RM was corrected by using the RMextract software package, the POMME10 geomagnetic field model, and the CODG/JPLG maps. The CODG time series show similar trend (e.g. the jump of the RM around the 15th of May 2016) despite the pulsars being significantly separated on the sky. The magnitude of these RM variations significantly exceeds those expected from astrophysical sources (see Section 4.4 for details). This implies that the origin of the correlations is not interstellar, but an insufficient modelling of the ionosphere. Moreover, if these maps provide unreliable information about the uncertainties of the TEC values, this will affect the uncertainties of the modelled ionospheric RM and, in turn, our ability to determine the significance of astrophysical RM variations.

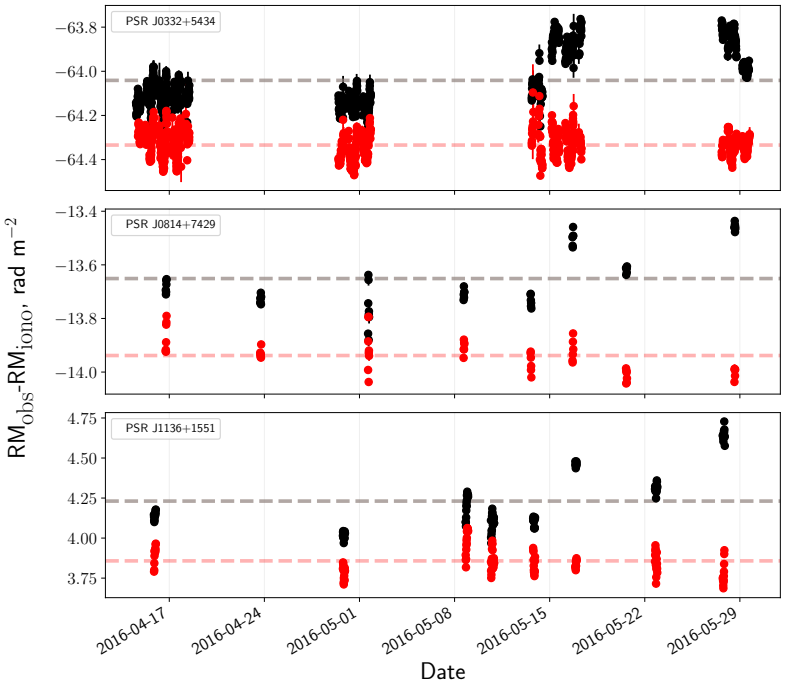

Figure 4.6: Residuals ($RM_{obs} - RM_{mod}$), while applying the CODG+POMME10 (black dots) and JPLG+POMME10 (red dots) models for three different pulsars observed with three different GLOW stations. *From top to bottom*: PSRs J0332+5434 (with DE609), J0814+7429 (with DE605), J1136+1551 (with DE601).

In order to solve for these issues, we conduct an independent search of the systematics in the modelled ionospheric RMs, with the aim of obtaining good estimates of the white-noise level and the uncertainties for the ionospheric RM time series.

Some of the observed structures in the residuals can be well explained by a diurnal sinusoid with amplitude $A_{\rm d}$, the effect of which is demonstrated in Figure 4.7 and Figure 4.3 B,C. Besides being responsible for a 1-day peak in the power spectrum of the RM residuals, it also creates a 1-year pseudo-periodicity in the data, as the transit time of the source shifts gradually during the day across the year.

After subtracting the 1-day sinusoid, the spectrum shows obvious evidence of red noise at high frequencies, and evolves into a white noise plateau at low frequencies (see Figure 4.8). Such a spectrum is described in our model by a Lorentzian function, also known as an Ornstein-Uhlenbeck process (Uhlenbeck & Ornstein, 1930). In the next two paragraphs we provide the reader with the mathematical description of the found systematics and introduce the criteria for the comparison of different ionospheric maps.

4.3.1 Analysis of RM residuals on timescales up to one year

The observational evidences, discussed in Section 4.3 allow us to define a mathematical model to describe the contributions to the observed RM time series with timescale shorter than a year. As will be pointed out in Section 4.4, the interstellar contribution $\mathrm{RM_{ISM}}$ is very small, and typically only visible on timescales of order of several years (Yan et al., 2011a). We have restricted the dataset considered in this section to only several months (Table 4.1), so we can assume this parameter to be constant and, thus, the contribution $\mathrm{RM_{ISM}}$ will not bias the estimates of the parameters of the systematics.

The vector $\mathbf{RM}_{\rm obs} = [\mathrm{RM}_{t_1}, \mathrm{RM}_{t_2}, ..., \mathrm{RM}_{t_N}]$ that contains the RM time series of a certain pulsar observed at N epochs t_i can be seen as a combination of deterministic and stochastic contributions:

$$\mathbf{RM}_{\rm obs} = \underbrace{\mathbf{RM}_{\rm iono} + \mathbf{RM}_{\rm 1day} + \mathrm{RM_{ISM}}}_{\rm deterministic} + \underbrace{\mathbf{RM}_{\rm noise} + \boldsymbol{n}}_{\rm stochastic}. \tag{4.3}$$

$\mathbf{RM}_{\rm iono}$ stands for the semi-empirical ionospheric thin layer model of RM variations described in Section 4.2.1. $\mathbf{RM}_{\rm 1day}$ is the harmonic signal with 1-day period, that can be parametrised as $\mathbf{RM}_{\rm 1day} = A_{\rm d}\sin(2\pi \boldsymbol{t}/1\mathrm{day} + \phi)$. $\mathbf{RM}_{\rm noise}$ and $\boldsymbol{n}$ are stochastic noise contributions. $\mathbf{RM}_{\rm noise}$ is given by the plateau of the Lorentzian spectrum, whose one-sided spectral density is described as:

$$S(f) = \frac{A_{\rm L}^2}{f_0\left[1 + \left(\frac{f}{f_0}\right)^2\right]}, \tag{4.4}$$

with $A_{\rm L}$ [rad m^{-2}] being the already mentioned amplitude of the stochastic signal and f_0 [day^{-1}] the turnover frequency. From this expression it can be easily shown that, while behaving like red noise on a short time scales, $\mathbf{RM}_{\rm noise}$ reduces to white noise for $f \ll f_0$ with a constant variance $A_{\rm L}^2$. By applying the Wiener-Khinchin theorem, the variance-covariance matrix of this process is then given by:

$$C_{\rm L} = A_{\rm L}^2 \exp(-f_0\tau), \tag{4.5}$$

where $\tau = 2\pi|t_i - t_j|$ with t_i and t_j are two different epochs.

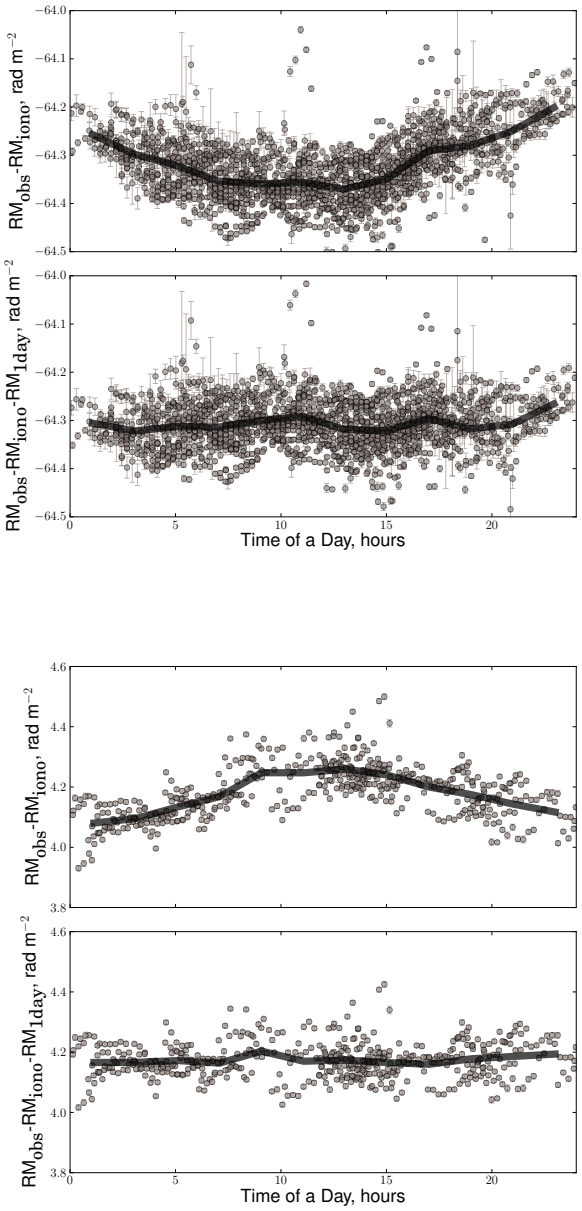

Figure 4.7: *Top figure*: Correlation pattern of the RM residuals after correcting for the ionosphere with respect to the time in a day of observations for PSR J0332+5434, while using JPLG+POMME10 model. *Upper panel*: before the subtraction of a 1-day sinusoid. *Lower panel*: after the subtraction of a 1-day sinusoid. The black thick line on both plots shows the result of data smoothing. *Bottom figure*: The same as in the upper figure for PSR J1136+1551 with UQRG+POMME10 model.

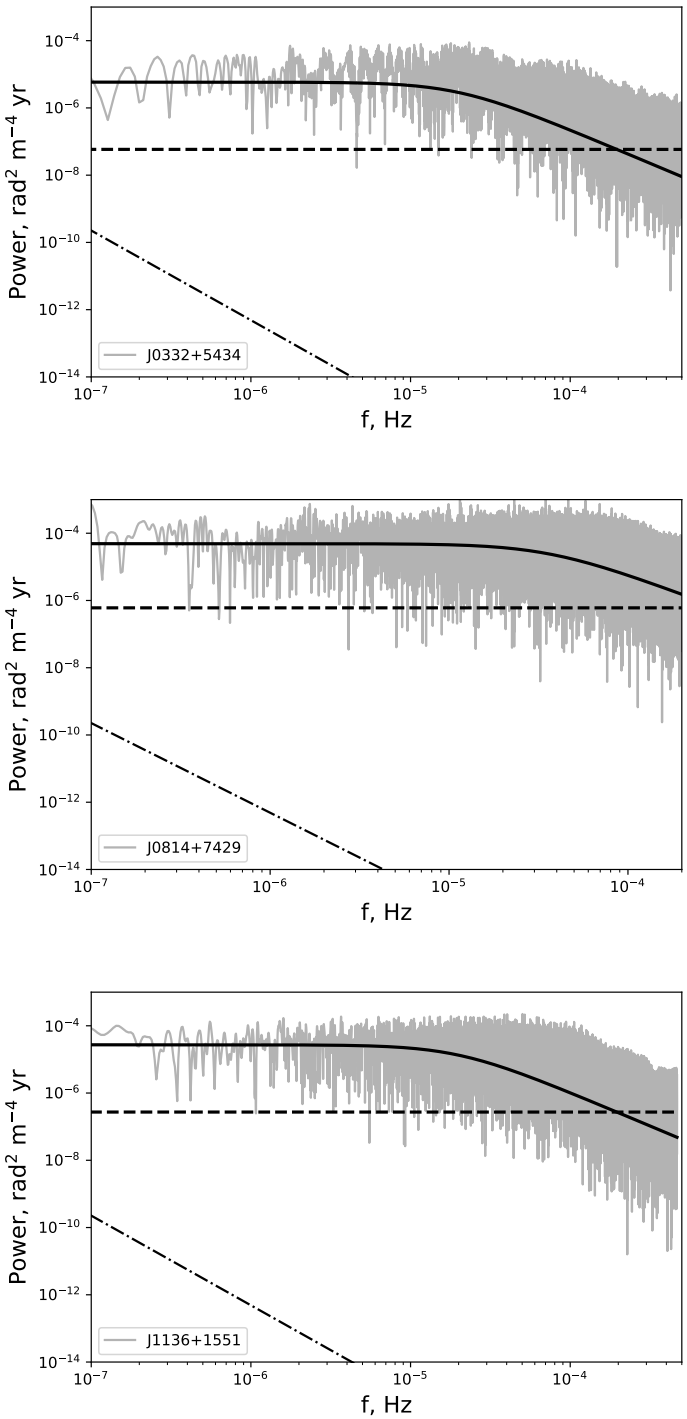

Figure 4.8: Power spectrum of the residuals ($\mathrm{RM_{obs}} - \mathrm{RM_{mod}} - \mathrm{RM_{1day}}$), shown with grey line, while applying JPLG+POMME10 model to a 6-month datasets of the circumpolar PSRs J0332+5434 (upper plot), J0814+7429 (middle plot) and J1136+1551 (lower plot). The solid black line shows the theoretical shape of a Lorentzian spectrum with A_{L} and f_0, defined in Table 4.2. The thick dashed line shows the level of the uncorrelated noise, as given by RM measurement uncertainties. The thin dot-dashed line shows the theoretically predicted power spectrum of ionised ISM turbulence (see Equation (4.10)).

The uncorrelated white noise component $\boldsymbol{n}$ in Equation (4.3), coming from the measurement noise of Stokes parameters (see Figure 3.1), has a flat power spectral density with variance-covariance of the form:

$$C_{\rm WN} = \sigma_i^2 \delta_{ij}, \tag{4.6}$$

with δ_{ij} being a Kronecker delta and $\boldsymbol{\sigma}$ the vector of the formal uncertainties of the observed RMs[14], determined via the Bayesian Lomb-Scargle Periodogram described at the end of Chapter 3.

In order to investigate the properties of the stochastic and deterministic signals that emerge in the RM residuals after the ionospheric correction, we use Bayesian inference in the time domain. Given the model in Equation (4.3), and assuming that the stochastic parts are drawn from random Gaussian processes, the posterior probability for the unknown parameters $\boldsymbol{\Theta} = [A_{\rm L}, f_0, A_{\rm d}, \phi, {\rm RM}_{\rm ISM}]$ is written as:

$$\begin{aligned} &\log P_{\rm pst}(\boldsymbol{\Theta}) \sim \log P_{\rm pr}(\boldsymbol{\Theta}) \\ &= -\sum_{i=1}^{N} \frac{1}{2} \left(\mathbf{RM}_{\rm obs} - \mathbf{RM}_{\rm iono} - \mathbf{RM}_{\rm 1day} - {\rm RM}_{\rm ISM}\right) \\ &\quad \times C^{-1} \times \left(\mathbf{RM}_{\rm obs} - \mathbf{RM}_{\rm iono} - \mathbf{RM}_{\rm 1day} - {\rm RM}_{\rm ISM}\right) - \frac{1}{2} \ln(2\pi {\rm det} C), \end{aligned} \tag{4.7}$$

where $C = C_{\rm L} + C_{\rm WN}$.

We have applied the model discussed in this paragraph to pulsar datasets that span less than a year (outlined in Table 4.1). The high S/Ns of our pulsars make us more sensitive to the signals generated by the imperfections of ionospheric RM modelling, described by Equation (4.8). The factor f_B was fixed to 1.11, as found in Section 4.3.2, and, thus, was excluded from the set of free parameters of the model.

In order to explore the 5-dimensional parameter space $\boldsymbol{\Theta}$ of Equation (4.3), we ran a Markov Chain Monte Carlo simulation, using the Bayesian inference tool `MultiNest` (Feroz et al., 2009). The priors of the parameters $P_{\rm pr}(\Theta)$ were chosen to be uninformative (see Caballero et al., 2016): uniform for $A_{\rm L}$, f_0, ϕ, and ${\rm RM}_{\rm ISM}$ and log-uniform for $A_{\rm d}$. A representative example of the obtained 2-dimensional posterior probability plot is shown in Figure 4.11.

Because we only used data from a limited group of pulsars, and probed a statistically not significant sample of LoS, the values given in Table 4.2 should not be treated as definitive solutions. However, our results give a qualitative estimation of the accuracy of different ionospheric maps.

4.3.2 Analyis of RM residuals on timescales beyond one year

After subtracting $\mathbf{RM}_{\rm iono}$ and $\mathbf{RM}_{\rm 1day}$ from the observed RM time series, the long term datasets still show a deterministic linear trends. The trend is not visible on a timescale of months, but it becomes obvious across several years (see Figure 4.9). We find that

[14] The uncertainties are modified by a factor η, see Equation (3.11)

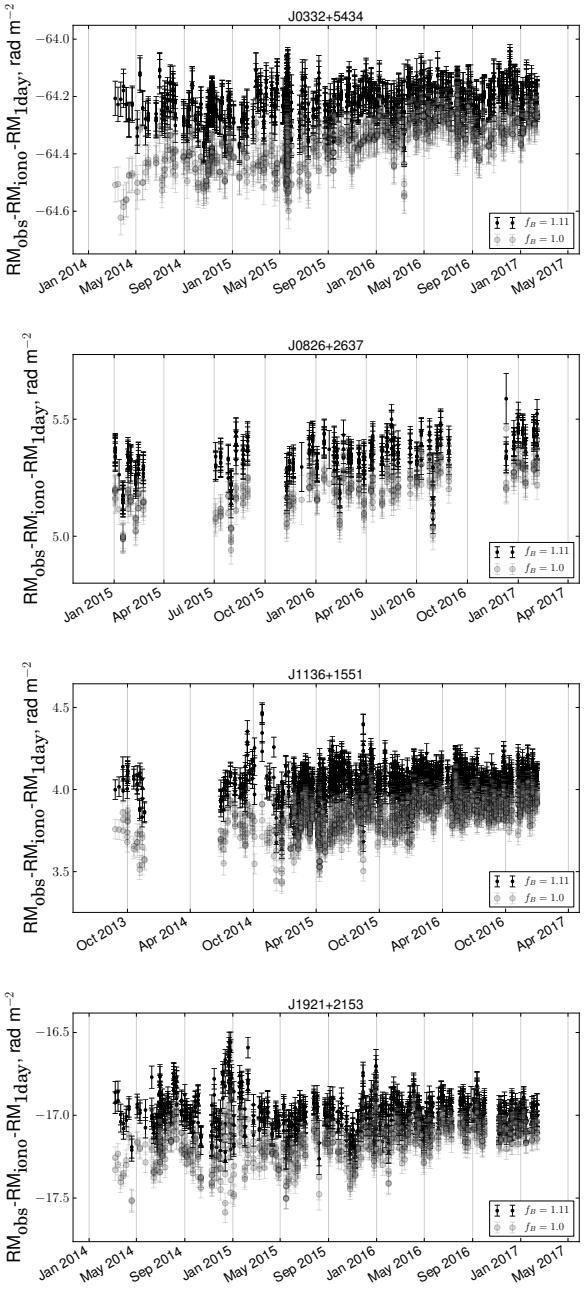

Figure 4.9: Absorption of the linear trend due to the application of the f_B factor. The grey circles correspond to the $f_B = 1$, black dots to $f_B = 1.11$. We here use three years of data for (from top to bottom) PSRs J0332+5434, J0826+2637, J1136+1551, J1921+2153. The ionospheric contribution is modelled with JPLG maps combined with POMME10 geomagnetic model.

such linear trend can be suppressed by scaling the $\mathbf{RM}_{\rm iono}$ time series (resulting from a thin layer model) by a constant factor f_B. In other words, Equation (4.3) is modified as

$$\mathbf{RM}_{\rm obs} = \frac{\mathbf{RM}_{\rm iono}}{f_B} + \mathbf{RM}_{\rm 1day} + \mathrm{RM}_{\rm ISM} + \mathbf{RM}_{\rm noise} + \boldsymbol{n}. \tag{4.8}$$

A positive trend of the order of $1 - 2 \times 10^{-4}$ rad m^{-2} day^{-1} was noticed in four pulsars observed with three GLOW stations. Removal of the linear trend, by applying the factor f_B, is demonstrated in Figure 4.9.

Making use of pulsar datasets that span more than one year (outlined in Table 4.1) and all six global ionospheric maps, considered in this paper, the least square fit estimate was found to be $f_B = 1.11^{+0.04}_{-0.04}$. The decrease in root-mean-square (rms), mostly due to the elimination of the linear trend, is illustrated in Figure 4.10. The results for all three geomagnetic models are identical.

There are several physical interpretations possible for the factor f_B. Among them is the possible overestimation of the geomagnetic strength, $B_{\rm LoS}$, and/or the underestimation of the ionospheric effective height (Birch et al., 2002) due to the poor knowledge of the electron density in Earth's plasmasphere. For instance, $f_B = 1.11$ is equivalent to an increase of the effective height from 450 km up to $\sim$ 700 km. An explanation to the trend might be searched in the complex dynamical behavior of the ionospheric effective height. As a matter of fact, it has been shown in multiple investigations (e.g. Hernández-Pajares et al., 2011; Arora et al., 2016), that the ionospheric effective height can vary from 300 up to 800 km, depending on the time of day, season, and level of Solar activity. For instance, the 11-year sunspot cycle, the last maximum of which was in 2014, can cause significant ionization in the ionospheric layer, thus both increasing the ionospheric thickness and ionospheric effective height (Liu et al., 2007). One promising way to improve the model is by using the effective heights determined via the IRI-Plas software (Gulyaeva et al., 2013), which takes into account plasmasphere contribution (Arora et al., 2016).

The nature of the factor f_B is still under investigation and is planned to be tested on a larger sample of pulsars in the future.

4.4 Discussions and Conclusions

In this paper, we have characterised and investigated the deterministic and stochastic RM variations generated by the ionospheric layer through pulsar observations taken with the German LOFAR stations. The main day-to-day variability was modelled by assuming a thin-layer ionosphere, located at 450 km above the Earth's surface. For this model, the magnetic field was taken from the publicly available geomagnetic maps (POMME10, EMM, IGRF), while the information about electron densities was extracted from the selection of different global ionospheric maps. Besides that, an additional signal peaked at a frequency of 1 day^{-1} in the power spectrum, which was significant in almost all processed datasets, and was removed by including in the model

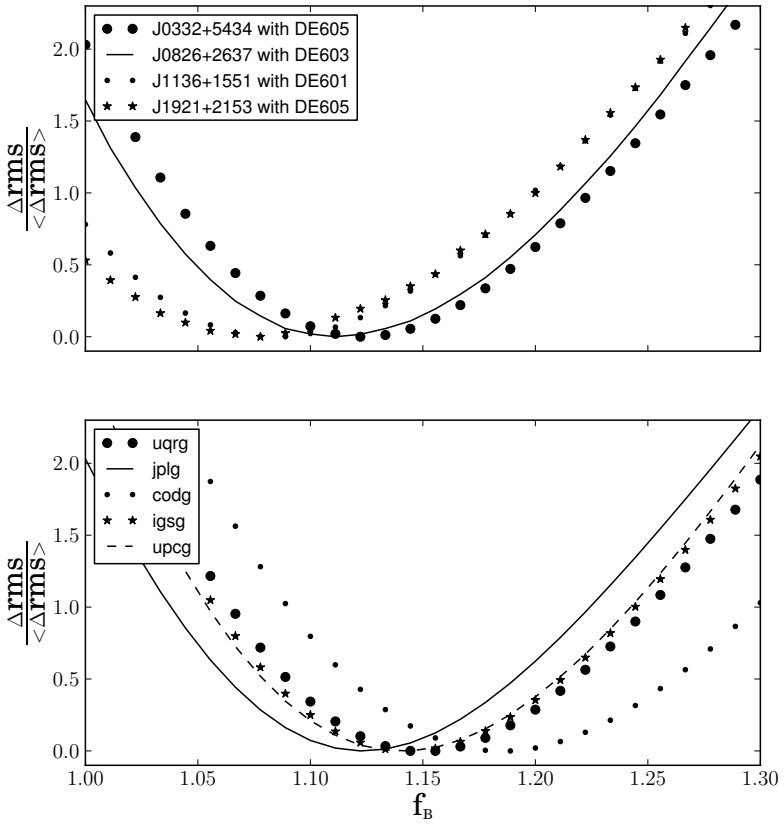

Figure 4.10: *Upper panel*: Rms of the RM residuals obtained by using the JPLG map (and normalised with respect to the minimum value for each case), vs the f_B factor. We here use 3 years of data for PSRs J0332+5434, J0826+2637, J1136+1551, J1921+2153 (see Table 4.1). *Lower panel*: Rms of the RM residuals obtained by using UQRG, JPLG, CODG, IGSG, and UPCG maps (and normalised with respect to the minimum value for each case) vs the f_B factor. We here use 3 years of data for PSR J0332+5434 observed with DE605 (see the text for more details). The trends show clear improvements of the modelling when using $f_B \simeq 1.10 - 1.14$

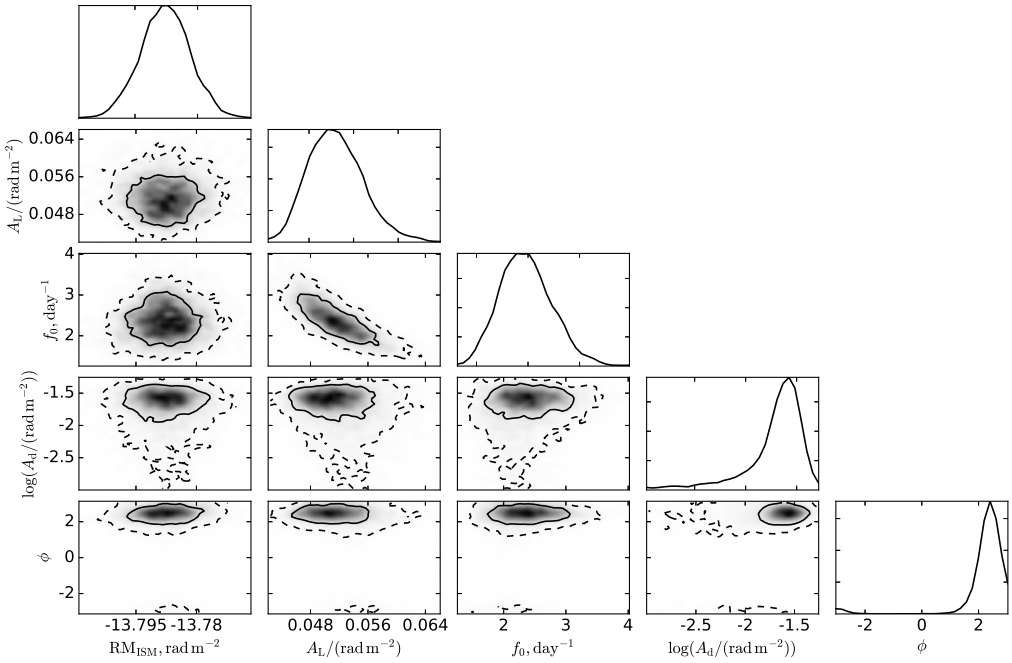

Figure 4.11: One and two-dimensional posterior distribution for a subset of the noise parameters that characterize the RM residuals of PSR J0814+7429 after the subtraction of the ionospheric model (using JPLG maps+POMME10 geomagnetic model). *From left to right*: rotation measure of ionised ISM $\mathrm{RM_{ISM}}$ [$\mathrm{rad\,m^{-2}}$], which is assumed to be constant on time scales of several months, the level of the white noise plateau A_L [$\mathrm{rad\,m^{-2}}$] in the Lorentzian spectrum, the turnover frequency f_0 [$\mathrm{day^{-1}}$] of the Lorentzian spectrum, the amplitude of the 1-year harmonic signal in the residuals A_d [$\mathrm{rad\,m^{-2}}$], the phase of the harmonic signal ϕ.

a 1-day period sinusoid. The residual noise could be described by a Lorentzian spectrum, which behaves like white noise on long timescales and defines our sensitivity to long-term RM variations. The parameters of the model were estimated by applying a Bayesian framework to the RM time series of three pulsars. The observed RM for each epoch was determined by using an improved RM synthesis technique, based on BGLSP, which accounts for non-regularly sampled data and constant offsets in Stokes Q and U due to instrumental effects. By running a Markov Chain Monte Carlo, we have estimated the amplitude of the Lorentzian spectrum (or variance of white noise) for all the ionospheric maps. An additional linear trend becomes visible on a timescale of several years. To account for this, we have applied a factor $f_B = 1.11$ to the ionospheric RM contribution that was modelled by RMextract, $\mathbf{RM}_\mathrm{mod}$, as determined in Section 4.3.2. This slightly reduces the level of the Lorentzian spectrum plateau for some of the pulsars, determined in Section 4.3.1.

Our results for the three pulsars are slightly different. Nevertheless, two of them (PSRs J0332+5434, J0814+7429) are consistent within 2-sigma, while J1136+1551 shows slightly higher values. We show that geomagnetic models mostly agree and that consequently the accuracy of ionospheric RM corrections is dominated by the uncertainties and inaccuracies in ionospheric TEC maps, which we have investigated in the paper. On average UQRG and JPLG, combined with one of the geomagnetic models, show better results than the other ionospheric maps. If one is going to use one of these two maps to correct for RM variations, the variance of the white noise can be conservatively set to $0.06-0.07\,\mathrm{rad\,m^{-2}}$ for observations taken in Europe after daily sin-waves and linear trend have been taken into account. This is approximately an order of the magnitude higher than the uncertainties on the observed RM, obtained from BGLSP, for the pulsars considered. As we have used the data of only three pulsars and our observational sites are located only in Germany, this value can vary, e.g. increasing significantly in places with sparse GNSS station coverage. Thus, in order to get reliable estimates of the sensitivity to long-term RM variations for a specific instrument, we recommend to undertake a similar kind of analysis for their sites independently.

Essentially, the determined values along with BGLSP uncertainties define the sensitivity of RM measurements to astrophysical signals. One of the promising signal of interest, when dealing with Faraday rotation studies, is the time-variable interstellar contribution to the RM. Let us assume that the ionised ISM is homogeneous. Then, the relative motion between a pulsar moving with velocity $\boldsymbol{v}$ and an observer can cause temporal RM variations induced by the change both in the projection of the magnetic field on the LoS and in the pulsar distance L. By differentiating Equation (2.13) under the assumption of a small change between the initial and the final position of a pulsar, we have:

$$\begin{aligned}\Delta\mathrm{RM} &\simeq -0.81 n_\mathrm{e} B\cdot v_\perp T\sin\theta + 0.81 n_\mathrm{e} B\cdot v_\parallel T\cos\theta \\ &\sim 3\times10^{-6}\,\mathrm{rad\,m^{-2}}\left(\frac{L}{1\,\mathrm{kpc}}\right)^{-1}\left(\frac{\mathrm{RM}}{30\,\mathrm{rad\,m^{-2}}}\right)\left(\frac{|\boldsymbol{v}_\perp|}{100\,\mathrm{km\,s^{-1}}}\right)\left(\frac{T}{\mathrm{yr}}\right)\end{aligned} \tag{4.9}$$

where θ is the angle between the magnetic field vector and the LoS, and T is the whole timespan.

Besides this deterministic signal, we expect a time-variable stochastic part of the interstellar contribution, as predicted by the Kolmogorov turbulence (Kolmogorov, 1941). As it was shown in Keith et al. (2013) the power spectral density of the stochastic contribution is $\mathrm{PSD_{KL}} = 0.0112\times D(\tau)\tau^{-\frac{5}{3}}f^{-\frac{8}{3}}$, where $D(\tau)$ is the structure function. The estimated rms of RM will increase with time T (Minter & Spangler, 1996; Xu & Zhang, 2016) as:

$$\begin{aligned}\mathrm{rms_{RM}} &\sim 0.81\sqrt{n_\mathrm{e}^2\sigma_B^2 + B_\parallel^2\sigma_n^2}L \sim \sqrt{\int_{1/T}^{\infty}\mathrm{PSD_{KL}}(f)\mathrm{d}f} \\ &= 6\times10^{-5}\,\mathrm{rad\,m^{-2}}\left(\frac{L}{1\,\mathrm{kpc}}\right)^{\frac{1}{2}}\left(\frac{|v|}{100\,\mathrm{km\,s^{-1}}}\right)^{\frac{5}{6}}\left(\frac{T}{\mathrm{yr}}\right)^{\frac{5}{6}}\end{aligned} \tag{4.10}$$

where σ_B^2 and σ_n^2 are the variances of magnetic field and electron density fluctuation,

respectively.

These calculations show that the signals of interest are characterised by a very small amplitudes, of the order of $10^{-5} - 10^{-4}\,\mathrm{rad\,m^{-2}}$, which is several orders of magnitude lower than the observed RM variations in this work. From the comparison of the power spectral densities[15] we can conclude that we need several decades of observations with the current sensitivity (mostly limited by the imperfections of the ionospheric modelling) for this kind of signals to become significant.

More promising signals of astrophysical nature could be registered thanks to extreme scattering events (ESEs, Coles et al., 2015), associated with the passage of a blob of high density plasma through the LoS, extreme magneto-ionic environment of the source (Desvignes et al., 2018), and coronal mass ejections Howard et al. (2016), which may cause more prominent RM perturbations.

A deeper understanding of the physics of ionospheric behaviour and instrumental GPS biases, along with the development of more regular GPS station arrays in the direct vicinity to the radio telescopes will improve the quality of the estimates of TEC in the ionospheric layer, which will, in turn, increase our sensitivity to the astrophysical RM variations.

[15] $\mathrm{PSD_{KL}} \simeq \mathrm{PSD_{WN}} = \sigma^2/f_{\mathrm{Ny}}$, where $\mathrm{PSD_{WN}}$ is the power spectral density of the white noise and f_{Ny} is the Nyquist frequency of our dataset.

PSR J0332+5434				
Model	$A_{\rm L}^{\rm med}$	$f_0^{\rm med}$	$A_{\rm d}^{\rm med}$	$\rm RM_{ISM}^{ML}$
UQRG	$0.045^{+0.003}_{-0.002}$	$1.5^{+0.2}_{-0.2}$	$0.012^{+0.007}_{-0.006}$	-64.16
JPLG	$0.050^{+0.002}_{-0.002}$	$1.7^{+0.2}_{-0.2}$	$0.025^{+0.007}_{-0.005}$	-64.21
EHRG	$0.054^{+0.003}_{-0.003}$	$1.2^{+0.1}_{-0.1}$	$0.012^{+0.007}_{-0.008}$	-64.05
IGSG	$0.060^{+0.003}_{-0.003}$	$1.2^{+0.1}_{-0.1}$	$0.02^{+0.005}_{-0.007}$	-64.08
ESAG	$0.068^{+0.005}_{-0.004}$	$1.1^{+0.1}_{-0.1}$	$0.025^{+0.007}_{-0.009}$	-64.05
UPCG	$0.073^{+0.003}_{-0.004}$	$0.9^{+0.1}_{-0.1}$	$0.025^{+0.008}_{-0.014}$	-64.17
CODG	$0.12^{+0.01}_{-0.01}$	$0.29^{+0.06}_{-0.06}$	$0.063^{+0.009}_{-0.009}$	-63.95
PSR J1136+1551				
Model	$A_{\rm L}^{\rm med}$	$f_0^{\rm med}$	$A_{\rm d}^{\rm med}$	$\rm RM_{ISM}^{ML}$
UQRG	$0.061^{+0.005}_{-0.004}$	$2.1^{+0.3}_{-0.3}$	$0.079^{+0.01}_{-0.009}$	4.16
JPLG	$0.073^{+0.004}_{-0.004}$	$1.9^{+0.6}_{-0.5}$	–	4.02
EHRG	$0.082^{+0.005}_{-0.004}$	$1.3^{+0.2}_{-0.2}$	$0.03^{+0.01}_{-0.02}$	4.22
IGSG	$0.142^{+0.008}_{-0.01}$	$0.6^{+0.1}_{-0.1}$	$0.04^{+0.02}_{-0.02}$	4.19
ESAG	$0.110^{+0.008}_{-0.007}$	$1.0^{+0.1}_{-0.1}$	$0.03^{+0.02}_{-0.01}$	4.26
UPCG	$0.123^{+0.010}_{-0.008}$	$0.9^{+0.2}_{-0.1}$	$0.08^{+0.02}_{-0.02}$	4.18
CODG	$0.21^{+0.02}_{-0.02}$	$0.14^{+0.03}_{-0.03}$	$0.08^{+0.02}_{-0.02}$	4.18
PSR J0814+7429				
Model	$A_{\rm L}^{\rm med}$	$f_0^{\rm med}$	$A_{\rm d}^{\rm med}$	$\rm RM_{ISM}^{ML}$
UQRG	$0.053^{+0.004}_{-0.003}$	$2.7^{+0.5}_{-0.5}$	$0.049^{+0.006}_{-0.007}$	-13.75
JPLG	$0.051^{+0.004}_{-0.003}$	$2.3^{+0.4}_{-0.4}$	$0.024^{+0.006}_{-0.008}$	-13.79
EHRG	$0.054^{+0.003}_{-0.003}$	$2.1^{+0.3}_{-0.3}$	$0.033^{+0.01}_{-0.02}$	-13.66
IGSG	$0.064^{+0.005}_{-0.004}$	$1.4^{+0.3}_{-0.3}$	$0.047^{+0.01}_{-0.008}$	-13.69
ESAG	$0.067^{+0.005}_{-0.005}$	$1.5^{+0.3}_{-0.3}$	$0.03^{+0.01}_{-0.01}$	-13.65
UPCG	$0.069^{+0.005}_{-0.005}$	$1.4^{+0.3}_{-0.3}$	$0.045^{+0.01}_{-0.01}$	-13.74
CODG	$0.10^{+0.01}_{-0.01}$	$0.7^{+0.1}_{-0.1}$	$0.07^{+0.02}_{-0.01}$	-13.62

Table 4.2: Estimation of the noise parameters based on the Bayesian analysis of RM residuals using POMME10 geomagnetic model and different ionospheric maps. The results for other two considered in this paper geomagnetic models (EMM and IGRF) are indistinguishable within the uncertainties. The used noise model is the one described in Equation (4.8). The factor $f_B = 1.11$ was applied.

Chapter 5

Investigation of magnetised interstellar turbulence with pulsars

Contents

5.1 Introduction 82
5.2 Observations 83
5.3 RM variations from the turbulent ISM: mathematical description 84
5.3.1 Theoretical structure function of RM variations 86
5.3.2 Theoretical covariance function of RM variations 87
5.4 Comparison with observations: parameter estimation and upper limits 88
5.4.1 Structure function analysis 88
5.4.2 Covariance function analysis 89
5.5 Conclusions 96

The study of magnetic-field turbulence is crucial for understanding various physical processes taking place in the magnetised plasma of the ISM such as cosmic-ray scattering, magnetic field reconnection and overall hydrostatic balance of the ISM. Achieving the detection of RM variations in pulsar emission due to the ionised ISM can shed light on the properties of the small-scale turbulent magnetic fields. Here, we attempt to measure these variations by using three-year-long datasets of four pulsars: PRSs J0332+5434, J0826+2637, J1136+1551 and J1921+2153, observed with German LOFAR stations. After mitigation of the ionospheric Faraday rotation, the datasets of two of these pulsars, PSRs J1136+1551 and J1921+2153, exhibit correlated noise, in the same fashion as expected from ISM turbulence. We speculate that these variations can be caused by the residual ionospheric Faraday rotation or instrumental noise, as no convincing evidence of astrophysical origin of these variations has been found. We set an upper limit on the power of the magnetic field fluctuations. Our most stringent constraints obtained with the datasets of PSRs J0332+5434 and J0826+2637 lie below magnetic-field amplitudes derived in Haverkorn et al. (2008), however, are still 4 to 16 times higher than the expected conservative value predicted in Minter & Spangler (1996) with 95% confidence. Finally, we analyse the prospects of detecting of the

magnetic field turbulence and conservatively conclude that, assuming the current sensitivity, we would need about 20 years of observing timespan to confidently detect the signal as predicted in Minter & Spangler (1996).

5.1 Introduction

Turbulence in the Milky Way is systemic. Among the most striking evidence is the 'Big Power Law' of electron density fluctuations (Armstrong et al., 1995), fractal structure of molecular clouds (Stutzki et al., 1998) and structures in HI data cubes (see e.g. Crovisier & Dickey, 1983; Green, 1991; Stanimirovic et al., 1999). Interstellar turbulent plasma has been investigated extensively over a wide range of scales from 10^{-11} to several pc (Spangler & Gwinn, 1990; Armstrong et al., 1995; Stinebring et al., 2000; Wang et al., 2005; Chepurnov & Lazarian, 2010), however there is a dearth of observational information on turbulent magnetic fields. Magnetic fields have a crucial role in various astrophysical processes, such as star formation (McKee & Ostriker, 2007) and cosmic-ray propagation (Kóta & Jokipii, 2000), and can significantly alter the properties of turbulence. Astrophysical magnetic fields cannot be probed directly: observables which encapsulate information on these fields, typically depend on other quantities, which one tries to disentangle in order to study these fields directly. One of the tools to prove the magnetised turbulence in the ISM is the RM of background polarised sources, which is the integrated magnetic field parallel to the LoS, weighted by the electron density (see Section 1.4.3). On scales of $\sim 10-100\,\mathrm{pc}$, magnetic-field statistics have been mainly inferred from studies of RMs of an ensemble of extragalactic sources (Simonetti & Cordes, 1986; Minter & Spangler, 1996; Clegg et al., 1992; Haverkorn et al., 2008; Oppermann et al., 2012). *Structure functions* (SFs) of extragalactic RM maps[1] derived in the aforementioned works, all exhibit similar behaviour. It was found that the SFs have shallower slopes than expected from Kolmogorov turbulence and tend to flatten on larger scales. The scale at which the SFs saturate is commonly associated with the injection scale of turbulence, and varies substantailly across the Galaxy (see e.g. Haverkorn et al., 2008).

In this chapter, we discuss which additional information can be inferred about the magnetised ionised phases of the ISM from time-dependent RM measurements of pulsars. The astrophysical variations in RM are caused by the intrinsic motion of pulsars, which changes both the direction and length of the LoS. We have mostly focused our analyses on RM variations caused by the transverse pulsar motion. Due to this motion the LoS samples different parts of the turbulent ISM, which induces a stochastically changing, epoch-dependent RM estimate. Through the investigation of these variations, we can gain insights about the turbulent components of the electron density and magnetic fields on $10^{-4} - 10^{-3}$ pc-scales[2]. Moreover, by simultaneously measuring RMs and DMs of a pulsar, the electron-density and magnetic-field components can be

[1] SFs measure the mean value of the measurement variance as a function of time difference of two observations or angular separation on the sky.

[2] Assuming a typical pulsar velocity of $200\,\mathrm{km\,s^{-1}}$, the distance that a pulsar travels through the medium within a year is of order $10^{-4}\,\mathrm{pc}$.

disentangled and one can estimate the pure contribution of the interstellar magnetic fields to the RM variations.

The RM variations induced by astrophysical (non-terrestrial) plasmas have been observed for only a few pulsars. Perhaps, the most remarkable example is the Galactic-centre magnetar PSR J1745−2900, which exhibits strong RM variations and up to $3500\,\mathrm{rad\,m^{-2}}$ (Desvignes et al., 2018). The origin of these large RM variations are, most likely, local magnetic phenomena in the Galactic-centre neighbourhood. Johnston et al. (2005) observed RM variations of $1000\,\mathrm{rad\,m^{-2}}$ for PSR B1259-63, which is part of a binary system. These observations are consistent with the interpretation that the pulsar emission passes through the dense magnetised disk ($n_e > 10^8 - 10^{10}$ cm^{-3}) of its Be star companion. The Vela and Crab pulsars also show changes in RM ($>4\,\mathrm{rad\,m^{-2}}$) and DM (Hamilton et al., 1977; Rankin et al., 1988), which are associated with the filamentary structure of their corresponding supernova remnants observed by the Hubble Space Telescope[3]. Additionally, the abrupt changes in RM and DM can arise due to ionised shells with a much finer structure than the aforementioned filaments. These fine structures were traced via observations of discrete moving echoes from the Crab pulsar (Lyne et al., 2001).

While all the above sources are associated with extreme local environments, there has been no clear evidence of RM variations along LoSs probing the diffuse ISM (Yan et al., 2011b). In this chapter, we investigate the prospects of detecting RM variations caused by ordinary ISM turbulence using LOFAR pulsar observations. In Section 5.2, we report the details of the observations and data processing. The mathematical formalism for expected stochastic RM variations is developed in Section 5.3. In Section 5.4 we analyse the observed RM time series and set upper limits on the turbulent component of interstellar magnetic field. In Section 5.5 we summarise our results.

5.2 Observations

The data that are used in this chapter were taken with the LOFAR HBAs and are described in detail in Chapter 4. In order to investigate the prospects of detecting interstellar magnetic fluctuations, which are expected to affect the RM time series at longer time scales (e.g. Lazarian & Pogosyan, 2016), we have chosen a long-term dataset, composed of $\sim$ 3-year observations of four pulsars: PSRs J0332+5434, J0826+2637, J1136+1551 and J1921+2153[4]. The specifications of the dataset are given in Table 4.1. The pre-processing routines, including folding, implementation of the beam model and RFI mitigation are described in detail in Section 4.2. The ionospheric mitigation was performed with the software `RMextract`[5]. The geomagnetic field was modelled with POMME10[6] and the electron density in the ionosphere was reconstructed using UQRG maps (Orús et al., 2005), which on average perform better than other maps, as detailed in Chapter 4. The additional systematics, namely the annual sinusoid and

[3] https://archive.stsci.edu/

[4] PSRs B0329+54, B0823+26, B1133+16 and B1919+21 when original B1950 coordinates are used.

[5] https://github.com/lofar-astron/RMextract

[6] http://geomag.org/models/pomme10.html

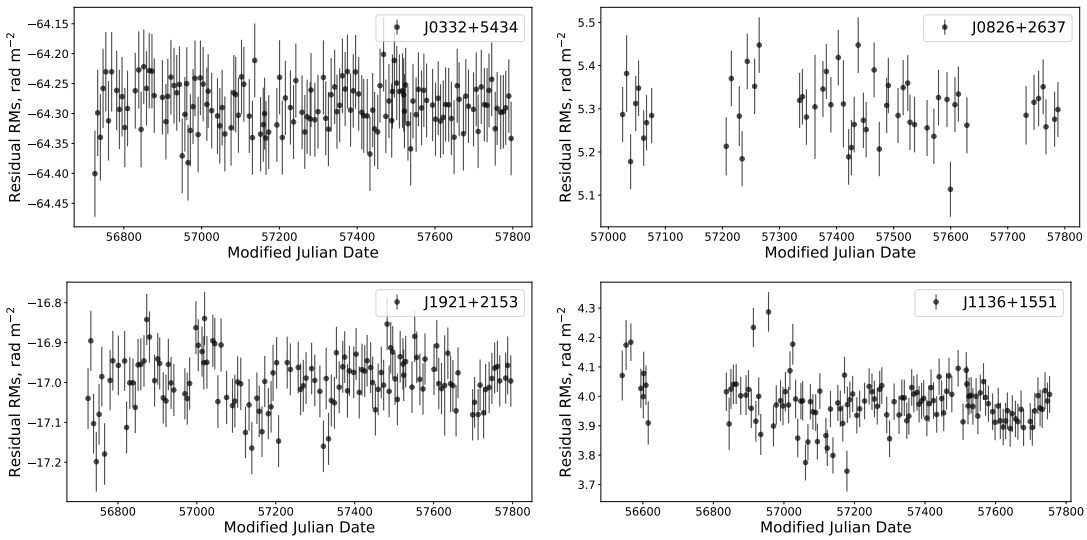

Figure 5.1: The RM time series of PSRs J0332+5434, J0826+2637, J1136+1551 and J1921+2153 after mitigation of the ionospheric effects, including the an annual sine wave and the linear trend.

the long-term linear trends, which are associated with imperfections in ionospheric modelling and are described in Chapter 4, were fitted and removed by subtracting the best-fit solution. The remaining RM residuals were binned on daily intervals. The final RM datasets are shown in Figure 5.1.

5.3 RM variations from the turbulent ISM: mathematical description

In this section, we develop the mathematical framework that we used to describe the stochastic interstellar contributions to the observed RMs of pulsars. The RM variations of interest arise due to the relative motion of the source and observer, both parallel and perpendicular to the LoS. Changes in the distance to the pulsar (obtainable with the pulsar motion parallel to the LoS) and in the projection of the average magnetic field on the LoS (obtainable with both parallel and transverse motion) can cause linear RM variations (see Equation (4.9)). Beside the systematic trend, a pulsar's transverse motion induces correlated noise in the RM time series. The power spectrum of such a time series would show an excess of power at lower frequencies.

In order to quantitatively describe the statistical properties of these stochastic variations, we use a geometry framework equivalent to Minter & Spangler (1996). The observer is placed at the origin of the Cartesian coordinate system. The initial LoS is directed along the z axis; the current LoS is along the ζ axis; the current and initial LoSs are separated by an angle $\delta\theta = v_\perp t$, where $v_\perp$ is the transverse velocity of a pulsar. We have assumed that the magnetic field and electron density in the ISM have

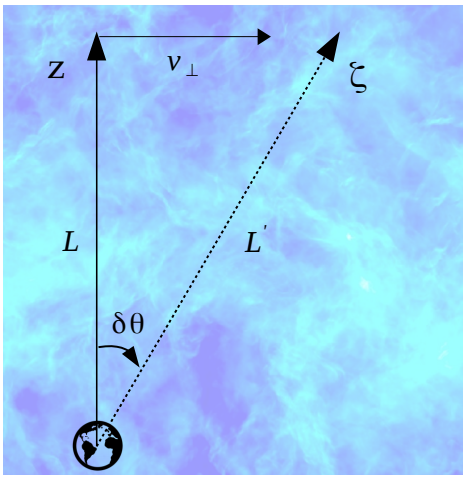

Figure 5.2: The geometry that is used to derive the $\mathrm{SF}_{\mathrm{ISM}}(\delta\theta)$ and $C_{\mathrm{ISM}}(\delta\theta)$. The observer is at the origin of the coordinate system. The pulsar is moving perpendicular to the z axis with transverse velocity equal to $v_\perp$. The initial and final directions towards the pulsar are along z and ζ axis, respectively. The angle between the initial and final LoSs is $\delta\theta = v_\perp t$. The background picture of turbulence is adapted from Federrath et al. (2010).

the following form:

$$\begin{aligned} n &= n_0 + \delta n\,, \\ \boldsymbol{B} &= \boldsymbol{B}_0 + \delta\boldsymbol{B}\,, \end{aligned} \tag{5.1}$$

where n_0 and $\boldsymbol{B}_0$ are the mean components. The random fluctuating terms, δn and $\delta\boldsymbol{B}$, are assumed to be zero-mean and follow Gaussian statistics. Additionally, it was assumed that fluctuations in the magnetic field and electron density are independent[7].

To describe both electron-density and magnetic-field fluctuations we used a power-law wavenumber spectrum, given by:

$$P_n(q) = \mathcal{C}_n^2 \left(\frac{q^2+q_0^2}{\mathrm{pc}^{-2}}\right)^{-\alpha_n/2}\,,\; P_B(q) = \mathcal{C}_B^2 \left(\frac{q^2+q_0^2}{\mathrm{pc}^{-2}}\right)^{-\alpha_B/2}\,, \tag{5.2}$$

where q is the wavenumber. In the above expressions $\mathcal{C}_n^2$ and $\mathcal{C}_B^2$ are the spectral coefficients and α_n and α_B are the spectral indices of the electron-density and magnetic-field fluctuations, respectively. For homogeneous and incompressible turbulence, the spectral index is 11/3; this is commonly referred to as Kolmogorov turbulence. The *outer scale* of fluctuations $l_0 = 2\pi/q_0$ indicates at which wavenumber the power spectrum

[7] This condition may not hold under certain conditions (Beck, 2001). The relaxation of this condition will be considered in future work.

flattens and is assumed to be the same for both electron-density and magnetic-field fluctuations. From the above expressions, the spatial correlation relations for the electron density and magnetic field are respectively given by:

$$\begin{aligned}\langle \delta n(\boldsymbol{r_1})\delta n(\boldsymbol{r_2})\rangle &= \int \mathrm{d}^3 q P_n(q) e^{-i\boldsymbol{q}|\boldsymbol{r_1}-\boldsymbol{r_2}|},\\ \langle \delta B_j(\boldsymbol{r_1})\delta B_j(\boldsymbol{r_2})\rangle &= \int \mathrm{d}^3 q P_B(q) e^{-i\boldsymbol{q}|\boldsymbol{r_1}-\boldsymbol{r_2}|},\end{aligned} \tag{5.3}$$

where the angle brackets denote the ensemble average, δB_j is the component of $\delta \boldsymbol{B}$ along the j-axis, and $\boldsymbol{r_1}$ and $\boldsymbol{r_2}$ denote the vectors towards the source at two different arbitrary epochs.

5.3.1 Theoretical structure function of RM variations

A powerful statistical tool which is widely used to study turbulence is the SF. The SF of RM measurements towards different LoSs separated by an angle $\delta\theta$ on the sky, is given by:

$$\begin{aligned}\mathrm{SF}(\delta\theta) &= \langle [\mathrm{RM}(\theta) - \mathrm{RM}(\theta+\delta\theta)]^2\rangle \\ &= \langle [\int_0^L n(z,0)B_z(z,0)\mathrm{d}z - \int_0^{L'} n(\zeta\cos\delta\theta, \zeta\sin\delta\theta)B_\zeta(\zeta\cos\delta\theta,\zeta\sin\delta\theta)\mathrm{d}\zeta]^2\rangle,\end{aligned} \tag{5.4}$$

where L and L' are the length of the LoSs, and $B_z = B_{0z} + \delta B_z$ is the magnetic field component along the z axis. For a power-law wavenumber spectrum with $2 < \alpha_{n,B} < 4$, given by Equation (5.2), under the assumptions that $L \simeq L'$, $L\delta\theta \ll l_0$ and $l_0 < L$, the theoretical $\mathrm{SF_{ISM}}$ of RM variability produced by the motion of a pulsar is expressed as (Minter, 1995; Minter & Spangler, 1996):

$$\begin{aligned}\mathrm{SF_{ISM}}(\delta\theta) = (0.81)^2[&f(\rho_n)B_{0z}^2\mathcal{C}_n^2 L^{2\rho_n+1}(\delta\theta)^{2\rho_n} + f(\rho_B)n_0^2\mathcal{C}_B^2 L^{2\rho_B+1}(\delta\theta)^{2\rho_B} + \\ &\mathcal{C}_n^2\mathcal{C}_B^2 k(\rho_n,\rho_B) q_0^{1-\rho_n-\rho_B} L^{\rho_n+\rho_B+1}\left\{\frac{(\delta\theta)^{2\rho_n}\Gamma(1-\rho_n)}{2\Gamma(\rho_n+1)} + \frac{(\delta\theta)^{2\rho_B}\Gamma(1-\rho_B)}{2\Gamma(\rho_B+1)}\right\}],\end{aligned} \tag{5.5}$$

where Γ is the gamma function, and

$$\begin{aligned}\rho &= \alpha/2 - 1,\\ f(\rho) &= \frac{4\pi^2\Gamma(1-\rho)}{2^{2\rho}(2\rho+1)\rho\Gamma(1+\rho)},\\ k(\rho_n,\rho_B) &= \frac{\pi^3\Gamma(0.5\rho_n + 0.5\rho_B - 0.5)^2}{\rho_n\rho_B(\rho_n+\rho_B+1)\Gamma(\rho_n+\rho_B-1)}.\end{aligned} \tag{5.6}$$

For a purely Kolmogorov spectrum ($\rho_n = \rho_B = 5/6$) the $\mathrm{SF_{ISM}}$ behaves as a power law with a slope of 5/3. For $\delta\theta L \gtrsim l_0$, $\mathrm{SF_{ISM}}$ becomes flat, i.e. the RM variations become less correlated.

By comparing the theoretical and observed SFs, one can infer the properties of the ISM turbulence, e.g. turning points and slopes of the power spectra. However, as was shown in Emmanoulopoulos et al. (2010), model parameters estimated via SF analysis should be interpreted with caution. The major problem is that statistical routines (least-square minimisation, maximum-likelihood estimation) which are commonly used for fitting the observed SF to the model, assume that fitted SF measurements are statistically independent and follow a Gaussian distribution. Both of these assumptions are not valid in reality. Non-Gaussianity and lack of statistical independence of SF measurements can reinforce underestimation of uncertainties in the model parameters. Additionally, the irregular sampling and finite length of a dataset introduce further biases in the derived quantities.

5.3.2 Theoretical covariance function of RM variations

Alternatively, in order to quantify the RM variability of pulsars, one can use the auto-covariance function $C(\delta\theta)$:

$$C(\delta\theta) = \langle \mathrm{RM}(\theta)\mathrm{RM}(\theta+\delta\theta)\rangle. \tag{5.7}$$

For a given geometry applying the conditions in equations (5.2) and (5.3) and assuming again $L \simeq L^{'}$, $Ll_0^{-1}\delta\theta < 1$ and $l_0 < L$, we have parameterised the covariance function as[8]:

$$\begin{aligned} C_{\mathrm{ISM}}(\delta\theta) &= \langle \int_0^L n(z,0)B_z(z,0)\mathrm{d}z \int_0^{L^{'}} n(\zeta\cos\delta\theta,\zeta\sin\delta\theta)B_\zeta(\zeta\cos\delta\theta,\zeta\sin\delta\theta)\mathrm{d}\zeta\rangle \\ &= C_0 - \frac{1}{2}\mathrm{SF}_{\mathrm{ISM}}(\delta\theta), \\ C_0 &= (0.81)^2 L\pi^2 \left(B_{0z}^2 \frac{2\mathcal{C}_n^2}{\rho_n q_0^{2\rho_n}} + n_0^2 \frac{2\mathcal{C}_B^2}{\rho_B q_0^{2\rho_B}} + \pi\mathcal{C}_n^2\mathcal{C}_B^2 q0^{-2\rho_n-2\rho_B+1} \frac{4^{\rho_n+\rho_B}\Gamma(\rho_n+\rho_B-0.5)^2}{2\rho_n\rho_B\Gamma(2\rho_n+2\rho_B-1)} \right) \end{aligned} \tag{5.8}$$

In contrast to the SF formalism, within the formalism used in the covariance function, one directly 'fits' observed RMs, which are assumed to be statistically independent, to the theoretical model (see Equation 5.9). Therefore, the covariance function analysis is expected to recover the true underlying variability with greater robustness. Due to aforementioned reasons, our quantitative results are primarily based on the covariance function approach, while the SF analysis was used only for qualitative tests. The technical details of the comparison of theoretical models to the real data and its application are demonstrated below.

[8] The form of the theoretical covariance function was derived within this thesis and was based on calculations performed in Minter (1995).

5.4 Comparison with observations: parameter estimation and upper limits

5.4.1 Structure function analysis

Although the parameters inferred from fitting the SFs can be biased, the SF is a useful illustrative tool for inspecting the evidence of turbulence in the RM and DM of pulsars. As discussed in Section 5.3.1, in the regime where the data are dominated by ISM turbulence, the SFs follow power laws, while in the noise-dominated regime the SFs are expected to be flat. We have calculated the RM SFs using Equation (5.4) for all four pulsars. Because the considered time series are all irregularly sampled, we have applied logarithmic binning of the SFs such that the shortest time lag is the mean sampling time of the dataset ($\sim$ 7 days). The SF uncertainties were estimated with Monte-Carlo simulations by varying the RM time series within the corresponding measurement uncertainties; the resultant uncertainties were calculated as 1-σ confidence intervals of the SF distribution over 1000 iterations. Figure 5.3 shows the estimated SFs for each pulsar. We find that SFs of PSRs J0332+5434 and J0826+2637 are flat within the uncertainties and consistent with SFs of purely white noise, while PRSs J1136+1551 and J1921+2153 marginally exhibit a positive power-law scaling in a manner similar to that expected from Kolmogorov turbulence.

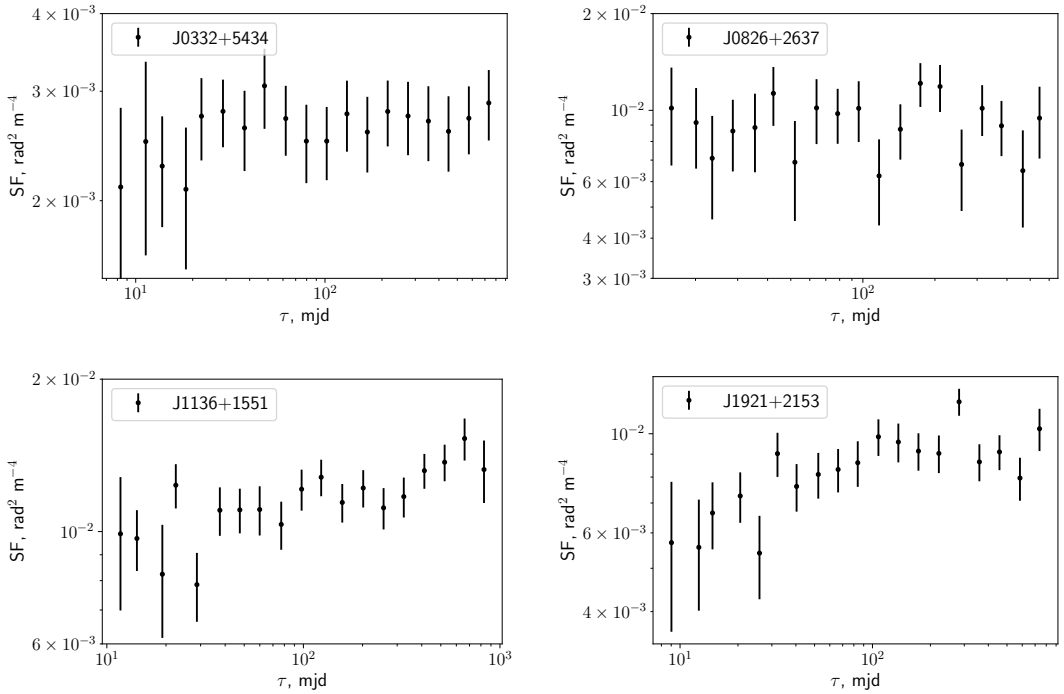

Figure 5.3: SFs of the RM time series from Figure 5.1.

5.4.2 Covariance function analysis

In this section we describe how to model the data within the covariance function formalism using Bayesian statistics. Within the Bayesian framework the data are fixed and the model parameters are treated as random variables. The multivariate posterior probability of model parameters is then given by:

$$
\begin{aligned}
&P_{\rm post}(\mathcal{C}_n, \mathcal{C}_B, \alpha_n, \alpha_B, q_0, n_0, B_{\rm LoS}, \boldsymbol{\kappa}, \Sigma | \mathbf{RM}_{\rm obs}) = \\
&\frac{1}{\sqrt{(2\pi)^n \det C}} \times \exp\left[-\frac{1}{2}(\mathbf{RM}_{\rm obs} - \mathbf{RM}_{\rm mod}(\boldsymbol{\kappa}))^T C^{-1} (\mathbf{RM}_{\rm obs} - \mathbf{RM}_{\rm mod}(\boldsymbol{\kappa}))\right], \\
&C = C_{\rm WN} + C_{\rm ISM},
\end{aligned}
\tag{5.9}
$$

where $\mathbf{RM}_{\rm obs}$ is the vector which contains the RM time series of a pulsar observed for a range of $\delta\theta$. $\mathbf{RM}_{\rm mod}$, which depends on the parameter vector $\boldsymbol{\kappa}$, contains all deterministic systematics. Specifically in our case, the parameters characterising the linear trend are expected to be significantly covariant with $\mathcal{C}_B$ and α_B and were therefore included in the model in order to increase the robustness of the results. Therefore, $\mathbf{RM}_{\rm mod} = \kappa_1 + \kappa_2 \boldsymbol{t}$, where $\boldsymbol{t}$ is the vector of observational epochs. $C_{\rm WN} = (\sigma_i^2 + \Sigma^2)\delta_{ij}$ is the covariance of the uncorrelated white-noise component, where σ_i are the formal uncertainties of measured RMs, and Σ is the variance of a common white-noise process, associated with the limited accuracy of the modelled ionospheric RMs[9]. To estimate the parameters of interest, namely $\mathcal{C}_B$ and α_B, one needs to reconstruct the posterior probability $P_{\rm post}$ while simultaneously marginalising (numerically or analytically) over unwanted parameters. In our case, the vast majority of model parameters have been fixed to their *a priori* known values adapted from the literature, implying that their prior distributions are Dirac delta functions[10]. Specifically, the distances L were taken from the ATNF catalogue (Manchester et al., 2005), estimated using the combined parallax and HI methods (Verbiest et al., 2012). The proper motions measured with radio interferometric and timing measurements were also obtained from the ATNF catalogue. The average LoS electron densities were inferred from DM measurements (Bilous et al., 2016), such that $n_0 = \langle {\rm DM} \rangle / L$ (see Section 1.4.1). The average magnetic field strength towards the pulsars was estimated using Equation (1.13). LoS dependent parameters are given in Table 5.1.

Building upon previous studies (e.g. Cordes et al., 1985; Armstrong et al., 1995; Donner et al., 2019), electron-density fluctuations were assumed to be purely Kolmogorov with a power-law index $\alpha_n = 11/3$ and spectral coefficient $\mathcal{C}_n^2 = 10^{-4}$ cm^{-6} pc^3. Analyses of the RM of polarised extragalactic sources have shown that the outer scale of turbulence differs significantly across the Galaxy (Haverkorn et al., 2008, and references therein). The inferred outer scale is smaller than about 10 pc for

[9] As shown in Chapter 4, the noise associated with the imperfectness of ionospheric modelling on longer time scales can be modelled as an additional white component with variance of $\sim$0.06 rad m^{-2}.

[10] The uncertainties in the distances and proper motions have not been taken into account. For PSRs J0332+5434, J0826+2637 and J1136+1551 we expect less than 20% change in the upper limits. However, due to the large uncertainty in the distance towards J1921+2153, the inferred C_B can be significantly biased. Nevertheless, our overall results and conclusions won't change.

Jname	Bname	L, kpc	μ, mas yr^{-1}	$\langle$DM$\rangle$, cm^{-3} pc	$\langle$RM$\rangle$, rad m^{-2}	n_0, cm^{-3}	$B_{\rm LOS}$, μG	
J0332+5434	B0329+54	$1.0^{+0.1}_{-0.1}$	19.5(4)	26.2	−64.29	0.03	−3.0	
J0826+2637	B0823+26	$0.32^{+0.08}_{-0.05}$	108(3)	19.5	5.30	0.06	0.3	
J1136+1551	B1133+16	$0.35^{+0.02}_{-0.02}$	375.5(4)	4.8	3.97	0.01	1.0	
J1921+2153	B1919+21	$0.3^{+0.8}_{-0.2}$	36(6)	12.4	−17.03	0.04	−1.7	

Table 5.1: The pulsar parameters that have been fixed in the analysis. The DMs are adapted from (Bilous et al., 2016), the distances and proper motions are obtained from the ATNF catalogue (see text for details). The RMs are obtained in this work.

the spiral arms, while it is around 100 pc for the interarm regions. Two extreme values of 5 and 100 pc are considered in the current analysis. When all aforementioned parameters are fixed, the resultant posterior probability is $P_{\rm post}(\mathcal{C}_B, \alpha_B, \boldsymbol{\kappa}, \Sigma|\mathbf{RM}_{\rm obs})$. The sampling of $P_{\rm post}(\mathcal{C}_B, \alpha_B, \boldsymbol{\kappa}, \Sigma|\mathbf{RM}_{\rm obs})$ was performed using the `MultiNest` software (Feroz et al., 2009). The prior distribution of the non-fixed parameters was chosen to be uninformative, i.e. log-uniform for $\mathcal{C}_B$ and uniform for other parameters. The full list of all the parameters (fixed and non-fixed) is given in Table 5.2.

Parameter estimation. The reconstructed posterior probabilities for PSRs J0332+5434 and J0826+2637 (see Figure 5.4) do not show any evidence of the signal described by Equation (5.8). The posterior probabilities for PSRs J1136+1551 and J1921+2153 are non-uniform, implying the presence of correlated noise, and are shown in Figure 5.5. The inferred C_B and α_B are in good agreement with the results obtained with the SFs, which are demonstrated in the lower panel of Figure 5.5. The obtained power spectral indices (α_B ∼2.2−2.5) are much shallower than what we expect from Kolmogorov turbulence.

The origin of these signals is still under scrutiny. Beside being caused by the Kolmogorov-type turbulence in the ISM, the observed signals could be of terrestrial nature, e.g. unmodelled long-term ionospheric Faraday rotation. As astrophysical RM variations are thought to be mainly guided by fluctuations in electron density (Minter & Spangler, 1996; Haverkorn et al., 2004), a strong confirmation of the astrophysical nature of the observed changes in RM would be covariance with simultaneously measured DMs. The DM measurements were obtained via timing with a frequency-resolved template-matching technique described in e.g. Donner et al. (2019); Tiburzi et al. (2019). This method was applied to the same pulsar datasets, with the DM measurements provided by J.Donner (private communication). The top panel of Figure 5.6 demonstrates the scatter plot of RM vs DM measurements for PSRs J1136+1551 and J1921+2153. The Pearson correlation coefficients for PSRs J1136+1551 and J1921+2153 are -0.09 ± 0.05 and -0.05 ± 0.08, respectively, implying no significant

Parameter	Value	Description	References
n_0	See Table 5.1	LoS average electron density, cm^{-3}	$n_0 = \langle \mathrm{DM} \rangle / L$
B_{LoS}	See Table 5.1	LoS average magnetic field, μG	$B_{\mathrm{LoS}} = 1.23 \langle \mathrm{RM} \rangle / \langle \mathrm{DM} \rangle$
L	See Table 5.1	Pulsar distance, pc	Manchester et al. (2005)
μ	See Table 5.1	Proper motion, mas yr^{-1}	Manchester et al. (2005)
q_0	5, 100	Outer scale of turbulence, pc	Haverkorn et al. (2008)
$\mathcal{C}_n$	10^{-2}	Electron-density power-law amplitude, $\mathrm{cm}^{-3}\,\mathrm{pc}^{3/2}$	Armstrong et al. (1995)
α_n	11/3	Electron-density power-law index	Armstrong et al. (1995)
$\mathcal{C}_B$	$[10^{-5}; 10^{2}]$	Magnetic-field power-law amplitude, $\mu\mathrm{G}\,\mathrm{pc}^{3/2}$	Minter & Spangler (1996)
			Haverkorn et al. (2008)
α_B	[2; 4]	Magnetic-field power-law spectral index	Minter & Spangler (1996)
$\boldsymbol{\kappa}$	κ_1: [-10; 10]	Linear trend parameters:	–
	κ_2: [-1; 1]	$\kappa_1[\mathrm{rad\ m}^{-2}] + \kappa_2[\mathrm{rad\ m}^{-2}\ \mathrm{day}^{-1}]t$	–
Σ	[0; 1]	Common white-noise variance, $\mathrm{rad\ m}^{-2}$	–

Table 5.2: List of parameters used for the Bayesian analysis.

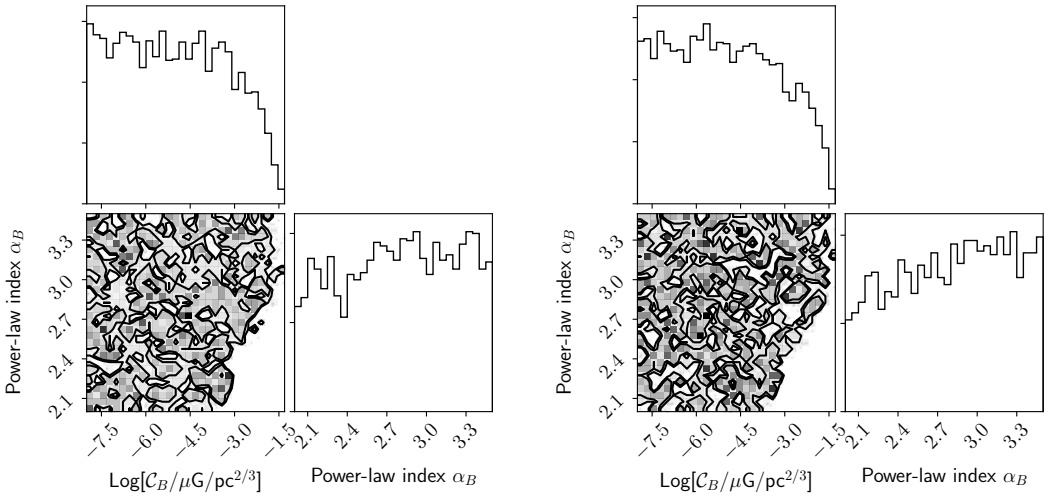

Figure 5.4: One- and two-dimensional posterior distributions for $\mathcal{C}_B$ and α_B of PSRs J0332+5434 (left) and J0826+2637 (right). The posterior probabilities are flat, therefore, the RM time series of these two pulsars do not display correlated noise of the functional form described by Equation (5.8).

correlation between pulsar RMs and DMs. We have additionally carried out a more robust correlation test, where we have explored the statistical relation of *detrended* RM and DM time series. For detrending we have used non-parametric *first differences* technique, within which we have regressed $\Delta\mathrm{RM} = \mathrm{RM}(t_{j+1}) - \mathrm{RM}(t_j)$ and $\Delta\mathrm{DM} = \mathrm{DM}(t_{j+1}) - \mathrm{DM}(t_j)$ against each other. The results are shown in the bottom panel of Figure 5.6; the inferred Pearson correlation coefficients for PSRs J1136+1551 and J1921+2153 are -0.01 ± 0.08 and -0.03 ± 0.1, respectively. Neither of the two correlation tests have shown statistical relation between RM and DM for either pulsar. Therefore, there is insufficient evidence to claim the astrophysical nature of the signal.

Upper limits. As no astrophysically significant signal has been found, we instead place an upper limit on the amplitude of the turbulent magnetic-field fluctuations. Within the Bayesian framework, the calculation of an upper limit on $\mathcal{C}_B$ is a matter of parameter estimation. In this framework, it is assumed that a signal is present in the data, and its amplitude is less than $\mathcal{C}_B^*$, with 95%-probability, which is the 95%-Bayesian upper limit. In order to set an upper limit on $\mathcal{C}_B$ as a function of α_B, we divide the range of α_B in small bins, in which we separately reconstruct the joint posterior probability of non-fixed parameters. In order to obtain robust upper limits, the prior distribution of $\mathcal{C}_B$ was chosen to be non-informative and conservative, e.g uniform. The Bayesian upper limit $\mathcal{C}_B^*$ was chosen as the 95%-quantile of the reconstructed posterior distribution of $\mathcal{C}_B$ numerically marginalised over all other parameters.

Figure 5.7 (left) shows the upper limits on the spectral coefficient $\mathcal{C}_B^2$ as a function

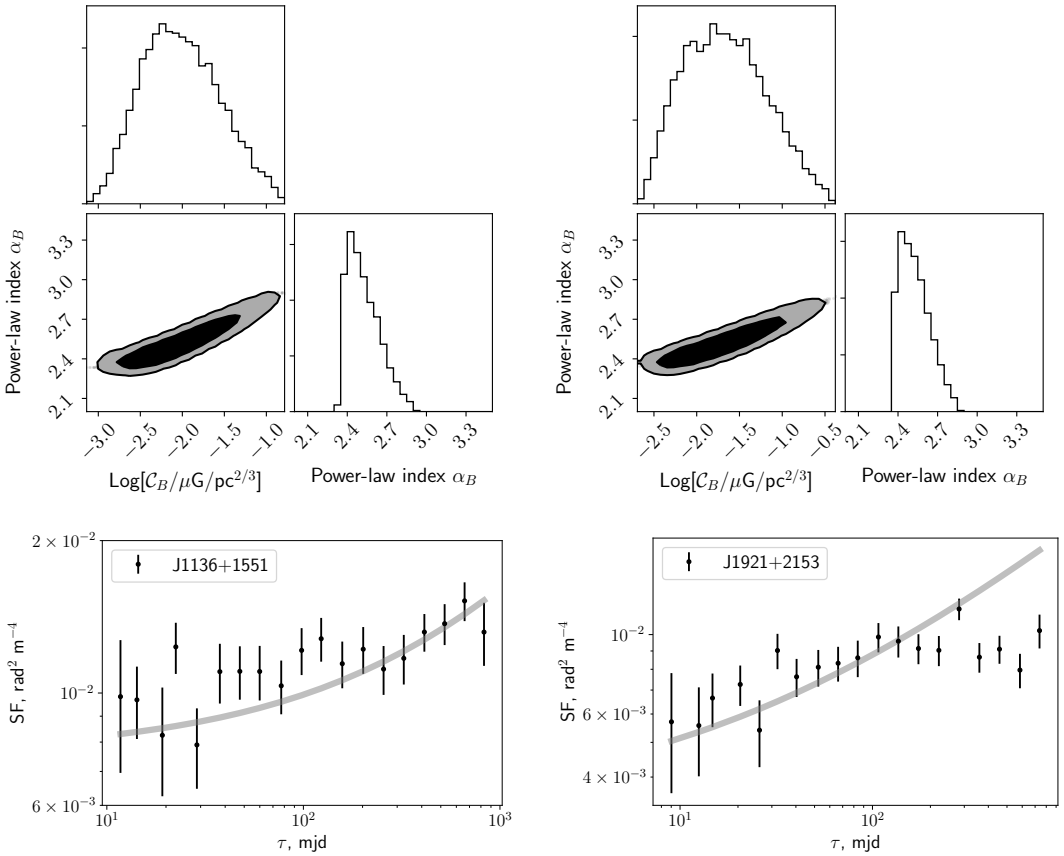

Figure 5.5: *Top*: One- and two-dimensional posterior distributions for $\mathcal{C}_B$ and α_B of PSRs J1136+1551 (left) and J1921+2153 (right). The black and grey regions indicate the 68% and 95% confidence intervals. The inferred parameters are $\log(\mathcal{C}_B/(\mu\mathrm{G\,pc}^{3/2})) = -1.9^{+0.4}_{-0.4}$ and $\alpha_B = 2.57^{+0.1}_{-0.07}$ for PSR J1921+2153; $\log(\mathcal{C}_B/(\mu\mathrm{G\,pc}^{3/2})) = -2.2^{+0.4}_{-0.4}$ and $\alpha_B = 2.46^{+0.1}_{-0.07}$ for PSR J1136+1551. *Bottom*: The observed SFs (black points) overplotted with the theoretically predicted SFs (grey lines). The theoretically predicted SFs were calculated as $2\Sigma^2 + \mathrm{SF}_{\mathrm{ISM}}$ (see Equation (5.5)), where we have used the median value of $\mathcal{C}_B$ and α_B from the covariance function analysis.

of the magnetic-field index α_B obtained from the analysis of $\sim$ 3-year RM time-series of PSRs J0332+5434, J0826+2637, J1136+1551 and J1921+2153. Due to the lack of direct measurements of $\mathcal{C}_B^2$ and α_B at the considered scales of 10^{-4} pc, we have compared our upper limits to the values adopted from Minter & Spangler (1996) and Haverkorn et al. (2008). In both works, parameters of the magnetic-field turbulence were inferred from the investigation of SFs of extragalactic RMs. By analysing the properties of turbulence in the region at high Galactic latitudes, Minter & Spangler

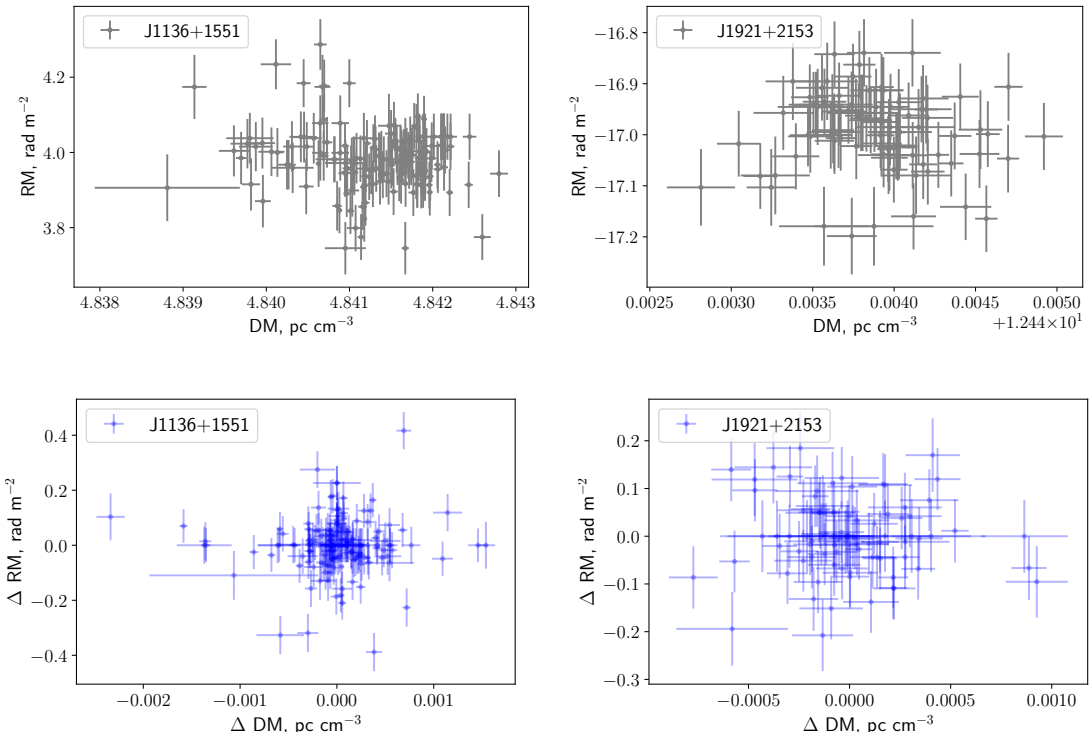

Figure 5.6: *Top panel* - Distribution of DM vs RM measurements of PSRs J1136+1551 (left) and J1921+2153 (right). The Pearson correlation coefficients are -0.09 ± 0.05 and -0.05 ± 0.08, respectively. *Bottom panel* - Distribution of ΔDM vs ΔRM measurements of PSRs J1136+1551 (left) and J1921+2153 (right). The Pearson correlation coefficients are -0.01 ± 0.08 and -0.03 ± 0.1, respectively. Neither plot shows evidence for a correlation between RM and DM.

(1996) have inferred $\mathcal{C}_B^2 = 2.2 \times 10^{-2}\,\mu\mathrm{G}^2\,\mathrm{pc}^3$ for $\alpha_B = 11/3$. In Haverkorn et al. (2008), authors used a set of extragalactic sources behind the inner Galactic plane. Under the assumption of pure Kolmogorov turbulence ($\alpha_B = 11/3$), the inferred $\mathcal{C}_B^2 \sim 0.6 - 4\,\mu\mathrm{G}^2\,\mathrm{pc}^3$. Results of both works are shown in Figure 5.7 with dashed grey lines.

However, it is worth mentioning that the values inferred from studies of extragalactic sources should be compared to the results of our analysis with caution. To start with, the scales probed in this thesis are $v_\perp t \simeq 10^{-6} - 10^{-3}\,\mathrm{pc}$, with the lower limit defined by the cadence of our observations and the upper limit by the timespan of the dataset. The inquired scales in Minter & Spangler (1996) and Haverkorn et al. (2008) are several orders of magnitude larger: from 1 to 10^3 pc, limited by the range of probed angular separations of used sources. Secondly, the radiation from extragalactic sources propagates through the entire column of the Galactic medium, while pulsars used in this chapter are only probing a small fraction of it. And lastly, in Minter & Spangler (1996); Haverkorn et al. (2008) the RMs of extragalactic sources were not corrected for the intrinsic and extragalactic Faraday rotation, therefore, the results of these studies can be biased.

Because of the high proper motion and large average electron density along the LoS, the most stringent constraints on $\mathcal{C}_B^2$ are set with the RM time series of PSR J0826+2637. The upper limits obtained with PSRs J0332+5434 and J0826+2637 are already astrophysically interesting as they lie below $\mathcal{C}_B^2 = 0.6\,\mu\mathrm{G}^2\,\mathrm{pc}^3$ predicted in Haverkorn et al. (2008), implying that magnetic-field fluctuations with this amplitude should have been detected already. However, the aforementioned upper limits are still a factor of 4 – 16 higher than the values derived in Minter & Spangler (1996). The upper limits obtained with PSRs J1136+1551 and J1921+2153 are less constraining due to the presence of correlated noise.

We additionally analysed how our upper limits will improve with time. Figure 5.7 (right) shows the upper limits on the spectral coefficient $\mathcal{C}_B^2$ as a function of the magnetic-field index, obtained with the simulated datasets, assuming the RMs are measured at the $0.06\,\mathrm{rad\,m^{-2}}$ accuracy level (see Chapter 4). The proper motion of a source placed 1 kpc from Earth was set to $200\,\mathrm{km\,s^{-1}}$ (the average two-dimensional pulsar velocity from Hobbs et al., 2005). The average electron density and magnetic field towards the pulsar were assumed to be $n_0 = 0.01\,\mathrm{cm^{-3}}$ and $B_{\mathrm{LoS}} = \mu\mathrm{G}$, respectively. We have considered three different setups: a) a data span of 5 years and observing cadence of 7 days are assumed, while the outer scale of turbulence is fixed to $q_0 = 100\,\mathrm{pc}$; b) a data span of 5 years and observing cadence of 7 days are assumed, while the outer scale of turbulence is fixed to $q_0 = 5\,\mathrm{pc}$; c) a data span of 20 years and observing cadence of 14 days are assumed, while the outer scale of turbulence is fixed to $q_0 = 100\,\mathrm{pc}$. Assuming the current sensitivity, we would be sensitive to magnetic field turbulence in ~ 20 years (assuming the predictions by Minter & Spangler, 1996).

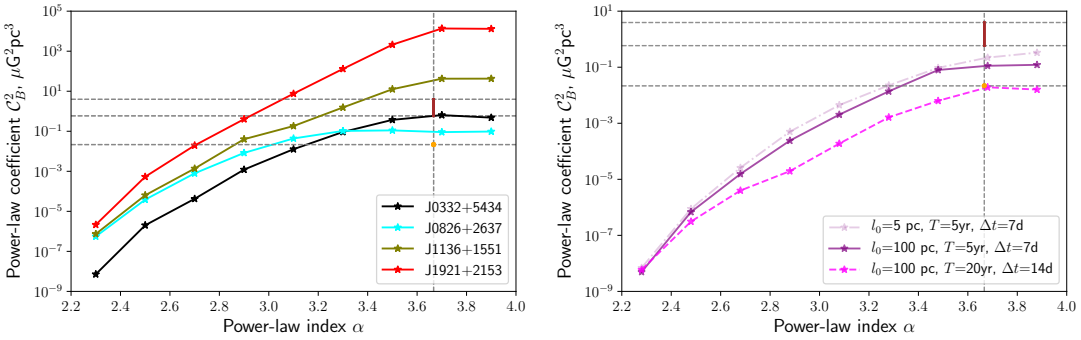

Figure 5.7: Upper limits on the spectral coefficient $\mathcal{C}_B^2$ as a function of magnetic field spectral index α_B. The grey lines at $\alpha_B = 11/3$ indicates where we expect the signal induced by interstellar magnetic field turbulence. The yellow dot indicates the $\mathcal{C}_B^2$ derived in Minter & Spangler (1996), while the brown line shows a range of $\mathcal{C}_B^2$ derived in Haverkorn et al. (2008). *Left*: upper limits obtained with the real RM time series of PSRs J0332+5434, J0826+2637, J1136+1551 and J1921+2153. The outer scale was assumed to be $l_0 = 100\,\mathrm{pc}$. *Right*: upper limits obtained with simulated datasets, using the assumption that the RM can be measured with a precision of $0.06\,\mathrm{rad\,m^{-2}}$. Case: a) 5-year data span, 7-day cadence, $l_0 = 100\,\mathrm{pc}$; b) 5-year data span, 7-day cadence, $l_0 = 5\,\mathrm{pc}$; c) 20-year data span, 14-day cadence, $l_0 = 100\,\mathrm{pc}$.

5.5 Conclusions

The weekly observations of pulsars with international LOFAR stations undertaken within the GLOW campaign provide an outstanding data set for long-term studies of propagation effects and the properties of intervening media. In this chapter we have investigated the prospects of detecting temporal variations in RM due to the ISM in pulsar data. These variations are believed to originate from the pulsar's transverse motion, which causes the LoS to sample different parts of the turbulent ISM. The astrophysical RM variations were modelled as the sum of two contributions coming from electron-density and magnetic-field fluctuations, respectively. In earlier studies, it was assumed that magnetic fields are frozen in the plasma and, therefore, the two types of fluctuations were assumed to follow identical power laws. Recent studies on magneto-hydrodynamic turbulence have shown that the assumption of frozen-in magnetic fields breaks down (Lazarian et al., 2012; Eyink et al., 2013). We have relaxed the above assumption and assumed that the magnetic-field and electron-density turbulence follow different power laws. Using low-frequency observations of four pulsars, we have set an upper limit on the power of fluctuations of interstellar magnetic fields. Our best results are obtained with the RM time series of PSRs J0332+5434 and J0826+2637, which are just below the magnetic-field amplitude observed in Haverkorn et al. (2008), and are 4 – 16 times higher than the value inferred from RM measurements of extragalactic sources in Minter & Spangler (1996).

We have also investigated how our sensitivity will improve with time. Assuming

typical characteristics of the ISM towards the pulsar and a realistic noise level which is mostly defined by the imperfections in the ionospheric modelling, we conservatively found that our dataset becomes sensitive to interstellar RM fluctuations in ~ 20 years. This number can be reduced by choosing pulsars with larger apparent velocities and higher average electron densities along the LoSs as well as by improving the quality of ionospheric modelling.

Two pulsars in our sample, PSRs J1136+1551 and J1921+2153, exhibit correlated noise in the RM time series, across about three years of data. The origin of the correlated signal is still not ascertained. Among the possible sources are the inaccurately mitigated ionospheric Faraday rotation or instrumental biases. If these effects are not the cause of the observed signal, then it is likely that our observations of those two pulsars have indeed detected magnetic-field turbulence in the ISM. The inferred power-law indices are much shallower than what we expect from 3D Kolmogorov turbulence. However, the observed signals are in good agreement with two-dimensional turbulence, which predicts a power-law index of 8/3. 2D Kolmogorov turbulence can be observed if one probes turbulent matter within a thin sheet or filament, when the angular separation is greater than the thickness of the screen (Minter & Spangler, 1996). Moreover, recent simulations have shown that shallower power-law indices are also expected in the supersonic regime of turbulence (see e.g. Federrath, 2013; Lazarian & Pogosyan, 2016, and reference therein). In order to investigate the possible astrophysical nature of the signal, we have additionally tested the covariance between the RM and DM measurements. No correlation between the DM and RM of the pulsars measured at the same epochs has been found. The astrophysical nature of these signals are still under debate and will be explored further in future work.

Chapter 6

Parkes Pulsar Timing Array constraints on ultralight scalar-field dark matter

The work presented in this section is based on the following article:

- N. K. Porayko, X.-J. Zhu, Y. Levin, L. Hui, G. Hobbs, A. Grudskaya, K. Postnov, M. Bailes, R.N.D. Bhat, W. Coles, S. Dai, J. Dempsey, M.J. Keith, M. Kerr, M. Kramer, P.D. Lasky, R.N. Manchester, S. Osłowski, A. Parthasarathy, V. Ravi, D.J. Reardon, P.R. Rosado, C.J. Russell, R.M. Shannon, R. Spiewak, W. van Straten, L. Toomey, J. Wang, L. Wen, X. You, PPTA Collaboration; *"Parkes Pulsar Timing Array constraints on ultralight scalar-field dark matter"*, 2018, Phys.Rev.D, 98, 102002

The text, figures, and tables have only been modified to match the style, spelling and format of the rest of this thesis. X.-J. Zhu and I are the main authors of the paper. For this publication, I have used the newest PPTA dataset to analyse properties of the timing data within Bayesian framework, and to set Bayesian upper limits on the ultralight scalar-field dark matter density in the Galaxy. Further, I have investigated how our sensitivity will increase with future upcoming radio facilities.

Contents

6.1 Introduction 100
6.2 The pulsar timing residuals from fuzzy dark matter 104
6.3 PPTA data and noise properties 105
6.3.1 Observations and timing analysis 105
6.3.2 The likelihood function 106
6.3.3 Noise modeling 108
6.4 Search techniques and Results 113
6.4.1 Bayesian analysis 113
6.4.2 Frequentist analysis 117
6.4.3 Upper limits 118
6.5 Future prospects 120
6.6 Conclusions 123

It is widely accepted that dark matter contributes about a quarter of the critical mass-energy density in our Universe. The nature of dark matter is currently unknown, with the mass of possible constituents spanning nearly one hundred orders of magnitude. The ultralight scalar field dark matter, consisting of extremely light bosons with $m \sim 10^{-22}\,\mathrm{eV}$ and often called "fuzzy" dark matter, provides intriguing solutions to some challenges at sub-Galactic scales for the standard cold dark matter model. As shown by Khmelnitsky and Rubakov, such a scalar field in the Galaxy would produce an oscillating gravitational potential with nanohertz frequencies, resulting in periodic variations in the times of arrival of radio pulses from pulsars. The Parkes Pulsar Timing Array (PPTA) has been monitoring 20 millisecond pulsars at two to three weeks intervals for more than a decade. In addition to the detection of nanohertz gravitational waves, PPTA offers the opportunity for direct searches for fuzzy dark matter in an astrophysically feasible range of masses. We analyze the latest PPTA data set which includes timing observations for 26 pulsars made between 2004 and 2016. We perform a search in this data set for evidence of ultralight dark matter in the Galaxy using Bayesian and Frequentist methods. No statistically significant detection has been made. We, therefore, place upper limits on the local dark matter density. Our limits, improving on previous searches by a factor of 2 to 5, constrain the dark matter density of ultralight bosons with $m \leq 10^{-23}\,\mathrm{eV}$ to be below $6\,\mathrm{GeV\,cm^{-3}}$ with 95% confidence in the Earth neighborhood. Finally, we discuss the prospect of probing the astrophysically favored mass range $m \gtrsim 10^{-22}\,\mathrm{eV}$ with next-generation pulsar timing facilities.

6.1 Introduction

Dark matter, a concept established in the early 1930s for the purpose of explaining the observed enigmatic dynamics of disk galaxies and motion of galaxies in clusters (Zwicky, 1933, 1937; Smith, 1936), is nowadays considered to be an essential ingredient of the Universe. It is instrumental in explaining a wide range of astrophysical phenomena, such as strong gravitational lensing of elliptical galaxies (Koopmans & Treu, 2003), the dynamics of interacting clusters (Clowe et al., 2004) and the large-scale structure of the Universe (Tegmark et al., 2004). The latest analysis of temperature and polarization anisotropies of the cosmic microwave background (Planck Collaboration et al., 2016) suggested that the Universe contains 26% dark matter, which is five times more than ordinary baryonic matter such as stars and galaxies.

The most popular dark matter candidates are weakly interacting massive particles (WIMPs) and quantum chromodynamics (QCD) axions. We refer to both as standard cold dark matter, or simply CDM. The CDM paradigm has met with impressive success in matching observational data on large cosmological scales (see Bertone et al., 2005; Primack, 2012, for reviews). Recently, there has been an increased number of ideas about dark matter that go beyond the standard paradigm, building on old ideas in some cases (see e.g. Battaglieri et al., 2017, for an overview).

One such idea – an ultralight axion or axion-like particle – can be thought of as a generalization of the QCD axion. An axion is an angular field, i.e. the field

range is finite and periodic with a periodicity $2\pi F_{\rm axion}$ with $F_{\rm axion}$ often referred to as the axion decay constant. A simple axion Lagrangian has a standard kinetic term, and a self-interaction potential V generated by non-perturbative effects (that can be approximated by instanton potential),

$$V(\phi) = m^2 F_{\rm axion}^2 [1 - \cos(\phi/F_{\rm axion})]\,, \tag{6.1}$$

where m is the mass of the axion ϕ. The non-perturbative effects are typically highly suppressed (e.g. exponentially suppressed by an instanton action), leading to a fairly low energy scale $\sqrt{mF_{\rm axion}}$. In the early Universe, the scalar field is frozen at its primordial value, generically expected to be order of $F_{\rm axion}$. When the Hubble expansion rate drops below the mass scale m, the scalar field oscillates with an amplitude that redshifts with the expansion of the Universe. Averaging over oscillation cycles, ϕ behaves like CDM with a relic density of (see e.g. Arvanitaki et al., 2010; Hui et al., 2017)[1]

$$\Omega_{\rm axion} \sim 0.1 \left(\frac{m}{10^{-22}\,{\rm eV}}\right)^{1/2} \left(\frac{F_{\rm axion}}{10^{17}\,{\rm GeV}}\right)^2 . \tag{6.2}$$

String theory contains many axion candidates with $F_{\rm axion}$ somewhere in the range $10^{16} - 10^{18}\,{\rm GeV}$ (Svrcek & Witten, 2006). Equation (6.2) tells us that a very low m is preferred if the axion were to account for dark matter. It should be emphasized though that there is a fairly large possible range for m; in fact, the relic abundance is more sensitive to $F_{\rm axion}$ than to m. A lighter mass, e.g., $m \sim 10^{-23}\,{\rm eV}$, can be easily accommodated by a slightly higher $F_{\rm axion}$, though it is disfavored by astrophysical observations such as the existence and structure of dwarf galaxies[2].

Such an ultralight axion has a macroscopic de Broglie wavelength $\lambda_{\rm dB}$, given by

$$\frac{\lambda_{\rm dB}}{2\pi} = \frac{\hbar}{mv} \approx 60\,{\rm pc} \left(\frac{10^{-22}{\rm eV}}{m}\right) \left(\frac{10^{-3}c}{v}\right) , \tag{6.3}$$

where v is the velocity, implying wave-like phenomena on astronomically accessible scales, unlike standard CDM. In linear perturbation theory, the wave-like property leads to a suppression of power on small scales (small compared to the Jeans scale, which is a geometric mean of the Compton and Hubble scale). It is this property that motivated Hu et al. (2000) to propose an ultralight boson as an alternative to standard CDM, and to coin the term "fuzzy dark matter" (FDM). The term FDM refers generally to a scalar dark matter particle with a very small mass, such that its de Broglie wavelength is macroscopic. An ultralight axion is a particularly compelling realization. Our constraints derived in this paper apply to the ultralight axion, as well as the broader class of FDM.

The thinking was that the suppression of power on small scales would help resolve certain small-scale problems of CDM, which generally have to do with CDM predicting

[1] The relic density computation follows the classic arguments of Preskill et al. (1983); Abbott & Sikivie (1983); Dine & Fischler (1983), which were developed for the QCD axion.

[2] Note that the requisite $\sqrt{mF_{\rm axion}}$ is much less than the QCD scale; hence this is not the QCD axion.

too much small-scale structure compared to that observed. There is a vast literature on this subject, but it remains a matter of debate as to whether the perceived small-scale structure problems of CDM are in fact amenable to astrophysical solutions (such as feedback processes modifying the mass distribution within Galactic halos; see Bullock & Boylan-Kolchin, 2017, for a review).

There exist several different bounds on the FDM model. One class of bounds comes from measurements of the linear power spectrum at high redshifts, such as from the microwave background (e.g. Hložek et al., 2018), and from the Lyman-alpha forest (Iršič et al., 2017; Kobayashi et al., 2017). In particular, the Lyman-alpha forest data appear to disfavor a FDM mass lighter than about $10^{-21}\,\mathrm{eV}$. Another example of a bound of this kind come from 21-cm observations – the recent detection of a global 21-cm absorption signal at redshift around 18 (Bowman et al., 2018) puts a lower limit on the FDM mass similar to the Lyman-alpha forest bound (Schneider, 2018; Lidz & Hui, 2018; Sullivan et al., 2018). Yet another class of bounds comes from dynamical data on the density profiles of galaxies (e.g. Calabrese & Spergel, 2016; Deng et al., 2018; Bar et al., 2018). Many of these bounds are subject to their own astrophysical uncertainties. For instance, the Lyman-alpha forest bound is predicated upon the correct modeling of fluctuations from such as the ionizing background, the temperature and feedback processes. The 21-cm bound relies on assumptions about star formation (that it tracks the halo formation and that the fraction of baryons that form stars is less than about 5%), and of course, assumes the validity of the detection. Constraints from rotation curve measurements generally make assumptions about how feedback processes, such as from stellar explosions, affect (or do not affect) density profiles.

Recently, a number of authors, based on numerical simulations and analytical arguments, pointed out additional testable astrophysical implications of FDM, especially in the nonlinear regime (Schive et al., 2014; Mocz & Succi, 2015; Veltmaat & Niemeyer, 2016; Hui et al., 2017; Nori & Baldi, 2018; Veltmaat et al., 2018). A particularly interesting probe of ultralight dark matter using PTAs was pointed out by Khmelnitsky & Rubakov (2014). Through purely gravitational coupling, scalar field dark matter induces periodic oscillations in gravitational potentials with frequency twice the field mass $f \sim 2m \sim 5 \times 10^{-8}\,\mathrm{Hz}\,(m/10^{-22}\,\mathrm{eV})$. The oscillating gravitational potentials along the line of sight of pulsars cause sinusoidal variations in the ToAs of radio pulses. The frequency of such variations lies right in the sensitivity band of PTAs. This way of detecting or constraining FDM is completely independent of other methods (and their assumptions), and provides a useful check. As shown in Khmelnitsky & Rubakov (2014); Porayko & Postnov (2014); De Martino et al. (2017); Blas et al. (2017) and later in this paper, the current PTA data can only be sensitive to very low-mass FDM ($m < 10^{-23}\,\mathrm{eV}$). We will discuss what would be required to probe the higher and cosmologically more favorable masses.

The concept of a PTA is to regularly monitor ToAs of pulses from an array of the most rotationally stable millisecond pulsars (Sazhin, 1978; Detweiler, 1979b; Hellings & Downs, 1983; Foster & Backer, 1990). Measured ToAs are fitted with a deterministic timing model that accounts for the pulsar spin behavior and for the geometrical effects due to the motion of the pulsar and the Earth. The difference between the observed

ToAs and those predicted by the best-fit timing model are called timing residuals (see Section 2.3 for more details). By analyzing the pulsar timing residuals, we can obtain the information about other physical processes that affect the propagation of radio pulses through the Galaxy, for instance, the presence of ultralight scalar field dark matter in the Galaxy.

The Parkes Pulsar Timing Array (PPTA, Manchester et al., 2013) uses the 64-m Parkes radio telescope in Australia. Building on earlier pulsar timing observations at Parkes, it started in 2005 to time 20 millisecond pulsars at a regular interval of two to three weeks. PPTA and its counterparts in North America (NANOGrav, McLaughlin, 2013) and Europe (EPTA, Kramer & Champion, 2013) have joined together to form the International Pulsar Timing Array (IPTA, Hobbs et al., 2010a; Verbiest et al., 2016), aiming for a more sensitive data set. The IPTA currently observes around 70 pulsars using the world's most powerful radio telescopes.

The first PPTA data release was published in 2013 (Manchester et al., 2013). It included six years of observations for 20 pulsars. This data set was used to search for a stochastic GW background (Shannon et al., 2013), continuous GWs (Zhu et al., 2014) and GW bursts with memory (Wang et al., 2015a). The second data release is still being actively developed, but for this paper, we have made use of a data set that contains observations made between 2004 and 2016 with five new pulsars added since 2010. An early subset of this data was used to place the most constraining limit to date on the amplitude of a stochastic GW background in the nHz regime (Shannon et al., 2015).

In this work we search for evidence of ultralight scalar field dark matter in the Galaxy using the PPTA data. A similar study was carried out through Bayesian analysis by Porayko & Postnov (2014), using the NANOGrav 5-yr 17-pulsar data set published in Demorest et al. (2013). Our work improves on that of Porayko & Postnov (2014) in several ways. First, we make use of an independent data set with much longer data span and smaller errors in the timing residuals. Second, we use an up-to-date Bayesian inference packages for PTA data analysis, `PAL2` (Ellis & van Haasteren, 2017) and `NX01` (Taylor & Baker, 2017), and include proper treatment of the noise processes. Re-analyzing the NANOGrav data with the improved analysis, we find that the sensitivity was overestimated by a factor of ten in Porayko & Postnov (2014). Third, we also adopt a standard Frequentist searching method and obtain consistent results with Bayesian analysis.

Our paper is organized as follows. In Section 6.2, we describe pulsar timing residuals expected in the presence of ultralight scalar field dark matter in the Galaxy. In Section 6.3, we introduce our data set, the likelihood function and our Bayesian and Frequentist methods to model the noise properties of PPTA data. We also present results of our noise analysis. In Section 6.4, we describe our search techniques and apply them to the PPTA data set. As we find no significant signals, we set upper limits on the local density of FDM in the Galaxy. In Section 6.5, we discuss how the sensitivity will be improved in the future. Finally, we provide concluding remarks in Section 6.6.

6.2 The pulsar timing residuals from fuzzy dark matter

In this section we briefly describe the magnitude and time dependence of timing residuals induced by the scalar field dark matter in the Galaxy. A detailed derivation can be found in Khmelnitsky & Rubakov (2014).

Because of the huge occupation number, the collection of ultralight dark matter particles behaves like a classical scalar field ϕ. To a very good approximation, here we ignore quartic self-interaction and coupling of ultralight dark matter particles to other fields[3] (Krnjaic et al., 2018; Brdar et al., 2018). The scalar action in this case can be written as

$$S_\phi = \int d^4x\sqrt{-g}\left[\frac{1}{2}g^{\mu\nu}D_\nu\phi D_\mu\phi - \frac{1}{2}m^2\phi^2\right], \tag{6.4}$$

to which the standard Einstein-Hilbert action for the metric should be added. The ϕ equation of motion is the Klein-Gordon-Fock Equation: $(\Box_g + m^2)\phi(x) = 0$. We are interested in a computation of ϕ and the metric $g_{\mu\nu}$ inside the Galaxy. The metric is approximately Minkowski plus corrections at the level of 10^{-6}. To good approximation, ϕ everywhere in the Galaxy oscillates at an angular frequency $mc^2/\hbar$ (corrections due to the momentum of the particles and the gravitational potential are small). The energy-momentum tensor to the leading order diagonal and its spatial components (pressure) oscillate at twice the field particle mass. This produces time-dependent gravitational potentials $g_{00} = 1 + 2\Phi(t)$ and $g_{ij} = -1 - 2\Psi(t)\delta_{ij}$ in the metric tensor (in the Newtonian covariant form) with leading oscillating contributions at a frequency

$$f = \frac{2mc^2}{h} \approx 4.8\times10^{-8}\left(\frac{m}{10^{-22}\,\mathrm{eV}}\right)\mathrm{Hz}\,. \tag{6.5}$$

The amplitude of oscillating parts of the potentials Ψ and Φ are a factor of $(v/c)^2$ smaller than the time-independent parts $\Phi_0 = -\Psi_0 \sim G\rho_{\mathrm{FDM}}\lambda_{\mathrm{dB}}^2$, where ρ_{FDM} is the local scalar field dark matter density. For cosmologically favored boson masses $\sim 10^{-22}\,\mathrm{eV}$, the frequency is fortuitously located in the sensitivity range of PTAs.

As in the case of GWs (Detweiler, 1979b), pulsar photons propagating in a time-dependent metric undergo a frequency shift $\delta\nu$, which is related to timing residuals (Khmelnitsky & Rubakov, 2014)

$$\begin{aligned} s(t) = \int_0^t \frac{\delta\nu}{\nu}dt = {} & \frac{\Psi_c(x_e)}{2\pi f}\sin[2\pi f t + 2\alpha(x_e)] \\ & - \frac{\Psi_c(x_p)}{2\pi f}\sin\left[2\pi f\left(t - \frac{L}{c}\right) + 2\alpha(x_p)\right] \\ & + \left(\frac{\Psi+\Phi}{2\pi f}\right)\mathcal{O}\left(\frac{v}{c}\right), \end{aligned} \tag{6.6}$$

where L is the distance to the pulsar and Ψ_c is the amplitude of cosine component of the oscillating part of the energy-momentum tensor. The subsequent terms in Equation (6.6) are suppressed with respect to Ψ_c by a factor $v/c \simeq 10^{-3}$, and to the leading order the signal $s(t)$ does not depend on the oscillating part of the potential Φ.

[3] In the axion context, the oscillation amplitude of ϕ gradually diminishes due to the expansion of the universe, making the quadratic $m^2\phi^2/2$ an excellent approximation to the potential in Equation (6.1).

As one can see in Equation (6.6), the dark matter signal also has 'Earth' and 'pulsar' terms. Oscillation frequencies at the Earth and at the pulsar are identical, which makes it analogous to the case of nonevolving continuous GWs (Zhu et al., 2016). The scalar-field oscillation phases on the Earth $\alpha(x_e)$ and pulsar $\alpha(x_p)$ generally take different values; but they become correlated when the Earth and a pulsar are located within the coherence de Broglie wavelength $\lambda_{\rm dB}$.

The amplitude Ψ_c, which can be effectively probed in pulsar timing experiments, depends on the local density of dark matter $\rho_{\rm FDM}$,

$$\Psi_c = \frac{G\rho_{\rm FDM}}{\pi f^2} \approx 6.1 \times 10^{-18} \left(\frac{m}{10^{-22}\,{\rm eV}}\right)^{-2} \left(\frac{\rho_{\rm FDM}}{\rho_0}\right) , \tag{6.7}$$

where $\rho_0 = 0.4\,{\rm GeV\ cm^{-3}}$ is the measured local dark matter density (Bovy & Tremaine, 2012; Read, 2014; Sivertsson et al., 2018). The rms amplitude of induced pulsar-timing residuals is

$$\delta t \approx 0.02\,{\rm ns} \left(\frac{m}{10^{-22}\,{\rm eV}}\right)^{-3} \left(\frac{\rho_{\rm FDM}}{0.4\,{\rm GeV\,cm^{-3}}}\right) . \tag{6.8}$$

The expected signal amplitude scales strongly with the boson mass. At $10^{-22}\,{\rm eV}$ and above, the signal is negligibly small. For mass below $10^{-23}\,{\rm eV}$, the induced rms residuals ($\gtrsim 20\,{\rm ns}$) are comparable to current timing precision for the best pulsars, as we discuss in Section 6.3.1.

In this work, we assume the Earth term and pulsar terms have the same amplitude Ψ_c. This is a reasonable approximation since most PPTA pulsars are relatively close ($\lesssim 1\,{\rm kpc}$) to the Earth (see Table 6.1). We discuss effects of the dark matter density variability in Section 6.5. Under this assumption, Equation (6.6) can be written into a more compact form,

$$s(t) = \frac{\Psi_c}{\pi f} \sin(\alpha_e - \theta_p) \cos(2\pi f t + \alpha_e + \theta_p) , \tag{6.9}$$

where we have defined $\alpha_e = \alpha(x_e)$ and $\theta_p = \alpha_p - \pi f L/c$ with $\alpha_p = \alpha(x_p)$. Defining θ_p this way allows us searching for a single phase parameter per pulsar. One should note, however, that the parameter pair (α_e, θ_p) is indistinguishable from $(\alpha_e \pm \pi, \theta_p \pm \pi)$.

6.3 PPTA data and noise properties

6.3.1 Observations and timing analysis

Here we provide a brief overview of the data set used in this work. The data set is available from the CSIRO pulsar data archive[4]. The observing systems and data processing techniques are similar to the first data release (DR1) as described in Manchester et al. (2013). Table 6.1 summarizes key characteristics of the PPTA data set, including the median ToA uncertainties, weighted rms values of timing residuals, data spans and the number of observations.

[4] https://doi.org/10.4225/08/5afff8174e9b3

Our data set consists of observations for 26 pulsars collected between 2004, February 5 and January 31, 2016 using the Parkes telescope. It includes DR1 data that were acquired between March 2005 and March 2011 for 20 pulsars, along with some earlier data for some pulsars that were observed in the 20-cm observing band prior to the official start of the PPTA project. Currently, the PPTA observes 25 pulsars, with PSR J1732−5049 having been removed from the pulsar sample in 2011 because we were unable to obtain high quality data sets for this pulsar. The observing cadence is normally once every two to three weeks. In each session, every pulsar was observed in three radio bands (10, 20 and 50 cm) with a typical integration time of one hour. Twenty of these pulsars were monitored for more than ten years up to twelve years; only five pulsars have data spans less than five years. For this data set, the median ToA uncertainties vary from 149 ns (PSR J0437−4715) to 4.67 μs (PSR J2124−3358); the weighted rms residuals in this data set vary from 152 ns (PSR J0437−4715) to 16.53 μs (PSR J1824−2452A). PSRs J1939+2134 and J1824−2452A were excluded from the search analysis, as they show strong evidence for a large unmodeled red-noise component[5]. For our purpose, we find these two pulsars make little contribution to the sensitivity.

During pulsar timing observations, ToAs are first referred to a local hydrogen maser frequency standard at the observatory. These ToAs are further transformed to Coordinated Universal Time (UTC) and then to a TT as published by the Bureau International des Poids et Mesures. For the current data set, we used TT(BIPM2015) and adopted the JPL DE418 (Folkner et al., 2007) SSE model to project ToAs to the solar-system barycenter. Potential errors in SSE models are accounted for in our Bayesian analysis (Section 6.4.1).

Before performing the search for dark matter signals, we fit pulsar ToAs with a timing model using the standard `TEMPO2` software package (Hobbs et al., 2006; Edwards et al., 2006). Typical parameters included in this fit are the pulsar sky location (RAJ and DecJ), spin frequency and spin-down rate, dispersion measure, proper motion, parallax and (when applicable) binary orbital parameters. Additionally, constant offsets or jumps were fitted among ToAs collected with different receiver/backend systems. Below we describe our methods to estimate the noise properties of the PPTA data.

6.3.2 The likelihood function

The likelihood function for pulsar timing residuals, marginalized over the m timing model parameters, can be written as (van Haasteren et al., 2009; van Haasteren & Levin, 2013),

$$\begin{aligned}\mathcal{L}(\boldsymbol{\vartheta}, \boldsymbol{\psi}|\delta\boldsymbol{t}) = &\frac{\sqrt{\det(M^T C^{-1} M)^{-1}}}{\sqrt{(2\pi)^{n-m}\det C}} \\ &\times \exp\left[-\frac{1}{2}(\delta\boldsymbol{t} - \boldsymbol{s}')^T C'(\delta\boldsymbol{t} - \boldsymbol{s}')\right],\end{aligned} \tag{6.10}$$

[5]This is evident as their rms residuals are much larger than the median ToA uncertainties given in Table 6.1. This may be accounted for using system- and band-specific noise terms (Lentati et al., 2016).

Jname	σ (μs)	rms (μs)	$T_{\rm obs}$ (yr)	Range	$N_{\rm obs}$	L (kpc)
J0437−4715	0.15	0.15	11.98	2004.02−2016.01	3820	0.16
J0613−0200	1.20	1.38	11.98	2004.02−2016.01	969	0.78
J0711−6830	3.29	1.58	11.98	2004.02−2016.01	1017	0.11
J1017−7156	0.97	0.76	5.54	2010.07−2016.01	524	0.26
J1022+1001	2.23	2.11	11.98	2004.02−2016.01	1008	1.13
J1024−0719	3.39	3.61	11.87	2004.02−2015.12	679	1.22
J1045−4509	3.82	3.35	11.98	2004.02−2016.01	854	0.34
J1125−6014	1.59	1.29	10.12	2005.12−2016.01	203	0.99
J1446−4701	1.81	1.47	5.19	2010.11−2016.01	161	1.57
J1545−4550	1.08	1.01	4.74	2011.05−2016.01	215	2.25
J1600−3053	0.91	0.71	11.98	2004.02−2016.01	969	1.80
J1603−7202	2.13	1.43	11.98	2004.02−2016.01	747	0.53
J1643−1224	1.75	2.96	11.98	2004.02−2016.01	713	0.74
J1713+0747	0.38	0.24	11.98	2004.02−2016.01	880	1.18
J1730−2304	2.01	1.48	11.98	2004.02−2016.02	655	0.62
J1732−5049	2.55	2.75	7.23	2004.03−2011.12	144	1.87
J1744−1134	0.68	0.61	11.98	2004.02−2016.01	855	0.40
J1824−2452A	2.67	16.5	10.36	2005.05−2015.10	339	5.50
J1832−0836	0.53	0.25	2.86	2012.11−2015.10	68	0.81
J1857+0943	2.00	1.93	11.98	2004.02−2016.01	580	1.20
J1909−3744	0.25	0.16	11.98	2004.02−2016.01	1670	1.14
J1939+2134	0.36	1.43	11.87	2004.03−2016.01	591	3.50
J2124−3358	4.67	2.52	11.98	2004.02−2016.01	889	0.41
J2129−5721	1.82	1.19	11.65	2004.06−2016.01	540	3.20
J2145−0750	1.71	1.16	11.86	2004.03−2016.01	881	0.53
J2241−5236	0.44	0.28	5.98	2010.02−2016.01	615	0.96

Table 6.1: Key characteristics of the PPTA data set: σ – median ToA uncertainty, rms – weighted root-mean-square of timing residuals, $T_{\rm obs}$ – data span and its start and end months, $N_{\rm obs}$ – number of observations, L – pulsar distance taken from the ATNF Pulsar catalogue (Manchester et al., 2005).

where $\delta\boldsymbol{t}$ is a vector of timing residuals with length n, $\boldsymbol{s}'$ is the deterministic signal vector, including the dark matter signal as described in Section 6.2 and deterministic systematics, M is the $(n \times m)$ design matrix or regression matrix of the linear model (Press et al., 1996) that describes how ToAs depend on timing model parameters[6]. The noise covariance matrix $C = C_{\rm WN}+C_{\rm SN}+C_{\rm DM}$ includes contributions from uncorrelated white noise ($C_{\rm WN}$), time-correlated spin noise ($C_{\rm SN}$) and dispersion measure variations ($C_{\rm DM}$). In Equation (6.10), we have defined $C' = C^{-1} - C^{-1}M(M^TC^{-1}M)^{-1}M^TC^{-1}$. The covariance matrix C depends on the set of noise parameters $\boldsymbol{\vartheta}$, and $\boldsymbol{\psi}$ denotes deterministic signal parameters so that $\boldsymbol{s}' = \boldsymbol{s}'(\boldsymbol{\psi})$. As a result, this form of the likelihood, which was first implemented in van Haasteren et al. (2009), depends both on $\boldsymbol{\vartheta}$ and $\boldsymbol{\psi}$, and provides the possibility of proper treatment of the signal in the presence of correlated noise and systematics. The likelihood in Equation (6.10) can be further reduced to a more compact form (see van Haasteren & Levin, 2013, for details):

$$\begin{aligned} \mathcal{L}(\boldsymbol{\vartheta}, \boldsymbol{\psi}|\delta\boldsymbol{t}) &= \frac{1}{\sqrt{(2\pi)^{n-m}\det(G^TCG)}} \\ \times \exp\left[-\frac{1}{2}(\delta\boldsymbol{t} - \mathrm{s}')^TG(G^TCG)^{-1}G^T(\delta\boldsymbol{t} - \mathrm{s}')\right], \end{aligned} \tag{6.11}$$

where the $n \times (n-m)$ dimension matrix G is obtained through the singular-value decomposition of the design matrix M. Specifically, $M = USV^*$ where U and V are unitary matrices with $n \times n$ and $m \times m$ dimension respectively, and S is an $n \times m$ diagonal matrix containing singular values of M. The G matrix is obtained such that $U = (U_1\, G)$ with U_1 and G consisting of the first m and the remaining $n-m$ columns of U respectively.

In this work, we assume that only the dark matter signal, noise processes (that will be described in the next subsection) and deterministic systematics, associated with SSE errors, contribute to the data. We neglect errors in terrestrial time standards and other common noise processes (such as a stochastic GW background). Therefore, the likelihood function for the full PTA can be expressed as a product:

$$\mathcal{L}(\boldsymbol{\vartheta}, \boldsymbol{\psi}|\delta\boldsymbol{t}) = \prod_{i=1}^{N_p} \mathcal{L}(\boldsymbol{\vartheta}_i, \boldsymbol{\psi}_i|\delta\boldsymbol{t}_i)\,, \tag{6.12}$$

where N_p is the number of pulsars in the timing array.

6.3.3 Noise modeling

For each pulsar in the PPTA data set, we estimate its noise properties using both Bayesian and Frequentist approaches. We present a general description of possible noise sources here.

Stochastic noise processes can be divided into the time-correlated and uncorrelated components. The uncorrelated (white) noise is represented by the uncertainties of the measured ToAs derived through cross-correlation of the pulsar template and the

[6] It can be obtained with the `TEMPO2 designmatrix` plugin.

integrated profile. However, it is common that ToA uncertainties underestimate the white noise present in pulsar timing data. This might be caused by, e.g. radio frequency interference, pulse profile changes or instrumental artifacts. Two parameters, namely, `EFAC` (Error FACtor) and `EQUAD` (Error added in QUADrature), are included to account for excess white noise. They are introduced for each observing system used in the data set. Following standard conventions, different parameterizations are used for `EFAC` and `EQUAD`. In `TEMPO2` and for our Frequentist analysis, the re-scaled ToA uncertainties (σ_s) are related to their original values (σ) by

$$\sigma_s^2 = \texttt{T2EFAC}^2(\sigma^2 + \texttt{T2EQUAD}^2). \tag{6.13}$$

In Bayesian analysis, we use the following relation

$$\sigma_s^2 = (\texttt{EFAC}\,\sigma)^2 + \texttt{EQUAD}^2. \tag{6.14}$$

Numerous studies (Boynton et al., 1972; Blandford et al., 1984; Hobbs et al., 2010b) have found evidence for additional low-frequency noise in pulsar timing data. This time-correlated stochastic process is dominated by two components: *achromatic* (i.e independent of radio frequency) spin noise and *chromatic* (i.e dependent on radio frequency) such as DM variations. The former is intrinsic to the pulsar and might be related to pulsar rotational instabilities. The latter is associated with the interstellar medium which introduces time delays in pulsar ToAs. As pulsar travels in the tangent plane, the line of sight intersects spatially variable interstellar medium characterized by different column electron densities. For current receivers, the bandpass is generally not broad enough to resolve these kind of variations in each individual observation. Therefore, a typical strategy is to observe pulsars at widely separated radio bands, allowing the correction of DM variations.

Below we discuss details of noise modeling in the Bayesian and Frequentist frameworks.

6.3.3.1 Bayesian framework

The Bayesian framework provides a consistent approach to the estimation of a set of parameters $\boldsymbol{\Theta}$ by updating the initial distribution of those parameters $P_{\rm pr}(\boldsymbol{\Theta})$ as more information becomes available. Bayes' theorem states:

$$P_{\rm pst}(\boldsymbol{\Theta}|\boldsymbol{D}) = \frac{\mathcal{L}(\boldsymbol{\Theta}|\boldsymbol{D})P_{\rm pr}(\boldsymbol{\Theta})}{Z}, \tag{6.15}$$

where $P_{\rm pst}(\boldsymbol{\Theta}|\boldsymbol{D})$ stands for the posterior (or updated) distribution of the parameters $\boldsymbol{\Theta}$, given the data (or external information) $\boldsymbol{D}$, $\mathcal{L}(\boldsymbol{\Theta}|\boldsymbol{D})$ is the likelihood function, and Z is known as Bayesian evidence and defined as:

$$Z = \int \mathcal{L}(\boldsymbol{\Theta}|\boldsymbol{D})P_{\rm pr}(\boldsymbol{\Theta})d^n(\boldsymbol{\Theta}) \tag{6.16}$$

The Bayesian evidence is a normalizing factor for parameter estimation problem and is a key criterion for model selection and decision making. Here Z does not depend

on $\boldsymbol{\Theta}$ and it holds that $P_{\rm pst}(\boldsymbol{\Theta}|\boldsymbol{D}) \propto \mathcal{L}(\boldsymbol{\Theta}|\boldsymbol{D})P_{\rm pr}(\boldsymbol{\Theta})$. When applied for the case of PTAs, data $\boldsymbol{D}$ includes an array of pulsar timing ToAs $\delta\boldsymbol{t}$, $\boldsymbol{\Theta}$ includes $[\boldsymbol{\vartheta}, \boldsymbol{\psi}]$ and the likelihood $\mathcal{L}(\boldsymbol{\Theta}|\boldsymbol{D})$ is given by Equation (6.10). The set of parameters, used for the Bayesian analysis, and the corresponding priors are described in Table 6.2.

For computational purposes, the noise covariance matrix C from Equation (6.10) can be split as a sum of a diagonal matrix $C_{\rm WN}$ and a large dense matrix $K = C_{\rm SN} + C_{\rm DM} = F\Phi F^T$, where $\Phi = \Phi_{\rm SN} + \Phi_{\rm DM}$ is the diagonal matrix $(2k \times 2k)$, $k << n$, where k is the number of terms in the approximation sum. By using the Woodbury matrix lemma[7] (William, 1989), the computationally heavy inversion of covariance matrix C, involving $\mathcal{O}(n^3)$ operations, is reduced to lower rank diagonal matrix inversion Φ^{-1}. More details on this technique can be found in (Arzoumanian et al., 2014; van Haasteren & Vallisneri, 2015).

In this work we have used the so-called "Fourier-sum" prescription (or "time-frequency" method), introduced in Lentati et al. (2013). In this case, the Fourier transform matrix $\boldsymbol{F}$ for achromatic processes can be written as:

$$\begin{aligned} \boldsymbol{F} &= (\boldsymbol{F^s F^c}), \\ F^s_{ji} = \sin(2\pi\nu_i t_j), F^c_{ji} &= \cos(2\pi\nu_i t_j)\,, \end{aligned} \tag{6.17}$$

where $\nu_i = i/T$, where T is the whole timespan of the PPTA data set, 11.98 years. The dimensionality of the Fourier matrix $\boldsymbol{F}$ is $(n \times 2k)$, where k is number of frequency components, which in our case is 30. The noise vector for a specific noise process can be expressed as $\tau_j = \sum_i F_{ji}a_i = \sum_i a^s_i \sin 2\pi\nu_i t_j + a^c_i \cos 2\pi\nu_i t_j$, where $\boldsymbol{a} = (\boldsymbol{a^s}, \boldsymbol{a^c})$ is the vector of Fourier coefficients.

The covariance matrix of Fourier coefficients Φ can be derived from the covariance matrix of the theoretical power spectrum of a specific type of noise. Within Bayesian framework, we use the following parametrization for power-law noise:

$$P(f) = \frac{A^2}{12\pi^2}\mathrm{yr}^3\left(\frac{f}{\mathrm{yr}^{-1}}\right)^{-\gamma}. \tag{6.18}$$

Therefore, the elements of the matrix Φ, which are identical for both spin and DM noises, are expressed as:

$$\Phi_{ij} = \frac{A^2}{12\pi^2}\frac{\nu_i^{-\gamma}}{T}\mathrm{yr}^3\delta_{ij}\,, \tag{6.19}$$

where i, j iterates over different Fourier frequencies and δ_{ij} is a Kronecker delta. If multiband observations are available, the degeneracy between the spin noise and DM contributions can be broken, because of the dependency of the amplitude of the DM variations on the observational frequency f_o. This dependency enters in the Fourier transform matrix as:

$$\begin{aligned} \boldsymbol{F}_{\rm DM} &= (\boldsymbol{F^s}_{\rm DM}\boldsymbol{F^c}_{\rm DM}), \\ F^s_{{\rm DM},ji} = \frac{\sin(2\pi\nu_i t_j)}{K f^2_{o,j}}, F^c_{{\rm DM},ji} &= \frac{\cos(2\pi\nu_i t_j)}{K f^2_{o,j}}\,, \end{aligned} \tag{6.20}$$

[7] $(N + F\Phi F^T)^{-1} = N^{-1} - N^{-1}F(\Phi^{-1} + F^T N^{-1}F)^{-1}F^T N^{-1}$

Table 6.2: List of parameters and prior distributions used for the Bayesian analysis. U and log-U stand for uniform and log-uniform priors, respectively.

Parameter	Description	Prior	Comments
	Noise parameters ($\boldsymbol{\vartheta}$)		
`EFAC`	White-noise modifier per backend	U[0, 10]	fixed for setting limits
`EQUAD`	Additive white noise per backend	log-U[−10, −4]	fixed for setting limits
$A_{\rm SN}$	Spin-noise amplitude	log-U[−20, −11] (search) U[10^{-20}, 10^{-11}] (limit)	one parameter per pulsar
γ_{SN}	Spin-noise spectral index	U[0, 7]	one parameter per pulsar
A_{DM}	DM-noise amplitude	log-U[−20, −6.5] (search) U[10^{-20}, $10^{-6.5}$] (limit)	one parameter per pulsar
γ_{DM}	DM-noise spectral index	U[0, 7]	one parameter per pulsar
	Signal parameters ($\boldsymbol{\psi}$)		
Ψ_c	Oscillation amplitude	log-U[−20, −12] (search) U[10^{-20}, 10^{-12}] (limit)	one parameter per PTA
$\alpha_{\rm e}$	Oscillation phase on Earth	U[0, 2π]	one parameter per PTA
$\theta_{\rm p}$	$\theta_p = \alpha_p - \pi f L/c$	U[0, 2π]	one parameter per pulsar
f (Hz)	Oscillation frequency	log-U[−9, −7]	delta function for setting limits
	`BayesEphem` parameters ($\boldsymbol{\psi}^{\rm sys}$)		
$z_{\rm drift}$	Drift-rate of Earth's orbit about ecliptic z-axis	U[-10^{-9}, 10^{-9}] rad yr^{-1}	one parameter per PTA
$\Delta M_{\rm jupiter}$	Perturbation of Jupiter's mass	$\mathcal{N}(0, 1.5\times10^{-11})M_\odot$	one parameter per PTA
$\Delta M_{\rm saturn}$	Perturbation of Saturn's mass	$\mathcal{N}(0, 8.2\times10^{-12})M_\odot$	one parameter per PTA
$\Delta M_{\rm uranus}$	Perturbation of Uranus' mass	$\mathcal{N}(0, 5.7\times10^{-11})M_\odot$	one parameter per PTA
$\Delta M_{\rm neptune}$	Perturbation of Neptune's mass	$\mathcal{N}(0, 7.9\times10^{-11})M_\odot$	one parameter per PTA
PCA_i	Principal components of Jupiter's orbit	U[−0.05, 0.05]	six parameters per PTA

where $K = 2.41 \times 10^{-16}\,\mathrm{Hz}^{-2}\,\mathrm{cm}^{-3}\,\mathrm{pc\ s}^{-1}$ and $f_{o,j}$ is the radio observing frequency at time t_j. Using this terminology, the time delay δt between signal received at radio frequency f_0 and one received at $f \to \infty$ is given by $\delta t = K^{-1} f_0^{-2}\mathrm{DM} = 4.15 \times 10^6 f_0^{-2}\mathrm{DM\,ms}$. Note that the linear and quadratic trends in DM variations get absorbed by timing model parameters DM1 and DM2, which are included in the Bayesian timing model. The inclusion of the DM derivatives in our analysis absolves us from the spectral leakage problem (Lentati et al., 2014).

The formalism, described in this subsection, was implemented in a range of publicly available codes. For the single pulsar analysis we have used `PAL2` Software – a package for the Bayesian processing of the pulsar timing data. Efficient sampling from the posteriors is performed by the Bayesian inference tool `MULTINEST` (Feroz et al., 2009), running in constant efficiency mode, a computational technique that allows one to maintain the user-defined sampling efficiency for high-dimensional problems (see Feroz et al., 2013, for more details). For each PPTA pulsar we perform separately a full noise modeling analysis, simultaneously including all stochastic components discussed above. The noise parameters $\boldsymbol{\vartheta}$, estimated within single pulsar analysis, are given in Table 6.3. The marginalized posterior probabilities for the six most sensitive pulsars in PPTA (see Section 6.4.1) are presented in Appendix B.

As was shown in Keith et al. (2013) and Coles et al. (2015), and later confirmed in Lentati et al. (2016), data for PSR J1603−7202 and PSR J1713+0747 show significant evidence for non-stationary ESEs, which are usually associated with the passage of high density plasma blobs along the line of sight of a pulsar. ESEs are modeled as deterministic signals $t_{\mathrm{ESE,i}}$ (Lentati et al., 2016):

$$t_{\mathrm{ESE},i} = \frac{\mathcal{S}(t_i, \boldsymbol{A}_{\mathrm{ESE}}, \mathcal{W})}{K f_{o,i}^2}\,, \tag{6.21}$$

by making use of shapelet basis function expansion:

$$\begin{aligned} \mathcal{S}(t, \boldsymbol{A}_{\mathrm{ESE}}, \mathcal{W}) &= \sum_{j=0}^{j_{\max}} A_{\mathrm{ESE,j}} B_j(t, \mathcal{W})\,, \\ B_j(t, \mathcal{W}) &= [2^j j! \mathcal{W}\sqrt{\pi}]^{-1/2} H_j\left(\frac{t-t_0}{\mathcal{W}}\right) \exp\left[-\frac{(t-t_0)^2}{2\mathcal{W}^2}\right]\,, \end{aligned} \tag{6.22}$$

where t_0 is the epoch of ESE, $\mathcal{W}$ stands for the characteristic length scale of ESE, H_j is the j-th Hermitian polynomial, $j_{\max}$ is the number of terms used in the expansion, which is 3 in our case, $\boldsymbol{A}_{\mathrm{ESE}}$ is a vector of shapelet amplitudes. The inclusion of non-stationary ESEs in the noise model (see Table 6.3) leads to smaller DM spectral amplitudes A_{DM} and slightly steeper slopes, characterised by γ_{DM}, which is consistent with results presented in Lentati et al. (2016).

6.3.3.2 Frequentist methods

In the Frequentist framework, we use the method that was originally introduced in You et al. (2007a) and further improved in Keith et al. (2013) for correcting DM variations.

The basic idea works as follows. Timing residuals are separated into two components, one dependent on the radio wavelength, namely, dispersion measure variations DM(t), and the other independent of the radio wavelength. The latter could contain red noise, GWs or dark matter signals. Since pulsar timing data are irregularly sampled, we use a linear interpolation scheme to estimate DM(t) at regular intervals. For the PPTA data, we estimate one DM(t) every 60-180 days using observations taken at three bands (10, 20, 50 cm). The time epochs and the estimated DM offsets are stored as `DMOFF` parameters in the `TEMPO2 .par` files. We model the red spin noise on data that have been corrected for DM variations, in which case, the noise covariance matrix contains only the white noise and spin noise terms.

Following the `TEMPO2` convention, for our Frequentist analysis the intrinsic spin noise is parameterized using the following power-law spectrum

$$P(f) = \frac{P_0}{\left[1 + \left(\frac{f}{f_c}\right)^2\right]^{\alpha/2}}, \tag{6.23}$$

where P_0 is an overall amplitude (normally expressed in yr^3), f_c is the so-called corner frequency, α is the power-law exponent. The covariance matrix for such a red noise process is given by

$$\begin{aligned} \mathcal{C}(\tau) &= \int_0^\infty P(f)\cos\tau f \mathrm{d}f \\ &= \frac{2^{(1-\alpha)/2}}{f_c^{-(1+\alpha)/2}} \frac{P_0\sqrt{\pi}\tau^{(\alpha-1)/2} J_{\frac{1-\alpha}{2}}\left(f_c\tau\right)}{\Gamma\left(\frac{\alpha}{2}\right)}, \end{aligned} \tag{6.24}$$

where $\tau = 2\pi|t_i - t_j|$ with t_i and t_j being the ToA at the i-th and j-th observation respectively, J is the modified Bessel function of second kind and Γ is the Gamma function.

We follow the method described in Coles et al. (2011) to estimate red noise properties iteratively. We fit a power-law model of the form given by Equation (6.23) to the power spectrum of timing residuals, leading to an initial estimate of the noise covariance matrix. We then use the Cholesky decomposition of this matrix to transform the data. The power spectrum of the transformed residuals should be white. We repeat the above procedure to obtain improved estimates of the spectrum. The iteration is considered converged if the whitened data show a sufficiently flat spectrum for which the spectral leakage is not dominant. The results are usually validated with simulations. We list our best estimates of red noise parameters in Table 6.3.

6.4 Search techniques and Results

6.4.1 Bayesian analysis

Within a Bayesian framework, the signal detection problem is addressed through model selection. Given the observational data, we wish to choose between two mutually exclusive hypotheses: the null hypothesis $\mathcal{H}_0$ that the signal is absent and the alternative

Table 6.3: Noise properties of PPTA pulsars, determined through Bayesian and Frequentist analyses. The comparison of the results for intrinsic spin noise determined via two methods, can be performed when $f_c T \ll 1$, such as $P_0 \to A_{\rm SN}^2/(12\pi^2 f_c^2)$. Dashed lines indicate either that noise parameters are not constrained, i.e., flat posterior probabilities (Bayesian) or that no spin noise is detected (Frequentist). In the two note columns, C is for "constrained" distributions, whereas SC stands for 'semiconstrained' distributions which exhibit long tails and significant deviation from Gaussianity (possibly due to correlation with other parameters); See Figure B.1 in Appendix B for illustrations. The last two rows list results when parameters for non-stationary ESEs are included. Only pulsars with a † symbol next to their names are used for setting Bayesian upper limits.

Pulsar Name	Bayesian						Frequentist		
	$\log 10(A_{SN})$	γ_{SN}	*note*	$\log 10(A_{DM})$	γ_{DM}	*note*	α	$f_c(\mathrm{yr}^{-1})$	$P_0(\mathrm{yr}^3)$
J0437−4715†	$-13.96^{+0.05}_{-0.05}$	$2.0^{+0.2}_{-0.2}$	C	$-10.90^{+0.04}_{-0.04}$	$3.2^{+0.2}_{-0.2}$	C	3.5	0.08	2.37×10^{-27}
J0613−0200	$-16.89^{+1.9}_{-1.9}$	$3.4^{+2.0}_{-2.0}$	SC	$-10.62^{+0.05}_{-0.05}$	$2.1^{+0.3}_{-0.3}$	C	2.5	0.08	1.30×10^{-26}
J0711−6830	$-14.1^{+0.5}_{-0.4}$	$4.2^{+1.2}_{-1.1}$	C	$-12.1^{+0.8}_{-1.7}$	$3.9^{+1.6}_{-1.7}$	SC	4.0	0.08	3.98×10^{-26}
J1017−7156	$-13.5^{+0.3}_{-0.6}$	$3.6^{+1.9}_{-1.5}$	C	$-10.12^{+0.06}_{-0.06}$	$3.2^{+0.4}_{-0.4}$	C	6.0	1.0	9.54×10^{-28}
J1022+1001	$-16.9^{+2.4}_{-1.7}$	$2.9^{+2.1}_{-2.0}$	SC	$-11.3^{+0.3}_{-0.4}$	$3.2^{+1.2}_{-0.8}$	C	2.0	0.08	3.04×10^{-26}
J1024−0719	$-14.6^{+0.4}_{-0.5}$	$6.1^{+0.6}_{-0.9}$	SC	$-11.6^{+0.4}_{-0.6}$	$4.2^{+1.3}_{-1.2}$	C	3.0	0.08	4.30×10^{-25}
J1045−4509	$-12.85^{+0.2}_{-0.5}$	$2.0^{+1.1}_{-0.6}$	C	$-9.73^{+0.04}_{-0.04}$	$2.8^{+0.3}_{-0.3}$	C	3.0	0.3	7.44×10^{-27}
J1125−6014	$-14.5^{+0.4}_{-0.4}$	$6.0^{+0.7}_{-0.7}$	C	$-11.6^{+0.5}_{-0.5}$	$4.3^{+1.1}_{-1.2}$	C	3.0	0.2	5.79×10^{-27}
J1446−4701	...	...		...	...		...	...	...
J1545−4550	...	...		$-10.8^{+0.3}_{-0.4}$	$4.6^{+1.3}_{-1.3}$	C	3.0	0.1	1.66×10^{-26}
J1600−3053†	$-16.8^{+1.7}_{-1.9}$	$3.3^{+2.1}_{-1.9}$	SC	$-10.6^{+0.08}_{-0.09}$	$2.7^{+0.3}_{-0.3}$	C	2.0	0.08	1.05×10^{-27}
J1603−7202	$-13.3^{+0.2}_{-0.5}$	$2.4^{+1.2}_{-0.7}$	C	$-10.20^{+0.05}_{-0.05}$	$2.5^{+0.3}_{-0.3}$	C	3.0	0.08	8.39×10^{-26}
J1643−1224	$-12.40^{+0.05}_{-0.05}$	$1.5^{+0.4}_{-0.3}$	C	$-9.81^{+0.04}_{-0.04}$	$1.6^{+0.3}_{-0.3}$	C	1.5	0.08	3.43×10^{-26}
J1713+0747	$-13.5^{+0.1}_{-0.1}$	$2.4^{+0.3}_{-0.3}$	C	$-10.79^{+0.07}_{-0.06}$	$1.7^{+0.3}_{-0.3}$	C	...	...	...
J1730−2304	$-17.2^{+1.7}_{-1.7}$	$3.2^{+2.0}_{-2.0}$	C	$-11.2^{+0.3}_{-0.4}$	$3.6^{+0.9}_{-0.7}$	C	2.0	0.08	2.17×10^{-26}
J1732−5049	$-16.1^{+2.3}_{-2.3}$	$3.3^{+2.1}_{-1.9}$	SC	$-10.6^{+0.6}_{-5.7}$	$3.2^{+1.7}_{-1.3}$	SC	...	...	...
J1744−1134†	$-13.33^{+0.06}_{-0.06}$	$1.2^{+0.3}_{-0.3}$	SC	$-11.5^{+0.3}_{-0.5}$	$3.3^{+1.2}_{-0.7}$	SC	6.0	1.0	2.55×10^{-28}
J1824−2452A	$-12.60^{+0.07}_{-0.12}$	$3.7^{+1.4}_{-0.4}$	SC	$-9.74^{+0.07}_{-0.06}$	$2.5^{+0.4}_{-0.4}$	C	4.0	0.1	1.22×10^{-23}
J1832−0836	...	...		...	...		...	...	...
J1857+0943	$-15.1^{+1.1}_{-2.4}$	$4.0^{+1.7}_{-2.0}$	SC	$-10.6^{+0.1}_{-0.2}$	$2.3^{+0.5}_{-0.5}$	C	...	...	...
J1909−3744†	$-14.5^{+0.5}_{-0.7}$	$2.4^{+1.1}_{-0.8}$	C	$-11.09^{+0.04}_{-0.04}$	$1.6^{+0.3}_{-0.2}$	C	2.5	0.07	7.54×10^{-28}
J1939+2134	$-13.34^{+0.1}_{-0.2}$	$3.2^{+0.6}_{-0.4}$	C	$-10.25^{+0.04}_{-0.04}$	$3.1^{+1.8}_{-1.5}$	C	4.0	0.08	2.50×10^{-25}
J2124−3358	...	...		$-11.9^{+0.9}_{-4.5}$	$2.8^{+0.9}_{-0.9}$	SC	5.0	1.0	5.64×10^{-27}
J2129−5721	$-16.9^{+1.8}_{-1.8}$	$3.2^{+2.0}_{-2.0}$	SC	$-10.9^{+0.1}_{-0.1}$	$2.3^{+0.5}_{-0.5}$	C	2	0.08	1.37×10^{-26}
J2145−0750	$-13.04^{+0.06}_{-0.06}$	$1.4^{+0.2}_{-0.2}$	C	$-11.1^{+0.2}_{-0.2}$	$2.9^{+0.6}_{-0.6}$	C	1.0	0.08	5.13×10^{-27}
J2241−5236†	$-13.48^{+0.08}_{-0.1}$	$1.4^{+0.6}_{-0.5}$	C	$-12.8^{+1.0}_{-4.8}$	$3.9^{+2.1}_{-2.4}$	SC	...	...	...
Including extreme scattering events									
J1603−7202	$-13.3^{+0.2}_{-0.2}$	$2.3^{+0.5}_{-0.6}$	C	$-10.55^{+0.08}_{-0.08}$	$2.6^{+0.3}_{-0.3}$	C			
J1713+0747†	$-13.50^{+0.08}_{-0.08}$	$2.3^{+0.3}_{-0.3}$	C	$-11.2^{+0.1}_{-0.1}$	$2.5^{+0.4}_{-0.4}$	C			

hypothesis $\mathcal{H}_1$ that the signal is present. We compute the evidences $\mathcal{Z}$, defined in Equation (6.16), of the two hypotheses, $\mathcal{H}_0$ and $\mathcal{H}_1$. Assuming a priori equal probability for both hypotheses, the following evidence ratio (commonly called Bayes factor) quantifies the support of $\mathcal{H}_1$ against $\mathcal{H}_0$

$$\mathcal{B} = \frac{\mathcal{Z}_1}{\mathcal{Z}_0} = \frac{\int \mathcal{L}(\boldsymbol{\vartheta}, \boldsymbol{\psi}, \boldsymbol{\psi}^{\rm sys}|\delta\boldsymbol{t}) P_{\rm pr}(\boldsymbol{\vartheta}, \boldsymbol{\psi}, \boldsymbol{\psi}^{\rm sys}) {\rm d}\boldsymbol{\vartheta} {\rm d}\boldsymbol{\psi}^{sys} {\rm d}\boldsymbol{\psi}}{\int \mathcal{L}(\boldsymbol{\vartheta}, \boldsymbol{\psi}^{\rm sys}|\delta\boldsymbol{t}) P_{\rm pr}(\boldsymbol{\vartheta}, \boldsymbol{\psi}^{\rm sys}) {\rm d}\boldsymbol{\vartheta} {\rm d}\boldsymbol{\psi}^{\rm sys}}, \tag{6.25}$$

where $\boldsymbol{\psi}^{\rm sys}$ are the parameters of the deterministic systematics, SSE errors in our case, which should be distinguished from dark matter signal parameters $\boldsymbol{\psi}$. In order to obtain accurate evidence estimates, we carry out numerical integration via `MULTINEST` with enabled importance nested sampling in constant efficiency mode. With the current PPTA data, we find a log Bayes factor $\ln \mathcal{B}$ of 2.1 in the frequency range $[10^{-9}, 8 \times 10^{-8}]$ Hz, implying that our data are consistent with containing only noise. When we extend the search frequency to 10^{-7} Hz, the signal hypothesis is favored against the null hypothesis with $\ln \mathcal{B} = 70$. We suspect this is caused by the unmodeled perturbations of the mass and orbital elements of Mercury, for which the synodic period is ~ 116 days, corresponding to a frequency of 10^{-7} Hz. We defer the investigation of this feature to a future work.

In order to set an upper limit on the signal amplitude within the Bayesian framework, we perform the parameter estimation routine. By sampling from the posterior probabilities of model parameters, we can numerically marginalize over nuisance parameters, and get the posterior distribution for the amplitude Ψ_c. We define the 95% Bayesian upper limit $\bar{\Psi}_c$, such that 95% of the samples from the posterior probability lie within the range $[0, \bar{\Psi}_c]$:

$$\begin{aligned} 0.95 \quad = \quad & \int_0^{\bar{\Psi}_c} {\rm d}\Psi_c \int {\rm d}\boldsymbol{\psi}' {\rm d}\boldsymbol{\vartheta} \mathcal{L}(\Psi_c, \boldsymbol{\psi}', \boldsymbol{\vartheta}|\delta\boldsymbol{t}) P_{\rm pr}(\Psi_c) \\ & P_{\rm pr}(\boldsymbol{\psi}') P_{\rm pr}(\boldsymbol{\vartheta}). \end{aligned} \tag{6.26}$$

We split the frequency range between 10^{-9} and 10^{-7} Hz into a number of small bins and find $\bar{\Psi}_c$ for each bin separately.

To reduce the computational costs of numerical marginalization, a common practice is to fix the noise model parameters to their maximum likelihood values (Babak et al., 2016; Arzoumanian et al., 2014), determined from single pulsar analysis. However such a procedure can possibly lead to upper limits biased by a factor of $\lesssim 2$ (Arzoumanian et al., 2014). In this work we allow both signal and correlated noise parameters to vary simultaneously. The white noise EFACs and EQUADs, which should have little or no correlation with dark matter parameters, are fixed to the maximum-likelihood values obtained from single pulsar analysis.

Recently, it was shown that the search for a stochastic GW background can be seriously affected by the uncertainties in the SSE (Arzoumanian et al., 2018b; Tiburzi et al., 2016). We employ a physical model `BayesEphem` to account for the SSE uncertainties that are most relevant for pulsar timing. The `BayesEphem` model has 11 parameters, including 4 parameters which describe the perturbations in the masses of

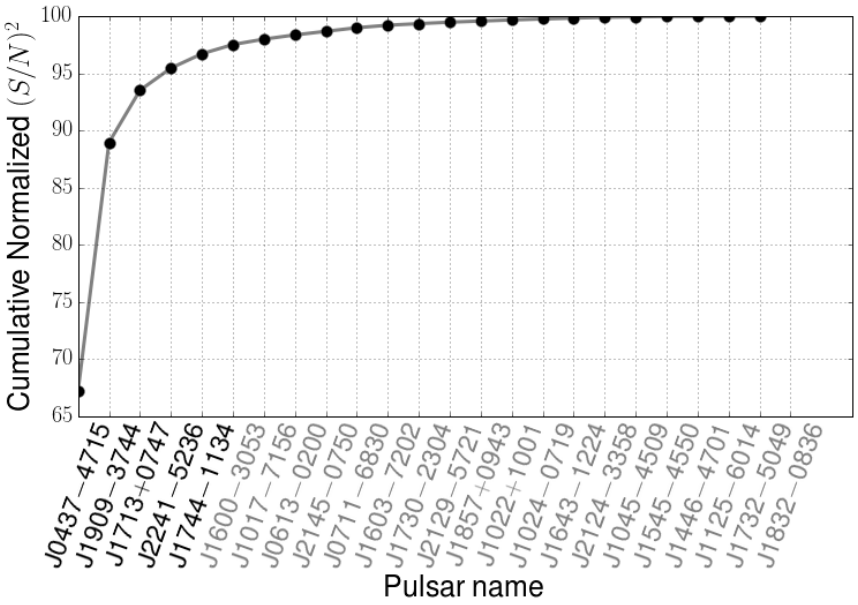

Figure 6.1: Cumulative normalized $(S/N)^2$. The pulsars are ranked according to their contribution to the PPTA sensitivity between $5 \times 10^{-9} - 2 \times 10^{-8}$ Hz (see text for details).

outer planets, 1 parameter which is associated with the uncertainty in the semi-major axis of Earth-Moon barycenter orbit, and 6 parameters that characterize the perturbation of the Earth's orbit due to errors in the Jovian average orbital elements. The `BayesEphem` modeling technique is described in Arzoumanian et al. (2018b) in detail, and implemented in publicly available software packages, such as `enterprise` and `NX01`. The latter was used to put robust constrains on the amplitude of the FDM in this work.

The number of free parameters for the PPTA data set is $5 \times N_p + 3 + 11 = 144$ (see Table 6.2), where N_p is the number of pulsars in PTA. In order to further reduce the computational costs, we have formed the "restricted data set" by choosing the five best pulsars. As shown in Figure 6.1, they contribute to more than 95% sensitivity of the full PPTA. Here pulsars are ranked according to their contribution to the squared signal-to-noise ratio $(S/N)^2$; see Equation (6.29) in the next section. We carry out the calculations by adding detectable signals to 1000 noise realizations, sampled from individual pulsar noise posterior distribution obtained in Section 6.3.3.1.

6.4.1.1 Validation of the search results

In order to validate our upper limits and test the robustness of our algorithms, we have injected a signal with $f = 2 \times 10^{-9}$ Hz and amplitude $\Psi_c = 10^{-14}$ into our restricted data set. At this frequency, the amplitude of the injected signal is comparable to the Bayesian upper limit. In order to recover this signal we run the full Bayesian analysis, simultaneously accounting for both dark matter signal and noise. The posterior probabilities are demonstrated in Figure 6.2, indicating successful recovery of the injected

signal.

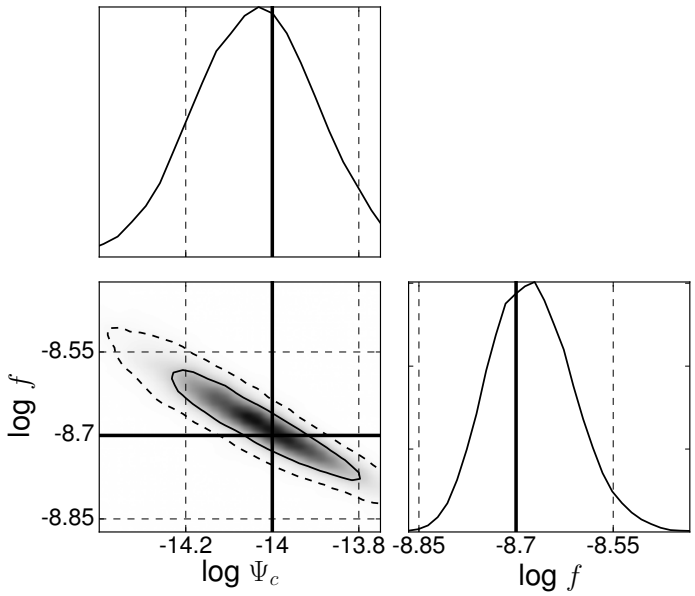

Figure 6.2: The marginalized posterior distributions for the amplitude Ψ_c and frequency f for a signal injection in the actual PPTA data. The thick black lines mark the injected values and the contours are 1- and 2-σ credible regions.

6.4.2 Frequentist analysis

In a Frequentist framework, signal detection is essentially a statistical hypothesis testing problem; we wish to choose between the null hypothesis $\mathcal{H}_0$ and the signal hypothesis $\mathcal{H}_1$ based on the observations. The task is to find an optimal statistic that maximizes the signal detection probability at a fixed false alarm probability. Following the Neyman-Pearson criterion, the log-likelihood ratio is an optimal statistic

$$\ln \Lambda \equiv \ln \frac{\mathcal{L}(\mathcal{H}_1|\delta\mathbf{t})}{\mathcal{L}(\mathcal{H}_0|\delta\mathbf{t})} = \sum_{i=1}^{N_p} \left[(\delta\mathbf{t}_i|\mathbf{s}_i) - \frac{1}{2}(\mathbf{s}_i|\mathbf{s}_i) \right] , \tag{6.27}$$

where we have used Equations (6.11)-(6.12) to derive the second equality above, and the inner product between two time series $\mathbf{x}$ and $\mathbf{y}$ is defined as

$$(\mathbf{x}|\mathbf{y}) = \mathbf{x}^T G (G^T C G)^{-1} G^T \mathbf{y} \, . \tag{6.28}$$

It is useful to define the signal-to-noise ratio in the following form

$$\mathrm{S/N} = \sqrt{2\langle \ln \Lambda \rangle} = \left[\sum_{i=1}^{N_p} (\mathbf{s}_i|\mathbf{s}_i) \right]^{1/2} , \tag{6.29}$$

where $\langle ... \rangle$ stands for the expectation value over a large number of noise realizations. In this work, we adopt $2 \ln \Lambda$ as our detection statistic. For our Frequentist analysis, noise model parameters are fixed at their maximum likelihood values. The signal parameters in question are: the amplitude of dark matter induced gravitational-potential oscillations Ψ_c, oscillation frequency f, phase parameters α_e and θ_p; see Equation (6.9). It turns out that the statistic can be analytically maximized over Ψ_c and thus the parameter space that needs to be numerically searched over is $N_p + 2$ dimensional. For our data this corresponds to 28 dimensions, making a grid-based search unfeasible. We employ the Particle Swarm Optimization technique (Eberhart & Kennedy, 1995), which has been demonstrated to be very effective for searches for continuous GWs with PTAs (Wang et al., 2015b; Zhu et al., 2016). The detection statistic follows a χ^2 distribution with one degree of freedom for noise-only data.

Since we find no evidence for statistically significant signals in the data, which is consistent with results from the Bayesian analysis as described in the previous subsection, we set upper limits on the dimensionless amplitude Ψ_c. We compute the 95% confidence upper limits for a number of frequency bins between 10^{-9} and 10^{-7} Hz. At each frequency, we compute the S/N for 10^3 simulated signals with random phase parameters and a fixed Ψ_c. The 95% confidence upper limit on $\bar{\Psi}_c$ corresponds to the amplitude at which 95% of signals result in S/N $\geq$ 2.4. Here the S/N threshold is chosen such that the expectation value for our detection statistic in the presence of signals, given by $1 + (\mathrm{S/N})^2$, is greater than the detection threshold that corresponds to 1% false alarm probability. It implies that: if there was a signal with an amplitude higher than $\bar{\Psi}_c$ present in the data, it would have been detectable with more than 95% probability.

6.4.3 Upper limits

Figure 6.3 shows the 95% upper limits on the amplitude Ψ_c, calculated within Bayesian (black solid line) and frequentist frameworks (purple solid line). As one can see, Bayesian upper limits are a factor of 2−3 worse than frequentist upper limits in the low-frequency regime, while in the mid-to-high frequency range both methods produce comparable results. The difference might be predominantly attributed to the covariance between signal and noise (especially the red spin noise). Frequentist upper limits were calculated by fixing noise parameters at their maximum likelihood values, whereas we search simultaneously over signal and noise parameters in the Bayesian analysis.

The Bayesian upper limits, obtained with 5-year NANOGrav data set (Demorest et al., 2013), are also plotted as the thin dash-dotted (taken from Porayko & Postnov, 2014) and dashed (recalculated in this paper) lines. We note that upper limits presented in Porayko & Postnov (2014) were underestimated by a factor of 10 due to the less conservative[8] choice of prior (log-uniform) probability of the amplitude Ψ_c, as well as the noninclusion of DM variations and additional white noise terms (`EFAC` and `EQUAD`). From Figure 6.3, one can see that our data set is a factor of 5 more sensitive to the dark

[8] We note that uniform priors result in upper limits that are a factor of ~ 5 higher than log-uniform priors.

matter signal than NANOGrav 5-year data at low frequencies, corresponding to boson masses $m \lesssim 10^{-23}$ eV. In the intermediate regime, the improvement is about a factor of 2. This is expected because of our much longer data span and higher observing cadence. It is interesting to note that the upper limit curves in Figure 6.3 exhibit similar frequency dependencies to the sky-averaged upper limits for continuous GWs (see e.g. Zhu et al., 2014). In Appendix A, we present Frequentist upper limits obtained by including in the analysis only Earth terms. We also show how Bayesian upper limits are modified if different fixed SSE models are used.

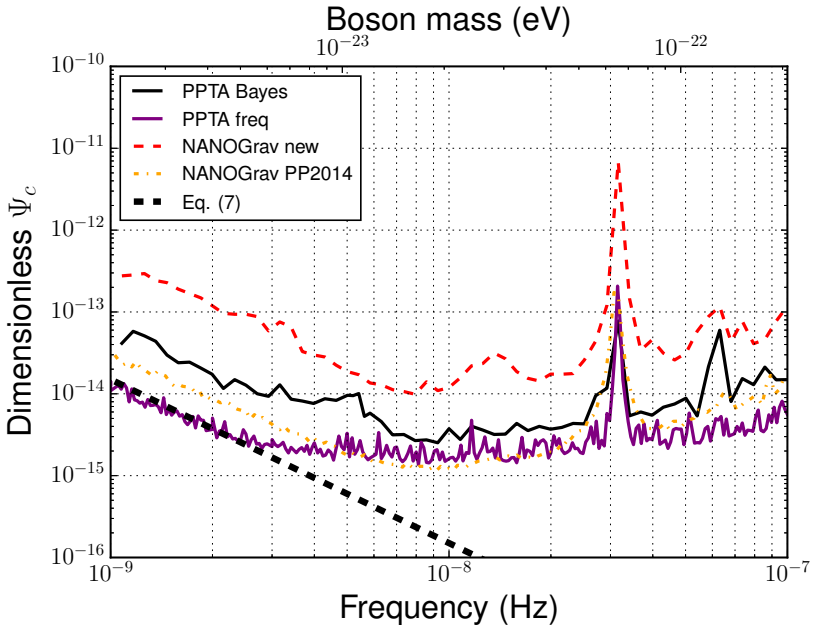

Figure 6.3: Upper limits on the signal amplitude Ψ_c, generated by the scalar field dark matter in the Galaxy, as a function of frequency (boson mass). The purple solid line shows results from Frequentist analysis of the full data set of 24 pulsars, while the black solid line demonstrates the upper limits derived within a Bayesian framework (only the five best pulsars were used). These are compared with previous studies using the NANOGrav 5-yr data set: dash-dotted orange – upper limits set in Porayko & Postnov (2014), dashed red – upper limits recalculated in this work. The thick black dashed line shows the model amplitude Ψ_c, assuming $\rho_{\rm FDM} = 0.4\,{\rm GeV\,cm^{-3}}$, given by Equation (6.7).

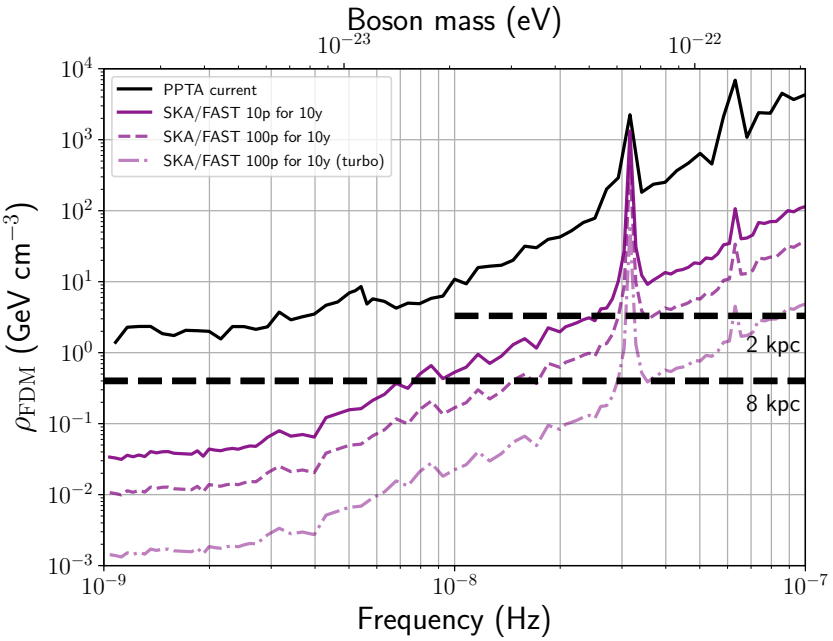

Figure 6.4: Upper limits on the dark matter density ρ in the Galaxy. The current PPTA upper limits (black solid line) are shown along with projected limits in the FAST/SKA era (purple lines, all assuming 10-yr data span): a) 10 pulsars, 14-day cadence, 30-min integration, b) 100 pulsars, 14-day cadence, 30-min integration, and c) 100 pulsars, 1-day cadence, 2-hours integration (turbo). The black dashed lines show the dark matter density in the Halo at 8 kpc ($\rho_{\rm FDM} = 0.4\,{\rm GeV\,cm^{-3}}$) and 2 kpc ($\rho_{\rm FDM} = 3.4\,{\rm GeV\,cm^{-3}}$) from the Galactic Center, assuming NFW profile. The 8 kpc line demonstrates the predicted dark matter density, applicable to current PPTA pulsars and the Earth, while the 2 kpc line applies to pulsars located at 2 kpc distance from the Galactic Center. For boson masses $m \lesssim 4 \times 10^{-23}$ eV the size of the solitonic core becomes larger than 2 kpc (Schive et al., 2014), and the dark matter density will deviate from the NFW prediction towards higher values (see text for details).

6.5 Future prospects

In this section we discuss the future improvement in sensitivity of PTAs to the dark matter signal. In particular, the FAST radio telescope (Nan et al., 2011) in China, MeerKAT (Bailes et al., 2018) – a precursor for the planned Square Kilometre Array (SKA, Lazio, 2013) – and ultimately the SKA, are expected to significantly increase the sensitivities of PTAs. With broad frequency bands and massive collecting areas, the radiometer noise for some of the brightest pulsars can be reduced from current 100 ns level down to below 10 ns (Hobbs et al., 2014). However, it might be too optimistic to assume a white noise level of 10 ns because of the so-called jitter noise, which is thought

Table 6.4: White noise for 10 PPTA pulsars in the FAST/SKA era.

Jname	$\sigma_{\rm r}$ (ns)	σ_J (ns)	σ (ns)
J0437−4715	0.06	50.4	50.4
J1017−7156	4.6	13.7	14.5
J1446−4701	26.0	22.1	34.1
J1545−4550	15.6	36.1	39.3
J1600−3053	2.9	26.6	26.8
J1713+0747	0.8	35.1	35.1
J1744−1134	3.9	41.2	41.4
J1832−0836	3.7	14.2	14.8
J1909−3744	1.2	11.2	11.3
J2241−5236	1.5	15.4	15.5

to be associated with the intrinsic and stochastic variability in the shape of individual pulses (Osłowski et al., 2011). Such a limitation implies that the timing precision stops improving for the brightest pulsars even when better instruments are used. The level of jitter noise can be approximately estimated with the following relation (Shannon & Cordes, 2012)

$$\sigma_J \approx 0.2W\sqrt{\frac{P}{T_{\rm int}}}, \tag{6.30}$$

where $T_{\rm int}$ is the time of integration, W and P are the pulse width and pulse period, respectively. Note that the only way to reduce jitter noise is to increase $T_{\rm int}$. In comparison, the radiometer noise is given by Hobbs et al. (2014)

$$\sigma_{\rm r} \approx \frac{W}{\rm S/N} \approx \frac{WS_{\rm sys}}{S_{\rm mean}\sqrt{2\Delta f T_{\rm int}}}\sqrt{\frac{W}{P-W}}\,, \tag{6.31}$$

where S/N is the pulse profile signal-to-noise ratio, $S_{\rm sys}$ is the system-equivalent flux density, $S_{\rm mean}$ is the pulsar mean flux density and Δf is the observing bandwidth. We adopt nominal SKA parameters[9], $S_{\rm sys} = 1.8\,{\rm Jy}$, $\Delta f = 770\,{\rm MHz}$ and set a fiducial $T_{\rm int} = 30\,{\rm minutes}$.

Table 6.4 lists white noise budgets ($\sigma_{\rm r}$, σ_J and the total white noise σ) expected in the FAST/SKA era for ten PPTA pulsars that have the lowest value of σ. As one can see, for the SKA, jitter noise will dominate over the radiometer noise for the majority of bright pulsars. In order to realistically estimate the PTA sensitivity in the FAST/SKA era, we use the total white noise given in Table 6.4 plus the intrinsic spin noise (where appropriate) with parameters determined from the Bayesian analysis.

Figure 6.4 shows forecasted upper limits on the density of FDM in the Galaxy for three cases, all assuming a data span of ten years. Case a) is a conservative PTA that includes only ten pulsars as listed in Table 6.4 and an observing cadence of once every 14 days. Upper limits in this case are obtained by running full Bayesian analysis of

[9]SKA1 system baseline V2 description https://www.skatelescope.org/

simulated data. We analytically scale this limit curve to two more ambitious cases[10]. We increase the number of pulsars to 100 in case b), leading to a factor of $\sqrt{10}$ improvement. For case c), we further increase the cadence to once every day and adopt an integration time of two hours, providing another factor of $\sqrt{4 \times 14}$ improvement. Case c) might be an interesting option in the SKA era since small radio telescopes (compared to SKA/FAST) such as Parkes, can be dedicated for high-cadence and long integration observations of the brighter pulsars.

As one can see from Figure 6.4, we will be able to constrain the contribution of FDM to the local dark matter density below 10% for $m \lesssim 10^{-23}\,\mathrm{eV}$ in ten years under the conservative assumption for SKA sensitivity. However, it is more challenging for boson masses above $10^{-22}\,\mathrm{eV}$; we estimate that decade-long observations of hundreds of pulsars timed at nearly daily cadence with precision $\lesssim 20\,\mathrm{ns}$ are necessary to place interesting limits.

There are a couple of ways to improve our analysis. First, the coherence between pulsar terms and Earth terms can be used to enhance the sensitivity. When a pulsar and the Earth are located within a de Broglie wavelength λ_{dB}, the oscillation phases, which have been assumed to be independent in the current analysis, are correlated. However, for $m \gtrsim 10^{-22}\,\mathrm{eV}$, this effect will have no impact on the current results, since $\lambda_{\mathrm{dB}} = 60\,\mathrm{pc}\,(10^{-22}\,\mathrm{eV}/m)$ and no pulsars have been found within 60 pc to the Earth. Another interesting point is that pulsars that are close to each other within λ_{dB} also experience phase-coherent oscillations (De Martino et al., 2017). We plan to explore these features in a future work.

Second, the oscillation amplitude Ψ_c is proportional to the local dark matter density. Thus, in contrast to the amplitude of the Earth term, the amplitude of the pulsar term varies from pulsar to pulsar; see Equation (6.7). In Λ-FDM cosmological simulations (De Martino et al., 2017; Schive et al., 2014), it was shown that due to wave interference the dark matter forms gritty pattern with typical granule size of around λ_{dB}. When averaged over $\gg \lambda_{\mathrm{dB}}$ scales, the periphery ($> 1\,\mathrm{kpc}$) density profile is similar to the classical Navarro-Frenk-White (NFW) profile, whereas a distinct density peak is seen in the central regions (usually called solitonic core, see Schive et al., 2014, for details).

Figure 6.5 shows the expected signal amplitude for PPTA pulsars assuming the NFW dark matter density profile (Navarro et al., 1996b) with parameters from Sofue (2012). As one can see, pulsars closer to the Galactic Center provide better sensitivity to the dark matter signal. The amplitude of the dark matter signal becomes even larger than NFW prediction within the central solitonic core ($\lesssim 1\,\mathrm{kpc}$, De Martino et al., 2017). For the current PPTA sample, PSR J1824−2452A is expected to have the largest signal amplitude, a factor of ~ 5 larger than other pulsars[11]. However, this pulsar is nearly the worst timer in PPTA (see Table 6.1 and Figure 6.1). Existing

[10] Note that the scaling factor should be a good approximation at high frequencies where red noise plays a less important role.

[11] The density of the scalar field dark matter in globular clusters is not expected to deviate significantly from the general trend as λ_{dB} is larger than typical sizes of globular clusters. Thus, the amplitude of the oscillation at J1824−2452A, located in a globular cluster, is expected to follow the NFW prediction.

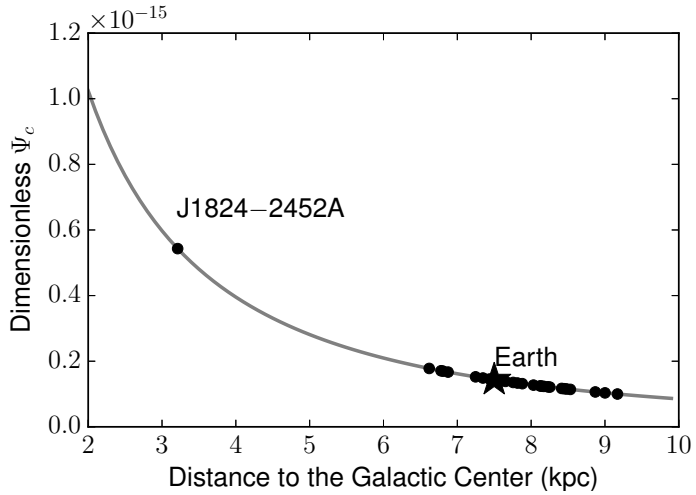

Figure 6.5: The amplitude of the expected dark matter signal for different pulsars, assuming NFW dark matter density profile. The mass of the scalar dark matter particles is assumed to be 2×10^{-23} eV.

and future pulsar surveys might help find high quality millisecond pulsars close to the Galactic Center and thus provide better sensitivity to the dark matter searches (Kramer et al., 2004).

6.6 Conclusions

Pulsar timing is a powerful tool to study a wide variety of astrophysical phenomena. By exploiting precision timing observations from an array of the most stable millisecond pulsars, PTAs allow us to measure minute correlations in the ToAs of different pulsars. Like continuous GWs from individual supermassive binary black holes, FDM in the Galaxy produces periodic variations in pulsar ToAs. We perform a search for evidence of ultralight dark matter in the latest PPTA data set. Finding no statistically significant signals, we place upper limits on the dark matter density: for boson mass $m \lesssim 10^{-23}$ eV, our analysis constrains the density below $6\,\mathrm{GeV\,cm^{-3}}$ with 95% confidence; at $m \approx 10^{-22}$ eV, our upper limits remain 3 orders of magnitude above the local dark matter density $0.4\,\mathrm{GeV\,cm^{-3}}$ inferred from kinematics measurements of stars in the Galaxy (Sivertsson et al., 2018).

We derived the noise properties of PPTA data and obtain dark matter constraints using both Bayesian and Frequentist methods. Our upper limits from the two methods are broadly consistent. We reanalyzed the NANOGrav 5-yr data set and found that the PPTA data result in a factor of 2 to 5 improvement in dark matter constraints. We studied potential systematics due to SSE errors in our analysis and found that the search for ultralight dark matter is insensitive to such errors. We have ignored effects from instabilities in terrestrial time standards; such clock errors produce a monopolar broad-band noise (Hobbs et al., 2012). Whereas this effect should be distinguishable

from the sinusoidal ToA variations due to ultralight dark matter, one needs to include it in a future study to quantitatively assess the impact.

We forecasted the PTA sensitivity in the FAST/SKA era while accounting for realistic noise levels. We found that observing the ten best PPTA pulsars for ten years would constrain the density of FDM below $0.05\,\mathrm{GeV\,cm^{-3}}$ for $m \lesssim 10^{-23}\,\mathrm{eV}$, about 10% of measured total dark matter density. At $m \approx 2 \times 10^{-23}\,\mathrm{eV}$, our projected limit is around $0.4\,\mathrm{GeV\,cm^{-3}}$; for higher boson masses, the upper limits increase as $\sim m^3$. Above $m \approx 10^{-22}\,\mathrm{eV}$, the projected limits are more than one order of magnitude above the local dark matter density. To place interesting limits in this mass range, an ambitious timing program in which hundreds of pulsars timed with daily cadence and high precision ($\lesssim 20\,\mathrm{ns}$) for more than a decade is required. Finally, we point out that high-quality pulsars in the vicinity of the Galactic Center will be ideal tools to test the fuzzy dark matter hypothesis.

Chapter 7

Concluding remarks and future plans

Contents

7.1 Studying the magnetised ISM with pulsars 125
7.1.1 Future plans 126
7.2 Studying dark matter with pulsars 127
7.2.1 Future plans 128

The primary scientific motivation of this thesis is the investigation of effects which influence the propagation of pulsar signals, in order to probe the properties of the intervening medium and its constituents. We mainly focus our analysis on probing the turbulence in the magnetised ionised ISM using Faraday rotation of pulsars, and dark matter in the Galaxy using a high-precision pulsar timing technique. We investigate how the recent, highly sensitive data can constrain (or measure!) the aforementioned propagation effects that haven't been studied extensively before. The most significant accomplishments of the work in this thesis as well as potential improvements and future plans are summarised below.

7.1 Studying the magnetised ISM with pulsars

Pulsars are known to be a powerful probe of the magnetoionic phase of the ISM in the Milky Way. Specifically in this thesis we used Faraday rotation of linearly polarised radiation from pulsars to study the diffuse magnetic field in the Milky Way. Since ISM effects are more prominent at longer wavelengths, we have conducted the pulsar observations with the low-frequency radio interferometer LOFAR. The RMs of pulsars were obtained with the novel BGLSP technique, which provides reliable estimates of the uncertainties on the observed RMs, and is described in **Chapter 3**. It was found that detected RM variations are dominated by the Faraday rotation taking place in the Earth's ionosphere, which is five to six orders of magnitude greater than what we expect from the ISM. In order to compensate for the ionospheric RM we have used a conventional thin-layer ionospheric approximation. The Earth's magnetic field was reconstructed with so-called geomagnetic field models produced using magnetic field measurements from satellites and approximately 200 operating magnetic observatories

around the globe. The electron density in the ionosphere was modelled using a selection of global free-electron density maps, produced by different scientific groups via various numerical techniques using GPS data. In **Chapter 4** we compared different geomagnetic models and free-electron density maps, and investigated the reconstruction quality of ionospheric Faraday rotation using several months of LOFAR observations of selected pulsars. We found that on average the UQRG and JPLG maps perform better than other ionospheric maps, while the performance of different geomagnetic models is indistinguishable with our current sensitivity. After subtraction of the deterministic systematics that left residual unmodelled ionospheric effects, the corrected RM measurements have a precision of $\sim 0.06{-}0.07\,\mathrm{rad\,m^{-2}}$. This number is approximately an order of magnitude higher than the uncertainties of the observed RMs for the considered pulsars and therefore defines our sensitivity to any sort of astrophysical RM variation.

One of the promising signals of interest are RM variations caused by turbulent ISM structures between the pulsar and the observer. In **Chapter 5** we made an effort to measure these RM variations using ∼3-year long LOFAR observations of pulsars. However, no astrophysically reliable signal has been found. We set an upper limit on the amplitude of any magnetic field fluctuations. Our best result, obtained with J0826+2637, is already below the value derived in Haverkorn et al. (2008), however still four times higher that the expected value observed in Minter & Spangler (1996). With a set of simulations we have shown that for a reliable detection we need ~ 20 years of regular monitoring of pulsars with LOFAR.

7.1.1 Future plans

In this section we summarise which steps should be undertaken in order to improve our sensitivity to RM variations of pulsars. These ideas are important for future initiatives as well as for current actions.

Regular monitoring of pulsars with low-frequency interferometers
Searching for RM variations in pulsar signals is an on-going study. German LOFAR stations are now observing more than 100 pulsars bi-weekly at 150 MHz. Such continuing monitoring campaigns of pulsars at low frequencies provide a valuable basis for investigating long-term RM changes. Besides the RM variations caused by the turbulent ISM, the same data set can be used to probe other RM signals of interest, such as those caused by the Solar wind (Oberoi & Lonsdale, 2012), ESEs (Fiedler et al., 1987; Cognard et al., 1993) and reconnection sheets in the ISM (Pen & Levin, 2014). Along with the RMs, the DMs of pulsars can be used to determine the electron density towards the pulsar, providing additional insight into the physical structures and processes taking place between the source and the observer. By simultaneously measuring the RMs and DMs of pulsars, one can probe the possible correlations of these quantities and increase the reliability of the results.

Improving ionospheric modelling As mentioned, the influence of the ionosphere

can be the main obstacle towards detecting astrophysical RM variations. Therefore, a conspicuous way of increasing the sensitivity towards signals of interest is by improving the quality of the ionospheric modelling. In this thesis we have used a simplified model within which the ionosphere is a thin single layer fixed at an altitude of 450 km. However in reality, the ionosphere is highly dynamic. In multiple studies it has been shown that the peak electron density height (and therefore the effective ionospheric height) varies significantly as a function of the time of day, season, and solar activity (Rama Rao et al., 2006; Gulyaeva et al., 2013; Wang et al., 2016). Therefore, a more realistic representation of the single-layer model would be taking into account variations of the effective ionospheric height. This can be carried out by combining the GPS-derived electron-density values with semi-empirical ionospheric profiles like the IRI (Bilitza et al., 2017) or the IRI-Plas (Arikan et al., 2015). An even more sophisticated analysis can be performed with multi-layer or 3D models of the ionosphere, created using the GPS data combined with electron-density measurements from on-site ionosondes (e.g. Ma et al., 2005). Alternatively, non-parametric routines can be used to account for the ionospheric contribution. An intriguing solution is to use a diffuse polarised background or a set of linearly polarised sources as calibrators to track the ionospheric Faraday rotation (Lenc et al., 2016). By analysing multiple observing snapshots made at different epochs, one can estimate the RM of the source of interest purified from the ionospheric contribution. However, the source and the calibrators should be located close enough on the sky, i.e within the coherence length of the ionosphere ($<10°$, Loi et al., 2015).

7.2 Studying dark matter with pulsars

Recent studies suggest that about 70% of the mass of the Milky Way comes from dark matter (Posti & Helmi, 2019). In astrophysical systems with sizes ranging from galactic to cosmological scales the dark-matter hypothesis is supported by various lines of observational evidence. Among the most striking proofs are rotation curves of galaxies, the angular power spectrum of the cosmic microwave background and enigmatic dynamics of galaxy clusters. The standard ΛCDM model has been remarkably successful in explaining many of these observational features, given that 27% of the critical mass-energy density consists of dark matter. However, on scales similar to those of galaxies, the ΛCDM model has been poorly tested and in most cases it is in tension with observational data. One of the viable alternatives is FDM, consisting of extremely light bosons with mass $m \sim 10^{-22}$ eV. As was shown in Khmelnitsky & Rubakov (2014), such FDM will produce oscillations of gravitational potentials at nHz frequencies. This time-dependent space-time will cause variations in ToAs of pulsar signals, which are correlated between different pulsars. In **Chapter 6** we attempt to measure these variations using the ∼12-year PPTA dataset. We performed a search for an FDM signal in the Milky Way using both frequentist and Bayesian approaches. As no statistically significant signal has been found, we put an upper limit on the dark matter density in

the Galaxy. Our best results at $m < 10^{-23}\,\mathrm{eV}$ are below $6\,\mathrm{GeV\,cm^{-3}}$, while our upper limit at $m = 10^{-22}\,\mathrm{eV}$ is still three orders of magnitude higher than the expected dark matter density of $0.4\,\mathrm{GeV\,cm^{-3}}$, obtained from kinematic studies of stars in the Galaxy.

7.2.1 Future plans

Investigation of the dark matter problem is of great importance in cosmology. The work presented in this thesis provides our modest contribution towards revealing the nature of dark matter. Additional methods to improve the data analysis and increase our sensitivity to FDM are proposed below.

Mitigation of correlated noise and systematics in the PTA data The presence of various noise processes significantly increases the complexity of the analysis and, what is more important, degrades the sensitivity of PTAs (see Verbiest & Shaifullah, 2018, and reference therein).

One of the bottlenecks for high precision PTAs is DM variations caused by the ionised ISM (see e.g. **Chapter 6**) and Solar wind (Tiburzi et al., 2019). As we are more sensitive to propagation effects at lower frequencies, one of the promising techniques to correcting DM variations is to use low-frequency observations (Janssen et al., 2015). However, due to DM chromaticity (Cordes et al., 2016; Donner et al., 2019) the effect can be removed only partially.

It has already been shown in multiple works that even with our current sensitivity pulsar timing is sensitive to errors in the SSEs and time standard (Tiburzi et al., 2016; Caballero et al., 2018). These two types of errors are the source of correlated noise with monopolar and dipolar spatial correlations, respectively. As was shown in Tiburzi et al. (2016), the presence of this correlated noise increases the false-alarm probability of GW detection with PTAs. In the case of a signal coming from FDM we would be especially affected by the correlated noise from clocks, due to the monopolar nature of the FDM signal. Some techniques, such as including the SSEs in the timing model (Champion et al., 2010; Caballero et al., 2018; Arzoumanian et al., 2018b), have already been successfully adopted in PTAs. Another viable method is non-parametric suppression of correlated noise from terrestrial clock standards and SSEs (Taylor et al., 2017).

In the era of more sensitive instruments the problem of correlated noises and systematics will be further exacerbated. Therefore, mitigation of these effects for current and especially future PTA analysis is of great importance.

New and upcoming radio facilities A new generation of radio telescopes will soon be available at full capacity and will assist the PTA campaigns. Two of these are the 500-meter-FAST radio telescope (Nan et al., 2011) in the Northern hemisphere and MeerKAT (Booth & Jonas, 2012), a phased array formed by 64 13.5-meter-dishes, in the Southern hemisphere. Both of these saw the 'first light' in 2016. The even more ambitious SKA radio telescope (Bull et al., 2018), which will be formed by thousands of small antennas located on two continents in the Southern

hemisphere, will become operational in the next decade. Huge collecting areas of the aforementioned telescopes combined with their low system temperatures will increase the S/N of already detected pulsars, and therefore significantly improve the sensitivity of PTAs as a whole. In **Chapter 6** we have investigated how the PTA sensitivity to an FDM signal will increase with upcoming radio facilities. We found that stringent constraints below $0.05\,\mathrm{GeV\,cm^{-3}}$ can be put for $m < 10^{-23}\,\mathrm{eV}$, when observing the ten best PPTA pulsars for ten years with future facilities. For putting astrophysically interesting upper limits for $m > 10^{-22}$ eV a more ambitious observing programme in which hundreds of pulsars are observed daily, is required. Moreover, the higher sensitivity of the upcoming radio telescopes is expected to significantly increase the number of known pulsars, and may populate PTA family with more stable MSPs. As the density of dark matter increases towards the central regions of our Galaxy, pulsars detected closer to the Galactic Centre will provide better sensitivity to an FDM signal.

Appendix A

Earth-term limits and effects of SSE

When searching for continuous GWs in PTA data, it is common to use only the Earth terms. Similarly, for the case of scalar field dark matter, we can include in the analysis only Earth terms in Equation (6.6). Although pulsar and Earth terms lie in the same frequency bin, we expect that for a sufficiently large set of pulsars, pulsar terms will be averaged out, as they all have different phases. In the left panel of Figure A.1, we compare the Frequentist upper limits on the density of scalar field dark matter $\rho_{\rm SF}$ when only Earth terms are considered (black dashed) and when the full signal is used (purple solid). We find that both limits are comparable to each other. The noisy features in the (purple) solid curve are due to the amplitude modulation of pulsar terms; see Equation (6.9).

We also demonstrate the effects of SSE errors. In the right panel of Figure A.1, we show the upper limits obtained when DE418 and DE435 planetary ephemeris are used. The results with fixed ephemeris are overplotted with upper limits obtained with `BayesEphem` model, which accounts for uncertainties in the SSE. We see that the results are comparable, indicating the search for FDM signal, or continuous waves in general, is insensitive to SSE errors.

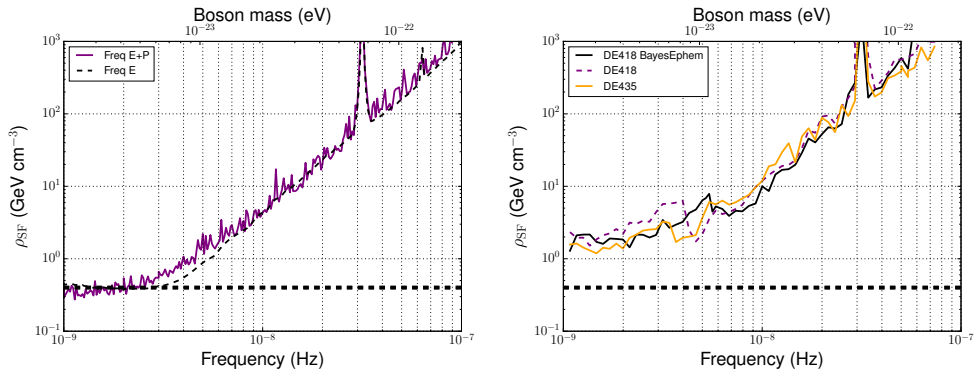

Figure A.1: Upper limits on the density of fuzzy dark matter $\rho_{\rm SF}$ in the Galaxy, as a function of frequency (boson mass). *Left*: results from Frequentist analysis when only the Earth term is included (Freq E) or both terms are used (Freq E+P). *Right*: Bayesian upper limits when SSE parameters are included in the search (BayesEphem), or using fixed DE418 and DE435 planet ephemerids. The horizontal black dashed line marks the measured local dark matter density $0.4\,\mathrm{GeV\,cm^{-3}}$ (Sivertsson et al., 2018).

Appendix B

Noise properties for six PPTA pulsars

Figure B.1 shows results of the Bayesian noise parameter estimation, described in Section 6.3.3.1, for the six most sensitive pulsars in the current PPTA data set.

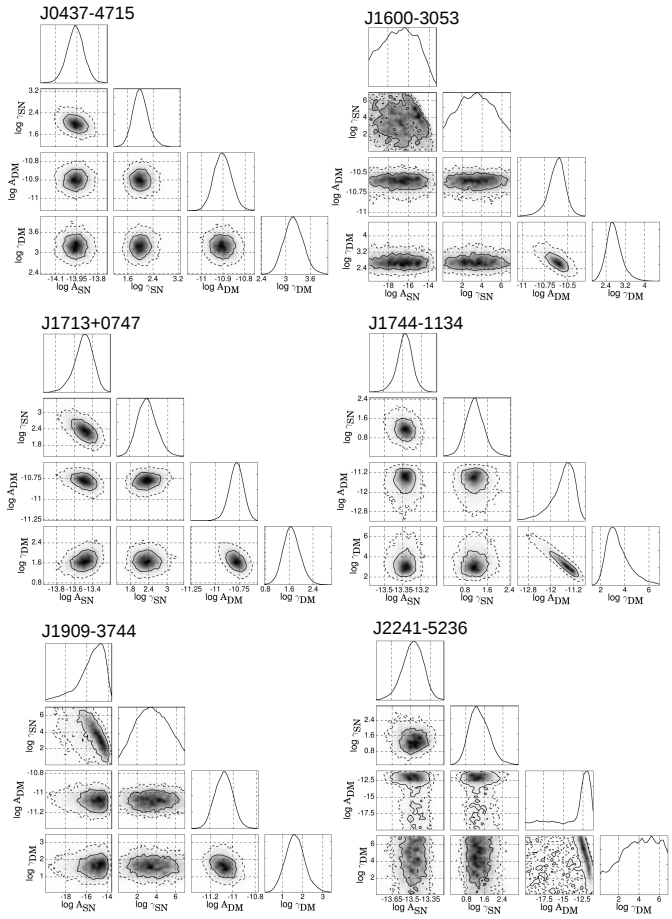

Figure B.1: The one- and two-dimensional marginalized posterior distributions for the log-amplitude and slope of the DM and spin noises for the six best pulsars in the current PPTA data set.

Bibliography

Abbott L. F., Sikivie P., 1983, Phys. Lett. B, 120, 133 (Cited on page 101.)

Aggarwal K., et al., 2018, arXiv e-prints, (Cited on page 20.)

Ambartsumyan V. A., Saakyan G. S., 1960, Soviet Ast., 4, 187 (Cited on page 4.)

Antoniadis J., et al., 2013, Science, 340, 448 (Cited on page 19.)

Archibald R. F., et al., 2016, ApJ, 819, L16 (Cited on page 10.)

Archibald A. M., et al., 2018, Nature, 559, 73 (Cited on page 19.)

Arikan F., Sezen U., Gulyaeva T. L., Cilibas O., 2015, Advances in Space Research, 55, 2106 (Cited on page 127.)

Armstrong J. W., Rickett B. J., Spangler S. R., 1995, ApJ, 443, 209 (Cited on pages 22, 58, 82, 89 and 91.)

Arnett D., 1996, Supernovae and Nucleosynthesis: An Investigation of the History of Matter from the Big Bang to the Present (Cited on page 5.)

Arora B. S., et al., 2016, PASA, 33, e031 (Cited on page 74.)

Arvanitaki A., Dimopoulos S., Dubovsky S., Kaloper N., March-Russell J., 2010, Phys. Rev. D, 81, 123530 (Cited on pages 24 and 101.)

Arzoumanian Z., et al., 2014, ApJ, 794, 141 (Cited on pages 110 and 115.)

Arzoumanian Z., et al., 2018a, ApJS, 235, 37 (Cited on page 19.)

Arzoumanian Z., et al., 2018b, ApJ, 859, 47 (Cited on pages 20, 38, 115, 116 and 128.)

Asgekar A., Deshpande A. A., 1999, Bulletin of the Astronomical Society of India, 27, 209 (Cited on page 30.)

Asseo E., Pelletier G., Sol H., 1990, MNRAS, 247, 529 (Cited on page 9.)

Baade W., Zwicky F., 1934, Proceedings of the National Academy of Science, 20, 254 (Cited on page 4.)

Babak S., et al., 2016, MNRAS, 455, 1665 (Cited on pages 20 and 115.)

Backer D. C., 1970, Nature, 228, 42 (Cited on page 8.)

Backer D. C., Hellings R. W., 1986, ARA&A, 24, 537 (Cited on page 37.)

Bailes M., et al., 2018, in Proceedings of MeerKAT Science2016. p. 11 (arXiv:1803.07424) (Cited on page 120.)

Banerjee R., Klessen R. S., Fendt C., 2007, ApJ, 668, 1028 (Cited on page 21.)

Bar N., Blas D., Blum K., Sibiryakov S., 2018, preprint, (arXiv:1805.00122) (Cited on page 102.)

Bassa C. G., et al., 2016, MNRAS, 456, 2196 (Cited on page 29.)

Bates S. D., Lorimer D. R., Verbiest J. P. W., 2013, MNRAS, 431, 1352 (Cited on pages 6 and 58.)

Battaglieri M., et al., 2017, arXiv e-prints, (Cited on page 100.)

Beck R., 2001, Space Sci. Rev., 99, 243 (Cited on page 85.)

Becker W., ed. 2009, Neutron Stars and Pulsars Astrophysics and Space Science Library Vol. 357, doi:10.1007/978-3-540-76965-1. (Cited on page 5.)

Becker W., Bernhardt M. G., Jessner A., 2013, Acta Futura, Issue 7, p. 11-28, 7, 11 (Cited on page 20.)

Begeman K. G., Broeils A. H., Sanders R. H., 1991, MNRAS, 249, 523 (Cited on page 23.)

Beresnyak A., 2012, Phys. Rev. Lett., 108, 035002 (Cited on page 21.)

Bertone G., Hooper D., Silk J., 2005, Phys. Rep., 405, 279 (Cited on pages 22 and 100.)

Beskin V. S., Philippov A. A., 2012, MNRAS, 425, 814 (Cited on page 8.)

Beskin V. S., Gurevich A. V., Istomin I. N., 1988, Ap&SS, 146, 205 (Cited on page 9.)

Bhat N. D. R., Gupta Y., Rao A. P., 1998, ApJ, 500, 262 (Cited on page 58.)

Bhattacharya D., van den Heuvel E. P. J., 1991, Phys. Rep., 203, 1 (Cited on page 12.)

Bienaymé O., et al., 2014, A&A, 571, A92 (Cited on page 22.)

Bilitza D., Altadill D., Zhang Y., Mertens C., Truhlik V., Richards P., McKinnell L.-A., Reinisch B., 2014, Journal of Space Weather and Space Climate, 4, A07 (Cited on page 59.)

Bilitza D., Altadill D., Truhlik V., Shubin V., Galkin I., Reinisch B., Huang X., 2017, Space Weather, 15, 418 (Cited on pages 63 and 127.)

Bilous A. V., et al., 2016, A&A, 591, A134 (Cited on pages 89 and 90.)

Birch M. J., Hargreaves J. K., Bailey G. J., 2002, Radio Science, 37, 15 (Cited on page 74.)

Bird M. K., et al., 1985, Sol. Phys., 98, 341 (Cited on page 18.)

Blandford R., Narayan R., Romani R. W., 1984, Journal of Astrophysics and Astronomy, 5, 369 (Cited on page 109.)

Blas D., Nacir D. L., Sibiryakov S., 2017, Phys. Rev. Lett., 118, 261102 (Cited on pages 24 and 102.)

Blinnikov S., Dolgov A., Porayko N. K., Postnov K., 2016, J. Cosmology Astropart. Phys., 11, 036 (Cited on page 24.)

Bode P., Ostriker J. P., Turok N., 2001, ApJ, 556, 93 (Cited on page 24.)

Booth R. S., Jonas J. L., 2012, African Skies, 16, 101 (Cited on pages 31 and 128.)

Bovy J., Tremaine S., 2012, ApJ, 756, 89 (Cited on page 105.)

Bowman J. D., Rogers A. E. E., Monsalve R. A., Mozdzen T. J., Mahesh N., 2018, Nature, 555, 67 (Cited on page 102.)

Boynton P. E., Groth E. J., Hutchinson D. P., Nanos Jr. G. P., Partridge R. B., Wilkinson D. T., 1972, ApJ, 175, 217 (Cited on page 109.)

Brandenburg A., Subramanian K., 2005, Phys. Rep., 417, 1 (Cited on page 21.)

Brdar V., Kopp J., Liu J., Prass P., Wang X.-P., 2018, Phys. Rev. D, 97, 043001 (Cited on page 104.)

Brentjens M. A., de Bruyn A. G., 2005, A&A, 441, 1217 (Cited on pages 43, 45, 46 and 61.)

Bretthorst G. L., 2001, in Mohammad-Djafari A., ed., American Institute of Physics Conference Series Vol. 568, Bayesian Inference and Maximum Entropy Methods in Science and Engineering. pp 241–245, doi:10.1063/1.1381888 (Cited on page 50.)

Buhari S. M., Abdullah M., Hasbi A. M., Otsuka Y., Yokoyama T., Nishioka M., Tsugawa T., 2014, J. of Geophysical Research (Space Physics), 119, 10 (Cited on page 17.)

Bull P., et al., 2018, arXiv e-prints, (Cited on page 128.)

Bullock J. S., Boylan-Kolchin M., 2017, Annu. Rev. Astron. Astrophys., 55, 343 (Cited on page 102.)

Burgay M., et al., 2003, Nature, 426, 531 (Cited on page 18.)

Burkhart B., Lazarian A., Gaensler B. M., 2012, ApJ, 749, 145 (Cited on page 21.)

Burn B. J., 1966, MNRAS, 133, 67 (Cited on pages 42, 45 and 61.)

Caballero R. N., et al., 2016, MNRAS, 457, 4421 (Cited on page 72.)

Caballero R. N., et al., 2018, MNRAS, 481, 5501 (Cited on pages 20, 38 and 128.)

Calabrese E., Spergel D. N., 2016, MNRAS, 460, 4397 (Cited on page 102.)

Chadwick J., 1932, Nature, 129, 312 (Cited on page 4.)

Chamel N., Haensel P., 2008, Living Reviews in Relativity, 11, 10 (Cited on page 5.)

Champion D. J., et al., 2010, ApJ, 720, L201 (Cited on pages 20, 38 and 128.)

Chandrasekhar S., 1931, ApJ, 74, 81 (Cited on page 4.)

Chen K., Ruderman M., 1993, ApJ, 402, 264 (Cited on page 11.)

Chepurnov A., Lazarian A., 2010, ApJ, 710, 853 (Cited on page 82.)

Chester T. J., Butman S. A., 1981, Telecommunications and Data Acquisition Progress Report, 63, 22 (Cited on page 20.)

Cho J., Lazarian A., 2009, ApJ, 701, 236 (Cited on page 21.)

Clark H. A., Lewis G. F., Scott P., 2016, MNRAS, 456, 1402 (Cited on page 24.)

Clegg A. W., Cordes J. M., Simonetti J. M., Kulkarni S. R., 1992, ApJ, 386, 143 (Cited on page 82.)

Clesse S., García-Bellido J., 2017, Physics of the Dark Universe, 18, 105 (Cited on page 24.)

Clowe D., Gonzalez A., Markevitch M., 2004, ApJ, 604, 596 (Cited on page 100.)

Cognard I., Bourgois G., Lestrade J.-F., Biraud F., Aubry D., Darchy B., Drouhin J.-P., 1993, Nature, 366, 320 (Cited on page 126.)

Cole T. W., 1969, Nature, 221, 29 (Cited on page 29.)

Coles W., Hobbs G., Champion D. J., Manchester R. N., Verbiest J. P. W., 2011, MNRAS, 418, 561 (Cited on page 113.)

Coles W. A., et al., 2015, ApJ, 808, 113 (Cited on pages 78 and 112.)

Colín P., Avila-Reese V., Valenzuela O., 2000, ApJ, 542, 622 (Cited on page 24.)

Conway R. G., Kellermann K. I., Long R. J., 1963, MNRAS, 125, 261 (Cited on page 30.)

Cooper B. F. C., Price R. M., 1962, Nature, 195, 1084 (Cited on page 43.)

Cordes J. M., Lazio T. J. W., 2002, ArXiv Astrophysics e-prints, (Cited on page 58.)

Cordes J. M., Lazio T. J. W., 2003, arXiv Astrophysics e-prints, (Cited on page 22.)

Cordes J. M., Rankin J., Backer D. C., 1978, ApJ, 223, 961 (Cited on page 8.)

Cordes J. M., Weisberg J. M., Boriakoff V., 1985, ApJ, 288, 221 (Cited on page 89.)

Cordes J. M., Weisberg J. M., Frail D. A., Spangler S. R., Ryan M., 1991, Nature, 354, 121 (Cited on page 22.)

Cordes J. M., Shannon R. M., Stinebring D. R., 2016, ApJ, 817, 16 (Cited on page 128.)

Cromartie H., et al., 2019, arXiv e-prints, (Cited on page 19.)

Crovisier J., Dickey J. M., 1983, A&A, 122, 282 (Cited on page 82.)

Cumming A., Zweibel E., Bildsten L., 2001, ApJ, 557, 958 (Cited on page 12.)

Damour T., Deruelle N., 1986, Ann. Inst. Henri Poincaré Phys. Théor., Vol. 44, No. 3, p. 263 - 292, 44, 263 (Cited on page 38.)

Damour T., Taylor J. H., 1992, Phys. Rev. D, 45, 1840 (Cited on page 38.)

Davies J. G., Hunt G. C., Smith F. G., 1969, Nature, 221, 27 (Cited on pages 4 and 9.)

De K., Gupta Y., 2016, Experimental Astronomy, 41, 67 (Cited on page 29.)

De Martino I., Broadhurst T., Tye S.-H. H., Chiueh T., Schive H.-Y., Lazkoz R., 2017, Phys. Rev. Lett., 119, 221103 (Cited on pages 102 and 122.)

Del Popolo A., Le Delliou M., 2017, Galaxies, 5, 17 (Cited on page 23.)

Demorest P. B., et al., 2013, ApJ, 762, 94 (Cited on pages 103 and 118.)

Deng X. P., et al., 2013, Advances in Space Research, 52, 1602 (Cited on page 20.)

Deng H., Hertzberg M. P., Namjoo M. H., Masoumi A., 2018, Phys. Rev. D, 98, 023513 (Cited on page 102.)

Dessart L., Burrows A., Ott C. D., Livne E., Yoon S.-C., Langer N., 2006, ApJ, 644, 1063 (Cited on page 5.)

Desvignes G., et al., 2016, MNRAS, 458, 3341 (Cited on page 19.)

Desvignes G., et al., 2018, ApJ, 852, L12 (Cited on pages 17, 29, 78 and 83.)

Detweiler S., 1979a, ApJ, 234, 1100 (Cited on page 19.)

Detweiler S., 1979b, ApJ, 234, 1100 (Cited on pages 102 and 104.)

Deutsch A. J., 1955, Annales d'Astrophysique, 18, 1 (Cited on page 5.)

Diaferio A., Schindler S., Dolag K., 2008, Space Sci. Rev., 134, 7 (Cited on page 22.)

Dine M., Fischler W., 1983, Phys. Lett. B, 120, 137 (Cited on page 101.)

Dobbs C. L., Glover S. C. O., Clark P. C., Klessen R. S., 2008, MNRAS, 389, 1097 (Cited on page 21.)

Donner J. Y., et al., 2019, A&A, 624, A22 (Cited on pages 89, 90 and 128.)

Draine B. T., 2011, Physics of the Interstellar and Intergalactic Medium (Cited on page 21.)

Drake F. D., Craft H. D., 1968, Nature, 220, 231 (Cited on page 8.)

Eatough R. P., et al., 2013, Nature, 501, 391 (Cited on page 17.)

Eberhart R. C., Kennedy J., 1995, in Proceedings of the sixth international symposium on micro machine and human science. IEEE, pp 39–43 (Cited on page 118.)

Edwards R. T., Hobbs G. B., Manchester R. N., 2006, MNRAS, 372, 1549 (Cited on pages 35 and 106.)

Ellingson S. W., Clarke T. E., Cohen A., Craig J., Kassim N. E., Pihlstrom Y., Rickard L. J., Taylor G. B., 2009, IEEE Proceedings, 97, 1421 (Cited on page 31.)

Ellis J., van Haasteren R., 2017, jellis18/PAL2: PAL2, doi:10.5281/zenodo.251456, `https://doi.org/10.5281/zenodo.251456` (Cited on page 103.)

Emmanoulopoulos D., McHardy I. M., Uttley P., 2010, MNRAS, 404, 931 (Cited on page 87.)

Erickson W. C., Perley R. A., Flatters C., Kassim N. E., 2001, A&A, 366, 1071 (Cited on page 59.)

Ertl T., Janka H.-T., Woosley S. E., Sukhbold T., Ugliano M., 2016, ApJ, 818, 124 (Cited on page 5.)

Espinoza C. M., Lyne A. G., Stappers B. W., 2017, MNRAS, 466, 147 (Cited on page 10.)

Everett J. E., Weisberg J. M., 2001, ApJ, 553, 341 (Cited on page 8.)

Ewen H. I., Purcell E. M., 1951, Nature, 168, 356 (Cited on page 29.)

Eyink G., et al., 2013, Nature, 497, 466 (Cited on page 96.)

Fallows R. A., et al., 2014, Journal of Geophysical Research (Space Physics), 119, 10 (Cited on page 16.)

Farah W., et al., 2018, MNRAS, 478, 1209 (Cited on page 29.)

Federrath C., 2013, MNRAS, 436, 1245 (Cited on page 97.)

Federrath C., Roman-Duval J., Klessen R. S., Schmidt W., Mac Low M.-M., 2010, A&A, 512, A81 (Cited on pages 21 and 85.)

Feroz F., Hobson M. P., Bridges M., 2009, MNRAS, 398, 1601 (Cited on pages 72, 90 and 112.)

Feroz F., Hobson M. P., Cameron E., Pettitt A. N., 2013, preprint, (arXiv:1306.2144) (Cited on page 112.)

Fiedler R. L., Dennison B., Johnston K. J., Hewish A., 1987, Nature, 326, 675 (Cited on page 126.)

Folkner W., Standish E., Williams J., Boggs D., 2007, Jet Propulsion Laboratory, Memorandum IOM 343R-08-003 (Cited on page 106.)

Foster R. S., Backer D. C., 1990, ApJ, 361, 300 (Cited on pages 19 and 102.)

Frail D. A., Kulkarni S. R., 1991, Nature, 352, 785 (Cited on page 4.)

Freire P. C. C., et al., 2012, MNRAS, 423, 3328 (Cited on pages 19 and 24.)

Friis H. T., Feldman C. B., 1937, The Bell System Technical Journal, 16, 337 (Cited on page 31.)

Gaensler B. M., et al., 2011, Nature, 478, 214 (Cited on page 21.)

Gamow G., Schoenberg M., 1941, Physical Review, 59, 539 (Cited on page 4.)

Ginzburg V. L., 1970, The propagation of electromagnetic waves in plasmas (Cited on page 8.)

Gold T., 1968, Nature, 218, 731 (Cited on page 4.)

Gold T., 1969, Nature, 221, 25 (Cited on page 4.)

Goldreich P., Julian W. H., 1969, ApJ, 157, 869 (Cited on page 6.)

Goodman J., 2000, New Astronomy, 5, 103 (Cited on page 24.)

Gould D. M., Lyne A. G., 1998, MNRAS, 301, 235 (Cited on page 8.)

Governato F., et al., 2012, MNRAS, 422, 1231 (Cited on page 23.)

Green D. A., 1991, MNRAS, 253, 350 (Cited on page 82.)

Gulyaeva T. L., Arikan F., Hernandez-Pajares M., Stanislawska I., 2013, Journal of Atmospheric and Solar-Terrestrial Physics, 102, 329 (Cited on pages 74 and 127.)

Hamaker J. P., Bregman J. D., Sault R. J., 1996, Astronomy and Astrophysics Supplement, 117, 137 (Cited on page 61.)

Hamilton P. A., McCulloch P. M., Manchester R. N., Ables J. G., Komesaroff M. M., 1977, Nature, 265, 224 (Cited on page 83.)

Han J. L., Manchester R. N., Lyne A. G., Qiao G. J., van Straten W., 2006, ApJ, 642, 868 (Cited on pages 22 and 59.)

Han J. L., Manchester R. N., van Straten W., Demorest P., 2018, ApJS, 234, 11 (Cited on page 58.)

Hankins T. H., Rickett B. J., 1975, Methods in Computational Physics, 14, 55 (Cited on page 28.)

Haverkorn M., Gaensler B. M., McClure-Griffiths N. M., Dickey J. M., Green A. J., 2004, ApJ, 609, 776 (Cited on page 90.)

Haverkorn M., Gaensler B. M., McClure-Griffiths N. M., Dickey J. M., Green A. J., 2006, ApJS, 167, 230 (Cited on page 42.)

Haverkorn M., Brown J. C., Gaensler B. M., McClure-Griffiths N. M., 2008, ApJ, 680, 362 (Cited on pages 81, 82, 89, 91, 93, 95, 96 and 126.)

Hayya J., Armstrong D., N. G., 1975, Management Science, 21, 1338 (Cited on page 53.)

Heald G., 2009, in Strassmeier K. G., Kosovichev A. G., Beckman J. E., eds, IAU Symposium Vol. 259, Cosmic Magnetic Fields: From Planets, to Stars and Galaxies. pp 591–602, doi:10.1017/S1743921309031421 (Cited on page 46.)

Heger A., Fryer C. L., Woosley S. E., Langer N., Hartmann D. H., 2003, ApJ, 591, 288 (Cited on page 5.)

Heiles C., Campbell D. B., 1970, Nature, 226, 529 (Cited on page 8.)

Helfand D. J., Manchester R. N., Taylor J. H., 1975, ApJ, 198, 661 (Cited on pages 8, 9 and 35.)

Hellings R. W., Downs G. S., 1983, ApJ, 265, L39 (Cited on pages 19 and 102.)

Helmboldt J. F., Lazio T. J. W., Intema H. T., Dymond K. F., 2012, Radio Science, 47, RS0L02 (Cited on page 17.)

Hennebelle P., Falgarone E., 2012, A&A Rev., 20, 55 (Cited on page 21.)

Hernández-Pajares M., Juan J. M., Sanz J., Aragón-Àngel À., García-Rigo A., Salazar D., Escudero M., 2011, Journal of Geodesy, 85, 887 (Cited on page 74.)

Hewish A., Bell S. J., Pilkington J. D. H., Scott P. F., Collins R. A., 1968, Nature, 217, 709 (Cited on pages 3, 4 and 58.)

Hildebrand R. H., 1983, QJRAS, 24, 267 (Cited on page 20.)

Hložek R., Marsh D. J. E., Grin D., 2018, MNRAS, 476, 3063 (Cited on pages 24 and 102.)

Hobbs G., Lorimer D. R., Lyne A. G., Kramer M., 2005, MNRAS, 360, 974 (Cited on page 95.)

Hobbs G. B., Edwards R. T., Manchester R. N., 2006, MNRAS, 369, 655 (Cited on pages 39 and 106.)

Hobbs G., et al., 2010a, Classical and Quantum Gravity, 27, 084013 (Cited on page 103.)

Hobbs G., Lyne A. G., Kramer M., 2010b, MNRAS, 402, 1027 (Cited on page 109.)

Hobbs G., et al., 2012, MNRAS, 427, 2780 (Cited on pages 34, 37 and 123.)

Hobbs G., Dai S., Manchester R. N., Shannon R. M., Kerr M., Lee K. J., Xu R., 2014, preprint, (arXiv:1407.0435) (Cited on pages 120 and 121.)

Högbom J. A., 1974, A&ASuppl., 15, 417 (Cited on page 46.)

Hoogeveen G. W., Jacobson A. R., 1997, Annales Geophysicae, 15, 236 (Cited on page 17.)

Hotan A. W., van Straten W., Manchester R. N., 2004, PASA, 21, 302 (Cited on pages 34 and 60.)

Howard T. A., Stovall K., Dowell J., Taylor G. B., White S. M., 2016, ApJ, 831, 208 (Cited on pages 58 and 78.)

Hu W., Barkana R., Gruzinov A., 2000, Phys. Rev. Lett., 85, 1158 (Cited on pages 24 and 101.)

Hui L., Ostriker J. P., Tremaine S., Witten E., 2017, Phys. Rev. D, 95, 043541 (Cited on pages 24, 101 and 102.)

Hulse R. A., Taylor J. H., 1975, ApJ, 195, L51 (Cited on page 18.)

Ilie C. D., Johnston S., Weltevrede P., 2019, MNRAS, 483, 2778 (Cited on page 8.)

Iršič V., Viel M., Haehnelt M. G., Bolton J. S., Becker G. D., 2017, Phys. Rev. Lett., 119, 031302 (Cited on page 102.)

Irwin A. W., Fukushima T., 1999, A&A, 348, 642 (Cited on page 37.)

Izvekova V. A., Kuzmin A. D., Malofeev V. M., Shitov I. P., 1981, Ap&SS, 78, 45 (Cited on page 6.)

Janssen G., et al., 2015, Advancing Astrophysics with the Square Kilometre Array (AASKA14), p. 37 (Cited on page 128.)

Jenet F. A., Anderson S. B., Kaspi V. M., Prince T. A., Unwin S. C., 1998, ApJ, 498, 365 (Cited on page 8.)

Jensen E. A., Hick P. P., Bisi M. M., Jackson B. V., Clover J., Mulligan T., 2010, Sol. Phys., 265, 31 (Cited on page 18.)

Johnston S., Karastergiou A., 2017, MNRAS, 467, 3493 (Cited on page 10.)

Johnston S., Ball L., Wang N., Manchester R. N., 2005, MNRAS, 358, 1069 (Cited on pages 17 and 83.)

Johnston S., et al., 2008a, Experimental Astronomy, 22, 151 (Cited on page 31.)

Johnston S., Karastergiou A., Mitra D., Gupta Y., 2008b, MNRAS, 388, 261 (Cited on pages 8 and 58.)

Jones M. L., et al., 2017, ApJ, 841, 125 (Cited on page 14.)

Kaplinghat M., Knox L., Turner M. S., 2000, Phys. Rev. Lett., 85, 3335 (Cited on page 24.)

Karastergiou A., Johnston S., 2007, MNRAS, 380, 1678 (Cited on page 9.)

Karuppusamy R., Stappers B. W., van Straten W., 2010, A&A, 515, A36 (Cited on page 29.)

Kashiyama K., Oguri M., 2018, arXiv e-prints, (Cited on page 24.)

Kazantsev A. P., 1968, Soviet Journal of Experimental and Theoretical Physics, 26, 1031 (Cited on page 21.)

Keith M. J., et al., 2013, MNRAS, 429, 2161 (Cited on pages 14, 77 and 112.)

Kennett M., Melrose D., 1998, PASA, 15, 211 (Cited on page 8.)

Khmelnitsky A., Rubakov V., 2014, JCAP, 2, 019 (Cited on pages 102, 104 and 127.)

Kijak J., Basu R., Lewandowski W., Rożko K., Dembska M., 2017, ApJ, 840, 108 (Cited on page 8.)

Klypin A., Kravtsov A. V., Valenzuela O., Prada F., 1999, ApJ, 522, 82 (Cited on page 23.)

Klypin A., Karachentsev I., Makarov D., Nasonova O., 2015, MNRAS, 454, 1798 (Cited on page 23.)

Kobayashi T., Murgia R., De Simone A., Iršič V., Viel M., 2017, Phys. Rev. D, 96, 123514 (Cited on page 102.)

Kolmogorov A. N., 1941, Akademiia Nauk SSSR Doklady, 32, 16 (Cited on pages 21 and 77.)

Komesaroff M. M., 1970, Nature, 225, 612 (Cited on pages 6 and 9.)

Koopmans L. V. E., Treu T., 2003, ApJ, 583, 606 (Cited on page 100.)

Kóta J., Jokipii J. R., 2000, ApJ, 531, 1067 (Cited on page 82.)

Kotelnikov V. A., 1933, Procs. of the first All-Union Conference on the technological reconstruction of the communications sector and low-current engineering (Cited on page 28.)

Koushiappas S. M., Zentner A. R., 2006, ApJ, 639, 7 (Cited on page 19.)

Kramer M., 1994, A&ASuppl., 107, 527 (Cited on page 35.)

Kramer M., 1995, PhD thesis, University of Bonn (Cited on page 10.)

Kramer M., Champion D. J., 2013, Classical and Quantum Gravity, 30, 224009 (Cited on page 103.)

Kramer M., Xilouris K. M., Lorimer D. R., Doroshenko O., Jessner A., Wielebinski R., Wolszczan A., Camilo F., 1998, ApJ, 501, 270 (Cited on page 6.)

Kramer M., Backer D. C., Cordes J. M., Lazio T. J. W., Stappers B. W., Johnston S., 2004, New Astr. Rev., 48, 993 (Cited on page 123.)

Kramer M., Lyne A. G., O'Brien J. T., Jordan C. A., Lorimer D. R., 2006a, Science, 312, 549 (Cited on page 6.)

Kramer M., et al., 2006b, Science, 314, 97 (Cited on page 19.)

Kritsuk A. G., Norman M. L., Padoan P., Wagner R., 2007, ApJ, 665, 416 (Cited on page 21.)

Krnjaic G., Machado P. A. N., Necib L., 2018, Phys. Rev. D, 97, 075017 (Cited on page 104.)

Krumholz M. R., Matzner C. D., McKee C. F., 2006, ApJ, 653, 361 (Cited on page 21.)

Kuethe D. O., Caprihan A., Gach H. M., Lowe I. J., Fukushima E., 2000, Journal of Applied Physiology, 88, 2279 (Cited on page 53.)

Landau L. D., 1932, Phys. Zs. Sowjet., vol.1, p.285, 1932 (English and German), 1, 285 (Cited on page 4.)

Large M. I., Vaughan A. E., Mills B. Y., 1968, Nature, 220, 340 (Cited on pages 4 and 12.)

Lazarian A., 2009, Space Sci. Rev., 143, 357 (Cited on page 21.)

Lazarian A., Pogosyan D., 2016, ApJ, 818, 178 (Cited on pages 83 and 97.)

Lazarian A., Eyink G. L., Vishniac E. T., 2012, Physics of Plasmas, 19, 012105 (Cited on page 96.)

Lazarian A., de Gouveia Dal Pino E. M., Melioli C., eds, 2015, Magnetic Fields in Diffuse Media Astrophysics and Space Science Library Vol. 407, doi:10.1007/978-3-662-44625-6. (Cited on page 21.)

Lazarus P., et al., 2014, MNRAS, 437, 1485 (Cited on page 40.)

Lazarus P., Karuppusamy R., Graikou E., Caballero R. N., Champion D. J., Lee K. J., Verbiest J. P. W., Kramer M., 2016, MNRAS, 458, 868 (Cited on page 60.)

Lazio T. J. W., 2013, Classical and Quantum Gravity, 30, 224011 (Cited on page 120.)

Lazio T. J. W., Gaensler B. M., 2007, Highlights of Astronomy, 14, 390 (Cited on page 30.)

Lee E. J., Murray N., Rahman M., 2012, ApJ, 752, 146 (Cited on page 21.)

Lenc E., et al., 2016, ApJ, 830, 38 (Cited on pages 59 and 127.)

Lentati L., Alexander P., Hobson M. P., Taylor S., Gair J., Balan S. T., van Haasteren R., 2013, Phys. Rev. D, 87, 104021 (Cited on page 110.)

Lentati L., Alexander P., Hobson M. P., Feroz F., van Haasteren R., Lee K. J., Shannon R. M., 2014, MNRAS, 437, 3004 (Cited on pages 40 and 112.)

Lentati L., et al., 2015, MNRAS, 453, 2576 (Cited on page 19.)

Lentati L., et al., 2016, MNRAS, 458, 2161 (Cited on pages 15, 106 and 112.)

Levy G. S., Sato T., Seidel B. L., Stelzried C. T., Ohlson J. E., Rusch W. V. T., 1969, Science, 166, 596 (Cited on page 18.)

Lidz A., Hui L., 2018, Phys. Rev. D, 98, 023011 (Cited on page 102.)

Lipunov V. M., 1992, Astrophysics of Neutron Stars (Cited on page 12.)

Liu H., Stolle C., FöRster M., Watanabe S., 2007, Journal of Geophysical Research (Space Physics), 112, A11311 (Cited on page 74.)

Loi S. T., et al., 2015, Geoph. Research Lett., 42, 3707 (Cited on pages 17 and 127.)

Lorimer D. R., Kramer M., 2004, Handbook of Pulsar Astronomy (Cited on pages 5, 9, 11, 14, 17, 35 and 39.)

Lorimer D. R., Yates J. A., Lyne A. G., Gould D. M., 1995, MNRAS, 273, 411 (Cited on page 6.)

Lyne A. G., Manchester R. N., 1988, MNRAS, 234, 477 (Cited on page 9.)

Lyne A. G., Rickett B. J., 1968, Nature, 219, 1339 (Cited on page 16.)

Lyne A. G., Smith F. G., 1968, Nature, 218, 124 (Cited on page 8.)

Lyne A. G., Pritchard R. S., Graham-Smith F., 2001, MNRAS, 321, 67 (Cited on page 83.)

Lyne A. G., et al., 2004, Science, 303, 1153 (Cited on pages 18 and 19.)

Ma X. F., Maruyama T., Ma G., Takeda T., 2005, Journal of Geophysical Research (Space Physics), 110, A05308 (Cited on page 127.)

Ma Y. K., Mao S. A., Basu A., Heiles C., West J., 2017, Galaxies, 5, 66 (Cited on page 47.)

Macciò A. V., Kang X., Fontanot F., Somerville R. S., Koposov S., Monaco P., 2010, MNRAS, 402, 1995 (Cited on page 23.)

Mahoney M. J., Erickson W. C., 1985, Nature, 317, 154 (Cited on page 29.)

Malbon R. K., Baugh C. M., Frenk C. S., Lacey C. G., 2007, MNRAS, 382, 1394 (Cited on page 19.)

Malofeev V. M., Malov I. F., 1980, Soviet Ast., 24, 90 (Cited on page 8.)

Malofeev V. M., Malov O. I., Shchegoleva N. V., 2000, Astronomy Reports, 44, 436 (Cited on page 29.)

Manchester R. N., Hobbs G. B., Teoh A., Hobbs M., 2005, VizieR Online Data Catalog, 7245 (Cited on pages 11, 18, 89, 91 and 107.)

Manchester R. N., et al., 2013, PASA, 30, e017 (Cited on pages 19, 103 and 105.)

Mao S. A., Gaensler B. M., Haverkorn M., Zweibel E. G., Madsen G. J., McClure-Griffiths N. M., Shukurov A., Kronberg P. P., 2010, ApJ, 714, 1170 (Cited on page 45.)

Maron J., Goldreich P., 2001, ApJ, 554, 1175 (Cited on page 21.)

Maron O., Kijak J., Kramer M., Wielebinski R., 2000, A&ASuppl., 147, 195 (Cited on page 6.)

Maus S., Rother M., Stolle C., Mai W., Choi S., Lühr H., Cooke D., Roth C., 2006, Geochemistry, Geophysics, Geosystems, 7, Q07008 (Cited on page 65.)

McGaugh S. S., Lelli F., Schombert J. M., 2016, Phys. Rev. Lett., 117, 201101 (Cited on page 23.)

McKay-Bukowski D., et al., 2015, IEEE Transactions on Geoscience and Remote Sensing, 53, 1440 (Cited on page 33.)

McKee C. F., 1989, ApJ, 345, 782 (Cited on page 21.)

McKee C. F., Ostriker E. C., 2007, ARA&A, 45, 565 (Cited on page 82.)

McLaughlin M. A., 2013, Classical and Quantum Gravity, 30, 224008 (Cited on page 103.)

Migdal A. B., 1959, Nucl. Phys. A, 13, 655 (Cited on page 4.)

Minter A. H., 1995, PhD thesis, THE UNIVERSITY OF IOWA. (Cited on pages 86 and 87.)

Minter A. H., Spangler S. R., 1996, ApJ, 458, 194 (Cited on pages 77, 81, 82, 84, 86, 90, 91, 93, 95, 96, 97 and 126.)

Mitra D., Wielebinski R., Kramer M., Jessner A., 2003, A&A, 398, 993 (Cited on page 17.)

Mocz P., Succi S., 2015, Phys. Rev. E, 91, 053304 (Cited on page 102.)

Mortier A., Faria J. P., Correia C. M., Santerne A., Santos N. C., 2015, A&A, 573, A101 (Cited on pages 50 and 51.)

Mosert M., Gende M., Brunini C., Ezquer R., Altadill D., 2007, Advances in Space Research, 39, 841 (Cited on page 59.)

Nadyozhin D. K., Imshennik V. S., 2005, International Journal of Modern Physics A, 20, 6597 (Cited on page 5.)

Nan R., et al., 2011, International Journal of Modern Physics D, 20, 989 (Cited on pages 120 and 128.)

Narayan R., 1992, Philosophical Transactions of the Royal Society of London Series A, 341, 151 (Cited on page 16.)

Navarro J. F., Eke V. R., Frenk C. S., 1996a, MNRAS, 283, L72 (Cited on page 23.)

Navarro J. F., Frenk C. S., White S. D. M., 1996b, ApJ, 462, 563 (Cited on page 122.)

Nori M., Baldi M., 2018, MNRAS, 478, 3935 (Cited on page 102.)

Norman C., Silk J., 1980, ApJ, 238, 158 (Cited on page 21.)

Noutsos A., Johnston S., Kramer M., Karastergiou A., 2008, MNRAS, 386, 1881 (Cited on pages 22 and 43.)

Noutsos A., et al., 2015, A&A, 576, A62 (Cited on pages 8, 45 and 61.)

Novikov A. Y., Popov M. V., Soglasnov V. A., Bruk Y. M., Ustimenko B. Y., 1984, AZh, 61, 343 (Cited on page 29.)

Nyquist H., 1928, Transactions of the American Institute of Electrical Engineers, Volume 47, Issue 2, pp. 617-624, 47, 617 (Cited on page 28.)

O'Sullivan S. P., et al., 2012, MNRAS, 421, 3300 (Cited on pages 42 and 47.)

Oberoi D., Lonsdale C. J., 2012, Radio Science, 47, RS0K08 (Cited on pages 18 and 126.)

Oh S.-H., de Blok W. J. G., Brinks E., Walter F., Kennicutt Jr. R. C., 2011, AJ, 141, 193 (Cited on page 23.)

Oppenheimer J. R., Volkoff G. M., 1939, Phys. Rev., 55, 374 (Cited on page 4.)

Oppermann N., et al., 2012, A&A, 542, A93 (Cited on page 82.)

Orús R., Hernández-Pajares M., Juan J. M., Sanz J., 2005, Journal of Atmospheric and Solar-Terrestrial Physics, 67, 1598 (Cited on pages 67 and 83.)

Osłowski S., van Straten W., Hobbs G. B., Bailes M., Demorest P., 2011, MNRAS, 418, 1258 (Cited on page 121.)

Ostriker J., 1968, Nature, 217, 1227 (Cited on page 4.)

Özel F., Freire P., 2016, ARA&A, 54, 401 (Cited on page 19.)

Pacholczyk A. G., Swihart T. L., 1970, ApJ, 161, 415 (Cited on page 8.)

Pacini F., 1967, Nature, 216, 567 (Cited on page 4.)

Parsons A. R., et al., 2010, AJ, 139, 1468 (Cited on page 31.)

Pavlov G. G., Rangelov B., Kargaltsev O., Reisenegger A., Guillot S., Reyes C., 2017, ApJ, 850, 79 (Cited on page 12.)

Pen U.-L., Levin Y., 2014, MNRAS, 442, 3338 (Cited on page 126.)

Petit G., 2004, in Finkelstein A., Capitaine N., eds, Proceedings of the Journées 2003 "Systèmes deréférence spatio-temporels": Astrometry, Geodynamics and Solar System Dynamics: from milliarcseconds to microarcseconds. pp 314–317 (Cited on page 37.)

Petrova S. A., 2001, A&A, 378, 883 (Cited on page 8.)

Philippov A., Uzdensky D. A., Spitkovsky A., Cerutti B., 2019, arXiv e-prints, (Cited on page 9.)

Phinney E. S., 2001, arXiv Astrophysics e-prints, (Cited on page 19.)

Piontek R. A., Ostriker E. C., 2007, ApJ, 663, 183 (Cited on page 21.)

Planck Collaboration et al., 2016, A&A, 594, A13 (Cited on pages 22 and 100.)

Porayko N. K., Postnov K. A., 2014, Phys. Rev. D, 90, 062008 (Cited on pages 102, 103, 118 and 119.)

Posti L., Helmi A., 2019, A&A, 621, A56 (Cited on pages 22 and 127.)

Preskill J., Wise M. B., Wilczek F., 1983, Phys. Lett. B, 120, 127 (Cited on page 101.)

Press W. H., Teukolsky S. A., Vetterling W. T., Flannery B. P., 1996, Numerical Recipes in C. Vol. 2, Cambridge university press Cambridge (Cited on page 108.)

Primack J. R., 2012, Annalen der Physik, 524, 535 (Cited on pages 22 and 100.)

Radhakrishnan V., Cooke D. J., 1969, Astrophys. Lett., 3, 225 (Cited on pages 6 and 8.)

Radhakrishnan V., Srinivasan G., 1982, Current Science, 51, 1096 (Cited on page 12.)

Rajwade K., Lorimer D. R., Anderson L. D., 2016, MNRAS, 455, 493 (Cited on page 8.)

Rama Rao P. V. S., Niranjan K., Prasad D. S. V. V. D., Gopi Krishna S., Uma G., 2006, Annales Geophysicae, 24, 2159 (Cited on page 127.)

Rankin J. M., 1993, ApJ, 405, 285 (Cited on page 9.)

Rankin J. M., Comella J. M., Craft Jr. H. D., Richards D. W., Campbell D. B., Counselman III C. C., 1970, ApJ, 162, 707 (Cited on page 29.)

Rankin J. M., Campbell D. B., Isaacman R. B., Payne R. R., 1988, A&A, 202, 166 (Cited on page 83.)

Ransom S. M., 2001, PhD thesis, Harvard University (Cited on page 29.)

Ransom S. M., et al., 2014, Nature, 505, 520 (Cited on page 19.)

Rathnasree N., Rankin J. M., 1995, ApJ, 452, 814 (Cited on pages 9 and 35.)

Read J. I., 2014, Journal of Phys. G Nuclear Physics, 41, 063101 (Cited on page 105.)

Rickett B. J., 1977, ARA&A, 15, 479 (Cited on page 58.)

Rickett B. J., 1990, ARA&A, 28, 561 (Cited on page 16.)

Rishbeth H., Garriott O. K., 1969, Introduction to ionospheric physics (Cited on page 63.)

Roberts J. A., Ables J. G., 1982, MNRAS, 201, 1119 (Cited on page 16.)

Sarkar A., Mondal R., Das S., Sethi S. K., Bharadwaj S., Marsh D. J. E., 2016, JCAP, 4, 012 (Cited on page 24.)

Saslaw W. C., 1968, Nature, 217, 1222 (Cited on page 4.)

Sazhin M. V., 1978, Soviet Ast., 22, 36 (Cited on pages 19 and 102.)

Sazonov V. N., 1969, Soviet Ast., 13, 396 (Cited on page 8.)

Schive H.-Y., Chiueh T., Broadhurst T., 2014, Nature Phys., 10, 496 (Cited on pages 102, 120 and 122.)

Schneider A., 2018, Phys. Rev. D, 98, 063021 (Cited on page 102.)

Schneider A., Trujillo-Gomez S., Papastergis E., Reed D. S., Lake G., 2017, MNRAS, 470, 1542 (Cited on page 23.)

Schnitzeler D. H. F. M., Lee K. J., 2015, MNRAS, 447, L26 (Cited on pages 54 and 55.)

Schnitzeler D. H. F. M., Lee K. J., 2017, MNRAS, 466, 378 (Cited on pages 46, 51, 53 and 54.)

Schnitzeler D. H. F. M., Katgert P., de Bruyn A. G., 2009, A&A, 494, 611 (Cited on page 46.)

Schnitzeler D. H. F. M., Banfield J. K., Lee K. J., 2015, MNRAS, 450, 3579 (Cited on page 47.)

Seto N., Cooray A., 2007, ApJ, 659, L33 (Cited on page 24.)

Shannon C. E., 1949, IEEE Proceedings, 37, 10 (Cited on page 28.)

Shannon R. M., Cordes J. M., 2012, ApJ, 761, 64 (Cited on page 121.)

Shannon R. M., et al., 2013, Science, 342, 334 (Cited on page 103.)

Shannon R. M., et al., 2015, Science, 349, 1522 (Cited on pages 19 and 103.)

Shapiro I. I., 1964, Phys. Rev. Lett., 13, 789 (Cited on page 37.)

Shapiro S. L., Teukolsky S. A., 1983, Black holes, white dwarfs, and neutron stars: The physics of compact objects (Cited on page 5.)

Sheikh S. I., Pines D. J., Ray P. S., Wood K. S., Lovellette M. N., Wolff M. T., 2006, Journal of Guidance Control Dynamics, 29, 49 (Cited on page 20.)

Simonetti J. H., Cordes J. M., 1986, ApJ, 310, 160 (Cited on page 82.)

Sivertsson S., Silverwood H., Read J. I., Bertone G., Steger P., 2018, MNRAS, 478, 1677 (Cited on pages 105, 123 and 131.)

Smirnov O. M., 2011, A&A, 527, A106 (Cited on page 61.)

Smith S., 1936, ApJ, 83, 23 (Cited on page 100.)

Sofue Y., 2012, Pub. of the Astr. Soc. of Jap., 64, 75 (Cited on page 122.)

Sokoloff D. D., Bykov A. A., Shukurov A., Berkhuijsen E. M., Beck R., Poezd A. D., 1998, MNRAS, 299, 189 (Cited on pages 42, 43 and 50.)

Somerville R. S., 2002, ApJ, 572, L23 (Cited on page 23.)

Sotomayor-Beltran C., et al., 2013, A&A, 552, A58 (Cited on pages 59 and 65.)

Spangler S. R., Gwinn C. R., 1990, ApJ, 353, L29 (Cited on page 82.)

Spera M., Mapelli M., Bressan A., 2015, MNRAS, 451, 4086 (Cited on page 5.)

Spergel D. N., Steinhardt P. J., 2000, Phys. Rev. Lett., 84, 3760 (Cited on page 24.)

Spitkovsky A., 2004, in Camilo F., Gaensler B. M., eds, IAU Symposium Vol. 218, Young Neutron Stars and Their Environments. p. 357 (arXiv:astro-ph/0310731) (Cited on page 6.)

Spitler L. G., et al., 2014, ApJ, 780, L3 (Cited on page 16.)

Staelin D. H., Reifenstein III E. C., 1968, Science, 162, 1481 (Cited on pages 4, 12 and 29.)

Stahler S. W., Palla F., 2005, The Formation of Stars (Cited on page 21.)

Stanimirovic S., Staveley-Smith L., Dickey J. M., Sault R. J., Snowden S. L., 1999, MNRAS, 302, 417 (Cited on page 82.)

Stinebring D. R., Smirnova T. V., Hankins T. H., Hovis J. S., Kaspi V. M., Kempner J. C., Myers E., Nice D. J., 2000, ApJ, 539, 300 (Cited on page 82.)

Stokes G. G., 1851, Transactions of the Cambridge Philosophical Society, 9, 399 (Cited on page 42.)

Stutzki J., Bensch F., Heithausen A., Ossenkopf V., Zielinsky M., 1998, A&A, 336, 697 (Cited on page 82.)

Sullivan J. M., Hirano S., Bromm V., 2018, MNRAS, 481, L69 (Cited on page 102.)

Suresh A., Cordes J. M., 2019, ApJ, 870, 29 (Cited on page 13.)

Svrcek P., Witten E., 2006, JHEP, 06, 051 (Cited on page 101.)

Tamburro D., Rix H.-W., Leroy A. K., Mac Low M.-M., Walter F., Kennicutt R. C., Brinks E., de Blok W. J. G., 2009, AJ, 137, 4424 (Cited on page 21.)

Tanabashi M., et al., 2018, Phys. Rev. D, 98, 030001 (Cited on page 22.)

Tauris T. M., van den Heuvel E. P. J., 2006, Formation and evolution of compact stellar X-ray sources. pp 623–665 (Cited on page 12.)

Taylor Jr. J. H., 1991, IEEE Proceedings, 79, 1054 (Cited on page 34.)

Taylor J. H., 1992, Philosophical Transactions of the Royal Society of London Series A, 341, 117 (Cited on page 35.)

Taylor S., Baker P. T., 2017, stevertaylor/NX01 1.2, doi:10.5281/zenodo.250258, https://doi.org/10.5281/zenodo.250258 (Cited on page 103.)

Taylor J. H., Weisberg J. M., 1989, ApJ, 345, 434 (Cited on pages 4 and 39.)

Taylor J. H., Fowler L. A., McCulloch P. M., 1979, Nature, 277, 437 (Cited on page 18.)

Taylor S. R., Lentati L., Babak S., Brem P., Gair J. R., Sesana A., Vecchio A., 2017, Phys. Rev. D, 95, 042002 (Cited on page 128.)

Tegmark M., et al., 2004, ApJ, 606, 702 (Cited on page 100.)

Thébault E., et al., 2015, Earth, Planets, and Space, 67, 79 (Cited on page 65.)

Thompson A. R., Moran J. M., Swenson Jr. G. W., 2001, Interferometry and Synthesis in Radio Astronomy, 2nd Edition (Cited on page 58.)

Tiburzi C., et al., 2016, MNRAS, 455, 4339 (Cited on pages 38, 115 and 128.)

Tiburzi C., et al., 2019, arXiv e-prints, (Cited on pages 13, 15, 90 and 128.)

Timokhin A. N., Arons J., 2013, MNRAS, 429, 20 (Cited on page 9.)

Tingay S. J., et al., 2013, PASA, 30, e007 (Cited on page 31.)

Tribble P. C., 1991, MNRAS, 250, 726 (Cited on page 42.)

Turner M. S., 1983, Phys. Rev. D, 28, 1243 (Cited on page 24.)

Uhlenbeck G. E., Ornstein L. S., 1930, Phys. Rev., 36, 823 (Cited on page 69.)

Veltmaat J., Niemeyer J. C., 2016, Phys. Rev. D, 94, 123523 (Cited on page 102.)

Veltmaat J., Niemeyer J. C., Schwabe B., 2018, Phys. Rev. D, 98, 043509 (Cited on page 102.)

Verbiest J. P. W., Shaifullah G. M., 2018, Classical and Quantum Gravity, 35, 133001 (Cited on page 128.)

Verbiest J. P. W., Weisberg J. M., Chael A. A., Lee K. J., Lorimer D. R., 2012, ApJ, 755, 39 (Cited on page 89.)

Verbiest J. P. W., et al., 2016, MNRAS, 458, 1267 (Cited on pages 19 and 103.)

Wang N., Manchester R. N., Johnston S., Rickett B., Zhang J., Yusup A., Chen M., 2005, MNRAS, 358, 270 (Cited on page 82.)

Wang C., Han J. L., Lai D., 2011, MNRAS, 417, 1183 (Cited on pages 43 and 58.)

Wang H. G., et al., 2014, ApJ, 789, 73 (Cited on page 9.)

Wang J. B., et al., 2015a, MNRAS, 446, 1657 (Cited on page 103.)

Wang Y., Mohanty S. D., Jenet F. A., 2015b, ApJ, 815, 125 (Cited on page 118.)

Wang X.-L., Wan Q.-T., Ma G.-Y., Li J.-H., Fan J.-T., 2016, Research in Astronomy and Astrophysics, 16, 116 (Cited on page 127.)

Weisberg J. M., Cordes J. M., Kuan B., Devine K. E., Green J. T., Backer D. C., 2004, ApJS, 150, 317 (Cited on page 59.)

William H. W., 1989, SIAM Revew, 31, 221 (Cited on page 110.)

Williamson I. P., 1972, MNRAS, 157, 55 (Cited on pages 15 and 16.)

Wilson T. L., Rohlfs K., Hüttemeister S., 2013, Tools of Radio Astronomy, doi:10.1007/978-3-642-39950-3. (Cited on page 58.)

Woosley S. E., Heger A., Weaver T. A., 2002, Reviews of Modern Physics, 74, 1015 (Cited on pages 4 and 5.)

Xilouris K. M., Kramer M., Jessner A., von Hoensbroech A., Lorimer D. R., Wielebinski R., Wolszczan A., Camilo F., 1998, ApJ, 501, 286 (Cited on page 8.)

Xu S., Zhang B., 2016, ApJ, 824, 113 (Cited on page 77.)

Yan W. M., et al., 2011a, Ap&SS, 335, 485 (Cited on page 69.)

Yan W. M., et al., 2011b, MNRAS, 414, 2087 (Cited on pages 59 and 83.)

Yao J. M., Manchester R. N., Wang N., 2017, ApJ, 835, 29 (Cited on page 22.)

You X. P., et al., 2007a, MNRAS, 378, 493 (Cited on pages 58 and 112.)

You X. P., Hobbs G. B., Coles W. A., Manchester R. N., Han J. L., 2007b, ApJ, 671, 907 (Cited on page 58.)

Zhu X.-J., et al., 2014, MNRAS, 444, 3709 (Cited on pages 103 and 119.)

Zhu X.-J., Wen L., Xiong J., Xu Y., Wang Y., Mohanty S. D., Hobbs G., Manchester R. N., 2016, MNRAS, 461, 1317 (Cited on pages 105 and 118.)

Zrake J., 2014, ApJ, 794, L26 (Cited on page 21.)

Zwicky F., 1933, Helvetica Physica Acta, 6, 110 (Cited on pages 22 and 100.)

Zwicky F., 1937, ApJ, 86, 217 (Cited on page 100.)

van Haarlem M. P., et al., 2013, A&A, 556, A2 (Cited on pages 31 and 33.)

van Haasteren R., Levin Y., 2013, MNRAS, 428, 1147 (Cited on pages 106 and 108.)

van Haasteren R., Vallisneri M., 2015, MNRAS, 446, 1170 (Cited on page 110.)

van Haasteren R., Levin Y., McDonald P., Lu T., 2009, MNRAS, 395, 1005 (Cited on pages 106 and 108.)

van Straten W., Bailes M., 2011, PASA, 28, 1 (Cited on pages 34 and 60.)

van Straten W., Demorest P., Oslowski S., 2012, Astronomical Research and Technology, 9, 237 (Cited on page 61.)

van Weeren R. J., et al., 2016, ApJS, 223, 2 (Cited on page 61.)

List of Figures

1.1 A schematic model of a pulsar 7
1.2 Individual pulses and the integrated profile of PSR B1133+16 10
1.3 Period-Period derivative (P-$\dot{P}$) diagram 11
1.4 The effect of dispersion on timing data of PSR J0837+0610 14
1.5 The DM time series of PSR J0034−0534 15
1.6 Dark matter density profiles obtained from rotation curves of seven low surface brightness galaxies 23

2.1 The scheme of phased arrays antenna 30
2.2 The principal scheme of inverted-V LBA and bow-tie HBA 32
2.3 The scheme of the data flow in German LOFAR stations 33
2.4 The geometry of pulsar timing and pulsar timing residuals 36
2.5 Polarisation ellipse 41
2.6 Illustration of PPA fitting technique 44
2.7 Faraday rotation of PSR J0953+0755. Application of different RM measurement techniques 48

3.1 Distribution of the reconstructed RMs for simulated data of PSR J1136+1551 54

4.1 *Top panel*: A comparison between classical RM synthesis and BGLSP methods. *Bottom panel*: Harmonic variations in Stokes Q and U across the observed bandwidth 62
4.2 *Top panel*: The uncertainties on the RM values detected with BGLSP (black circles), overplotted with the variance of the distribution of the detected RMs obtained from Monte Carlo simulations. *Lower panel* The difference between the injected RMs and the mean values of the Monte Carlo distributions 63
4.3 Example of application of JPLG ionospheric maps and POMME10 geomagnetic model to real data of PSR J0332+5434 observed by DE609 . . 64
4.4 *Upper panel*: Comparison between ionospheric RMs in the direction of PSR J0332+5434 observed at constant 30° elevation, as modelled by different ionospheric maps and different geomagnetic models: POMME10, EMM and IGRF12 66
4.5 Difference between ionospheric RMs in the direction of PSR J0332+5434 observed at multiple elevations along the day as modelled by as modelled by POMME10, EMM and IGRF12 67
4.6 Residuals ($\mathrm{RM_{obs}} - \mathrm{RM_{mod}}$), while applying the CODG+POMME10 and JPLG+POMME10 models for three different pulsars observed with three different GLOW stations 68

4.7 Correlation pattern of the RM residuals after correcting for the ionosphere with respect to the time in a day of observations for PSRs J0332+5434 and J1136+1551, while using JPLG+POMME10 model 70
4.8 Power spectrum of the RM residuals while applying JPLG+POMME10 model to a 6-month datasets of the circumpolar PSRs J0332+5434, J0814+7429 and J1136+1551 71
4.9 Absorption of the linear trend due to the application of the f_B factor in the long-term datasets of three pulsars 73
4.10 *Upper panel*: Rms of the RM residuals obtained by using the JPLG map and long-term datasets of four pulsars vs the f_B factor. *Lower panel*: Rms of the RM residuals obtained by using UQRG, JPLG, CODG, IGSG, and UPCG maps vs the f_B factor 75
4.11 One and two-dimensional posterior distribution for a subset of the noise parameters that characterize the RM residuals of PSR J0814+7429 after the subtraction of the ionospheric model 76

5.1 The long-term RM time series of PSRs J0332+5434, J0826+2637, J1136+1551, J1921+2153 84
5.2 The geometry that is used to derive the $\mathrm{SF}_{\mathrm{ISM}}(\delta\theta)$ and $C_{\mathrm{ISM}}(\delta\theta)$ 85
5.3 SFs of the RM time series from Figure 5.1. 88
5.4 One- and two-dimensional posterior distributions for $\mathcal{C}_B$ and α_B of PSRs J0332+5434 and J0826+2637 92
5.5 Posterior distributions and SFs for $\mathcal{C}_B$ and α_B of PSRs J1136+1551 and J1921+2153 93
5.6 Correlation of DM vs RM measurements of PSRs J1136+1551 and J1921+2153 94
5.7 95%-upper limits on the spectral coefficient $\mathcal{C}_B^2$ as a function of magnetic field spectral index α_B 96

6.1 Cumulative normalized $(\mathrm{S/N})^2$ of PPTA pulsars 116
6.2 The marginalized posterior distributions for the amplitude Ψ_c and frequency f for a signal injection in the actual PPTA data 117
6.3 Upper limits on the signal amplitude Ψ_c, generated by the scalar field dark matter in the Galaxy, as a function of boson mass 119
6.4 Upper limits on the dark matter density ρ in the Galaxy 120
6.5 The amplitude of the expected dark matter signal for different pulsars, assuming NFW dark matter density profile 123

A.1 Upper limits on the density of fuzzy dark matter ρ_{SF} in the Galaxy, as a function of frequency (boson mass): probing different statistics and SSE models 131

B.1 The one- and two-dimensional marginalized posterior distributions for the log-amplitude and slope of the DM and spin noises for the six best pulsars in the current PPTA data set 133

List of Tables

2.1 The LOFAR stations in Europe 33

4.1 Details of the observations used for the short-term and long-term analysis 60
4.2 Estimation of the noise parameters based on the model described in Equation (4.8) 79

5.1 The pulsar parameters – L, μ, DM, RM, n_0, $B_{\rm LOS}$– used for upper limit analysis 90
5.2 List of parameters used for the Bayesian analysis 91

6.1 Key characteristics of the PPTA pulsars 107
6.2 List of parameters and prior distributions used for the Bayesian analysis 111
6.3 Noise properties of PPTA pulsars, determined through Bayesian and Frequentist analyses 114
6.4 White noise for 10 PPTA pulsars in the FAST/SKA era 121